INNOVATIVE fMRI DATA MODELING METHODS FOR BRAIN-RELATED DISEASES/DISORDERS

EDITED BY: Xiaopeng Song, Fei Du, Yajun Ma and Zachory Wei

PUBLISHED IN: Frontiers in Neuroscience

frontiers Research Topics

ISSN 1664-8714
ISBN 978-2-88976-650-5
DOI 10.3389/978-2-88976-650-5

About Frontiers

Frontiers is more than just an open-access publisher of scholarly articles: it is a pioneering approach to the world of academia, radically improving the way scholarly research is managed. The grand vision of Frontiers is a world where all people have an equal opportunity to seek, share and generate knowledge. Frontiers provides immediate and permanent online open access to all its publications, but this alone is not enough to realize our grand goals.

Frontiers Journal Series

The Frontiers Journal Series is a multi-tier and interdisciplinary set of open-access, online journals, promising a paradigm shift from the current review, selection and dissemination processes in academic publishing. All Frontiers journals are driven by researchers for researchers; therefore, they constitute a service to the scholarly community. At the same time, the Frontiers Journal Series operates on a revolutionary invention, the tiered publishing system, initially addressing specific communities of scholars, and gradually climbing up to broader public understanding, thus serving the interests of the lay society, too.

Dedication to Quality

Each Frontiers article is a landmark of the highest quality, thanks to genuinely collaborative interactions between authors and review editors, who include some of the world's best academicians. Research must be certified by peers before entering a stream of knowledge that may eventually reach the public - and shape society; therefore, Frontiers only applies the most rigorous and unbiased reviews.
Frontiers revolutionizes research publishing by freely delivering the most outstanding research, evaluated with no bias from both the academic and social point of view. By applying the most advanced information technologies, Frontiers is catapulting scholarly publishing into a new generation.

What are Frontiers Research Topics?

Frontiers Research Topics are very popular trademarks of the Frontiers Journals Series: they are collections of at least ten articles, all centered on a particular subject. With their unique mix of varied contributions from Original Research to Review Articles, Frontiers Research Topics unify the most influential researchers, the latest key findings and historical advances in a hot research area! Find out more on how to host your own Frontiers Research Topic or contribute to one as an author by contacting the Frontiers Editorial Office: frontiersin.org/about/contact

INNOVATIVE fMRI DATA MODELING METHODS FOR BRAIN-RELATED DISEASES/DISORDERS

Topic Editors:
Xiaopeng Song, Harvard Medical School, United States
Fei Du, Harvard Medical School, United States
Yajun Ma, University of California, San Diego, United States
Zachory Wei, Emory University, United States

Citation: Song, X., Du, F., Ma, Y., Wei, Z., eds. (2022). Innovative fMRI Data Modeling Methods for Brain-Related Diseases/Disorders. Lausanne: Frontiers Media SA. doi: 10.3389/978-2-88976-650-5

Table of Contents

frontiers in Neuroscience

ORIGINAL RESEARCH
published: 21 December 2020
doi: 10.3389/fnins.2020.616872

Topological Abnormalities of Functional Brain Network in Early-Stage Parkinson's Disease Patients With Mild Cognitive Impairment

Xiangbin Chen[1], Mengting Liu[2], Zhibing Wu[1] and Hao Cheng[3]**

[1] Department of TCM Internal Medicine, The First Affiliated Hospital of Guangzhou University of Traditional Chinese Medicine, Guangzhou, China, [2] School of Music, Jimei University, Xiamen, China, [3] Department of Ultrasonography, Shaanxi Cancer Hospital Affiliated to Xi'an Jiaotong University, Xi'an, China

OPEN ACCESS

Edited by:
Zachory Wei,
Emory University, United States

Reviewed by:
Junhui Wang,
University of Toronto, Canada
Xiaopeng Song,
Harvard Medical School, United States
Daniele Corbo,
University of Brescia, Italy
Han Zhou,
The Scripps Research Institute, United States

***Correspondence:**
Zhibing Wu
nbk_gzucm@foxmail.com
Hao Cheng
uscheng_86@163.com

Specialty section:
This article was submitted to Brain Imaging Methods, a section of the journal Frontiers in Neuroscience

Received: *13 October 2020*
Accepted: *18 November 2020*
Published: *21 December 2020*

Citation:
Chen X, Liu M, Wu Z and Cheng H (2020) Topological Abnormalities of Functional Brain Network in Early-Stage Parkinson's Disease Patients With Mild Cognitive Impairment. Front. Neurosci. 14:616872. doi: 10.3389/fnins.2020.616872

Recent studies have demonstrated structural and functional alterations in Parkinson's disease (PD) with mild cognitive impairment (MCI). However, the topological patterns of functional brain networks in newly diagnosed PD patients with MCI are unclear so far. In this study, we used functional magnetic resonance imaging (fMRI) and graph theory approaches to explore the functional brain network in 45 PD patients with MCI (PD-MCI), 22 PD patients without MCI (PD-nMCI), and 18 healthy controls (HC). We found that the PD-MCI, PD-nMCI, and HC groups exhibited a small-world architecture in the functional brain network. However, early-stage PD-MCI patients had decreased clustering coefficient, increased characteristic path length, and changed nodal centrality in the default mode network (DMN), control network (CN), somatomotor network (SMN), and visual network (VN), which might contribute to factors for MCI symptoms in PD patients. Our results demonstrated that PD-MCI patients were associated with disrupted topological organization in the functional network, thus providing a topological network insight into the role of information exchange in the underlying development of MCI symptoms in PD patients.

Keywords: Parkinson's disease, mild cognitive impairment, fMRI, graph theory, small world

INTRODUCTION

Parkinson's disease (PD) is one of the most common neurodegenerative diseases with multiple movement disorders and non-motor symptoms. Among newly diagnosed PD patients, more than 20% will develop mild cognitive impairment (MCI) after 3–5 years. MCI is considered to be a high-risk factor for the further development of dementia, which will seriously affect the quality of patients' lives (Kehagia et al., 2010). Unfortunately, the neural basis underlying the MCI in PD is still not well understood.

As one of the most promising neuroimaging methods, magnetic resonance imaging (MRI) involving voxel-based morphometry (VBM), diffusion tensor imaging (DTI), and functional magnetic resonance imaging (fMRI) has been widely used to explore the structural and functional abnormality of the brain in PD patients with MCI (PD-MCI). Evidence from VBM in PD-MCI

showed structural atrophy in temporal, frontal, hippocampus, and thalamus regions, compared with PD without MCI (PD-nMCI) (Beyer et al., 2007; Chen et al., 2016; Gao et al., 2017). In a DTI study, FA values were found to be significantly decreased in parts of the corpus callosum in PD-MCI compared with healthy controls (HC) and no significant difference between patients with PD-nMCI and PD-MCI (Hattori et al., 2012). Another recent longitudinal DTI study showed significant mean diffusivity increase mainly in the frontal regions in the PD-MCI group when compared with the PD group with normal cognition (Minett et al., 2018). Moreover, investigators using the amplitude of low-frequency fluctuations (ALFF) and regional homogeneity (ReHo) as indicators in resting-state fMRI found PD patients with MCI had abnormal resting brain activity in the left middle temporal gyrus, right superior temporal gyrus, left superior frontal gyrus, right inferior frontal gyrus (Gao et al., 2016; Wang et al., 2018), left insula, and left precuneus (Li et al., 2020), compared with PD patients without MCI. The "structural atrophy" and "functional activity abnormalities" could indicate changes of neuronal plasticity (or due to synaptic loss), hyperexcitability, and neuronal circuit changes. The abnormalities in these regions were hypothesized to be the basis of neuroanatomy and pathophysiology in PD patients with MCI.

Recently, several studies by using resting-state fMRI found that functional disconnection could be also associated with MCI in PD. For example, the default mode network, which is highly relevant for cognitive processes, was found to have altered connectivity in PD with MCI (Hou et al., 2016). However, the other study showed that functional connectivity of the default mode network was altered in PD patients regardless of cognitive status, while a functional disconnection in the frontoparietal network was found to be associated with PD-MCI without detectable structural changes (Amboni et al., 2015). The patients "regardless of cognitive status" might indicate general pathological changes in the brain. MCI-related "topological changes in newly diagnosed PD" was mentioned but not directly supported by their results. Furthermore, findings in dynamic functional connectivity showed dynamic functional brain deterioration in PD-MCI, which is not present in PD without MCI (Díez-Cirarda et al., 2018). This evidence suggests that not only abnormalities in specific, discrete brain regions but also disruptions in functional connectivity or functional networks may be involved in the neural mechanisms of PD-MCI.

As an emerging method of network analysis, the graph theory modeled the brain as a complex functional system with topological features (such as small-world properties and nodal centralities), which are disrupted in PD patients. However, the MCI-related topological changes in the functional network were rarely explored, especially in the early-stage or newly diagnosed PD. Given the existence of structural and functional abnormalities in specific brain regions as well as disruption of functional connectivity in PD patients, it is plausible that the abnormalities of whole-brain topological networks in PD patients with MCI may be observed. Therefore, our study aimed to use resting-state fMRI data to find the MCI-related topological changes in newly diagnosed PD patients. First, we assessed the small-world topology of PD-nMCI, PD-MCI, and HC. Second, we investigated the topological parameters of the functional network (clustering coefficient, characteristic path length, and small-world index). Finally, we would like to evaluate the regions' changes from the flow of information perspective among these three groups by using nodal centrality.

MATERIALS AND METHODS

Participants

All MRI and experimental data used in this study were obtained from the Parkinson's Progression Markers Initiative (PPMI)[1], which is a large-scale, comprehensive observational, multicenter project of PD progression biomarkers (Marek et al., 2011). A total of 85 participants were analyzed, comprising 45 participants in the PD-nMCI group (mean age = 62.64 ± 9.86, 30 males), 22 in the PD-MCI group (mean age = 66.09 ± 8.56, 17 males), and 18 age- and sex-matched HC (mean age = 64.33 ± 9.87, 14 males) (**Table 1**). All PD patients were diagnosed according to the criteria of the United Kingdom Brain Bank (Hughes et al., 1992). The study was approved by Institutional Review Boards/Independent Ethics Committees. Written informed consent was obtained from all subjects. For more details on the study, please see http://www.ppmi-info.org/wp-content/uploads/2013/02/PPMI-Protocol-AM5-Final-27Nov2012v6-2.pdf.

MRI Data Acquisition

Imaging data were acquired on Siemens 3T MRI scanners. High-resolution structural images were acquired using a T1-weighted gradient-echo 3D MPRAGE sequence (TR = 2,300 ms, TE = 2.98, FA = 9°, 1 mm^3 isotropic voxel). Resting-state fMRI scans were acquired with an echo-planar sequence (TR = 2,400 ms, TE = 25 ms, FA = 80°, voxel size = 3.3 mm^3, total of 210 volumes, 40 axial slices). Subjects were advised to relax quietly with their eyes open for the resting-state functional scans while trying not to fall asleep.

Data Preprocessing

The preprocessing workflow was performed using fMRIPrep 1.4.1 (Esteban et al., 2019), which is based on Nipype 1.2.0 (Gorgolewski et al., 2011) (details of the preprocessing process are provided in the **Supplementary Material**).

Regions of Interest Parcelation

In the current study, we used the Schaefer parcelation template (Schaefer et al., 2018) with 100 parcels, each of which is related with one of the brain networks from the Yeo seven-network parcelation (Thomas Yeo et al., 2011)–the visual network (VN), dorsal attention network (DAN), somatomotor network (SMN), default mode network (DMN), limbic network (LN), frontoparietal task control network (CN), and ventral attention network (VAN) (**Supplementary Table 2**).

[1]http://www.ppmi-info.org

TABLE 1 | Demographic and clinical data of the subjects.

	PD-nMCI (*N* = 45)	PD-MCI (*N* = 22)	HC (*N* = 18)	Test factor	*P*-value
Age (years)	62.64 ± 9.86	66.09 ± 8.56	64.33 ± 9.87	$F = 0.99$	0.38
Gender (M/F)	30/15	17/5	14/4	$\chi^2 = 1.23$	0.54
Disease duration (years)	2.43 ± 1.22	2.78 ± 1.34	–	$T = -1.07$	0.06
UPDRS-III	20.49 ± 10.11	24.72 ± 12.49	–	$T = -1.49$	0.14
H&Y stage	1.69 ± 0.47	1.86 ± 0.35	–	$T = -1.55$	0.13
MoCa	28.24 ± 1.32	25.00 ± 2.99	27.56 ± 1.50	$F = 21.34$	<0.001
Education (years)	15.33 ± 2.84	15.86 ± 2.92	16.72 ± 2.67	$F = 1.57$	0.21

Graph Theory Analysis of the Functional Brain Network

We transformed the matrix of the inter-regional correlation coefficient into a binary matrix: if the positive value of the correlation coefficient was larger than a certain threshold, there was a relationship (assigned "1") in the matrix of 100 (occasionally 100 correlation coefficient); otherwise, there was no relationship (assigned "0"). There is currently no consensus among researchers on how to choose a fixed threshold. So, we threshed each matrix of correlation over a wide range of density (10 to 50% with an increase of 1%), then we estimated the properties of the resulting graphs at each threshold value. It can also describe the network with a continuous weighting between nodes, but this will result in complicated statistical feature descriptions in the graph theoretical analysis (He et al., 2007). This research, therefore, used binarized networks for explanations of statistical characteristics, which are comparatively simpler.

The coefficient C of the cluster parameter represents the complexity of network clustering (Watts et al., 1998; Sporns et al., 2004). The shortest path length indicated the shortest path for the information from one node to another node in the network. System resources were saved while information was transmitted more quickly through the shortest possible path (Latora and Marchiori, 2001). Small-world networks combine the benefits of regular networks (with a larger cluster coefficient and a longer characteristic path length) and random networks (with a smaller cluster coefficient and a shorter characteristic path length), which ensure the local and global efficiency of information transmission (Watts et al., 1998). A small-world index ($\sigma = \gamma/\lambda$) was used to measure the "small-world" characteristics of the network (Achard, 2006; Humphries et al., 2006). The betweenness centrality from a perspective of information flow describes the centrality of nodes (Freeman, 1977). We used $b_i = B(i)/B$ to normalize $B(i)$, where B represents the mean betweenness centrality of all the nodes in the network (Melie-García et al., 2013). Then, we calculated the area under the curve (AUC) for each network to seek the group differences of b_i, which offers a more straightforward scalar for brain network topology than the single threshold selection.

Statistical Analysis

To determine if significant group differences existed in the parameters of the graph theory (cluster coefficient, characteristic path length, and nodal centrality), non-parametric permutation tests were performed between groups. In short, we first calculated the difference between groups in the average value of each parameter to test the null hypothesis for each parameter that the observed group difference could happen by chance. We then reassigned all the values into two groups randomly and recomputed the mean differences between the two randomized groups. This randomization procedure was repeated 10,000 times, resulting in distributions of differences between groups for each parameter. Finally, we used the 95% points of the distributions (two-tailed) as the confidence intervals to test the null hypothesis. If the null hypothesis was rejected (outside the confidence intervals), the differences of parameters in the functional brain network were thought to be significant.

RESULTS

The Small-World Topology of Functional Brain Network in PD-MCI, PD-nMCI, and HC

The functional brain networks in all the three groups had the characteristics of "small-world" networks. The small-world index of these three groups was larger than one ($\sigma > 1$) over an entire range of density thresholds, indicating that even in human brains afflicted with MCI, a relatively efficient network was needed to maintain the daily activities (**Figure 1C**).

PD-MCI Patients versus PD-nMCI Patients ($P < 0.05$, Two-Tailed)

Compared with PD-nMCI patients, the PD-MCI patients showed significantly decreased clustering coefficient Cp (density thresholds: 10–25%, 27–32%, 36%) (**Figure 1A**), small-world index σ (density thresholds: 17 and 18%) (**Figure 1C**), and increased characteristic path length Lp (density thresholds: 20–29%) (**Figure 1B**). Meanwhile, increased nodal centrality in the VN, DMN, and CN was observed in the PD-MCI group, while there was decreased nodal centrality in the SMN (**Table 2**).

PD-MCI Patients Versus the HC Group ($P < 0.05$, Two-Tailed)

Compared with the HC group, PD-MCI patients showed significantly decreased clustering coefficient Cp (density thresholds: 11%, 16–18%, 20–21%, 32–41%) (**Figure 1A**).

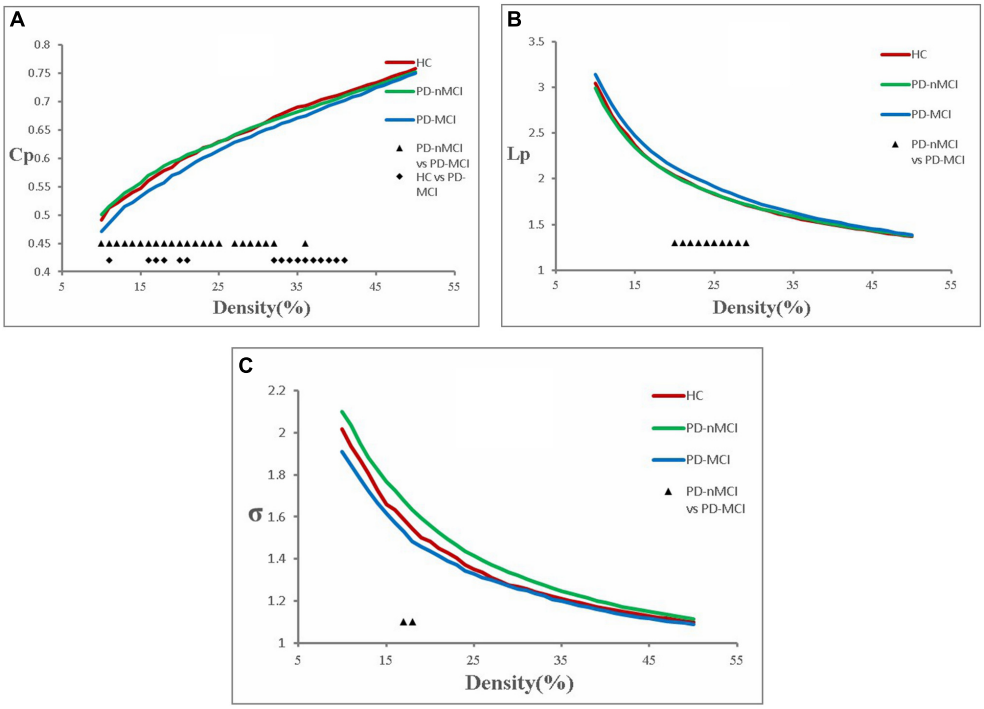

FIGURE 1 | Cluster coefficient (Cp), characteristic path length (Lp), and small-world index (σ) in PD-MCI, PD-nMCI, and HC. **(A)** The Cp from the three groups. The black triangle means significant differences between PD-nMCI and PD-MCI (density thresholds: 10–25%, 27–32%, 36%, $P < 0.05$, two-tailed). The black prismatic means significant differences between HC and PD-MCI (density thresholds: 11%, 16–18%, 20–21%, 32–41%, $P < 0.05$, two-tailed). **(B)** The Lp from the three groups. The black triangle means significant differences between PD-nMCI and PD-MCI (density thresholds: 20–29%, $P < 0.05$, two-tailed). **(C)** The σ from the three groups. The black triangle means significant differences between PD-nMCI and PD-MCI (density thresholds: 17–18%, $P < 0.05$, two-tailed).

PD-nMCI Patients versus the HC Group ($P < 0.05$, Two-Tailed)

There was no significant difference in Cp, Lp, and σ between the PD-nMCI and HC groups.

DISCUSSION

We employed an fMRI approach to seek the differences among PD-nMCI, PD-MCI, and HC to evaluate the topological changes of brain functional networks in early-stage PD patients with depression. Our results showed that compared with PD-nMCI, early-stage PD-MCI patients had decreased clustering coefficient, small-world index, and increased characteristic path length.

TABLE 2 | Nodal centrality differences between groups.

	ROI label	ROI name	ROI network	*P*-value
PD-MCI > PD-nMCI	3	7Networks_LH_Vis_3	VN	0.037
	41	7Networks_LH_Default_Par_2	DMN	0.002
	88	7Networks_RH_Cont_PFCmp_1	CN	0.042
PD-nMCI > PD-MCI	60	7Networks_RH_SomMot_2	SMN	0.027

ROI, region of interest.

Compared with the HC group, the PD-MCI groups showed a significantly decreased clustering coefficient. There was no significant difference in Cp, Lp, and σ between the PD-nMCI and HC groups. Therefore, we used nodal centrality to further test the hypothesis that small-world topology changes in PD-MCI patients may be accompanied by information communication alteration. Then, we found that nodal centrality was significantly increased in the VN, DMN, and CN, but significantly decreased in the SMN in PD-MCI compared with PD-nMCI. Due to the aim of seeking MCI-related changes in PD patients, we mainly focus on discussing the differences of topological organization between PD-MCI and PD-nMCI.

We found that the brain functional network of PD-MCI, PD-nMCI, and HC had a small-world property, which was consistent with many studies by using resting-state fMRI data in PD patients (Luo et al., 2015; Sang et al., 2015; Berman et al., 2016; Fang et al., 2017; Hou et al., 2020). Especially, in many studies of MCI and even dementia patients, the functional network still satisfies the network characteristics of the small world (Liu et al., 2012, 2014; Bai et al., 2013; Brier et al., 2014). Unlike a random network or regular network, a small-world network was found to be an optimized network for information separation and integration (Bullmore and Sporns, 2009). The brain functional network of PD-MCI and PD-nMCI patients also showed a small-world property in the current study, suggesting that even in patients

with neurological and psychotic disorders (such as Alzheimer's disease, PD, and MCI), a relatively efficient network was needed to maintain the daily activities.

Although the functional brain networks of these three groups retain small-world characteristics, it is found that the clustering coefficient and small-world index of the functional network in PD-MCI patients were significantly lower, and the characteristic path length was significantly longer than that in the PD-nMCI group. In a topological network, the clustering coefficient reflects the local efficiency and fault tolerance (Strogatz, 2001), while short characteristic path length ensures the prompt transfers and effective integration for information between distant brain areas (Sporns and Zwi, 2004). Therefore, the decreased clustering coefficient and increased characteristic path length of functional network in PD-MCI patients suggest that in the MCI state of PD, the local and global information processing efficiency of the patient's brain is significantly lower than that of the PD-nMCI state, and the brain's fault tolerance rate becomes worse. In addition, there was no significant difference of topological network between the PD-nMCI and HC groups. It means that the brain topology network of early PD-nMCI patients is similar to that of normal people. When PD patients are accompanied by MCI, the topology network begins to be damaged, which also explains the susceptibility of PD-MCI in topological network.

We also used betweenness centrality from a perspective of information flow to further support the hypothesis that increased characteristic path length and decreased clustering coefficient in PD-MCI patients may be accompanied by alterations of information communication. Our results showed that the regions with significant increased nodal centrality were located in the VN, DMN, and CN, while there was decreased centrality in the SMN. The DMN and CN are two networks closely related to cognitive processes in many neurologic and psychiatric disorders, including PD, AD, depression, and autism. In particular, in studies of PD patients with MCI, one study found significantly decreased functional connectivity within the DMN in the PD-MCI group compared with that in the PD-nMCI group (Hou et al., 2016). However, another study showed that a functional disconnection of the CN could be associated with MCI in PD, rather than the DMN (Amboni et al., 2015). Additionally, a recent fMRI study found no significant differences in nodal centralities between PD-MCI and PD-nMCI, but a changing trend in the DMN, CN, and SMN (Hou et al., 2020). These similar studies show that PD-MCI patients have evidence of cognitive-related network damage, but the damage pattern still needs more research to explore. The current study also found abnormalities of nodal centralities in SMN and VN, suggesting that sensorimotor and visual-related networks may be accompanied by changes in the cognitive process of PD. Taken together, we speculate that changes in nodal centrality in the DMN, CN, SMN, and VN may be contributing factors for MCI symptoms in PD patients, which may be an important mechanism for PD-MCI patients.

It is worth mentioning that although our study found that the PD-MCI group had significant abnormalities in topological network parameters compared with the PD-nMCI group, there were relatively few patients scanned by fMRI in the database, which limited our further research. First, the gender distribution within the group is uneven, that is, the number of male patients is more than twice as high as that of female patients. Since the potential incidence of Parkinson's disease in men is approximately twice that of women (Van Den Eeden et al., 2003), the gender distribution of groups is consistent with the incidence of Parkinson's disease in the population, but we cannot further reduce the impact of gender differences within the group on the results. Secondly, PD-MCI patients may also be accompanied by different mental illnesses including depression, anxiety, apathy, and so on. Because the number of subjects is relatively small, it is difficult to exclude these confounding factors in our results. However, our above research results are very similar to previous studies on PD-MCI. The abnormal network nodes we found are also located in common cognitive-related networks, such as the DMN and CN. Therefore, our results based on the current sample size are interpretable, but whether PD-MCI-related topological network abnormal patterns are fixed still requires more research, a larger sample size, and better elimination of various factors for further exploration.

CONCLUSION

We have investigated the topology of brain functional networks in early-stage PD patients with MCI using resting-state fMRI and graph theory analysis. Our result indicated that the brain of early-stage PD-MCI patients was related to decreased cluster coefficient, increased characteristic path length, and changed nodal centrality in the DMN, CN, SMN, and VN, which also provided a topological network insight into the role of information exchange in the underlying development of MCI symptoms in newly diagnosed PD patients.

DATA AVAILABILITY STATEMENT

The original contributions presented in the study are included in the article/**Supplementary Material**, further inquiries can be directed to the corresponding author/s.

ETHICS STATEMENT

The studies involving human participants were reviewed and approved by the Shaanxi Cancer Hospital Affiliated to Xi'an Jiaotong University. The patients/participants provided their written informed consent to participate in this study.

AUTHOR CONTRIBUTIONS

HC proposed the study concept, designed the experiments, and modified the manuscript. XC was responsible for performing the experiments and writing the original manuscript. ML was responsible for finding relevant literature and materials, and performing the experiments. ZW was responsible for revising the manuscript. All authors contributed to the article and approved the submitted version.

FUNDING

Data used in the preparation of this article were obtained from the Parkinson's Progression Markers Initiative database (www.ppmi-info.org/data). For up-to-date information on the study, visit www.ppmi-info.org. Parkinson's Progression Markers Initiative—a public–private partnership—was sponsored by the Michael J. Fox Foundation for Parkinson's Research (MJFF) and co-funded by MJFF, AbbVie, Avid Radiopharmaceuticals, Biogen Idec, Bristol-Myers Squibb, Covance, Eli Lilly & Co., F. Hoffman-La Roche, Ltd., GE Healthcare, Genentech, GlaxoSmithKline, Lundbeck, Merck, MesoScale, Piramal, Pfizer, and UCB. This project was also supported by Shaanxi Provincial Key R&D Plan (2020SF-163).

SUPPLEMENTARY MATERIAL

The Supplementary Material for this article can be found online at: https://www.frontiersin.org/articles/10.3389/fnins.2020.616872/full#supplementary-material

REFERENCES

Achard, S. (2006). A resilient, low-frequency, small-world human brain functional network with highly connected association cortical hubs. *J. Neurosci.* 26, 63–72. doi: 10.1523/JNEUROSCI.3874-05.2006

Amboni, M., Tessitore, A., Esposito, F., Santangelo, G., Picillo, M., Vitale, C., et al. (2015). Resting-state functional connectivity associated with mild cognitive impairment in Parkinson's disease. *J. Neurol.* 262, 425–434. doi: 10.1007/s00415-014-7591-5

Bai, L., Zhang, M., Chen, S., Ai, L., Xu, M., Wang, D., et al. (2013). Characterizing acupuncture de qi in mild cognitive impairment: relations with small-world efficiency of functional brain networks. *Evid. Based Complement. Alternat. Med.* 2013:304804. doi: 10.1155/2013/304804

Berman, B. D., Smucny, J., Wylie, K. P., Shelton, E., Kronberg, E., Leehey, M., et al. (2016). Levodopa modulates small-world architecture of functional brain networks in Parkinson's disease. *Mov. Disord.* 31, 1676–1684. doi: 10.1002/mds.26713

Beyer, M. K., Janvin, C. C., Larsen, J. P., and Aarsland, D. (2007). A magnetic resonance imaging study of patients with Parkinson's disease with mild cognitive impairment and dementia using voxel-based morphometry. *J. Neurol. Neurosurg. Psychiatry* 78, 254–259. doi: 10.1136/jnnp.2006.093849

Brier, M. R., Thomas, J. B., Fagan, A. M., Hassenstab, J., Holtzman, D. M., Benzinger, T. L., et al. (2014). Functional connectivity and graph theory in preclinical Alzheimer's disease. *Neurobiol. Aging* 35, 757–768. doi: 10.1016/j.neurobiolaging.2013.10.081

Bullmore, E., and Sporns, O. (2009). Complex brain networks: graph theoretical analysis of structural and functional systems. *Nat. Rev. Neurosci.* 10, 186–198. doi: 10.1038/nrn2575

Chen, F. X., Kang, D. Z., Chen, F. Y., Liu, Y., Wu, G., Li, X., et al. (2016). Gray matter atrophy associated with mild cognitive impairment in Parkinson's disease. *Neurosci. Lett.* 617, 160–165. doi: 10.1016/j.neulet.2015.12.055

Díez-Cirarda, M., Strafella, A. P., Kim, J., Peña, J., Ojeda, N., Cabrera-Zubizarreta, A., et al. (2018). Dynamic functional connectivity in Parkinson's disease patients with mild cognitive impairment and normal cognition. *NeuroImage Clin.* 17, 847–855. doi: 10.1016/j.nicl.2017.12.013

Esteban, O., Markiewicz, C. J., Blair, R. W., Moodie, C. A., Isik, A. I., Erramuzpe, A., et al. (2019). fMRIPrep: a robust preprocessing pipeline for functional MRI. *Nat. Methods* 16, 111–116. doi: 10.1038/s41592-018-02354

Fang, J., Chen, H., Cao, Z., Jiang, Y., Ma, L., Ma, H., et al. (2017). Impaired brain network architecture in newly diagnosed Parkinson's disease based on graph theoretical analysis. *Neurosci. Lett.* 657, 151–158. doi: 10.1016/j.neulet.2017.08.002

Freeman, L. C. (1977). A set of measures of centrality based on betweenness. *Sociometry* 40, 35–41. doi: 10.2307/3033543

Gao, L., Wu, X., Zhang, J., Chan, P., and Wu, T. (2016). Brain activity in Parkinson's disease patients with mild cognitive impairment. *Sci. Bull.* 61, 1876–1883. doi: 10.1007/s11434-016-12059

Gao, Y., Nie, K., Huang, B., Mei, M., Guo, M., Xie, S., et al. (2017). Changes of brain structure in Parkinson's disease patients with mild cognitive impairment analyzed via VBM technology. *Neurosci. Lett.* 658, 121–132. doi: 10.1016/j.neulet.2017.08.028

Gorgolewski, K., Burns, C. D., Madison, C., Clark, D., Halchenko, Y. O., Waskom, M. L., et al. (2011). Nipype: a flexible, lightweight and extensible neuroimaging data processing framework in Python. *Front. Neuroinform.* 5:13. doi: 10.3389/fninf.2011.00013

Hattori, T., Orimo, S., Aoki, S., Ito, K., Abe, O., Amano, A., et al. (2012). Cognitive status correlates with white matter alteration in Parkinson's disease. *Hum. Brain Mapp.* 33, 727–739. doi: 10.1002/hbm.21245

He, Y., Chen, Z. J., and Evans, A. C. (2007). Small-world anatomical networks in the human brain revealed by cortical thickness from MRI. *Cereb. Cortex* 17, 2407–2419. doi: 10.1093/cercor/bhl149

Hou, Y., Wei, Q., Ou, R., Yang, J., Gong, Q., and Shang, H. (2020). Impaired topographic organization in Parkinson's disease with mild cognitive impairment. *J. Neurol. Sci.* 414:116861. doi: 10.1016/j.jns.2020.116861

Hou, Y., Yang, J., Luo, C., Song, W., Ou, R., Liu, W., et al. (2016). Dysfunction of the default mode network in drug-naïve Parkinson's disease with mild cognitive impairments: a resting-state fMRI study. *Front. Aging Neurosci.* 8:247. doi: 10.3389/fnagi.2016.00247

Hughes, A. J., Daniel, S. E., Kilford, L., and Lees, A. J. (1992). Accuracy of clinical diagnosis of idiopathic Parkinson's disease: a clinico-pathological study of 100 cases. *J. Neurol. Neurosurg. Psychiatry* 55, 181–184. doi: 10.1136/jnnp.55.3.181

Humphries, M., Gurney, K., and Prescott, T. (2006). The brainstem reticular formation is a small-world, not scale-free, network. *Proc. R. Soc. B Biol. Sci.* 273, 503–511. doi: 10.1098/rspb.2005.3354

Kehagia, A. A., Barker, R. A., and Robbins, T. W. (2010). Neuropsychological and clinical heterogeneity of cognitive impairment and dementia in patients with Parkinson's disease. *Lancet Neurol.* 9, 1200–1213. doi: 10.1016/S1474-4422(10)70212-X

Latora, V., and Marchiori, M. (2001). Efficient behavior of small-world networks. *Phys. Rev. Lett.* 87:198701. doi: 10.1103/PhysRevLett.87.198701

Li, M. G., Liu, T. F., Zhang, T. H., Chen, Z. Y., Nie, B. B., Lou, X., et al. (2020). Alterations of regional homogeneity in Parkinson's disease with mild cognitive impairment: a preliminary resting-state fMRI study. *Neuroradiology* 62, 327–334. doi: 10.1007/s00234-019-023337

Liu, Y., Yu, C., Zhang, X., Liu, J., Duan, Y., Alexander-Bloch, A. F., et al. (2014). Impaired long distance functional connectivity and weighted network architecture in Alzheimer's disease. *Cereb. Cortex* 24, 1422–1435. doi: 10.1093/cercor/bhs410

Liu, Z., Zhang, Y., Yan, H., Bai, L., Dai, R., Wei, W., et al. (2012). Altered topological patterns of brain networks in mild cognitive impairment and Alzheimer's disease: a resting-state fMRI study. *Psychiatry Res.* 202, 118–125. doi: 10.1016/j.pscychresns.2012.03.002

Luo, C. Y., Guo, X. Y., Song, W., Chen, Q., Cao, B., Yang, J., et al. (2015). Functional connectome assessed using graph theory in drug-naive Parkinson's disease. *J. Neurol.* 262, 1557–1567. doi: 10.1007/s00415-015-77503

Marek, K., Jennings, D., Lasch, S., Siderowf, A., Tanner, C., Simuni, T., et al. (2011). The Parkinson progression marker initiative (PPMI). *Prog. Neurobiol.* 95, 629–635. doi: 10.1016/j.pneurobio.2011.09.005

Melie-García, L., Sanabria-Diaz, G., and Sánchez-Catasús, C. (2013). Studying the topological organization of the cerebral blood flow fluctuations in resting state. *Neuroimage* 64, 173–184. doi: 10.1016/j.neuroimage.2012.08.082

Minett, T., Su, L., Mak, E., Williams, G., Firbank, M., Lawson, R. A., et al. (2018). Longitudinal diffusion tensor imaging changes in early Parkinson's disease: ICICLE-PD study. *J. Neurol.* 265, 1528–1539. doi: 10.1007/s00415-018-88730

Sang, L., Zhang, J., Wang, L., Zhang, J., Zhang, Y., Li, P., et al. (2015). Alteration of brain functional networks in early-stage Parkinson's disease: a resting- state fMRI study. *PLoS One* 10:e0141815. doi: 10.1371/journal.pone.0141815

Schaefer, A., Kong, R., Gordon, E. M., Laumann, T. O., Zuo, X.-N., Holmes, A. J., et al. (2018). Local-global parcellation of the human cerebral cortex from intrinsic functional connectivity MRI. *Cereb. Cortex* 28, 3095–3114. doi: 10.1093/cercor/bhx179

Sporns, O., Chialvo, D. R., Kaiser, M., and Hilgetag, C. C. (2004). Organization, development and function of complex brain networks. *Trends Cogn. Sci.* 8, 418–425. doi: 10.1016/j.tics.2004.07.008

Sporns, O., and Zwi, J. D. (2004). The small world of the cerebral cortex. *Neuroinformatics* 2, 145–162. doi: 10.1385/NI:2:2:145

Strogatz, S. H. (2001). Exploring complex networks. *Nature* 410, 268–276. doi: 10.1038/35065725

Thomas Yeo, B. T., Krienen, F. M., Sepulcre, J., Sabuncu, M. R., Lashkari, D., Hollinshead, M., et al. (2011). The organization of the human cerebral cortex estimated by intrinsic functional connectivity. *J. Neurophysiol.* 106, 1125–1165. doi: 10.1152/jn.00338.2011

Van Den Eeden, S. K., Tanner, C. M., Bernstein, A. L., Fross, R. D., Leimpeter, A., Bloch, D. A., et al. (2003). Incidence of Parkinson's disease: variation by age, gender, and race/ethnicity. *Am. J. Epidemiol.* 157, 1015–1022. doi: 10.1093/aje/kwg068

Wang, Z., Jia, X., Chen, H., Feng, T., and Wang, H. (2018). Abnormal spontaneous brain activity in early Parkinson's disease with mild cognitive impairment: a resting-state fMRI Study. *Front. Physiol.* 9:1093. doi: 10.3389/fphys.2018.01093

Watts, D. J., Watts, D. J., Strogatz, S. H., and Strogatz, S. H. (1998). Collective dynamics of "small-world" networks. *Nature* 393, 440–442. doi: 10.1038/30918

Conflict of Interest: The authors declare that the research was conducted in the absence of any commercial or financial relationships that could be construed as a potential conflict of interest.

frontiers in Neuroscience

ORIGINAL RESEARCH
published: 11 January 2021
doi: 10.3389/fnins.2020.627062

Identifying Mild Hepatic Encephalopathy Based on Multi-Layer Modular Algorithm and Machine Learning

Gaoyan Zhang[1], Yuexuan Li[1], Xiaodong Zhang[2], Lixiang Huang[2], Yue Cheng[2] and Wen Shen[2]**

[1] College of Intelligence and Computing, Tianjin Key Lab of Cognitive Computing and Application, Tianjin University, Tianjin, China, [2] Department of Radiology, Tianjin First Central Hospital, Tianjin, China

Hepatic encephalopathy (HE) is a neurocognitive dysfunction based on metabolic disorders caused by severe liver disease, which has a high one-year mortality. Mild hepatic encephalopathy (MHE) has a high risk of converting to overt HE, and thus the accurate identification of MHE from cirrhosis with no HE (noHE) is of great significance in reducing mortality. Previously, most studies focused on studying abnormality in the static brain networks of MHE to find biomarkers. In this study, we aimed to use multi-layer modular algorithm to study abnormality in dynamic graph properties of brain network in MHE patients and construct a machine learning model to identify individual MHE from noHE. Here, a time length of 500-second resting-state functional MRI data were collected from 41 healthy subjects, 32 noHE patients and 30 MHE patients. Multi-layer modular algorithm was performed on dynamic brain functional connectivity graph. The connection-stability score was used to characterize the loyalty in each brain network module. Nodal flexibility, cohesion and disjointness were calculated to describe how the node changes the network affiliation across time. Results show that significant differences between MHE and noHE were found merely in nodal disjointness in higher cognitive network modules (ventral attention, fronto-parietal, default mode networks) and these abnormalities were associated with the decline in patients' attention and visual memory function evaluated by Digit Symbol Test. Finally, feature extraction from node disjointness with the support vector machine classifier showed an accuracy of 88.71% in discrimination of MHE from noHE, which was verified by different window sizes, modular partition parameters and machine learning parameters. All these results show that abnormal nodal disjointness in higher cognitive networks during brain network evolution can be seemed as a biomarker for identification of MHE, which help us understand the disease mechanism of MHE at a fine scale.

Keywords: mild hepatic encephalopathy, dynamic graph properties, multi-layer modular algorithm, disjointness, machine learning, individual discrimination, functional MRI, brain network evolution

OPEN ACCESS

Edited by:
Xiaopeng Song, Harvard Medical School, United States

Reviewed by:
Yanbo Zhang, University of Alberta, Canada
Pei Shang, Mayo Clinic, United States
Mingquan Lin, Emory University, United States
Bin Qiu, Yale University, United States

****Correspondence:***
Yue Cheng
Chengyue200017076@163.com
Wen Shen
shenwen66happy@163.com

Specialty section:
This article was submitted to Brain Imaging Methods, a section of the journal Frontiers in Neuroscience

Received: *08 November 2020*
Accepted: *15 December 2020*
Published: *11 January 2021*

Citation:
Zhang G, Li Y, Zhang X, Huang L, Cheng Y and Shen W (2021) Identifying Mild Hepatic Encephalopathy Based on Multi-Layer Modular Algorithm and Machine Learning. Front. Neurosci. 14:627062. doi: 10.3389/fnins.2020.627062

Abbreviations: Cerebelum_Crus1_R, right cerebellum crus 1 region; Cingulum_Mid_L/R, left or right middle cingulum region; Cuneus_L, left cuneus region; Frontal_Inf_Tri_L, left inferior triangle frontal region; Frontal_Mid_Orb_L/R, left or right orbital middle frontal region; Frontal_Sup_L/R, left or right superior frontal region; Frontal_Sup_Medial_L, left superior medial frontal region; Frontal_Sup_Medial_L/R, left or right superior medial frontal region; Insula_R, right insular region; Lingual_L/R, left or right lingual region; Occipital_Inf_R, right inferior occipital region; Parietal_Inf_R, right inferior parietal region; Precentral_L, left precentral gyrus; Precuneus_L/R:left or right precuneus; Supp_Motor_Area_L, left supplemental motor area; Temporal_Mid_R, right middle temporal region.

INTRODUCTION

Hepatic encephalopathy (HE) is a syndrome of central nervous system dysfunction based on metabolic disorders caused by severe liver disease (Agrawal et al., 2015; Zhang et al., 2017b). Mild hepatic encephalopathy (MHE), as a mildest form of HE spectrum, has no recognizable clinical symptoms of HE, but is characterized by subtle neurocognitive and psychomotor deficits, such as psychomotor slowing, shortened attention concentration, dysfunctional executive abilities, and memory loss (Agrawal et al., 2015). MHE impairs individual's daily functioning, driving performance, work performance and learning ability (Agrawal et al., 2015). MHE has a probability of 40% converting to overt HE within six months if not treated promptly, and once converted, patients will have increased falls, short survival and high mortality (Campagna et al., 2014; Zhang et al., 2018b). Early diagnosis and effective treatment are essential to reduce conversion to overt HE and to improve patients' quality of life. Currently, it is difficult to clinically diagnose MHE patients from cirrhotic patients with no HE (noHE). Therefore, it is of great significance to understand the dysfunction mechanism of MHE and to explore the biomarkers for precisely clinical diagnosis.

In the past years, resting state-functional magnetic resonance imaging (RS-fMRI) characterized by non-invasiveness, high sensitivity, ultra-fast imaging and no requirement of engaging in a task, has attracted more and more attention in the study of hepatic encephalopathy (Zhang et al., 2014a, 2017a). It measures the relative changes of blood oxygen level dependent (BOLD) signals as a representation of spontaneous neural activities in the human brain. A number of studies have explored changes in brain functional network that are related to cognitive function in patients with MHE. Zhang et al. (2014b) used graph theory analysis and found that changes in small-world property in patients with MHE were related to their cognitive impairment. Qi et al. (2012) used the independent component analysis (ICA) to evaluate the difference of resting state networks between MHE patients and healthy controls (HCs), revealing that MHE patients showed significantly decreased functional connectivity in dorsal attention network (DAN), both decreased and increased functional connectivity in default mode network (DMN), auditory network (AN) and visual network (VN). No significant differences were found in self-referential network (SFN) and sensorimotor network (SMN) between MHE and HCs. Regional homogeneity (ReHo) analysis of resting state brain activity showed that compared with the noHE patients, the MHE patients show decreased ReHo value in the bilateral parietal lobes including the precuneus, supplementary motor area, frontal lobes and occipital lobes including the cuneus. With whole-brain functional connectivity analysis, a study (Zhang et al., 2012) concluded that compared with HCs, MHE patients presented widespread cortical and subcortical functional connectivity alterations that were correlated with neuropsychologic impairment. Particularly, impairment in the basal ganglia-thalamocortical circuit may play a key role in mediating neurocognitive dysfunction, especially the psychomotor speed and attention deficits in MHE patients. These studies indicate that changes in resting state functional connectivity can reflect abnormal cognitive function in MHE patients. Some other studies combined the resting state brain activity or functional connectivity features with machine learning method (i.e. support vector machine, linear discriminant analysis) to investigate the early identification of MHE (Chen et al., 2014, 2016a,b; Jiao et al., 2017). However, the discrimination accuracy is not satisfying to meet the clinical demands. Moreover, these previous studies assumed the brain as a static functional connectivity pattern during the whole resting state scan (at least 5 min) and ignore the fact that the human brain is obviously a dynamically interactive system, and even at the relatively sluggish temporal resolution of fMRI (Cai et al., 2019).

Recently, dynamic functional connectivity analysis has drawn more and more attention in studies of brain disease (Hutchison et al., 2013; Calhoun et al., 2014; Kucyi and Davis, 2015), which can capture transient functional connectivity changes and describe dysfunction of MHE at a fine scale. For example, abnormality in dynamic brain function has been observed in autism spectrum disorder (Harlalka et al., 2019), and epilepsy (Tailby et al., 2018). Dynamic graph analysis is a promising avenue to quantitatively characterize the time evolving brain dynamics at a system level. It assumes the whole brain functional connectivity as a graph, there is a modular structure in the brain network graph (Rubinov and Sporns, 2010) and the modular structure evolves dynamically across time. It was reported that the modularity of dynamic functional connectivity networks can change on a very short time scale, and thus this approach may be able to track transient changes in functional connections between brain regions (Betzel et al., 2016). Bassett et al. (2011) and Cole et al. (2013) used multi-layer modular analysis on the dynamic graph structure of the brain imaging data and found that the modular structure in the dynamic network was able to represent the cognitive function. Therefore, we believe that dynamic graph analysis will give us a deeper insights into the abnormal cognitive function of MHE.

In this study, we intended to use a multi-layer modular analysis method to detect the changes of dynamic graph properties of brain network in patients with MHE, investigate the clinical correlation of these properties and further construct a machine learning model based on the selected network properties to identify MHE from noHE at the individual level. We hypothesized that dynamic brain connectivity analysis can reveal the complex, adaptive, cognitive dysfunction underlying MHE and the temporal variation of the brain network metrics could provide rich diagnostic information to discriminate MHE from noHE.

MATERIALS AND METHODS

Participants

A total of 103 participants was used in this study, including 30 MHE patients, 32 noHE patients and 41 HCs, see **Table 1**. HC group was added to study dysfunction mechanism as a contrast. The machine learning model was performed on the patient groups because the discrimination of cirrhosis with MHE from

TABLE 1 | Demographic, neuropsychological and clinical data.

Protocols	HC ($n = 41$)	noHE ($n = 32$)	MHE ($n = 30$)	p-value	χ^2/F/T value
Sex (M/F)	28/13	18/14	21/9	0.449^a	1.603^a
Age (years)	50.1 ± 7.3	47.9 ± 8.2	50.9 ± 6.3	0.153^b	1.917^b
Education (years)	13.0 ± 2.6	12.3 ± 3.5	12.3 ± 3.0	0.499^b	0.699^b
NCT-A (seconds)	41.6 ± 3.2	43.1 ± 12.7	78.9 ± 14.6	$<0.001^b$	93.427^b
	–	–	–	$<0.001^{c1}$	10.306^{c1}
	–	–	–	$<0.001^{c2}$	12.011^{c2}
	–	–	–	0.599^{c3}	0.528^{c3}
DST (score)	47.9 ± 10.2	43.1 ± 9.5	30.1 ± 11.7	$<0.001^b$	25.920^b
				$<0.001^{c1}$	-4.792^{c1}
	–	–	–	$<0.001^{c2}$	-6.685^{c2}
	–	–	–	0.043^{c3}	-2.071^{c3}
Prothrombin time (seconds)	–	16.8 ± 6.0	18.8 ± 5.2	0.105^{c1}	1.353^{c1}
Albumin (mg/dl)	–	32.0 ± 5.8	30.0 ± 5.9	0.565^{c1}	-1.355^{c1}
Total bilirubin (mg/dl)	–	96.1 ± 139.3	106.4 ± 170	0.737^{c1}	0.268^{c1}
Blood ammonia (μmol/L)	–	55.1 ± 21.3	72.6 ± 31.5	0.009^{c1}	2.543^{c1}
Child-Pugh A/B/C	–	5/15/11*	1/7/22	–	–

*Data are presented as mean ± standard deviation. *: One person lacked information.*
a: Pearson χ^2 test of three groups (two-tailed), b: One-way analysis of variance test among three groups (two-tailed), c1: Two-sample t test between MHE and noHE groups (two-tailed), c2: Two-sample t test between MHE and HC groups (two-tailed), c3: Two-sample t test between noHE and HC groups (two-tailed). DST, digit-symbol test; HC, healthy control; MHE, mild hepatic encephalopathy; NCT-A, number connection test of type A; noHE, cirrhotic patients without clinical hepatic encephalopathy.

that with no HE is the main concern of clinical doctors. This study was approved by the Medical Research Ethics Committee of Tianjin First Central Hospital. Written informed consent was obtained from each subject prior to participation in this study.

Before functional magnetic resonance imaging (fMRI) scanning, patients with cirrhosis were tested for blood ammonia, prothrombin time, total bilirubin, and albumin biochemical parameters to assess liver function (**Table 1**). Functional status of cirrhosis was assessed by child-pugh score (Pugh et al., 1973). The HC group had no liver or other systemic problems, no history of psychosis or neuropathy.

As recommended by previous studies (Weissenborn et al., 2001; Li et al., 2013), neuropsychological tests including Number Connectivity Test A (NCT-A) and Digit Symbol Test (DST) were performed on all subjects to diagnose MHE by clinic. To be specific, linear regression models of NCT-A and DST were estimated with regressors of age and education in the HC group, and then the model was used to predict scores of NCT-A and DST for subjects in patient groups. The difference between the predicted value and the true value was calculated, and the patient with either DST or NCT-A difference greater than 2 standard deviation was determined as MHE.

In addition, some patients used antibiotics if they have infections, such as spontaneous bacterial peritonitis, and pulmonary infection. Lactulose was used in 19 patients to improve feces excretion function, and they took 5–10 g lactulose three times a day. Patients were excluded if they took psychotropic medications, suffered from uncontrolled endocrine disorders, had other neuropsychiatric disorders or metabolic diseases, had alcohol abuse within 6 months prior to the study, or had large head motions during scanning. In the end, the aforementioned 103 participants were remained.

Overview of Methodology

An overview of the framework is summarized in **Figure 1**. First, resting-state fMRI data were preprocessed. Second, the nodal time series were extracted using a sliding time window to calculate the dynamic functional connection graph. Third, the dynamic functional connection matrix is constructed with Pearson correlation and these matrix can be seemed as a dynamic graph. Fourth, the multi-layer modularization algorithm is used to determine the temporal module structure in the dynamic graph. Fifth, several dynamic graph properties describing brain connection stability and node changes of module affiliation during brain network evolution over time were calculated. Sixth, inter-group difference of these metrics and their correlations with the neuropsychological and clinical test scores were performed at two levels of local network and individual node. Finally, the metrics with largest inter-group differences were selected as features to identify individual MHE from noHE by machine learning, and discriminant analysis were used to explore the contribution of each feature.

MRI Scanning Parameters

The MRI data were collected using a Siemens 3.0T (TIM-Trio, Siemens Medical Solutions, Erlangen, Germany) MRI scanner with a 32-channel head coil. Foam padding was used to reduce head motion. The scan sequences of each subject included conventional T2WI, 3D-T1WI and resting-state fMRI. Two-dimensional T2-weighted turbo spin echo (TSE) and T1-weighted MPRAGE sequences were used to detect brain lesions. Gradient echo plane imaging (EPI) sequence was used to obtain BOLD image with the following parameters: measurement = 200, echo time (TE) = 30ms, repeat time (TR) = 2500 ms, flip

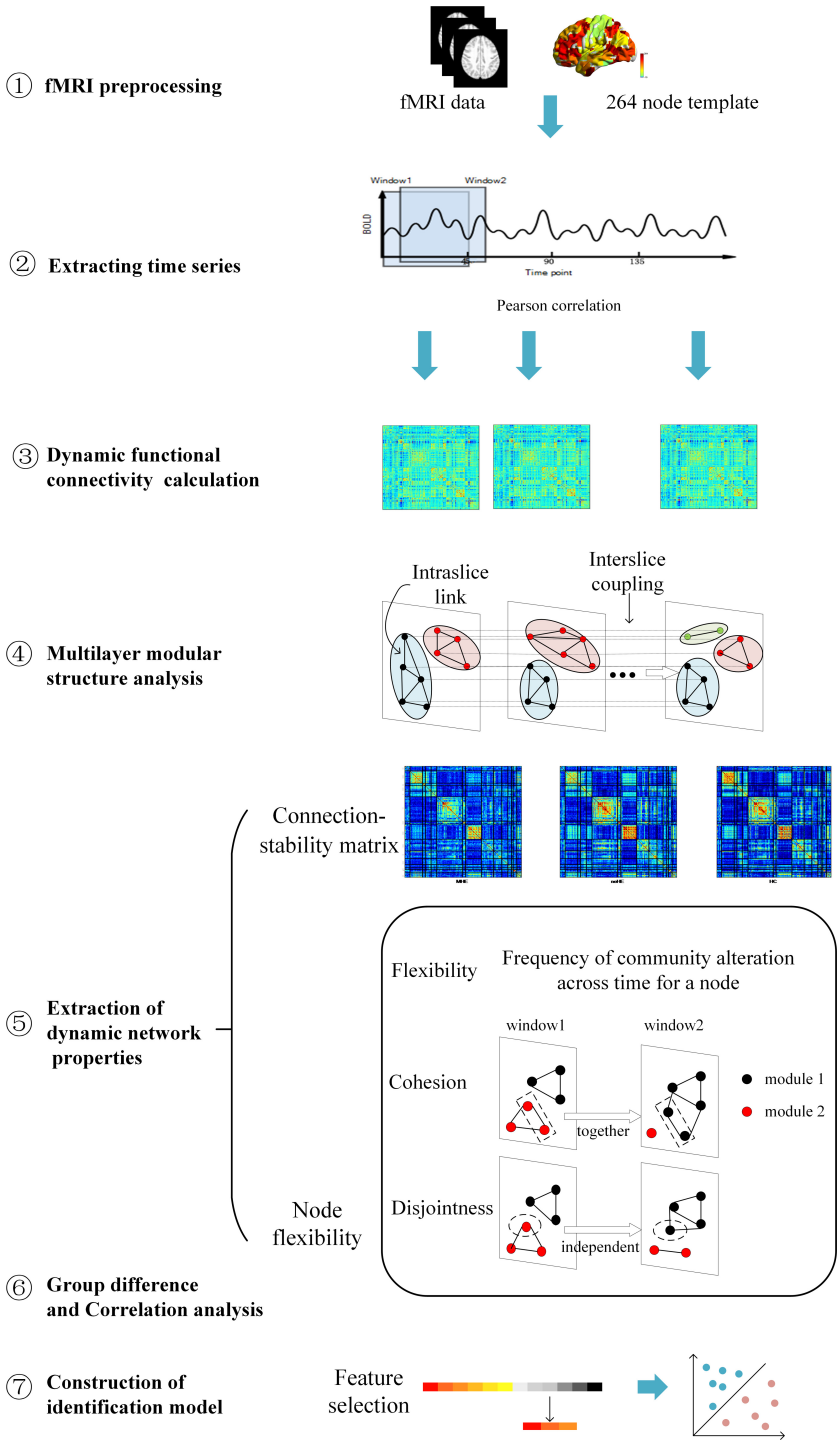

FIGURE 1 | An overview of data analysis pipeline. ①. fMRI data preprocessing; ②. Extracting regional time series based on Power's 264 atlas; ③. Sliding-window based dynamic functional connectivity matrix calculation; ④. Multi-layer modular structure calculation from the dynamic brain connectivity matrix; ⑤. Extraction of dynamic network properties; ⑥. Group difference of dynamic network properties and their correlations with clinical cognitive test scores; ⑦. Construction of identification model based on dynamical network properties for individual MHE discrimination.

angle (FA) = 90°, field of view (FOV) = 220 mm × 220 mm, matrix = 96 × 96, slice thickness = 3 mm, slice gap = 0.3 mm, and number of slices = 40. The total scan time of resting-state data was 500 s. The subjects were asked to close their eyes, relax physically and mentally, stay awake, keep their heads and bodies still, and try not to think about anything.

Data Preprocessing

The fMRI images were preprocessed using MATLAB 2013a (MathWorks, Natick, MA, United States) with the GRETNA software package[1]. The first 10 time points were removed to equalize the magnetization and to allow subjects to adapt to the scanning environment. Time slice correction and head motion correction were performed for the remaining 190 time points. We also calculate the frame-wise displacement (FD), which represents the volume changes of the head position. Subjects were removed with mean FD > 0.2 mm, maximum translation > 2 mm, maximum rotation > 2 degree (Greve and Fischl, 2009). The images were then normalized, including co-registered, segmented, normalized to EPI Spaces and resampled to 3 × 3 × 3 mm^3, After spatial smoothing of the image with a full width at half maxima (FWHM) kernel of 8 mm, linear trend of BOLD signal was removed and covariates such as white matter signal, cerebrospinal fluid signal (CSF) and 24 head motion parameters were regressed to reduce the influence of other factors. According to previous studies, global signal regression (GSR) has been shown to cause a possible inverse correlation effect in resting brain networks, so GSR is not used in image preprocessing (Murphy et al., 2009; Weissenbacher et al., 2009; Saad et al., 2012). Finally, the regression time series was temporal filtered (0.01–0.1Hz) (Liu and Duyn, 2013).

Dynamic Function Network Construction

We used a whole brain template to define the brain as 264 nodes (Power et al., 2011). The 14 functional networks were partitioned based on 264 nodes for subsequent network analysis (Power et al., 2013). The mapping between names of the network and their abbreviations, member nodes are provided in **Table 2**. The Pearson correlation was applied to obtain the whole brain functional connectivity matrix. Then, to track the dynamic changes in the brain over a short period of time, we used a sliding window length of 45TR (112.5s), which has been proved to achieve better identification performance around 110s based on a previous study (Liu et al., 2017), and the window moves with a step size of 1TR (2.5s). The remaining 190 time points were divided into 146 time windows (1-45, 2-46, 3-47..., 146-190). A Fisher Z-Transformation was performed on the connection matrix within each window of the subject for subsequent analysis. Therefore, the dynamic functional connectivity matrix was obtained and it can be viewed as a dynamic graph.

Multi-Layer Modular Algorithm

A multi-layer modular algorithm was used to determine the modular structure in the dynamic functional connection matrix.

In order to quantify the temporal and spatial interactions of brain nodes, we used an iterative and orderly Louvain algorithm to track the changes of community partition over time. Compared with the Louvain algorithm, the multi-layer modular algorithm adds one parameter called omega, which is used to control the strength of the coupling between time layers. The optimization goal is to maximize the modularity (Q) of the brain network. That is to maximize intra-modular connectivity and minimize inter-modular connectivity, so as to find a stable modular structure (Newman, 2004). The calculation method of multi-layer modularization is as follows:

$$Q(\gamma, \omega) = \frac{1}{2\mu} \sum_{ijsr} \left[\left(A_{ijs} - \gamma_s \frac{k_{is} k_{js}}{2m_s} \right) \delta(s, r) + \delta(i, j) \cdot \omega_{jrs} \right] \delta(M_{is}, M_{jr}) \quad (1)$$

$$m = \frac{1}{2} \sum_{ij} A_{ij} \quad (2)$$

$$\mu = \frac{1}{2} \sum_{jr} k_{jr} \quad (3)$$

where A_{ijs} is the correlation between nodes i and j under the sliding window of time point s, k_{is} is the degree of node i under time point s and $k_{is}k_{js}/2m_s$ represents the Newman-Girvan null model of intra-network connections. γ_s is the topological resolution parameter under a time point s or layer s. ω_{jrs} is the time-coupling parameter between node j in the time window r and node j in the time window s. For $\delta(M_{is}, M_{jr})$, if node i and j belong to the same module, it is 1; otherwise, it is 0. For $\delta(s, r)$, if $s = r$, it is 1; otherwise, it is 0. For $\delta(i, j)$, if $i = j$, it is 1; otherwise, it is 0.

In our study, we used Genlouvain Matlab toolbox (Jutla et al., 2011–2019) to calculate the modular structure of the brain. And the default value 1.0 was chosen as the gamma and omega values. Due to the variability in optimizing the partition, we repeated the algorithm 100 times.

Connection-Stability Matrix

In order to study the characteristics of nodal connection that are more stable in dynamic brain interaction, we calculated the connection-stability scores between nodes by dividing the module results. The connection-stability score was calculated as the proportion of time windows in which a given node pair is assigned into the same module, with nodal network membership defined on the basis of multi-layer modular algorithm (gamma = 1.0 and omega = 1.0). If two nodes were assigned to the same module in a time window, the connection-stability score is 1, else it is set 0. A higher value indicates that two nodes were relatively stable participating in the same community. The output is G = N × N matrix, where each element (m, n) is connection-stability scores between node m and node n. To avoid the chance of a result, the final result of each metric was the average of 100 runs.

Dynamic Nodal Metrics Extracted From Modular Structure

From modular partition result, we extracted three dynamic metrics to describe the nodal properties, namely nodal flexibility, cohesion, disjointness. These metrics measured the dynamic reconfiguration that occurs in the brain over time, and a higher dynamic metrics would imply a hypervariable connection. To avoid the chance of a result, the final result of each metric was the average of 100 runs.

[1]https://www.nitrc.org/projects/gretna/

TABLE 2 | The mapping between network names, their abbreviations and member nodes.

Networkindex	Network name	abbreviation	member node
1	Uncertain	Uncertain	1-12,84-85,132,140-142,182-185,247-250,253-254
2	Sensory_Somatomotor_Hand	SSHN	13-41,255
3	Sensory_Somatomotor_Mouth	SSMN	42-46
4	Cingulo-opercular_Task_Control	CON	47-60
5	Auditory	AN	61-73
6	Default_mode	DMN	74-83,86-131,137,139
7	Memory_retrieval	MRN	133-136,221
8	Ventral_attention	VAN	138,235-242
9	Visual	VN	143-173
10	Fronto-parietal_Task_Control	FPN	174-181,186-202
11	Salience	SN	203-220
12	Subcortical	Subcortical	222-234
13	Cerebellar	Cerebellar	243-246
14	Dorsal_attention	DAN	251-252,256-264

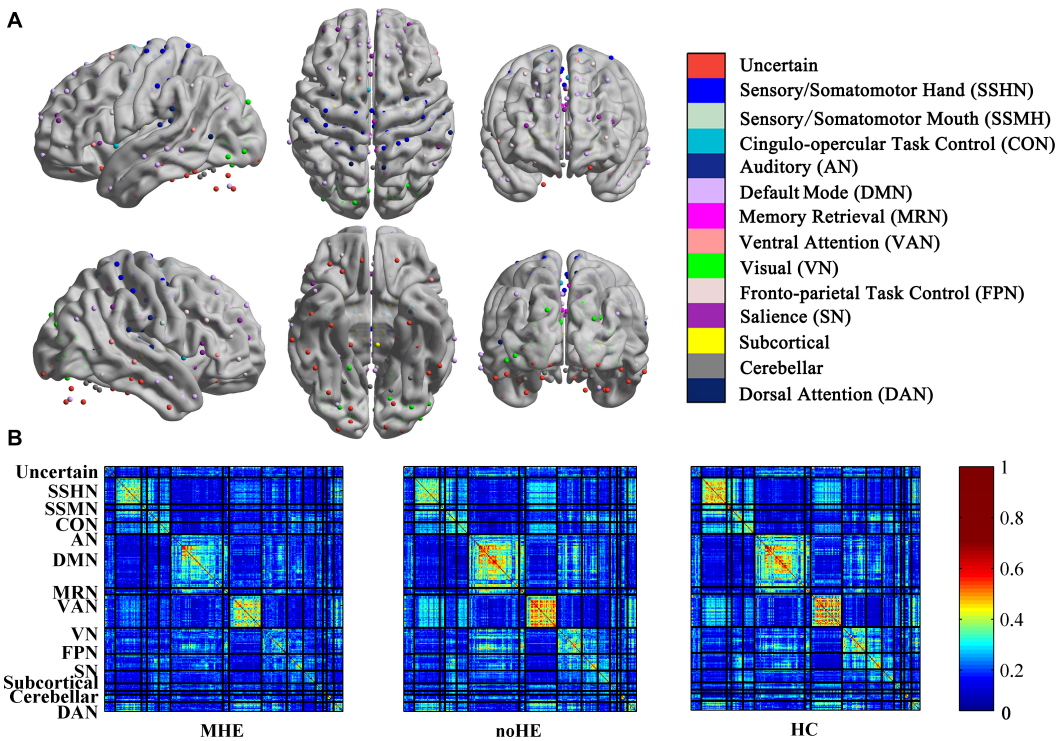

FIGURE 2 | The connection stability profile of the brain network across time in MHE, noHE and HC groups. **(A)** The distribution of 14 brain networks in the 264-node brain template; **(B)** The connection-stability matrix distributed in the 14 networks in MHE, noHE and HC groups. MHE, minimal hepatic encephalopathy; noHE, non-hepatic encephalopathy; HC, health control.

(1) Flexibility

Node flexibility is defined as the ratio of the number of times a node changes communities to the number of possible times a node changes communities. It's a number between 0 and 1 where 1 means that the node is most flexible over time.

$$f_i = 1 - \frac{1}{T-1}\sum_{s=1}^{T-1}\delta\left(G_{i,s}, G_{i,s+1}\right) \quad (4)$$

For $\delta\left(G_{i,s}, G_{i,s+1}\right)$, if node i and j belong to the same module, it is 1; otherwise, it is 0. T is the total number of time windows.

(2) Cohesion

Although node flexibility determines how often the node changes the community, it does not describe how the node changes the community. Node cohesion describes how often one node changes a community with another (Telesford et al., 2017). A high cohesion value indicates that

the node typically changes the community along with other nodes. A low cohesion value indicates that the node rarely changes the community with other nodes.

(3) Disjointness
Node disjointness is defined as the ratio of the number of times a node can change a community independently to the number of times a node can change a community (Telesford et al., 2017). It quantify the percentage of times a node changes its community independently. The global disjointness for each subject was calculated as the mean disjointness values of all nodes of each subject.

Group Differences in Dynamic Graph Metrics

We used Kruskal-Wallis nonparametric one-way analysis of variance (ANOVA) to analyze differences among three groups (MHE, noHE, and HCs) in dynamic indicators and connection-stability. The analyses were performed at two levels of brain network and brain region nodes. If there was a statistical difference, a *post hoc* test were performed to detect the inter-group difference. Significant group differences were tested at $p < 0.05$ after corrections for multiple comparisons.

Correlation With Neuropsychological Scores

We used partial correlation analysis to examine the relationship between dynamic metrics, connection-stability of each patient and the neuropsychological scores, meanwhile the age, gender, educational level, and head motion parameters were all used as covariates to avoid their influences. Multi-level correlations have been performed, from the network-level and individual node-level. At the network level, the 264 nodes were divided into 14 brain networks (Power et al., 2013).

Discrimination of Individual MHE From noHE

In this study, *F*-score was used as feature selection method to measure the ability of the dynamic graph metrics (Chen and Lin, 2006). The F score of the *i*th feature is defined as follows:

$$F(i) = \frac{\left(\bar{\bar{x}}_i^{(+)} - \bar{\bar{x}}_i\right)^2 + \left(\bar{\bar{x}}_i^{(-)} - \bar{\bar{x}}_i\right)^2}{\frac{1}{n_+ - 1}\sum_{k=1}^{n_+}\left(x_{k,i}^{(+)} - \bar{x}_i^{(+)}\right)^2 + \frac{1}{n_- - 1}\sum_{k=1}^{n_-}\left(x_{k,i}^{(-)} - \bar{x}_i^{(-)}\right)^2} \quad (5)$$

Where the $\bar{\bar{x}}$ is the average values of all the sample, while $\bar{\bar{x}}_i^{(+)}$ and $\bar{\bar{x}}_i^{(-)}$ represent the mean values of all the positive and negative samples, respectively. *k* represents each instance of the specific *i*th feature. *F*(*i*) calculated the difference of *i*th feature between the two groups. The larger the *F*-score, the stronger the discrimination of this feature. We ranked all the features according to the *F*-score, and selected the top k largest features for the following classification analysis. The k was determined based on the average classification performance of all loops. Finally, 23 features were selected in this study.

Support vector machine (SVM)[2] was applied to classify individual patient with MHE from the noHE using the extracted features because SVM is especially suitable for fMRI data with small samples and a high dimension. A leave-one-out cross-validation(LOOCV) method was used to estimate the classification performance due to its small-sample friendly nature (Pereira et al., 2009).

To assess the performance of our method, we calculated classification accuracy, sensitivity, and specificity, respectively. Sensitivity measures the proportion of positives that are correctly identified as such. Specificity measures the proportion of negatives that are correctly identified as such. In addition, the receiver operating characteristic (ROC) analysis was used to evaluate the performance of the classifier. The larger area under ROC curve (AUC) indicates a better discriminant power (Fawcett, 2006). We used 1000 permutation tests to determine whether the accuracy of the results were higher than the chance level. Because the LOOCV approach makes the feature selection of the sample subset in each fold slightly different, the discriminant features were defined as the top 23 frequently occurred features in all folds.

Validation

To validate the robustness of our findings, we also repeated the analysis using multiple parameters. As for the analysis results of correlation and group difference, we mainly verify the robustness of the results under different time windows and different modularization algorithm parameters. For the time window size, a window length of 40TR (100 s), 50TR (125 s) and 55TR (137.5 s) were considered. For multilayer modular parameters, values near gamma = 1.0 and omega = 1.0 were analyzed repeatedly. As for the classification results, the comparisons of feature selection method and classifier kernel function were performed. We used the commonly used relief method (Kira and Rendell, 1992) and the linear kernel SVM classifier as a comparison.

RESULTS

The results reported in the group comparison and correlation section are based on the parameters (gamma = 1.0; omega = 1.0; window size = 45TR) that can obtain the best identification accuracy. Results based on different parameters for validation were reported in the classification section.

Effect of Disease on Network Connection-Stability Matrix

The connection-stability matrix over time for MHE, noHE and HC was shown in **Figure 2**. Before comparison, the connection stability values were averaged in each network module. One-way ANOVA results indicated that average connection-stability score in sensory/somatomotor mouth network (SSMN), default mode network (DMN), cingulo-opercular task control network (CON), and frontro-parietal task control network (FPN) showed

[2]http://www.csie.ntu.edu.tw/∼cjlin/libsvm/

significant differences among the three groups, but only FPN survived false discovery rate (FDR) correction. *Post hoc* analyses were performed to detect the inter-group difference. Results showed that the average connection-stability scores of MHE patients were significantly lower than that of HC in CON and FPN, and marginally significant (adjusted $p = 0.054$) in DMN after FDR correction, but no significant differences were observed between other groups. The p-value in each comparison and significances after FDR correction were all listed in **Table 3**.

Correlation Results Between Network Connection-Stability and Clinical Scores

We also calculated the correlation between the average network connection-stability score and the clinical scores in all cirrhotic patients. The results showed a significant positive correlation between DST and network connection-stability scores in DMN, visual network (VN), FPN, salience network (SN), and subcortical network (**Table 4**). All the results were reported at $p < 0.05$ after corrections for multiple comparisons.

Effect of Disease on Dynamic Nodal Metrics

The results showed that the node disjointness score of MHE patients was significantly higher than that of noHE patients at some specific brain regions, which mainly fell in Frontal_Sup_Medial_L/R, Frontal_Mid_Orb_R, Frontal_Sup_L/R and Cingulum_Mid_L (**Figure 3A**). MHE patients were significantly lower than noHE patients only in the area of the Temporal_Mid_R. It can be seen that compared with noHE patients, MHE patients have more frequent single-node switching rate in regions in DMN and FPN and less frequent single-node switching rate in region of VAN.

In order to better understand the pathogenesis, we also conducted a control analysis between MHE patients and the HC group. The results showed a significant difference in Frontal_Inf_Tri_L, Frontal_Sup_Medial_L, Parietal_Inf_R, Cuneus_L, Frontal_Sup_R, Precuneus_R areas (**Figure 3B**). It can be seen that MHE patients had a higher single-node switching rate than HC in most regions, except in the Frontal_Inf_Tri_L region. The difference regions were located in DMN, FPN, ventral attention network (VAN), VN and SSHN.

Meanwhile, the noHE patients and the HC group were compared. The disjointness of noHE patients was significantly higher than HC in Insula_R, Precuneus_L, Frontal_Mid_L, but lower in Frontal_Mid_R (**Figure 3C**). The difference nodes mainly fell into DMN, FPN, SN and sensory/somatomotor hand network (SSHN).

In addition, we analyzed the effect of disease on flexibility and cohesion metrics, but no significant group difference

TABLE 3 | The differences in average network connection-stability scores among MHE, noHE and HC groups.

Network	*p* value (ANOVA)	*p* value (MHE vs. HC)	Median MHE	Median noHE	Median HC
Uncertain	0.941	–	0.260	0.259	0.268
SSHN	0.231	–	0.367	0.382	0.406
SSMN	**0.042**	**0.039**	0.488	0.492	0.565
CON	**0.022**	**0.006***	0.333	0.358	0.389
AN	0.32	–	0.349	0.345	0.366
DMN	**0.031**	**0.018**	0.307	0.351	0.356
MRN	0.26	–	0.455	0.517	0.502
VAN	0.392	–	0.324	0.333	0.317
VN	0.251	–	0.373	0.465	0.467
FPN	**0.001***	**<0.001***	0.308	0.331	0.389
SAN	0.054	–	0.287	0.355	0.347
Subcortical	0.772	–	0.330	0.324	0.323
Cerebellar	0.45	–	0.493	0.478	0.518
DAN	0.523	–	0.381	0.402	0.365

*Results with $p < 0.05$ are bold in the table. * indicates that $p < 0.05$ after FDR corrections for multiple comparisons.*

TABLE 4 | Networks showing significant correlation of connection-stability with clinical test scores.

Network	Blood ammonia[r]	Blood ammonia[p]	NCT[r]	NCT[p]	DST[r]	DST[p]
DMN	−0.12	0.37	−0.217	0.102	0.35	**0.007***
VN	−0.202	0.128	−0.132	0.324	0.376	**0.004***
FPN	0.004	0.979	−0.278	**0.035**	0.338	**0.009***
SN	−0.147	0.272	−0.212	0.111	0.525	**<0.001***
Subcortical	−0.053	0.69	−0.106	0.43	0.361	**0.005***

*Results with $p < 0.05$ are bold in the table. * indicates that p-value survived FDR correction.*

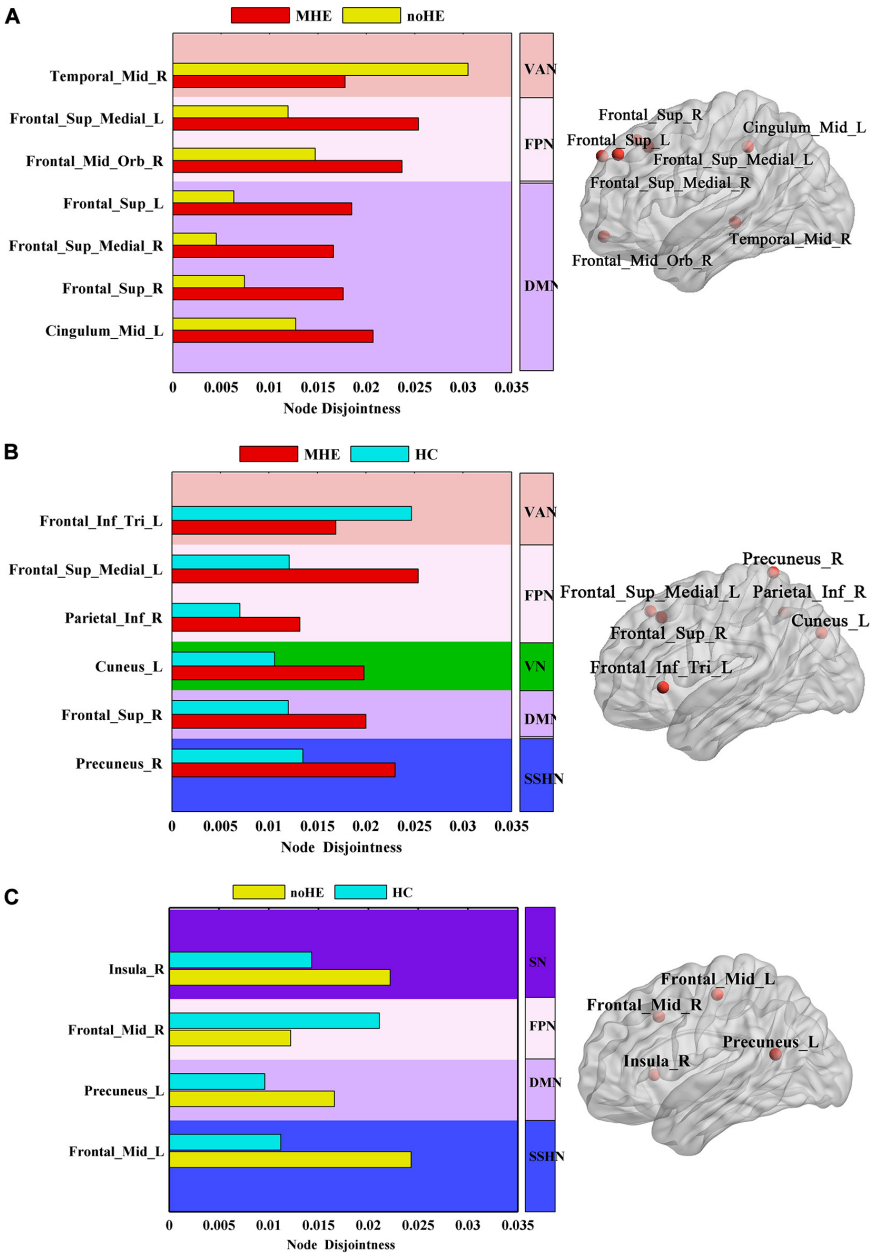

FIGURE 3 | The differences in node disjointness during brain network evolution among the three groups by one-way analysis of variance (ANOVA). **(A–C)** The difference regions of the brain networks and the corresponding spatial locations in *post hoc* comparison of MHE with noHE, MHE with HC and noHE with HC. MHE, minimal hepatic encephalopathy; noHE, non-hepatic encephalopathy; HC, health control.

was found at $p < 0.05$ after corrections for multiple comparisons.

Correlation Results Between Dynamic Nodal Metrics and Clinical Scores

At the network level, we observed a significant negative correlation between disjointness and DST score in DMN and SN ($p < 0.05$, $r > -0.4$) (**Figure 4**). We didn't find correlation between cohesion or flexibility and all the clinical testing scores.

At the node level, there are much more nodes showing correlation between disjointness and scores. These nodes are listed in **Supplementary Table 1**. Some correlative nodes were also found between cohesion or flexibility and clinical scores, but it should be noticed that these nodes were mostly similar. This suggests that the community flexibility is most likely caused by nodes partition change in pairs. The higher correlation in the disjointness metrics also indicates that community switching of nodes in the disease population were more likely changed individually.

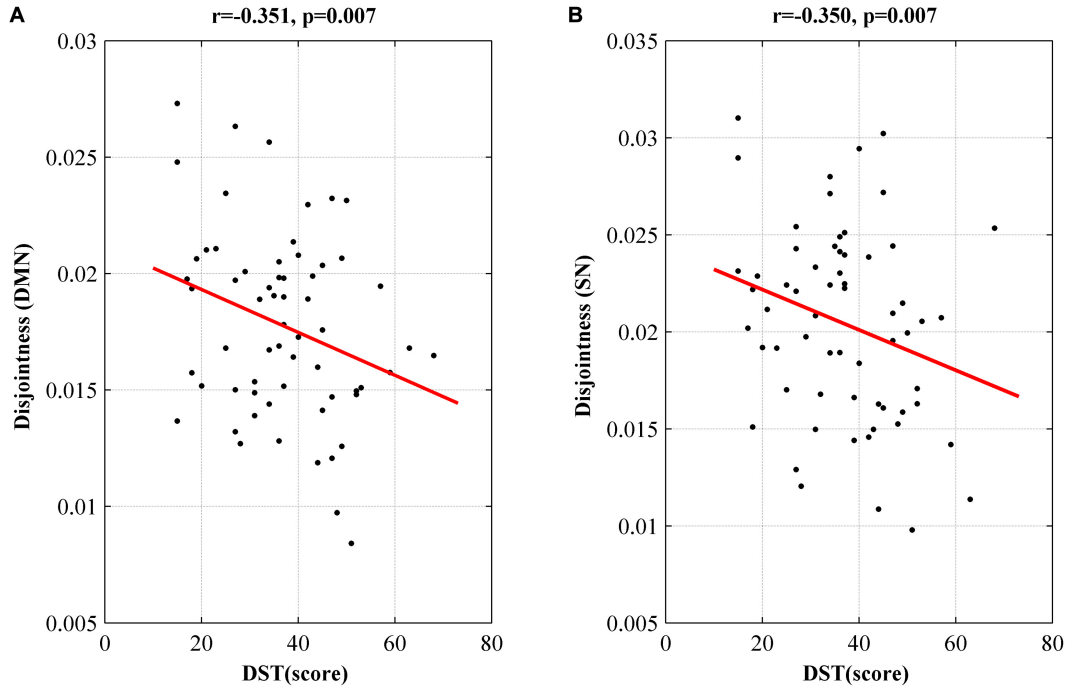

FIGURE 4 | Networks showing significant correlation of disjointness metric with DST score in DMN **(A)** and SN **(B)**. DMN, default model network; SN, salience network; DST, digit symbol test; MHE, minimal hepatic encephalopathy.

Validation analysis to check for robustness of correlation results with different modularity parameters or different window parameters are provided in the Supplementary Information (**Supplementary Tables 1–6**).

Classification Results of MHE From noHE

Considering node disjointness is the unique metric that can reveal difference between MHE and noHE among the three dynamic network properties, and it also shows correlation with neuropsychological scores in patient groups, we take this metric as discriminant features for identification MHE from noHE. The accuracy, sensitivity and specificity of SVM classifier with radial basis function (RBF) kernel were 88.71, 92.31, and 83.33%, respectively. The permutation tests reveal a significance level of $p < 0.001$ for accuracy, which suggests that the identification accuracy was significantly higher than chance level, indicating the effectiveness of the identification model.

The classification results of MHE from noHE based on difference window size are shown in **Table 5**. All results achieved a cross-validated classification accuracy above 83.87%, indicating the robustness of the selected window length. On the other hand, we obtained optimal window length of 45TR (112.5 s), basically consistent with the result that the optimal classification accuracy was obtained around the window length of 110s (Liu et al., 2017).

Figure 5 displays the classification accuracies based on different feature selection method, SVM kernel function and module partition parameters. For a fixed value of gamma (gamma = 1.0), we found a stable accuracy above 80% in omega value range between 0.6 and 1.4. When performing analysis in other topological scales (gamma = 0.8, gamma = 0.9, gamma = 1.1 with omega = 1.0), we observed a slightly accuracy decrease. We also paid attention to the impact of feature selection on classification accuracy. The commonly used feature selection method "relief" was used as a comparison, the results show almost no difference in classification accuracy. Altogether, the best accuracy is obtained at 88.71% with parameters of gamma = 1.0, omega = 1.0, *F*-score method and RBF kernel in SVM.

The ROC curve using each subject's classification score as a threshold are shown in **Figure 6A**. The area under the ROC curve (AUC) of the proposed method was 0.921, indicating an excellent discriminative power.

Because we used LOOCV strategy to train the model, features are different in different loops. The frequently occurred discriminative feature nodes in all loops were displayed in **Figures 6B–D**, which included Occipital_Inf_R, Precuneus_R, Cingulum_Mid_L, Frontal_Sup_L/R, Lingual_L/R, Frontal_Sup_Medial_L/R, Cuneus_L, Frontal_Mid_Orb_R, Precentral_L, Insula_R, Temporal_Mid_R, Putamen, Supp_Motor_Area_L, Cerebelum_Crus1_R.

DISCUSSION

Cognitive decline in cirrhotic patient with occurrence of MHE has been largely acknowledged (Damulin, 2018), but the current clinical diagnosis based on neuropsychological cognitive tests

TABLE 5 | The classification results with different window length.

	Windowlength (40TR)	Window length (45TR)	Window length (50TR)	Window length (55TR)
ACC	85.48%	**88.71%**	85.48%	83.87%
SEN	92%	**92.31%**	88.89%	85.71%
SPE	81.08%	**83.33%**	84.38%	82.35%

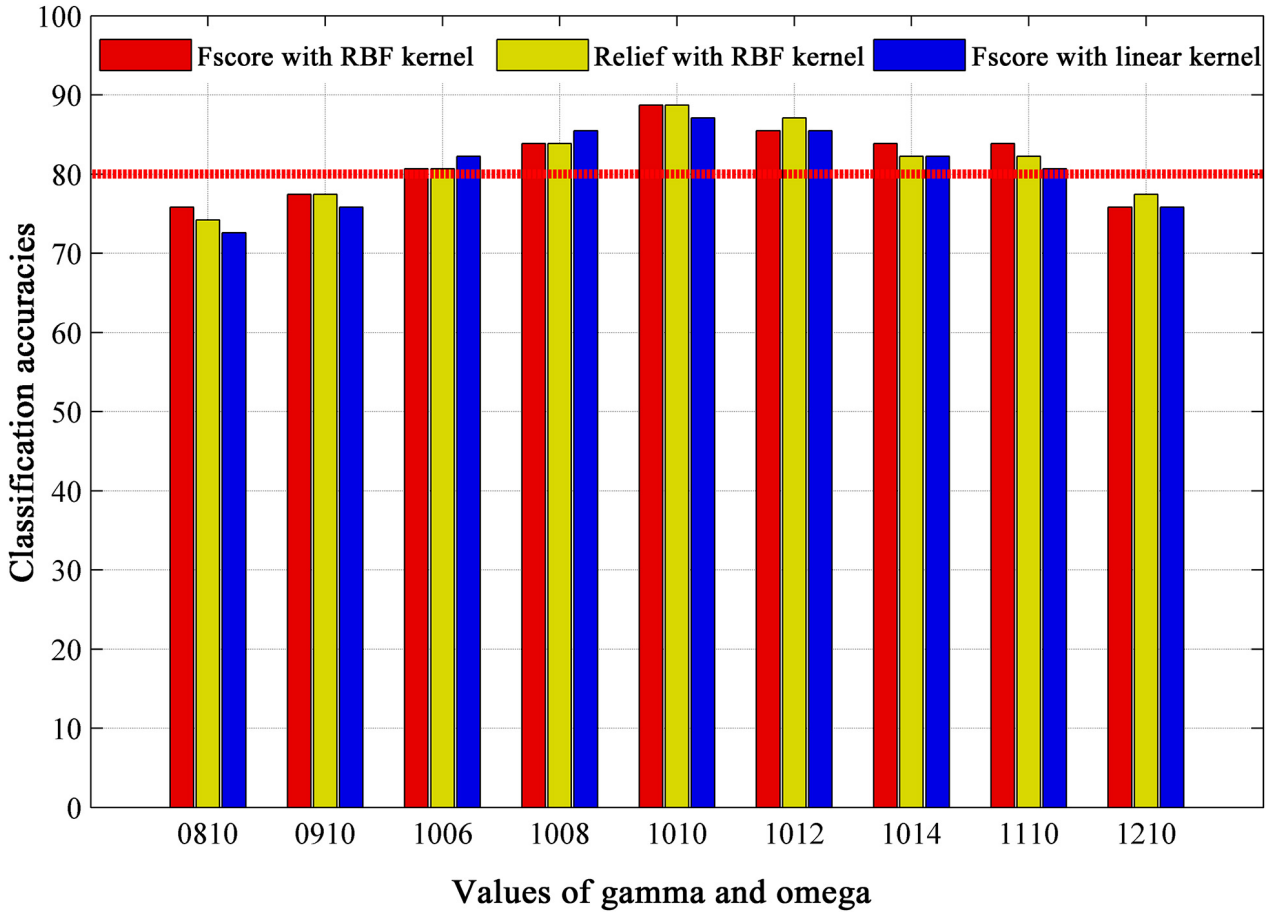

FIGURE 5 | The classification results based on different module partition parameters (gamma, omega), feature selection methods (Fscore and Relief), and kernel functions of classifier (RBF kernel and linear kernel), where omega is spatial resolution parameter, and gamma is temporal resolution parameter in multi-layer community structure calculation. Values of gamma and omega = 0810 mean gamma = 0.8, omega = 1.0. RBF = radial basis function.

is easily mixed by sex, age and education level. In this study, we aimed to investigate the biomark of MHE based on brain imaging data. From a view of dynamic brain graph analysis, we took the whole brain functional connectivity matrix as a graph and applied multi-layer modular algorithm to analyze the dynamic reorganization of the modules in brain graph of MHE patients. Connection-stability profile and nodal affiliation changes were used to describe the dynamic graph properties of the brain network. By comparing these metrics among groups, we found that in the connection-stability matrix, MHE and HC showed significant differences within specific networks, but there was no statistical significance between other groups at network level. In terms of nodal dynamic metrics, MHE and noHE showed significant differences merely in node disjointness. Further, we observed node disjointness in patient groups were correlated with neuropsychological scales. In order to test the discriminative power in identification MHE from noHE, we used SVM to classify the two groups based on node disjointness metric. Consistent discriminant nodes were identified contributing to a better explanation of dysfunctional mechanisms. The high classification accuracy of 88.71% also suggest the effectiveness of the dynamic brain functional metric in identification of individual MHE.

In our study, the connection-stability matrix quantifies the relative stability of node pairs in a dynamic process. A higher value means less flexibility of the node pairs. From the matrix profile of the three groups, it can be seen that the obtained connection-stability matrix in healthy control group showed

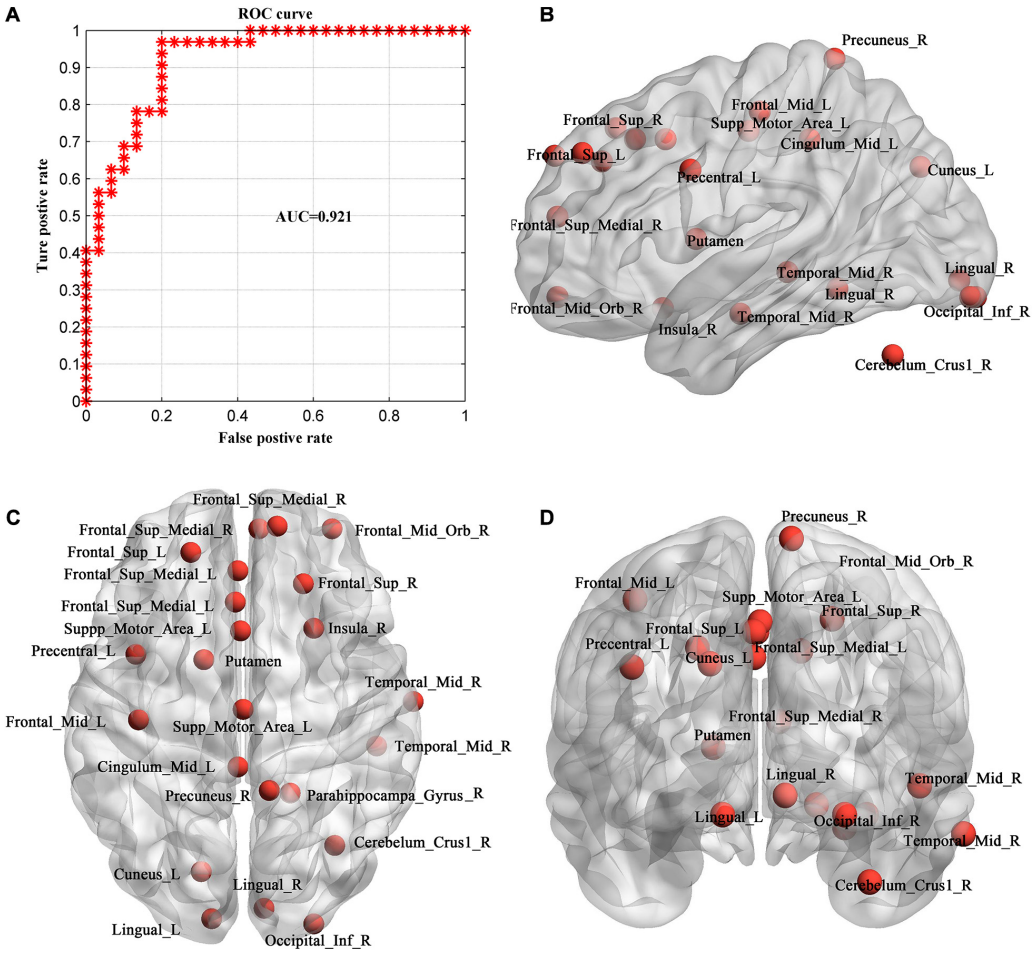

FIGURE 6 | Evaluation of individual MHE discrimination classifier. **(A)** ROC curve of the classifier. **(B–D)** The consistent discriminant nodes in SVM classification showing in sagittal **(B)**, axial **(C)** and coronal planes **(D)**. MHE, minimal hepatic encephalopathy. ROC, receiver operating characteristic; AUC, = area under ROC curve.

obvious modularity, which was similar to Power's 14 functional network partition results (Power et al., 2013). This suggests that the modular partition results in the present study are confidential and are consistent with brain functional network organization patterns. Compared with healthy control group, the average connection stability within SSMN, CON, DMN, and FPN were significantly reduced in MHE patients (**Table 3**). This is consistent with previous studies reporting that the abnormal network strength in these networks (Chen et al., 2014; Jao et al., 2015; Cheng et al., 2018). Because the SSMN is important for motor control function (Matyas et al., 2010), the CON, DMN and FPN are responsible for execute control function, attention, and working memory that are important in daily activities (Fox et al., 2005; Matyas et al., 2010), the abnormal connection stability with these networks may explain the impairs in daily functioning, driving performance, work capability and learning ability in MHE patients (Agrawal et al., 2015). There was no significant difference in the average connection-stability matrix between MHE and noHE at the network level, but at the node level, nodal disjointness difference was found between the two groups, indicating that conversion from noHE to MHE is represented by some nodal dysfunction within networks but not the whole network dysfunction.

Further analysis of three node properties in comparison of MHE with noHE indicates that significant differences were found merely in node disjointness metric. The regions that showed abnormal node disjointness were in middle temporal region, superior medial and lateral regions, orbital frontal region, middle cingulate cortex, and they mainly occupied the VAN, FPN and DMN, which are important for attention allocation and execution control functions that have decline in MHE patients (Rosazza and Minati, 2011; Zhang et al., 2014a). These damaged areas of MHE were also reported in previous studies (Chen et al., 2016a; Zhang et al., 2018a). Comparison of the three groups together, we can see in cirrhosis with no HE, the affected regions were located in both primary network (SSHN) and high level cognitive networks (SN, FPN, and DMN). When progression from noHE to MHE, the dysfunctional nodes were mainly distributed in the three high-level core cognitive networks (VAN, FPN, and DMN), demonstrating that occurrence of MHE is related to core

cognitive dysfunction. On flexibility and cohesion, we found no significant differences, suggesting that brain impairment in MHE patients might be caused by the abnormal proportion of nodes independently switching network affiliation but not the nodes that change network affiliation with other nodes together. The results also show that single-node switching may be more frequent in brain regions in MHE patients than in noHE patients. This may lead to cognition-related dysfunction in MHE patients.

The cognitive deficit of all cirrhotic patients was evaluated using DST and NCT-A scores in this study as recommended (Weissenborn et al., 2001; Li et al., 2013), in which DST evaluates cognitive function of attention and visual memory (Weissenborn et al., 2001; Zhang et al., 2017a). Correlation analysis showed that DST scores were positively correlated with the average connection stability scores of DMN, VN, FPN, SN, subcortical network and had negative correlations with the nodal disjointness values of the DMN and SN. Theoretically, a higher flexibility of the nodes corresponds to a lower average connection stability, and thus consistency in the two correlation analyses were found in DMN and SN. Both of the two networks are important for attention and working memory (Pessoa et al., 2002; Silk et al., 2010). DMN collectively comprises an integrated system for different aspects of self-referential mental processes and it is de-actived in a cognition-demanding task (Raichle et al., 2001). SN is important for detection and mapping of salient external inputs and internal brain events, and it drives the switching between default mode and central executive networks in a triple-network model underlying the high level cognitive function (Menon, 2011). Therefore, correlation between the node disjointness of the two networks and the DST scores indicates that increased single-node switching rate in DMN and SN may be responsible for decline in high level cognitive functions such as attention and working memory that are important in the cirrhotic patients' daily life.

Since we found significant differences between MHE and noHE merely in the node disjointness at network level and unique correlation with neuropsychological scores was also obtained in this metric, we used node disjointness to evaluate the discriminative power of classifier. The experiment results show its effectiveness in identification of individual MHE from noHE with an accuracy of 88.71%. Comparison analyses show that the spatial resolution parameter of omega had a greater impact on the results than temporal resolution parameter gamma. The best result was obtained when we chose the default values gamma $= 1.0$ and omega $= 1.0$ as the module partition parameters. With the best omega of 1.0, each network module was functionally explainable (see Figure 2). In respect of the impact of time window size, it is not a parameter that affects our main results. Results showed that the accuracy was highest when the time window length was 45TR (112.5 s), which is consistent with a previous study reported that classification accuracy was highest when the time window length was around 110s (Liu et al., 2017). With the comparisons of different combinations of feature selection method and classifiers, the best accuracy was obtained with F-score method and SVM with RBF kernel. In general, by validation on different parameters, our results showed a good discriminative power at individual level. Furthermore, by comparing the discriminative nodes obtained from individual diagnosis with the results from group statistical analysis, we can see not only overlapping regions, but also other regions were found in the discriminative analysis. This is because the discriminative analysis can grasp the whole pattern information in a multivariate way than the univariate group statistical analysis, demonstrating that combination of the dynamic features with machine learning model can provide more information.

However, some factors may limit the generalization of our findings in clinical application. First, because of the difficulty in patient recruitment, the sample size is small in this study, which may bias the result. Large samples can improve statistical power and reduce overfitting in the identification model. In the future, we will verify the identification model by both internal and external validations with lager sample size to provide a stable performance. Other more complex models like deep neural networks that can grasp deep and complex MHE characteristics can also be tried with larger dataset to provide better accuracy. Second, the laboratory test data was not used in the identification model. It could be combined with imaging data together into the identification model, which may provide a better identification accuracy. Third, different medications among patients may affect the findings in this study. In our study, lactulose was used in 19 patients to improve feces excretion function, and they took 5–10 g lactulose three times a day. Antibiotics was used in some patients who had infections such as spontaneous bacterial peritonitis, pulmonary infection, which may bias the findings because antibiotics may induce changes in synaptic plasticity and neural cell growth (Heiss and Olofsson, 2019). In addition, the smoking history may also affect the result, which should be considered in the future studies. Last, laboratory test data are needed for healthy controls to fully exclude the possible liver disease.

CONCLUSION

Previous studies mainly used static analysis features to study MHE, we used the multi-layer modular algorithm based dynamic functional connectivity features to study and identify MHE from noHE. The core of this method is to extract metrics describing network connection-stability and dynamic nodal affiliation based on dynamic module partition results. It is found that compared with HC, MHE showed differences in both primary sensory network module and high level cognitive networks, consistent with the symptom of decline in driving ability, daily functioning, learning and working performance. When progression from noHE to MHE, the cognitive impairments were mainly in higher cognitive networks of DMN and SN by disrupting network organization in a way of frequent single-node disjointness, which is associated with the neuropsychological score. Based on the node disjointness property, the individual discriminative model showed a diagnosis accuracy of 88.71%. Taken together, the results in this study suggest that dynamic graph analysis can reveal the brain network evolvement patterns from noHE to MHE, help us understand the dysfunction of the brain in a fine scale, and provide powerful features for the individual diagnosis. In the future, larger samples of patients with no mixture of

interference factors are needed to verify the findings and further optimize the model to improve the identification accuracy. We can further investigate the clinical features of MHE on electroencephalo-graph (EEG). EEG features and the clinical data from laboratory test can also be incorporated into the machine learning model to develop a tool that can be used with lower cost and rural areas without fMRI.

DATA AVAILABILITY STATEMENT

The original contributions presented in the study are included in the article/**Supplementary Material**, further inquiries can be directed to the corresponding author/s.

ETHICS STATEMENT

The studies involving human participants were reviewed and approved by Medical Research Ethics Committee of Tianjin First Central Hospital. The patients/participants provided their written informed consent to participate in this study.

AUTHOR CONTRIBUTIONS

YC and WS designed the experiment, recruited the participants, and revised the manuscript. GZ proposed the data analysis method, performed data analysis, and wrote and revised the manuscript. YL performed data analysis and wrote the original manuscript. XZ and LH contributed to data collection. All authors contributed to the article and approved the submitted version.

FUNDING

This study was supported by the National Natural Science Foundation of China (Nos. 61876126 and 81601482) and the Peiyang Scholar Program of Tianjin University (No. 2018XRG-0037).

SUPPLEMENTARY MATERIAL

The Supplementary Material for this article can be found online at: https://www.frontiersin.org/articles/10.3389/fnins.2020.627062/full#supplementary-material

REFERENCES

Agrawal, S., Umapathy, S., and Dhiman, R. K. (2015). Minimal hepatic encephalopathy impairs quality of life. *J. Clin. Exp. Hepatol.* 5, S42–S48. doi: 10.1016/j.jceh.2014.11.006

Bassett, D. S., Wymbs, N. F., Porter, M. A., Mucha, P. J., Carlson, J. M., and Grafton, S. T. (2011). Dynamic reconfiguration of human brain networks during learning. *Proc. Natl. Acad. Sci. U. S. A.* 108, 7641–7646. doi: 10.1073/pnas.1018985108

Betzel, R. F., Fukushima, M., He, Y., Zuo, X. N., and Sporns, O. (2016). Dynamic fluctuations coincide with periods of high and low modularity in resting-state functional brain networks. *Neuroimage* 127, 287–297. doi: 10.1016/j.neuroimage.2015.12.001

Cai, J. Y., Liu, A. P., Mi, T. M., Garg, S. R. A., Trappe, W. D., McKeown, M. R. T., et al. (2019). Dynamic graph theoretical analysis of functional connectivity in Parkinson's Disease: the importance of fiedler value. *IEEE J. Biomed. Health Informatics* 23, 1720–1729. doi: 10.1109/Jbhi.2018.2875456

Calhoun, V. D., Miller, R., Pearlson, G., and Adali, T. (2014). The chronnectome: time-varying connectivity networks as the next frontier in fMRI data discovery. *Neuron* 84, 262–274. doi: 10.1016/j.neuron.2014.10.015

Campagna, F., Montagnese, S., Schiff, S., Biancardi, A., Mapelli, D., Angeli, P., et al. (2014). Cognitive impairment and electroencephalographic alterations before and after liver transplantation: what is reversible? *Liver Trans.* 20, 977–986. doi: 10.1002/lt.23909

Chen, Y. W., and Lin, C. J. (2006). "Combining SVMs with various feature selection strategies," in *Feature Extraction* (Heidelberg: Springer), 315–324.

Chen, H. J., Wang, Y., Zhu, X. Q., Li, P. C., and Teng, G. J. (2014). Classification of cirrhotic patients with or without minimal hepatic encephalopathy and healthy subjects using resting-state attention-related network analysis. *PLoS One* 9:e89684. doi: 10.1371/journal.pone.0089684

Chen, H. J., Zhang, L., Jiang, L. F., Chen, Q. F., Li, J., and Shi, H. B. (2016a). Identifying minimal hepatic encephalopathy in cirrhotic patients by measuring spontaneous brain activity. *Metab. Brain Dis.* 31, 761–769. doi: 10.1007/s11011-016-9799-9

Chen, Q. F., Chen, H. J., Liu, J., Sun, T., and Shen, Q. T. (2016b). Machine learning classification of cirrhotic patients with and without minimal hepatic encephalopathy based on regional homogeneity of intrinsic brain activity. *PLoS One* 11:e0151263. doi: 10.1371/journal.pone.0151263

Cheng, Y., Zhang, G. Y., Shen, W., Huang, L. X., Zhang, L., Xie, S. S., et al. (2018). Impact of previous episodes of hepatic encephalopathy on short-term brain function recovery after liver transplantation: a functional connectivity strength study. *Metab. Brain Dis.* 33, 237–249. doi: 10.1007/s11011-017-0155-5

Cole, M. W., Reynolds, J. R., Power, J. D., Repovs, G., Anticevic, A., and Braver, T. S. (2013). Multi-task connectivity reveals flexible hubs for adaptive task control. *Nat. Neurosci.* 16, 1348–1355. doi: 10.1038/nn.3470

Damulin, I. V. (2018). Minimal hepatic encephalopathy: current clinical and pathogenetic aspects. *Ter. Arkh.* 90, 89–93. doi: 10.26442/terarkh201890289-93

Fawcett, T. (2006). An introduction to ROC analysis. *Pattern Recognit. Lett.* 27, 861–874. doi: 10.1016/j.patrec.2005.10.010

Fox, M. D., Snyder, A. Z., Vincent, J. L., Corbetta, M., Van Essen, D. C., and Raichle, M. E. (2005). The human brain is intrinsically organized into dynamic, anticorrelated functional networks. *Proc. Natl. Acad. Sci. U. S. A.* 102, 9673–9678. doi: 10.1073/pnas.0504136102

Greve, D. N., and Fischl, B. (2009). Accurate and robust brain image alignment using boundary-based registration. *Neuroimage* 48, 63–72. doi: 10.1016/j.neuroimage.2009.06.060

Harlalka, V., Bapi, R. S., Vinod, P. K., and Roy, D. (2019). Atypical flexibility in dynamic functional connectivity quantifies the severity in autism spectrum disorder. *Front. Hum. Neurosci.* 13:6. doi: 10.3389/fnhum.2019.00006

Heiss, C. N., and Olofsson, L. E. (2019). The role of the gut microbiota in development, function and disorders of the central nervous system and the enteric nervous system. *J. Neuroendocrinol.* 31:e12684. doi: 10.1111/jne.12684

Hutchison, R. M., Womelsdorf, T., Allen, E. A., Bandettini, P. A., Calhoun, V. D., Corbetta, M., et al. (2013). Dynamic functional connectivity: promise, issues, and interpretations. *Neuroimage* 80, 360–378. doi: 10.1016/j.neuroimage.2013.05.079

Jao, T., Schroter, M., Chen, C. L., Cheng, Y. F., Lo, C. Y. Z., Chou, K. H., et al. (2015). Functional brain network changes associated with clinical and biochemical measures of the severity of hepatic encephalopathy. *Neuroimage* 122, 332–344. doi: 10.1016/j.neuroimage.2015.07.068

Jiao, Y., Wang, X. H., Chen, R., Tang, T. Y., Zhu, X. Q., and Teng, G. J. (2017). Predictive models of minimal hepatic encephalopathy for cirrhotic patients based on large-scale brain intrinsic connectivity networks. *Sci. Rep.* 7:11512.

Jeub, L. G. S., Bazzi, M., Jutla, I. S., and Mucha, P. J. (2011–2019). *A Generalized Louvain Method for Community Detection Implemented in Matlab*. Available online at: http://netwiki.amath.unc.edu/GenLouvain

Kira, K., and Rendell, L. A. (1992). "The feature selection problem: traditional methods and a new algorithm. Proceedings of the tenth national conference on artificial intelligence," in *Proceedings of the 10th National Conference on Artificial Intelligence*, (Atlanta: AAAI Press), 129–134.

Kucyi, A., and Davis, K. D. (2015). The dynamic pain connectome. *Trends Neurosci.* 38, 86–95. doi: 10.1016/j.tins.2014.11.006

Li, S. W., Wang, K., Yu, Y. Q., Wang, H. B., Li, Y. H., and Xu, J. M. (2013). Psychometric hepatic encephalopathy score for diagnosis of minimal hepatic encephalopathy in China. *World J. Gastroenterol.* 19, 8745–8751. doi: 10.3748/wjg.v19.i46.8745

Liu, F., Wang, Y., Li, M., Wang, W., Li, R., Zhang, Z., et al. (2017). Dynamic functional network connectivity in idiopathic generalized epilepsy with generalized tonic-clonic seizure. *Hum. Brain Mapp.* 38, 957–973. doi: 10.1002/hbm.23430

Liu, X., and Duyn, J. H. (2013). Time-varying functional network information extracted from brief instances of spontaneous brain activity. *Proc. Natl. Acad. Sci. U. S. A.* 110, 4392–4397. doi: 10.1073/pnas.1216856110

Matyas, F., Sreenivasan, V., Marbach, F., Wacongne, C., Barsy, B., Mateo, C., et al. (2010). Motor control by sensory cortex. *Science* 330, 1240–1243. doi: 10.1126/science.1195797

Menon, V. (2011). Large-scale brain networks and psychopathology: a unifying triple network model. *Trends Cogn. Sci.* 15, 483–506. doi: 10.1016/j.tics.2011.08.003

Murphy, K., Birn, R. M., Handwerker, D. A., Jones, T. B., and Bandettini, P. A. (2009). The impact of global signal regression on resting state correlations: are anti-correlated networks introduced? *Neuroimage* 44, 893–905. doi: 10.1016/j.neuroimage.2008.09.036

Newman, M. E. J. (2004). Fast algorithm for detecting community structure in networks. *Phys. Rev. E* 69:066133. doi: 10.1103/PhysRevE.69.066133

Pereira, F., Mitchell, T., and Botvinick, M. (2009). Machine learning classifiers and fMRI: a tutorial overview. *Neuroimage* 45, S199–S209. doi: 10.1016/j.neuroimage.2008.11.007

Pessoa, L., Gutierrez, E., Bandettini, P. A., and Ungerleider, L. G. (2002). Neural correlates of visual working memory: fMRl amplitude predicts task performance. *Neuron* 35, 975–987. doi: 10.1016/S0896-6273(02)00817-6

Power, J. D., Cohen, A. L., Nelson, S. M., Wig, G. S., Barnes, K. A., Church, J. A., et al. (2011). Functional network organization of the human brain. *Neuron* 72, 665–678. doi: 10.1016/j.neuron.2011.09.006

Power, J. D., Schlaggar, B. L., Lessov-Schlaggar, C. N., and Petersen, S. E. (2013). Evidence for hubs in human functional brain networks. *Neuron* 79, 798–813. doi: 10.1016/j.neuron.2013.07.035

Pugh, R. N., Murray-Lyon, I. M., Dawson, J. L., Pietroni, M. C., and Williams, R. (1973). Transection of the oesophagus for bleeding oesophageal varices. *Br. J. Surg.* 60, 646–649. doi: 10.1002/bjs.1800600817

Qi, R. F., Zhang, L. J., Xu, Q., Zhong, J. H., Wu, S. Y., Zhang, Z. Q., et al. (2012). Selective impairments of resting-state networks in minimal hepatic encephalopathy. *PLoS One* 7:e37400. doi: 10.1371/journal.pone.0037400

Raichle, M. E., MacLeod, A. M., Snyder, A. Z., Powers, W. J., Gusnard, D. A., and Shulman, G. L. (2001). A default mode of brain function. *Proc. Natl. Acad. Sci. U. S. A.* 98, 676–682. doi: 10.1073/pnas.98.2.676

Rosazza, C., and Minati, L. (2011). Resting-state brain networks: literature review and clinical applications. *Neurol. Sci.* 32, 773–785. doi: 10.1007/s10072-011-0636-y

Rubinov, M., and Sporns, O. (2010). Complex network measures of brain connectivity: uses and interpretations. *Neuroimage* 52, 1059–1069. doi: 10.1016/j.neuroimage.2009.10.003

Saad, Z. S., Gotts, S. J., Murphy, K., Chen, G., Jo, H. J., Martin, A., et al. (2012). Trouble at rest: how correlation patterns and group differences become distorted after global signal regression. *Brain Connect.* 2, 25–32. doi: 10.1089/brain.2012.0080

Silk, T. J., Bellgrove, M. A., Wrafter, P., Mattingley, J. B., and Cunnington, R. (2010). Spatial working memory and spatial attention rely on common neural processes in the intraparietal sulcus. *Neuroimage* 53, 718–724. doi: 10.1016/j.neuroimage.2010.06.068

Tailby, C., Kowalczyk, M. A., and Jackson, G. D. (2018). Cognitive impairment in epilepsy: the role of reduced network flexibility. *Ann. Clin. Trans. Neurol.* 5, 29–40. doi: 10.1002/acn3.503

Telesford, Q. K., Ashourvan, A., Wymbs, N. F., Grafton, S. T., Vettel, J. M., and Bassett, D. S. (2017). Cohesive network reconfiguration accompanies extended training. *Hum. Brain Mapp.* 38, 4744–4759. doi: 10.1002/hbm.23699

Weissenbacher, A., Kasess, C., Gerstl, F., Lanzenberger, R., Moser, E., and Windischberger, C. (2009). Correlations and anticorrelations in resting-state functional connectivity MRI: a quantitative comparison of preprocessing strategies. *Neuroimage* 47, 1408–1416. doi: 10.1016/j.neuroimage.2009.05.005

Weissenborn, K., Ennen, J. C., Schomerus, H., Ruckert, N., and Hecker, H. (2001). Neuropsychological characterization of hepatic encephalopathy. *J. Hepatol.* 34, 768–773. doi: 10.1016/S0168-8278(01)00026-5

Zhang, D. Q., Tu, L. Y., Zhang, L. J., Jie, B., and Lu, G. M. (2018a). Subnetwork mining on functional connectivity network for classification of minimal hepatic encephalopathy. *Brain Imaging Behav.* 12, 901–911. doi: 10.1007/s11682-017-9753-4

Zhang, G. Y., Cheng, Y., and Liu, B. L. (2017a). Abnormalities of voxel-based whole-brain functional connectivity patterns predict the progression of hepatic encephalopathy. *Brain Imaging Behav.* 11, 784–796. doi: 10.1007/s11682-016-9553-2

Zhang, G. Y., Cheng, Y., Shen, W., Liu, B. L., Huang, L. X., and Xie, S. S. (2017b). The short-term effect of liver transplantation on the low-frequency fluctuation of brain activity in cirrhotic patients with and without overt hepatic encephalopathy. *Brain Imaging Behav.* 11, 1849–1861. doi: 10.1007/s11682-016-9659-6

Zhang, G. Y., Cheng, Y., Shen, W., Liu, B. L., Huang, L. X., and Xie, S. S. (2018b). Brain regional homogeneity changes in cirrhotic patients with or without hepatic encephalopathy revealed by multi-frequency bands analysis based on resting-state functional MRI. *Korean J. Radiol.* 19, 452–462. doi: 10.3348/kjr.2018.19.3.452

Zhang, L. J., Wu, S., Ren, J., and Lu, G. M. (2014a). Resting-state functional magnetic resonance imaging in hepatic encephalopathy: current status and perspectives. *Metab. Brain Dis.* 29, 569–582. doi: 10.1007/s11011-014-9504-9

Zhang, L. J., Zheng, G., Zhang, L., Zhong, J., Wu, S., Qi, R., et al. (2012). Altered brain functional connectivity in patients with cirrhosis and minimal hepatic encephalopathy: a functional MR imaging study. *Radiology* 265, 528–536. doi: 10.1148/radiol.12120185

Zhang, L. J., Zheng, G., Zhang, L. P., Zhong, J. H., Li, Q., Zhao, T. Z., et al. (2014b). Disrupted small world networks in patients without overt hepatic encephalopathy: a resting state fMRI study. *Eur. J. Radiol.* 83, 1890–1899. doi: 10.1016/j.ejrad.2014.06.019

Conflict of Interest: The authors declare that the research was conducted in the absence of any commercial or financial relationships that could be construed as a potential conflict of interest.

frontiers in Neuroscience

ORIGINAL RESEARCH
published: 18 January 2021
doi: 10.3389/fnins.2020.629667

Seizure Freedom After Epilepsy Surgery and Higher Baseline Cognition May Be Associated With a Negatively Correlated Epilepsy Network in Temporal Lobe Epilepsy

*Elliot G. Neal[1], Mike R. Schoenberg[1,2], Stephanie Maciver[2], Yarema B. Bezchlibnyk[1] and Fernando L. Vale[3]**

[1] Department of Neurosurgery and Brain Repair, University of South Florida, Tampa, FL, United States, [2] Department of Neurology, University of South Florida, Tampa, FL, United States, [3] Department of Neurosurgery, Medical College of Georgia, Augusta University, Augusta, GA, United States

Background: Brain regions positively correlated with the epileptogenic zone in patients with temporal lobe epilepsy vary in spread across the brain and in the degree of correlation to the temporal lobes, thalamus, and limbic structures, and these parameters have been associated with pre-operative cognitive impairment and seizure freedom after epilepsy surgery, but negatively correlated regions have not been as well studied. We hypothesize that connectivity within a negatively correlated epilepsy network may predict which patients with temporal lobe epilepsy will respond best to surgery.

Methods: Scalp EEG and resting state functional MRI (rsfMRI) were collected from 19 patients with temporal lobe epilepsy and used to estimate the irritative zone. Using patients' rsfMRI, the negatively correlated epilepsy network was mapped by determining all the brain voxels that were negatively correlated with the voxels in the epileptogenic zone and the spread and average connectivity within the network was determined.

Results: Pre-operatively, connectivity within the negatively correlated network was inversely related to the spread (diffuseness) of that network and positively associated with higher baseline verbal and logical memory. Pre-operative connectivity within the negatively correlated network was also significantly higher in patients who would go on to be seizure free.

Conclusion: Patients with higher connectivity within brain regions negatively correlated with the epilepsy network had higher baseline memory function, narrower network spread, and were more likely to be seizure free after surgery.

Keywords: epilepsy surgery, networks, resting fMRI, negative correlation, temporal lobe epilepsy

OPEN ACCESS

Edited by:
Xiaopeng Song, Harvard Medical School, United States

Reviewed by:
Masaki Iwasaki, National Center of Neurology and Psychiatry, Japan
Romain Carron, Hôpitaux Universitaires de Marseille Timone, APHM, France

***Correspondence:**
Fernando L. Vale
fvalediaz@augusta.edu

Specialty section:
This article was submitted to Brain Imaging Methods, a section of the journal Frontiers in Neuroscience

Received: *15 November 2020*
Accepted: *28 December 2020*
Published: *18 January 2021*

Citation:
Neal EG, Schoenberg MR, Maciver S, Bezchlibnyk YB and Vale FL (2021) Seizure Freedom After Epilepsy Surgery and Higher Baseline Cognition May Be Associated With a Negatively Correlated Epilepsy Network in Temporal Lobe Epilepsy. Front. Neurosci. 14:629667. doi: 10.3389/fnins.2020.629667

Abbreviations: (18F-FDG) PET, 18Fluoro-2-deoxyglucose positron emission tomography; BOLD, Blood oxygenation level dependent; BNT, Boston Naming Test; COWAT-FAS, Controlled Oral Word Association Test; ECoG, Electrocorticography; EEG, Electroencephalography; EMU, Epilepsy Monitoring Unit; MNI, Montreal Neurological Institute; rsfMRI, Resting state functional MRI; RAVLT6, Rey Auditory Verbal Learning Test, Trial 6; RAVLT7, Rey Auditory Verbal Learning Test, Trial 7; RFFT, Ruff Figural Fluency Test-unique designs; TLE, Temporal lobe epilepsy; FSIQ, Full Scale Intelligence Quotient: Wechsler Adult Intelligence Scale-4th Ed.; LM-I, Logical Memory Immediate recall subtest: Wechsler Memory Scale-4th Ed.; LM-II, Logical Memory Delayed recall subtest: Wechsler Memory Scale-4th Ed.; VR-I, Visual Reproduction Immediate Recall subtest: Wechsler Memory Scale-4th Ed.; VR-II, Visual Reproduction Delayed Recall subtest: Wechsler Memory Scale-4th Ed.

INTRODUCTION

Surgical Treatment of Temporal Lobe Epilepsy

Epilepsy is a common primary neurological disorder that affects 0.5–1% of the global population, of which 20–30% are refractory to medical management (Kwan and Brodie, 2000; Sander, 2003). For those patients who are refractory to medication, the next line of therapy involves some type of surgical intervention. If the epilepsy is focal and the epileptogenic zone can be localized to a temporal lobe using conventional techniques, which include electroencephalography (EEG), MRI, 18Fluoro-2-deoxyglucose positron emission tomography [(18F-FDG) PET], semiology, and neuropsychological testing, then a surgery can be planned to resect or ablate the hypothesized focus and disconnect the epileptogenic network. Surgeries that have been used to treat temporal lobe epilepsy include anterior temporal lobectomy, selective amygdalohippocampectomy, temporal lobectomy with amygdalectomy and minimal hippocampal resection, and stereotactic laser amygdalohippocampotomy (SLAH) (Schramm, 2008). Resective surgeries in the temporal lobe have been shown to result in seizure freedom in approximately two-thirds of patients, and an improved quality of life when compared to medical management alone (Wiebe et al., 2001; Bell et al., 2009; Engel et al., 2012; Vale et al., 2012). However, this still leaves the one-third of patients who undergo surgery in their temporal lobe who continue to have debilitating seizures.

Network Analysis in Surgical Planning

When seizures recur, or are insufficiently controlled following surgery, it is commonly assumed that the surgical intervention was insufficient to resect, ablate, or disconnect the epileptogenic brain region(s). This problem may arise when the epileptogenic zone is knowingly spared due to concerns for post-operative neurocognitive or neurological function, or when the epileptogenic zone is incompletely evaluated by the pre-operative work-up. Several authors have proposed a network model for epilepsy, whereby the pre-operative work-up is directed toward elucidating the connectivity within and extent of the epileptogenic network which is both necessary and sufficient for post-operative seizure control, as well as the relationship of this network with networks underlying neurocognitive function (Bartolomei et al., 2008; Bernhardt et al., 2013; Gonzalez et al., 2019; Morgan et al., 2019). Typically, this consists of invasive monitoring using intracranial EEG depth electrodes (Chauvel et al., 2019). However, such studies are labor-intensive, take time, and carry an inherent risk, leading to efforts to devise non-invasive strategies for modeling epilepsy-related functional networks that can be used to predict who is more likely to be relieved of seizures.

Non-invasive Epilepsy Network Modeling

We previously developed a network modeling algorithm that uses rsfMRI and surface EEG to generate a hypothesized epileptogenic zone non-invasively. This algorithm then generates a network of other regions with activation patterns that have a high degree of positive correlation with the epileptogenic zone in patients with temporal lobe epilepsy (Neal et al., 2018). With this model, we showed that the degree of spread of this positively correlated "epilepsy network" in patients with TLE was associated with relatively worse outcomes both in rates of seizure freedom and in measures of cognition including executive function and verbal memory (Neal et al., 2019). Furthermore, we showed that greater disconnection of this network after surgery was associated with a higher likelihood of seizure freedom (Neal et al., 2020). These results suggest that the positively correlated epilepsy network may be associated with impaired cognition in patients with temporal lobe epilepsy and that disconnection of this network may impede the generation and propagation of seizures. Thus far, the only network that we have studied is the positively correlated epilepsy network.

Negative Correlation in Network Analysis

A positive correlation in activation patterns indicates that one or more brain regions are likely connected in some way. However, the opposite case may also be true: negatively correlated brain regions may also be functionally connected (**Figure 1A**). For example, if a particular neuron or group of neurons has an inhibitory effect on its target, then every time the first neuron fires then the target would fire less frequently. Therefore, a positive activation in one region would be directly associated with a deactivation in the connected area (**Figure 1B**). Mathematically, this can be determined as a negative correlation value (Pearson correlation coefficient <0). Negative correlation between nodes of the DMN (default mode network) have been observed with relation to task positive networks in healthy patients (Uddin et al., 2009). Negative correlation has, for the most part, been studied in relation to generalized epilepsies, with findings being mostly related to the behavior of the DMN. Antagonism between the dorsal attention network, salience network, and DMN was shown to be related to impaired executive and attention function in patients with absence seizures (Li et al., 2015). A similar relationship between the task positive network and the DMN in children with benign childhood epilepsy with centrotemporal spikes was found when compared to a control group (Luo et al., 2016). Patients with idiopathic generalized epilepsy have been found to have segregation and negative correlation between regions of the DMN (McGill et al., 2012).

In temporal lobe epilepsy, network studies utilizing negative correlation have shown decreased connectivity in the temporal lobes and a compensatory increase in the default mode network connectivity over time (Zhang et al., 2010). In a SPECT-based network study in temporal lobe epilepsy examining the positive and negative network correlations, the authors found that alterations in consciousness during seizures were associated with increased cerebral blood flow (CBF) in the temporal lobes and midline subcortical structures, which was negatively correlated with CBF in the frontal and parietal association cortices (Blumenfeld et al., 2004). In a small study of patients who underwent surgery for temporal lobe epilepsy, a similar result was found. rsfMRIs performed in these patients demonstrated a negative correlation between the temporal lobe and widespread cortical and subcortical regions compared

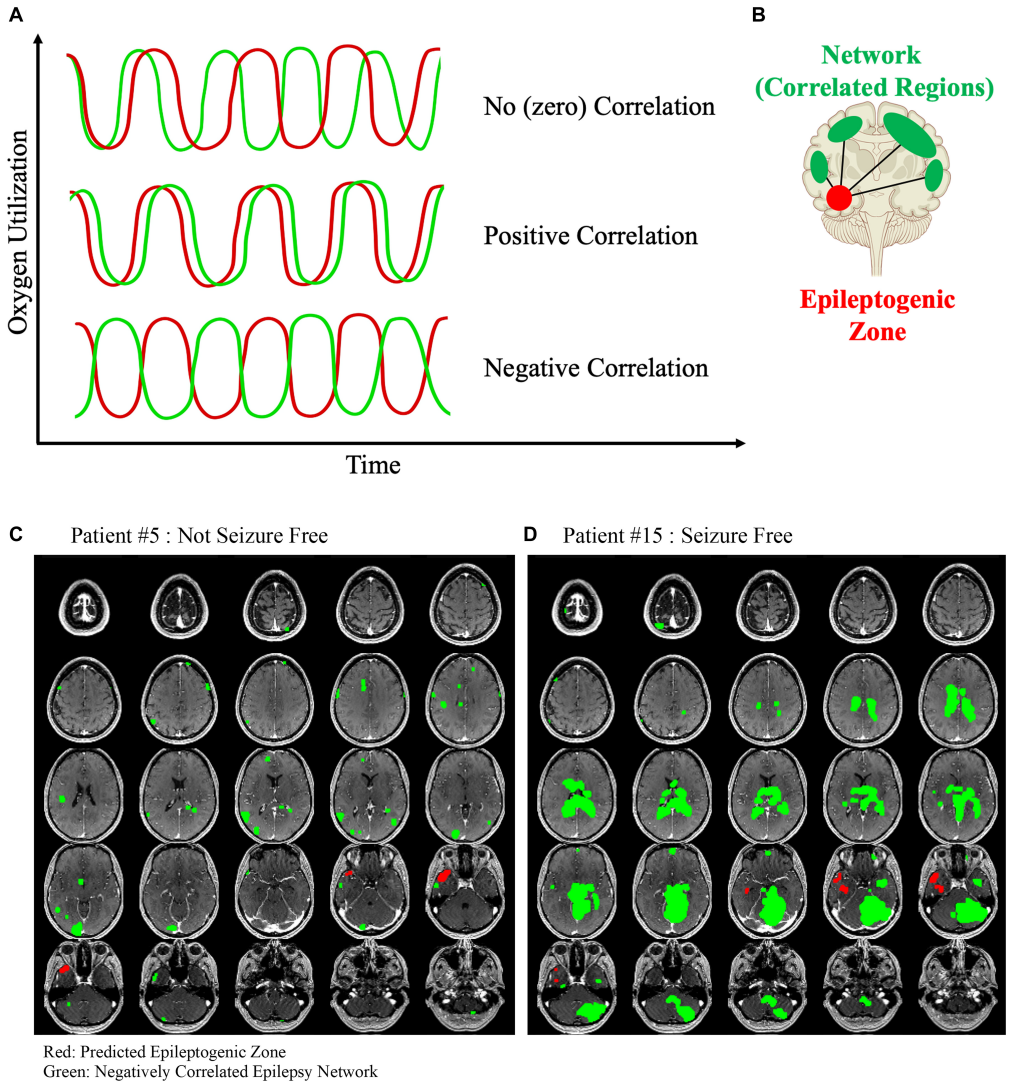

FIGURE 1 | (A) Three different example time series data from two hypothetical rsfMRI voxels are shown. First, the oxygen utilization over time between two hypothetical voxels is unrelated and therefore the correlation between the two is approximately zero. Next, the time series of each voxel behaves similarly and therefore have a positive correlated coefficient indicating that they are functionally similar and likely intraconnected. Finally, two voxels that behave antagonistically but are in-phase would have a negative correlation coefficient and we hypothesized that this relationship may represent a different type of functional connectivity than the positive correlated voxels. **(B)** The negatively correlated epilepsy network is then generated between the voxels in the epileptogenic zone and all of the other brain voxels with a below-threshold correlation coefficient. Two example patients are shown. **(C)** Patient #5 was not seizure free after surgery, and **(D)** Patient #15 was seizure free. The negatively correlated network is shown in green, and the hypothesized epileptogenic zone, generated from surface EEG, is shown in red. The lack of a clear organized negatively correlated network is obvious in the first patient, and the only visible areas are likely a contribution of the noisy rsfMRI signal and reflects the clear difference that exists in this network between patients who are more likely to be seizure free after surgery compared to those who are not.

to controls (Morgan et al., 2010). These regions included the thalamus, brainstem, frontal regions, and parietal regions, whereas the control group did not have this same widespread network of negatively correlated regions.

Objective

In the current study we hypothesize that the network consisting of brain regions negatively correlated with the epileptogenic zone can be determined in patients with temporal lobe epilepsy undergoing surgery and intraconnectivity and spread of that network may be predictive of seizure freedom and neuropsychological outcomes after surgery.

MATERIALS AND METHODS

Patient Demographics

All reported data followed the Strengthening the Reporting of Observational studies in Epidemiology (STROBE) guidelines for observational trials and the protocol and informed consent

was approved by our university's Institutional Review Board (IRB). Epileptic networks were modeled in nineteen patients with unilateral TLE who underwent open microsurgery directed toward the anterior/mesial temporal lobe. The patients included in this study represent a series of patients with TLE who signed consent and agreed to participate in this study between May 2017 and March 2020. They underwent this pre-operative network assessment and surgery at our tertiary referral center (**Table 1**). Exclusion criteria included all patients who had less than 1 year of follow up, pre-pubertal children (youngest patient was 17 years old at the time of surgery), and patients with any brain lesion except for mesial temporal sclerosis. Each patient underwent a standard pre-surgical evaluation for epilepsy surgery including MRI, epilepsy monitoring unit (EMU) video-EEG, Wada testing, (18F-FDG) PET, and neuropsychological testing. Surgery planning and post-surgical evaluation not related to network analysis were conducted by a care team blinded to the epileptic network modeling results.

Data Acquisition

Electroencephalography and rsfMRI were obtained on separate visits non-concurrently as part of the pre-surgical evaluation. No patient had a clinical seizure during the duration of the rsfMRI acquisition, though we cannot say with absolute certainty that patients did not have subclinical seizures during the acquisition period. In our cohort there were no patients that had interictal discharges more frequent than one per hour according to subsequent epilepsy monitoring unit results. EEG was acquired with 24 scalp electrodes in a standard International 10–20 configuration during the pre-operative EMU (Epilepsy Monitoring Unit) session. rsfMRI was conducted in a 3-Tesla MRI with a blood oxygenation level dependent (BOLD) MRI sequence. rsfMRI was acquired with the patient lying supine with eyes closed. The rsfMRI sequence consisted of a single 5-min acquisition with parameters as follows: echo time (TE) of 35 ms, repetition time (TR) of 3000 ms, and a voxel size of 4 mm × 3.75 mm × 3.75 mm. Volumetric T1-weighted thin slice (1.5 mm) MRI [Repetition Time (TR) 6.484, Echo Time (TE) 2.958, Inversion Time 18, Flip Angle 15, Field of View (FOV) 240 mm × 240 mm] was acquired during the same session. The post-operative MRI was conducted 4 months after the surgery to allow the acute surgery-related MRI signal to dissipate and not affect the results.

Network Modeling

The epilepsy network for each patient was modeled similar to what is previously described (Neal et al., 2018). Briefly, all MR image sets were motion corrected, smoothed, and transformed into Montreal Neurological Institute (MNI) space using the six-parameter rigid body spatial transformation algorithm and co-registered using SPM12 (Wellcome Department of Imaging Neuroscience, University College London, United Kingdom). The motion correction step was performed by least-squares approach to realign all images in the rsfMRI set to the first image in the series to reduce the effect of patient motion on the post-processing analysis. The Gaussian smoothing kernel full width at half maximum was 8 mm in all directions. The scalp EEG data were filtered to remove non-physiologic frequencies and cropped to include only the inter-ictal or ictal signals identified by a blinded neurophysiologist (MATLAB 2019b, Natick, MA, United States). A band pass filter was applied between 1 and 100 Hz, and a notch filter was applied at 60 Hz. Ictal and inter-ictal source discharges were localized by first generating a transformed mesh from the thin-slice T1-weighted MRI sequence. Then, cortical dipoles were modeled using a forward computation that was followed by an empirical Bayesian approach to inverse reconstruction, localizing the theoretical evoked response (SPM12). This process was used to generate a hypothesized epileptogenic or irritative zone source volume from both interictal and ictal discharges, which was co-registered to the rsfMRI in MNI space. The combined ictal and interictal regions in the temporal lobe ipsilateral to the planned surgical resection were included in the next steps of analysis for generating a model of the network.

The rsfMRI time-series signature was extracted from the epileptogenic zone volume and scaled to the global signal average to adjust for differences between scans. Intra-axial image voxels were extracted using a brain mask and compared to the voxels in the hypothesized epileptogenic zone to generate a Pearson correlation coefficient for each voxel with respect to the epileptogenic zone. In previous studies using this algorithm, the epilepsy network was defined as the collection of voxels that had an above-threshold Pearson correlation, with the threshold defined as the average Pearson correlation coefficient for each patient, so that all volumes generated were positively correlated with the epileptogenic zone. This type of analysis was done in the present study to generate an epilepsy network, but the primary aim of this study was to investigate the negatively correlated regions, so the inverse epilepsy network was defined as the voxels that had a Pearson correlation value less than −0.4. The threshold −0.4 was selected to standardize the analysis between patients, which has been shown to have a high sensitivity for detecting nodes within brain networks (van den Heuvel et al., 2008; Shen et al., 2013). Similar to our prior studies, intraconnectivity within this unique network was calculated by determining the correlation matrix for all the voxels involved in the inverse epilepsy network and computing an average value. This intraconnectivity is calculated from the within-network functional connectivity between voxels inside the negatively correlated epilepsy network, averaged across the entire network. To clarify, the intraconnectivity is not calculated between the negatively correlated network voxels and the hypothesized epileptogenic zone. Similarly, post-operative connectivity within the modeled network was determined by calculating the mean Pearson connectivity coefficient within the network when the same set of voxels were overlaid on the post-operative rsfMRI image set. The spread of the negatively correlated epilepsy network was defined as the median Euclidean distance of each voxel within the network from the centroid of the hypothesized epileptogenic zone generated from the EEG source localization. The network was mapped without prior knowledge of any parameters in the rsfMRI for each patient and is not related to any anatomical or functional atlas. Two examples, one of a negatively correlated that is

TABLE 1 | Demographics.

Patient number	Gender	Age at surgery	Anti-seizure medications (at surgery)	Surgery side	Dominant hemisphere (Wada)	Seizure free
1	Male	26	Levetiracetam, Lamotrigine	Left	Left	No
2	Male	17	Lamotrigine	Left	Right	No
3	Female	26	Vimpat, Aptiom	Right	Left	No
4	Female	35	Carbamazepine, Lamotrigine	Left	Left	No
5	Female	32	Levetiracetam, Topiramate	Left	Right	No
6	Female	40	Zonisamide	Right	Left	No
7	Female	36	Lamotrigine	Left	Left	No
8	Female	47	Gabapentin	Left	Left	Yes
9	Male	23	Levetiracetam	Left	Left	Yes
10	Female	34	Lacosamide, Levetiracetam	Left	Right	Yes
11	Female	19	Lamotrigine, Levetiracetam, Topiramate	Right	Left	Yes
12	Female	40	Oxcarbazepine	Right	Left	Yes
13	Male	26	Lacosamide, Levetiracetam, Topiramate	Left	Left	Yes
14	Female	33	Brivaracetam, Lacosamide, Lamotrigine	Left	Left	Yes
15	Male	32	Lacosamide	Left	Left	Yes
16	Female	28	Lamotrigine, Levetiracetam, Perampanel, Zonisamide	Left	Left	Yes
17	Female	24	Levetiracetam	Left	N/A	Yes
18	Male	25	Perampanel, Oxcarbazepine	Left	Left	Yes
19	Female	53	Lamotrigine	Left	Left	Yes

more diffuse (**Figure 1C**) and one that is highly organized and synchronized (**Figure 1D**) are shown. All network maps and hypothesized epileptogenic zones are also included in **Supplementary Figure 1**.

As a control comparison, a random ROI was used to generate a random negatively correlated network using the exact same method as described above. The random ROI used was in the occipital lobe and had a size of 907 voxels, similar to the average seed size for the hypothesized epileptogenic zone seeds. The same metrics of network spread and intraconnectivity were calculated as described above.

Neuropsychological Assessment

Pre-operatively, 19 patients had comprehensive neuropsychological assessment following NIH Epilepsy common data elements recommendations that quantify aspects of cognition including declarative memory, attention/executive, language, and visuoconstructional functions as well as general intellectual ability. Quality of life and mood status was also obtained. Pre- and post-operative data were available for a subset of patients (n = 13) because data from the remaining patients are still being collected and processed. Testing and scoring were conducted by clinicians blinded to the network modeling results. Subtests of the Wechsler Memory Scale-4th Ed. (WMS-IV) analyzed immediate or delayed logical memory (LM-I and LM-II) and immediate or delayed visual reproduction (VR-I and VR-II), a measure of visual memory. The Rey Auditory Verbal Learning Test short-delay (RAVLT Trials 6) and long-delay (RAVLT 7) was used to measure auditory-verbal memory, rate of learning, learning strategies, retroactive and proactive interference, the presence of confabulation in memory processes, retention of information, and differences between learning and retrieval. Both RAVLT 6 and 7 and LM-I and II are tests that measure verbal memory. Verbal fluency was measured using the Controlled Oral Word Association (FAS) and semantic fluency was measured using the Animal Naming Test. Word retrieval was measured using the Boston Naming Test (BNT). The Ruff Figural Fluency Test (RFFT) evaluated non-verbal mental flexibility, initiation, planning, and divergent reasoning. Finally, each patient completed the Wechsler Adult Intelligence Scale – 4th Ed (WAIS-IV) prorated full-scale intelligence index. Raw scores for all neuropsychological tests except for WAIS-IV IQ scores were used in analyses. We obtained a "difference score" – defined as the post-operative score minus the pre-operative score – such that higher difference scores correlate to relatively higher function post-operatively, and conversely lower scores representing a drop in these objective measures of cognition.

Statistical Analysis

A two-sample t-test was used to compare independent groups with continuous variables. P-values less than $\alpha = 0.05$ were considered significant. Spearman Rho correlation analysis was used to compare network connectivity to neuropsychometric testing results with a Bonferroni correction for multiple comparisons. Network modeling statistical tests were conducted using IBM SPSS Statistics Version 26 (IBM Corp., Armonk, New York, United States).

Data Availability

The data that support the findings of this study are available from the corresponding author, upon reasonable request.

RESULTS

Demographics

In the cohort of 19 patients with unilateral TLE, five (26%) were male and 14 (74%) were female. All underwent the complete phase 1 evaluation described in the methods, with three (16%) of those patients undergoing subsequent phase II invasive monitoring (stereo-electroencephalography or subdural strips/grids) for further clarification of epileptogenic focus localization. Fifteen (79%) patients were determined to have seizures originating from the left temporal lobe with the remaining four (21%) having seizures in the right temporal lobe. All patients underwent microsurgical resection with either selective amygdalohippocampectomy (n = 13) or temporal lobectomy with amygdalectomy and minimal hippocampal resection (n = 6). Pre-operatively, ten (53%) patients had suspicion of mesial temporal sclerosis on MRI, and none of the patients had any other MRI lesions elsewhere in the brain. After surgery, the same ten (53%) had tissue specimen proven hippocampus sclerosis. All patients were followed for at least 1 year after surgery, and with an average time to follow-up of 24 months. Demographic information is also shown in **Table 1**. All 19 patients had the negatively correlated epilepsy network mapped, and the surgery planning team was blinded to the results of the network result. In addition, the seed size was determined for each patient and found to be not significantly different between the seizure free and the not seizure free group (810 vs. 858 voxels, p = 0.7461). The seed size for each patient is included in **Supplementary Figure 1**.

Highly Intraconnected Negatively Correlated Epilepsy Networks Are Less Widespread

The relationship between the positively correlated network and outcomes after surgery has been assessed in previous papers, and this analysis was performed to determine if these two networks are independent from each other to prove that the negatively correlated epilepsy network is a unique prognostic tool. Across all patients, the degree of connectivity within each of these networks was not significantly correlated ($R = -0.255$, $p = 0.293$), suggesting that connectivity within the negatively correlated epilepsy networks and within the positively correlated epilepsy networks are independent variables. Next, the connectivity between the voxels of the negatively correlated network (the "intraconnectivity" of the network) was compared to the average connectivity between the individual voxels to the epileptogenic zone (negative correlation to the seed volume) and found to be not significantly related ($R = 0.130$, $p = 0.841$). This suggested that the intraconnectivity metric is independent from the negative correlation observed between the voxels of the network and the epileptogenic zone.

The intraconnectivity of the negatively correlated epilepsy network was significantly correlated to the spread of the network, such that the more highly intraconnected the network, the less it was spread out across the brain ($R = -0.6905$, $p = 0.0011$). A scatter plot of the network spread and intraconnectivity is shown in **Figure 2A**.

Correlation With Improved Baseline Memory Function and Decline in Post-operative Naming Function

We found that both immediate and delayed visual memory function were higher in patients with a more intraconnected negatively correlated network (VRI R = 0.561, p = 0.012; VRII $R = 0.549$, $p = 0.015$). No other significant correlations were found pre-operatively.

Neuropsychological function was also measured post-operatively for comparison to the pre-operative level. We observed a negative correlation between the difference score for naming and the pre-operative connectivity within the negatively correlated epilepsy network, suggesting that patients with more intraconnected negatively correlated epilepsy networks are more likely to experience a larger decrease in their naming function (BNT $R = -0.590$, $p = 0.045$). It should be noted that the pre-operative performance on the same test was not significantly correlated with negatively correlated epilepsy network connectivity ($R = 0.356$, $p = 0.134$), suggesting that the correlation of the difference in score was not likely related to a baseline deficit in the patients with less intraconnected networks.

Negatively Correlated Epilepsy Network Connectivity and Seizure Freedom

Seizure outcome was monitored at all stages of follow up after surgery, but the Engel classification used in the present study was determined at the most recent follow up for each patient. As of the most recent follow-up (range: 14–36 months), seven patients (37%) were not seizure free (Engel Class II, III, IV), and 12 patients (63%) were seizure free (Engel Class I). The connectivity within the pre-operative positively correlated epilepsy network was not significantly different between patients that were seizure free and those that were not (p = 1.00). However, the pre-operative connectivity within the negatively correlated network was significantly higher in patients who went on to be seizure free (p = 0.0095) (**Figure 2B**). Also, spread of the network (median distance) was significantly lower in patients who were seizure free compared to those who were not ($p = 0.0083$) (**Figure 2C**).

The control network maps consisting of the negatively correlated networks generated from a random ROI were analyzed in the same way and the results are shown in **Supplementary Figure 2**. In this control network comparison, the spread of the network was not correlated with within-network intraconnectivity (R = 0.2338, p = 0.3354). The spread of the randomly generated negative network was not significantly higher in the patients who were not seizure free ($p = 0.1570$), and the intraconnectivity was also not significantly different between the two groups ($p = 0.2901$) (**Supplementary Figure 2**).

The predictive value of the negatively correlated epilepsy network was also investigated. A receiver operating characteristics (ROC) curve was created. The area under the curve was determined to be 0.845 with the 95% confidence interval ranging from 0.670 to 1.00. The connectivity threshold

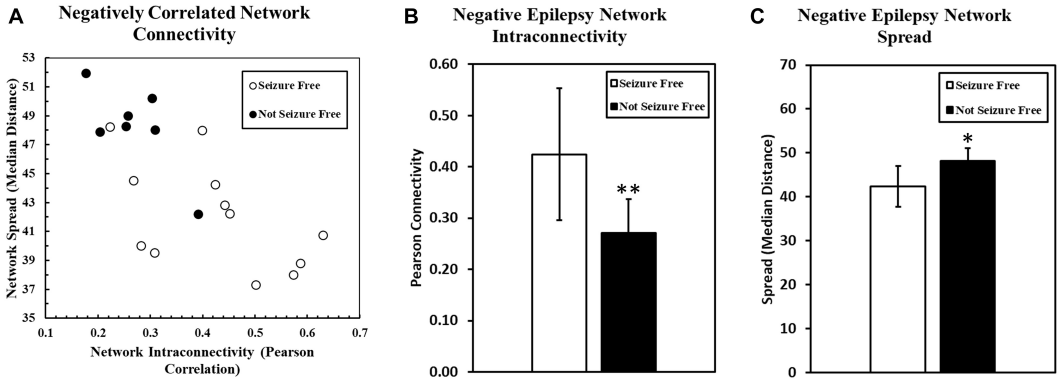

FIGURE 2 | (A) The relationship between the spread of the negatively correlated epilepsy network and the intraconnectivity of that network is shown. Intraconnectivity of the network was calculated by determining the average correlation value between each network voxel and all of the other voxels in the network. These data suggest that the intraconnectivity of the negatively correlated epilepsy network is inversely related to the spread of that network. Patients who are seizure free after surgery are more likely to have a highly connected and less spread out network. Two bar charts are shown here, with one **(B)** comparing the connectivity of the negatively correlated epilepsy network between patients who were seizure free after surgery and those who were not. The same groups are compared in the second bar chart **(C)** comparing the geographical spread of the network, with higher numbers representing a more diffuse, spread out network. (*$p < 0.05$, **$p < 0.01$).

that maximized specificity and sensitivity was (0.2728) (sensitivity 75%, specificity 71%). A threshold of 0.2136 maximized sensitivity (specificity 57%, sensitivity 92%) and a threshold of 0.3955 maximized specificity (specificity 100%, sensitivity 67%). The ROC curve is shown in **Figure 3**.

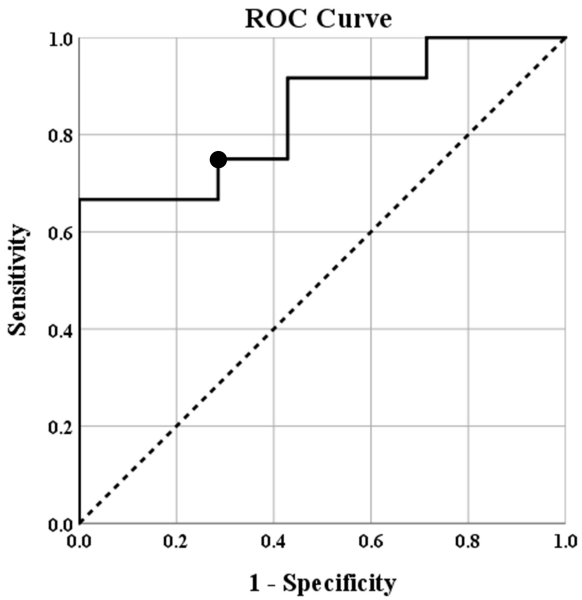

FIGURE 3 | Receiver operating characteristics (ROC) curve showing the predicted specificity and sensitivity of various thresholds of intraconnectivity of the negatively correlated epilepsy network. The diagonal line represents y = x reference line, the second line shows the sensitivity and specificity of predicting seizure freedom at incremental thresholds, and the circle marker represents the threshold (0.2728) that maximized sensitivity (75%) and specificity (71%) of this threshold to predict seizure freedom after surgery. The area under the curve was determined to be 0.845 with the 95% confidence interval ranging from 0.670 to 1.00.

DISCUSSION

Is Negatively Correlated Epilepsy Network Connectivity a Good Sign?

In this paper, we defined and analyzed the "negatively correlated epilepsy network" – a novel network that is negatively correlated with the epileptogenic zone in 19 patients with temporal lobe epilepsy who underwent open microsurgery. Pre-operatively, we found that patients with highly intraconnected negatively correlated epilepsy networks were more likely to have higher baseline verbal and logical memory. Furthermore, the same network was more highly intraconnected in patients that would go on to be seizure free after epilepsy surgery. High intraconnectivity and less spread in the negative network was interpreted as a network that is more organized, because it is more focal in its location in the brain, and all brain regions involved in the network work together in synchrony. Put simply, a more organized and homogeneous negatively network appears to be a good prognostic factor in patients with temporal lobe epilepsy undergoing surgery. Importantly, when these results were compared to the same relationship in networks generated from a random ROI, it was shown that there was no significant relationship between intraconnectivity, spread, and seizure freedom after surgery. This indicates that the negatively correlated epilepsy network generated from a seed volume consisting of the hypothesized epileptogenic zone is unique and appears to be uniquely correlated with a clinically significant outcome after surgery. It was shown that this simple, non-invasive test may be useful as a prognostic test to predict seizure freedom.

The network consists of a group of brain regions that are unique in that they have a negatively correlated rsfMRI

signature compared to the time series of the epileptogenic zone as determined based on the irritative zone identified on the pre-operative scalp EEG. We have previously described a positively correlated "epilepsy network," defined as the network of regions with activation patterns that have a high degree of positive correlation with the epileptogenic zone in patients with temporal lobe epilepsy, and we hypothesized that the negatively correlated regions might be similarly important in understanding the brain function of the patient with temporal lobe epilepsy. In our previous study, whereas the spread of the positively correlated network was associated with worse baseline function, baseline connectivity within the network was not predictive of which patients would benefit from surgery. The degree of disconnection in that network after surgery was, however, associated with more seizure free outcomes. In contrast, the data presented in the current study suggest that baseline connectivity within the negatively correlated epilepsy network help to select for patients who are most likely benefit from temporal lobe surgery.

A negative correlation, represented by a negative Pearson correlation value, has been associated with brain regions that act antagonistically (Uddin et al., 2009). Therefore, it is possible that the negatively correlated epilepsy network that is more intraconnected may antagonize the function of the epileptogenic zone in a way that benefits the patient both pre- and post-operatively. Perhaps the negatively correlated network acts opposed to the epileptogenic zone during inter-ictal periods and controls the negative effect that the aberrant activity in the epileptogenic zone have on normal cognition. This may explain why our cohort of patients with TLE had improved performance on neuropsychological evaluations (specifically in memory and executive function) that scaled directly with the degree of connectivity within the negatively correlated network.

Studies involving simultaneous acquisition of EEG and fMRI data have been conducted previously by several groups and involve an analysis of negatively contrasted images that is somewhat similar to the present study but with important differences. These studies demonstrated that such an analysis can be used to correlate hemodynamic changes in the brain with the epileptogenic zone, and have shown that resection of the epileptogenic zone, when closely associated with brain regions exhibiting changes in BOLD activation, is positively correlated with post-operative seizure control (Thornton et al., 2010; van Houdt et al., 2013; Coan et al., 2016). While similar to our approach, it is a crucial difference to note that in these studies EEG and rsfMRI data were acquired simultaneously, such that connectivity measurements were analyzed at the same time that epileptic discharges were detected. As such, these studies generate an ictal pattern of functional connectivity which can then be correlated to the electrophysiological data in a time-locked fashion. However, when data is acquired in this fashion, the discharges likely cause a momentary change in the connectivity patterns which is helpful for detecting the locally connected epileptic network. In the current study, we elected instead to measure EEG and rsfMRI non-concurrently. As such, our connectivity data reflects functional connectivity patterns existing in the interictal state, might well be different than those observed during a seizure or epileptic discharge, and could reflect network connectivity that is related to background normal function of the brain that is known to be impaired in patients with temporal lobe epilepsy. Alternatively, the results could represent a different set of network relationships influential in background memory and executive processing.

Is There Is Any Value in Epilepsy Surgery Planning?

Since higher connectivity within the negatively correlated epilepsy network was associated with a higher likelihood of seizure freedom post-operatively, the prognostic value of this single metric was also investigated. Within our cohort, an average connectivity within the negatively correlated epilepsy network of 0.2728 predicts seizure freedom with a specificity of 71% and a sensitivity of 79%. Clinically, this tool is non-invasive and easy to use. The negatively correlated network is created automatically with standard EEG and MRI technology that is available during a normal phase I epilepsy surgery evaluation, and so can be readily integrated into the standard pre-operative workflow of any comprehensive epilepsy center.

Future Studies

This is still preliminary data and any hypotheses about the exact mechanism of this negatively correlated epilepsy network still need to be confirmed in future studies by applying the thresholds calculated with the ROC analysis in an out-of-sample test group to see if the prediction holds. Also, there has been much work on multivariate predictive models in epilepsy surgery (Spencer et al., 2005; Jehi et al., 2015). In the future this unique connectivity metric may be able to add to the predictive value of these models. We will continue to collect data and build a larger database in the hopes of finding more subtle changes between our subgroups. We also plan to start including additional data such as semiology and PET scan to better define network characteristics. Magnetoencephalography and SEEG combined studies have also shown that a multimodal approach using those methods can help to further refine the localization of the epileptogenic zone, and we will explore the possibility of adding this type of data into future studies (Badier et al., 2017; Pizzo et al., 2019). These network imaging results will be discussed in the multi-disciplinary evaluation for epilepsy surgery in an effort to generate prospective, out-of-sample data to substantiate the conclusions of this study. The goal of this type of research would be to strengthen the argument that network analysis can be a valuable tool in predicting which patients will benefit from resective surgeries.

Limitations

While not detracting from the results presented here, some limitations to the applicability of this data should be considered. First, this is a prospective but small cohort and therefore represents preliminary data. Future studies will aim to address this limitation, as described above. Furthermore, the rsfMRI image sets collected in this

study are from a single session and may therefore have lower signal-to-noise ratios than comparable data taken across multiple sessions or for longer acquisition times. It is well known that surface EEG is limited in its precision and accuracy in estimating an epileptogenic zone, and the aim of this study was to determine if the utility of scalp EEG in defining an EZ and predicting post-operative surgical outcomes can be enhanced with the addition of different measures of functional connectivity. The attempt is not to localize the EZ with 100% accuracy, but to determine if clinically useful properties can be extracted from functional connectivity data acquired non-invasively. Finally, when undergoing rsfMRI imaging, we did not control for the presence of anti-epileptic drugs. It is possible that these drugs may inhibit certain neuronal processes and affect rsfMRI signal patterns, and it is unknown how these drugs would affect our results.

CONCLUSION

In this study, preliminary data was shown, and patterns of connectivity were explored within a newly defined "negatively correlated epilepsy network" in patients with refractory temporal lobe epilepsy undergoing surgery. In the network, defined as those areas of the brain that had a below-threshold negative Pearson correlation with the hypothesized epileptogenic zone estimated from surface EEG, intraconnectivity was directly related to pre-operative performance on objective neuropsychological evaluation of verbal and logical memory. Also, pre-operative negatively correlated epilepsy network connectivity was directly related to the likelihood of being seizure-free after surgery. These findings together suggest a benefit to the patient both pre- and post-operatively if they had a highly connected negatively correlated epilepsy network, which can be determined using commonly available, non-invasive methods (EEG and rsfMRI). Even though this study is limited in size, the preliminary, proof of concept findings suggest a novel methodology of detecting negatively correlated brain regions may be useful in deciding which patients would most likely benefit from surgery. These data represent a step toward proving the efficacy of non-invasive network mapping and should stimulate future exploration into the utility and value of such an algorithm in predicting outcomes after surgery.

DATA AVAILABILITY STATEMENT

The raw data supporting the conclusions of this article will be made available by the authors, without undue reservation.

ETHICS STATEMENT

The studies involving human participants were reviewed and approved by the University of South Florida Institutional Review Board. The patients/participants provided their written informed consent to participate in this study.

AUTHOR CONTRIBUTIONS

All authors listed have made a substantial, direct and intellectual contribution to the work, and approved it for publication.

ACKNOWLEDGMENTS

The authors thank students Long Di, Austin Finch, You Jeong Park, and Ferdinand Korneli for their assistance with data collection and pre-processing.

SUPPLEMENTARY MATERIAL

The Supplementary Material for this article can be found online at: https://www.frontiersin.org/articles/10.3389/fnins.2020.629667/full#supplementary-material

Supplementary Figure 1 | All hypothesized epileptogenic seed volumes are shown in red for each patient and the seed volume size is also given. The green volumes represent the negatively correlated epilepsy network for each patient. **(A)** Hypothesized epileptogenic zones and negatively correlated epilepsy networks for all patients who were not seizure free. **(B)** Seed volumes and negatively correlated epilepsy network are shown for all patients that were seizure free.

Supplementary Figure 2 | A randomly generated ROI was used to create a negatively correlated network using the same algorithm as described in the "Materials and Methods" section. **(A)** No significant relationship between network spread and intraconnectivity is seen when the negatively correlated epilepsy network maps are analyzed. **(B)** No significant difference in network intraconnectivity or **(C)** spread was found between patients that were seizure free after surgery and those who were not.

REFERENCES

Badier, J. M., Dubarry, A. S., Gavaret, M., Chen, S., Trebuchon, A. S., Marquis, P., et al. (2017). Technical solutions for simultaneous MEG and SEEG recordings: towards routine clinical use. *Physiol. Meas.* 38, N118–N127. doi: 10.1088/1361-6579/aa7655

Bartolomei, F., Wendling, F., and Chauvel, P. (2008). [The concept of an epileptogenic network in human partial epilepsies]. *Neurochirurgie* 54, 174–184. doi: 10.1016/j.neuchi.2008.02.013

Bell, M. L., Rao, S., So, E. L., Trenerry, M., Kazemi, N., Stead, S. M., et al. (2009). Epilepsy surgery outcomes in temporal lobe epilepsy with a normal MRI. *Epilepsia* 50, 2053–2060. doi: 10.1111/j.1528-1167.2009.02079.x

Bernhardt, B. C., Hong, S., Bernasconi, A., and Bernasconi, N. (2013). Imaging structural and functional brain networks in temporal lobe epilepsy. *Front. Hum. Neurosci.* 7:624. doi: 10.3389/fnhum.2013.00624

Blumenfeld, H., McNally, K. A., Vanderhill, S. D., Paige, A. L., Chung, R., Davis, K., et al. (2004). Positive and negative network correlations in temporal lobe epilepsy. *Cereb. Cortex* 14, 892–902. doi: 10.1093/cercor/bhh048

Chauvel, P., Gonzalez-Martinez, J., and Bulacio, J. (2019). Presurgical intracranial investigations in epilepsy surgery. *Handb. Clin. Neurol.* 161, 45–71. doi: 10.1016/B978-0-444-64142-7.00040-0

Coan, A. C., Chaudhary, U. J., Grouiller, F., Campos, B. M., Perani, S., De Ciantis, A., et al. (2016). EEG-fMRI in the presurgical evaluation of temporal lobe epilepsy. *J. Neurol. Neurosurg. Psychiatry* 87, 642–649. doi: 10.1136/jnnp-2015-310401

Engel, J. Jr., McDermott, M. P., Wiebe, S., Langfitt, J. T., Stern, J. M., Dewar, S., et al. (2012). Early surgical therapy for drug-resistant temporal lobe epilepsy: a randomized trial. *JAMA* 307, 922–930. doi: 10.1001/jama.2012.220

Gonzalez, H. F. J., Chakravorti, S., Goodale, S. E., Gupta, K., Claassen, D. O., Dawant, B., et al. (2019). Thalamic arousal network disturbances in temporal lobe epilepsy and improvement after surgery. *J. Neurol. Neurosurg. Psychiatry* 90, 1109–1116. doi: 10.1136/jnnp-2019-320748

Jehi, L., Yardi, R., Chagin, K., Tassi, L., Russo, G. L., Worrell, G., et al. (2015). Development and validation of nomograms to provide individualised predictions of seizure outcomes after epilepsy surgery: a retrospective analysis. *Lancet Neurol.* 14, 283–290. doi: 10.1016/S1474-4422(14)70325-4

Kwan, P., and Brodie, M. J. (2000). Early identification of refractory epilepsy. *N. Engl. J. Med.* 342, 314–319. doi: 10.1056/NEJM200002033420503

Li, Q., Cao, W., Liao, X., Chen, Z., Yang, T., Gong, Q., et al. (2015). Altered resting state functional network connectivity in children absence epilepsy. *J. Neurol. Sci.* 354, 79–85. doi: 10.1016/j.jns.2015.04.054

Luo, C., Yang, F., Deng, J., Zhang, Y., Hou, C., Huang, Y., et al. (2016). Altered functional and effective connectivity in anticorrelated intrinsic networks in children with benign childhood epilepsy with centrotemporal spikes. *Medicine* 95:e3831. doi: 10.1097/MD.0000000000003831

McGill, M. L., Devinsky, O., Kelly, C., Milham, M., Castellanos, F. X., Quinn, B. T., et al. (2012). Default mode network abnormalities in idiopathic generalized epilepsy. *Epilepsy Behav.* 23, 353–359. doi: 10.1016/j.yebeh.2012.01.013

Morgan, V. L., Gore, J. C., and Abou-Khalil, B. (2010). Functional epileptic network in left mesial temporal lobe epilepsy detected using resting fMRI. *Epilepsy Res.* 88, 168–178. doi: 10.1016/j.eplepsyres.2009.10.018

Morgan, V. L., Rogers, B. P., Gonzalez, H. F. J., Goodale, S. E., and Englot, D. J. (2019). Characterization of postsurgical functional connectivity changes in temporal lobe epilepsy. *J. Neurosurg.* 14, 1–11. doi: 10.3171/2019.3.JNS19350

Neal, E. G., Di, L., Reale-Caldwell, A., Maciver, S., Schoenberg, M. R., and Vale, F. L. (2019). Network connectivity separate from the hypothesized irritative zone correlates with impaired cognition and higher rates of seizure recurrence. *Epilepsy Behav.* 101:106585. doi: 10.1016/j.yebeh.2019.106585

Neal, E. G., Maciver, S., Schoenberg, M. R., and Vale, F. L. (2020). Surgical disconnection of epilepsy network correlates with improved outcomes. *Seizure* 76, 56–63. doi: 10.1016/j.seizure.2020.01.018

Neal, E. G., Maciver, S., and Vale, F. L. (2018). Multimodal, noninvasive seizure network mapping software: A novel tool for preoperative epilepsy evaluation. *Epilepsy Behav.* 81, 25–32. doi: 10.1016/j.yebeh.2018.01.033

Pizzo, F., Roehri, N., Medina Villalon, S., Trebuchon, A., Chen, S., Lagarde, S., et al. (2019). Deep brain activities can be detected with magnetoencephalography. *Nat. Commun.* 10:971. doi: 10.1038/s41467-019-08665-5

Sander, J. W. (2003). The epidemiology of epilepsy revisited. *Curr. Opin. Neurol.* 16, 165–170. doi: 10.1097/01.wco.0000063766.15877.8e

Schramm, J. (2008). Temporal lobe epilepsy surgery and the quest for optimal extent of resection: a review. *Epilepsia* 49, 1296–1307. doi: 10.1111/j.1528-1167.2008.01604.x

Shen, X., Tokoglu, F., Papademetris, X., and Constable, R. T. (2013). Groupwise whole-brain parcellation from resting-state fMRI data for network node identification. *Neuroimage* 82, 403–415. doi: 10.1016/j.neuroimage.2013.05.081

Spencer, S. S., Berg, A. T., Vickrey, B. G., Sperling, M. R., Bazil, C. W., and Shinnar, S. (2005). Predicting long-term seizure outcome after resective epilepsy surgery: the multicenter study. *Neurology* 65, 912–918. doi: 10.1212/01.wnl.0000176055.45774.71

Thornton, R., Laufs, H., Rodionov, R., Cannadathu, S., Carmichael, D. W., Vulliemoz, S., et al. (2010). EEG correlated functional MRI and postoperative outcome in focal epilepsy. *J. Neurol. Neurosurg. Psychiatry* 81, 922–927. doi: 10.1136/jnnp.2009.196253

Uddin, L. Q., Kelly, A. M., Biswal, B. B., Castellanos, F. X., and Milham, M. P. (2009). Functional connectivity of default mode network components: correlation, anticorrelation, and causality. *Hum. Brain Mapp.* 30, 625–637. doi: 10.1002/hbm.20531

Vale, F. L., Effio, E., Arredondo, N., Bozorg, A., Wong, K., Martinez, C., et al. (2012). Efficacy of temporal lobe surgery for epilepsy in patients with negative MRI for mesial temporal lobe sclerosis. *J. Clin. Neurosci.* 19, 101–106. doi: 10.1016/j.jocn.2011.08.009

van den Heuvel, M., Mandl, R., and Hulshoff Pol, H. (2008). Normalized cut group clustering of resting-state FMRI data. *PLoS One* 3:e2001. doi: 10.1371/journal.pone.0002001

van Houdt, P. J., de Munck, J. C., Leijten, F. S. S., Huiskamp, G. J. M., Colon, A. J., Boon, P., et al. (2013). EEG-fMRI correlation patterns in the presurgical evaluation of focal epilepsy: a comparison with electrocorticographic data and surgical outcome measures. *Neuroimage* 75, 238–248. doi: 10.1016/j.neuroimage.2013.02.033

Wiebe, S., Blume, W. T., Girvin, J. P., and Eliasziw, M. (2001). A randomized, controlled trial of surgery for temporal-lobe epilepsy. *N. Engl. J. Med.* 345, 311–318. doi: 10.1056/NEJM200108023450501

Zhang, Z., Lu, G., Zhong, Y., Tan, Q., Liao, W., Wang, Z., et al. (2010). Altered spontaneous neuronal activity of the default-mode network in mesial temporal lobe epilepsy. *Brain Res.* 1323, 152–160. doi: 10.1016/j.brainres.2010.01.042

Conflict of Interest: EN and FV are inventors and hold a US patent (#10,588,561) for the network modeling algorithm used in this study.

The remaining authors declare that the research was conducted in the absence of any commercial or financial relationships that could be construed as a potential conflict of interest.

frontiers in Neuroscience

ORIGINAL RESEARCH
published: 22 February 2021
doi: 10.3389/fnins.2021.625309

Assessing Uncertainty and Reliability of Connective Field Estimations From Resting State fMRI Activity at 3T

Azzurra Invernizzi[1,2†], Nicolas Gravel[1,2,3†], Koen V. Haak[4], Remco J. Renken[2] and Frans W. Cornelissen[1,2]*

[1] Laboratory for Experimental Ophthalmology, University of Groningen, University Medical Center Groningen, Groningen, Netherlands, [2] Cognitive Neuroscience Center, Department of Biomedical Sciences of Cells and Systems, University Medical Center Groningen, Groningen, Netherlands, [3] Neural Dynamics of Visual Cognition Group, Department of Education and Psychology, Freie Universität Berlin, Berlin, Germany, [4] Donders Institute for Brain, Cognition and Behaviour, Radboud University Medical Center, Nijmegen, Netherlands

OPEN ACCESS

Edited by:
Xiaopeng Song, Harvard Medical School, United States

Reviewed by:
Ali Golestani, University of Toronto, Canada
Olga V. Martynova, Institute of Higher Nervous Activity and Neurophysiology (RAS), Russia
Zhaoyue Shi, Houston Methodist Research Institute, United States

***Correspondence:**
Azzurra Invernizzi
a.invernizzi@umcg.nl

† These authors have contributed equally to this work

Specialty section:
This article was submitted to Brain Imaging Methods, a section of the journal Frontiers in Neuroscience

Received: *02 November 2020*
Accepted: *19 January 2021*
Published: *22 February 2021*

Citation:
Invernizzi A, Gravel N, Haak KV, Renken RJ and Cornelissen FW (2021) Assessing Uncertainty and Reliability of Connective Field Estimations From Resting State fMRI Activity at 3T. Front. Neurosci. 15:625309. doi: 10.3389/fnins.2021.625309

Connective Field (CF) modeling estimates the local spatial integration between signals in distinct cortical visual field areas. As we have shown previously using 7T data, CF can reveal the visuotopic organization of visual cortical areas even when applied to BOLD activity recorded in the absence of external stimulation. This indicates that CF modeling can be used to evaluate cortical processing in participants in which the visual input may be compromised. Furthermore, by using Bayesian CF modeling it is possible to estimate the co-variability of the parameter estimates and therefore, apply CF modeling to single cases. However, no previous studies evaluated the (Bayesian) CF model using 3T resting-state fMRI data. This is important since 3T scanners are much more abundant and more often used in clinical research compared to 7T scanners. Therefore in this study, we investigate whether it is possible to obtain meaningful CF estimates from 3T resting state (RS) fMRI data. To do so, we applied the standard and Bayesian CF modeling approaches on two RS scans, which were separated by the acquisition of visual field mapping data in 12 healthy participants. Our results show good agreement between RS- and visual field (VF)- based maps using either the standard or Bayesian CF approach. In addition to quantify the uncertainty associated with each estimate in both RS and VF data, we applied our Bayesian CF framework to provide the underlying marginal distribution of the CF parameters. Finally, we show how an additional CF parameter, *beta*, can be used as a data-driven threshold on the RS data to further improve CF estimates. We conclude that Bayesian CF modeling can characterize local functional connectivity between visual cortical areas from RS data at 3T. Moreover, observations obtained using 3T scanners were qualitatively similar to those reported for 7T. In particular, we expect the ability to assess parameter uncertainty in individual participants will be important for future clinical studies.

Keywords: resting-state fMRI, uncertainty, connective field modeling, bayesian modeling, visual field mapping, visual cortex

HIGHLIGHTS

- Local functional connectivity between visual cortical areas can be estimated from RS-fMRI data at 3T using both standard CF and Bayesian CF modeling.
- 3T observations were qualitatively similar to those previously reported at 7T.
- Bayesian CF modeling quantifies the model uncertainty associated with each CF parameter on RS and VF data, important in particular for future studies on clinical populations.

INTRODUCTION

Spontaneous blood-oxygen level dependent (BOLD) fluctuations have been used to study the intrinsic functional connectivity of the human brain. Biswal et al. (1995) observed, for the first time, the presence of bilateral spatial integration, coherent activity and functional connectivity between distant homotopic brain areas, even in the absence of a task. Ever since, resting-state fMRI (RS-fMRI or RS) has played a key role in understanding the temporal and spatial interactions of interconnected brain regions. In parallel, various fMRI data-analysis tools have been developed with the aim to describe the functional and neuroanatomical organization of the brain. One of these methods is connective field (CF) modeling (Haak et al., 2013b). CF, also known as the cortico-cortical population receptive field (cc-pRF), modeling allows to describe the response of a population of neurons in the cortex in terms of the activity in another region of the cortex. It translates the concept of the receptive field into the domain of connectivity by assessing the spatial dependency between signals in distinct cortical visual field regions (Haak et al., 2013b). Even though the approach is agnostic to different stimulus configurations, it has thus far been primarily developed and applied in vision research. A previous study by Gravel et al. (2014) showed that CFs, estimated from RS-fMRI data recorded at a high magnetic field (7T), reflect the visuotopic organization of early visual cortical maps. This indicates that even in the absence of any visual stimulation, CF modeling is able to describe the activity of voxels in a target region (e.g., V2 or V3) as a function of the aggregate activity in a source cortical visual area (e.g., V1).

While these previous results were obtained at 7T and in healthy participants, 3T scanners are much more common, and generally preferred for whole-brain analyses in patient studies (van der Kolk et al., 2013; Polimeni and Uludağ, 2018). Therefore, if RS data recorded at 3T can provide sufficient sensitivity to estimate the spatial integration and connectivity of BOLD signals in distinct regions of the early visual cortex (Gravel et al., 2020), this would open up the CF modeling approach to clinical studies performed at 3T and in individual cases. Amongst others, this would provide the important advantage that plasticity of visual cortical areas could be studied without a dependence on actual visual stimulation. This is important, as in ophthalmic and neurological patients visual input can already be disrupted, potentially resulting in spurious plasticity estimates (Baseler et al., 1999; Azzopardi and Cowey, 2001; Haak et al., 2013b; Carvalho et al., 2020).

In order to assess the suitability of the CF approach for studying unique patient cases at 3T, we will look beyond the classical variance explained as an indicator of modeling performance. To do so, we will assess the uncertainty of model parameter estimates using a Bayesian approach. These parameters are available to us by applying our recently developed Bayesian framework for the CF model (Bayesian CF, Invernizzi et al., 2020). In particular, this approach allows to estimate the variability for each CF parameter estimate such as CF size and beta. Moreover, when using our new Bayesian CF framework, we can obtain a data-driven threshold in order to select relevant voxels for both RS-fMRI and visual field mapping (VFM) data.

We applied both the standard CF estimation and the novel Bayesian approach to RS and VFM data acquired at 3T. Subsequently, we compared the CF maps and parameters obtained using the two CF approaches. Additionally, we assessed test-retest reliability between the two runs of RS data.

Finally, we will qualitatively compare our results to those obtained previously in Gravel et al. (2014).

To preview our results, we found a good agreement between RS- and visual field (VF) – based maps obtained with both the standard and Bayesian CF approach at 3T. Moreover, most observations were qualitatively similar to those previously observed for 7T data. This implies that local functional connectivity between visual cortical areas during RS can be estimated at 3T. No significant differences were found between the two runs of RS data on V1 > V2 areas. Furthermore, we showed how the parameter uncertainty can be used to assess the variability of parameters in RS-fMRI BOLD fluctuations. Therefore, the Bayesian CF approach presented here extends on previous approaches to provide an interpretable and independent measure of uncertainty in RS-based data. Finally, we show that the novel retained CF parameter, *beta*, can serve as a sensitive threshold for the selection of voxels and improve the reliability of estimates. Taken together, our results demonstrate the utility of applying a Bayesian CF approach to study inter areal cortical integration in the human visual cortex in health and disease.

MATERIALS AND METHODS

Participants

Twelve healthy female participants (mean age 22 years, s.d. = 1.8 years) with normal or corrected-to-normal vision and without a history of neurological disease were included. These data had been collected and used in previous projects (Halbertsma et al., 2019; Invernizzi et al., 2020). For each of the previous studies, the ethics board of the University Medical Center Groningen (UMCG) approved the study protocol. All participants provided written informed consent. The study followed the tenets of the Declaration of Helsinki.

Stimuli Presentation and Description

The visual stimuli were displayed on a MR compatible screen located at the head-end of the MRI scanner with a viewing

distance of 118 cm. The participant viewed the complete screen through a mirror placed at 11 cm from the eyes supported by the 32-channel SENSE head coil. Screen size was 36 × 23° of visual angle and the distance from the participant's eyes to the screen was approximately 75 cm. Stimuli were generated and displayed using the Psychtoolbox[1] and VISTADISP toolbox (VISTA Lab, Stanford University), both Matlab based (Brainard, 1997; Pelli, 1997). The stimulus consisted of drifting bar apertures (of 10.2° radius) with a high contrast checkerboard texture on a gray (mean luminance) background. A sequence of eight different bar apertures with four different bar orientations (horizontal, vertical, and diagonal orientations), two opposite motion directions and four periods of mean-luminance presentations completed the stimulus presentation that lasted 192 s. To maintain stable fixation, participants were instructed to focus on a small colored dot present in the center of the screen and press a button as soon as the dot changed color. The complete visual field mapping paradigm was presented to the participant six times, during six separate scans.

Resting State

During the RS-fMRI scans, the stimuli were replaced by a black monitor and the lights in the scanning room were turned off. All participants were instructed to keep their eyes closed, remain as still as possible, not to fall asleep, and try not to think of anything in particular.

Data Acquisition

Magnetic resonance imaging (MRI) and fMRI data were obtained using a 3T Philips Intera MRI scanner (Philips, Netherlands), with a 32-channel head coil. For each subject, a high-resolution T1-weighted three-dimensional structural scan was acquired (TR = 9.00ms, TE = 3.5 ms, flip-angle = 8, acquisition matrix = 251 mm × 251 mm × 170 mm, field of view = 256 × 170 × 232, voxel size = 1 mm × 1 mm × 1 mm). Then, six retinotopy (VFM) functional T2*-weighted, 2D echo planar images were obtained (TR = 1500 ms, field of view = 224 mm × 72 mm × 193.5 mm, voxel resolution of 2.33 mm × 2.33 mm × 3 mm). Finally two, full brain, resting-state (RS) functional T2*-weighted, 2D echo planar images were obtained using the following parameters: TR = 2000 ms, field of view = 220 mm × 121 mm × 220 mm, voxel size = 3.44 mm × 3.44 mm × 3.29 mm. The functional scans were acquired in the following order: (1) a RS-fMRI scan (RS1) lasted 708 s with a total of 350 volumes; (2) six VFM functional scans were collected, where each scan lasted for 204 s with a total of 136 volumes; (3) finally, a second RS-fMRI scan (RS2) with the same characteristic of RS1 (duration of 708 s with 350 volumes) was collected. MRI protocol differences between VFM and RS scans are due to the fact that RS was collected at whole-brain while VFM scans were geared to the visual areas in the occipital brain areas.

Prior to the first VFM scan, a short T1-weighted anatomical scan with the same field of view chosen for the functional scans were acquired and used for obtaining a better co-registration between functional and anatomical volume.

Data Analysis

Preprocessing and standard CF analysis of fMRI data were done using ITKGray[2], FreeSurfer (Fischl, 2012) and mrVista toolbox for Matlab environment (VISTASOFT)[3]. The Bayesian pRF and CF approaches were developed and implemented in Matlab 2016b (The MathWorks Inc., Natick, MA, United States). The code for the Bayesian pRF and CF frameworks will be made available via www.visualneuroscience.nl.

For each participant, the structural scan was aligned in a common space defined using the anterior commissure-posterior commissure line (AC-PC line) as reference. Next, gray and white matter were automatically segmented using FreeSurfer and manually adjusted using ITKGray[4], in order to minimize segmentation errors. Then, all functional data were pre-processed using mrVista toolbox. For both RS and retinotopy data the following steps are applied. First, head motion within and between scans were corrected by using robust multiresolution alignment of MRI brain volumes (Nestares and Heeger, 2000) an alignment of functional data into anatomical space and an interpolation of functional data with segmented anatomical gray and white matter. For RS-fMRI data, a few additional denoised steps were applied. These steps were possible since RS scans were acquired at the whole brain. First, spatial smoothing of 6 mm FWHM was applied in order to perform the denoising step based on ICA-AROMA that identified noise and motion related components (Pruim et al., 2015). These components were then removed from the unsmoothed RS-fMRI data that are now further filtered by applying a band-pass filter with high-pass discrete cosine transform with cut-off frequency of 0.01 Hz and a low-pass 4th order Butterworth filter with cut-off frequency of 0.1 Hz.

Bayesian Population Receptive Field Mapping Applied to VFM

Retinotopy scans were analyzed using a Bayesian population receptive field (pRF) framework. For a detailed account see Prabhakaran et al. (2020), which uses a Markov Chain Monte Carlo (MCMC) approach to sample the parameter space for the pRF mapping. Following the nomenclature of Dumoulin and Wandell (2008), Zeidman et al. (2018), Carvalho et al. (2020), Prabhakaran et al. (2020), we defined 2D symmetrical Gaussian kernel centered at (x_0, y_0) with width defined as the standard deviation σ, to define the pRF model. The best model fit was projected onto a smoothed 3D mesh of the cortex. Based on the obtained parameter-values, visual areas are outlined (V1, V2, V3, hV4, LO1, and LO2) to act as source (V1) or target region (all other) for subsequent RS analysis.

[1]https://github.com/Psychtoolbox-3/Psychtoolbox-3/

[2]http://www.itk.org

[3]http://vistalab.stanford.edu/

[4]http://itk.org

Standard Connective Field Mapping of RS Data

In the standard CF model, the optimal CF parameters (CF position and CF size, which define the 2D symmetric Gaussian kernel) were estimated based on a procedure that fitted the time-series for each location in the target region (e.g., V2 or V3) using a linear combination of the time-series in the source region (e.g., V1; Haak et al., 2013b). The best fitting models are retained and projected on a smoothed 3D mesh. The CF parameters associated with the best fitting model are converted from cortical units (cortical position) into visual field units (eccentricity and polar angle). This is done by inferring the pRF properties – obtained via the Bayesian pRF method Prabhakaran et al., 2020 of the center voxel in the source region for each target location (Haak et al., 2013b).

Bayesian Connective Field Mapping

Similar to the Bayesian pRF, the Bayesian CF framework uses a Markov Chain Monte Carlo (MCMC) approach to sample the source region efficiently. Again we used a 2D symmetric Gaussian kernel to predict the time series of the target regions. As in the standard CF modeling, the eccentricity and polar angle values associated with the CF centers are inferred from a pRF mapping. For the sake of completeness, the entire fitting procedure of the Bayesian CF model (option B) is described in the **Supplementary Material**.

For each participant, standard and Bayesian-CF models were estimated for both VFM and RS data. Target and source regions definitions were based on the Bayesian pRF analysis. For both Bayesian pRF and CF models, a total of 15000 iterations were computed, where the first 10% of iterations were discarded for the burn-in process (Chib, 2011; Liu et al., 2016) and the posterior probability distributions were estimated on the remaining samples.

Spatial Analysis

We used Pearson and circular correlations to compare and assess the topographic organization of eccentricity and polar angle, respectively, in both standard CF and Bayesian CF maps obtained on RS and VFM data. The same type of correlations were used to evaluate similarities in eccentricity and polar angle maps between the two RS-fMRI scans obtained with standard CF and Bayesian CF models. Furthermore, we computed the coefficient of variation (Shoukri et al., 2008) to evaluate the within-subject reproducibility of CF parameter estimates obtained by using the standard CF and Bayesian CF. Correlation values higher than 0.5 and p-values below 0.05 were considered statistically significant. Moreover, to compare the relation between CF size and eccentricity RS-based, we binned the eccentricity at 1° intervals and applied a linear fit over the mean per bin. A confidence interval (CI) of the fit was defined by applying a bootstrap technique 1000 times.

For the spatial analyses, only voxels for which the best-fitting CF model explained more than 15% of the time-series variance in the standard CF and eccentricity which is $<1°$ and $>7°$ were included. This arbitrary threshold level was chosen based on previous literature (Winawer et al., 2010; Baseler et al., 2011; Haak et al., 2012, 2013b).

Finally, the intraclass correlation coefficient (ICC) (McGraw and Wong, 1996; Perinetti, 2018) was computed to estimate the test-retest reliability between the two RS-fMRI scans obtained with standard CF and Bayesian CF models. *A priori* 5% strongest activated voxels based on VE was used as threshold to compute the ICC score. We also report the relation between ICC and five different thresholds (1%, 5%, 10%, 25% and 50%, **Supplementary Figure 4**).

Bayesian Analysis

Based on a quantile analysis of the posterior distribution (Invernizzi et al., 2020), we computed a voxel-wise uncertainty measure for each CF parameter by subtracting the upper (Q_3) and lower (Q_1) quantile of the posterior distribution. The estimated uncertainty was computed for both RS and VFM data for each participant and then projected onto a smoothed 3D mesh of the cortex. We repeated the same procedure for each CF parameter.

Beta Threshold

Following the procedure reported by Invernizzi et al. (2020) we test if *beta* – the scaling amplitude of the predictor to the amplitude of the measured signal – can serve as data-driven threshold for RS-data. As a proxy distribution for the null hypothesis (i.e., no correlation between source and target region), one surrogate BOLD time series was calculated for each voxel (Schreiber and Schmitz, 1996; Räth and Monetti, 2009; Lancaster et al., 2018). A surrogate time series was generated using the iterative amplitude adjusted Fourier transform method (IAAFT, Schreiber and Schmitz, 1996; Räth and Monetti, 2009). Then, the Bayesian CF model was fitted using this surrogate to real time series of the target region which were unchanged. Based on the best fit obtained in the MCMC iterations of the surrogate *beta*-estimate, we calculated a familywise error (FWE) corrected *beta*-threshold for all the voxels in the target region. Based on previous literature, we selected the cut-off value of the 95th percentile (Bornmann, 2013; Invernizzi et al., 2020) of the null distribution as FWE-corrected *beta* threshold. Finally, we compared the voxel selection at the single participant level using VE and the FWE *beta*-threshold approaches.

RESULTS

The CF maps obtained from RS-based data for eccentricity, polar angle and CF size were qualitatively comparable for the standard and Bayesian CF models. In contrast to the VFM data, the relation with CF size and eccentricity in RS data does not increase with visual hierarchy. Again, the same behavior was observed using both methods. No statistically significant difference was found between the two RS scans for any CF parameter. We estimated the uncertainty for the Bayesian CF parameters (CF size and beta). An higher uncertainty from the CF parameters was observed from both RS scans compared to VFM data and between RS2 and RS1 scans. Finally, we showed how to use a new threshold based

on the effect size of the model both in the presence and absence of visual stimuli.

CF Models Based on RS-fMRI Data

We used V1 as source region while V2, V3, hV4, LO1, and LO2 as target to derive CF maps projected on a smoothed 3D mesh on a single subject level (**Figure 1**). Such maps were created using both standard CF and Bayesian CF models (**Figures 1B–E**). Topographical maps for eccentricity, polar angle and CF size were comparable for both CF models using RS data (**Figure 1**). We used the VFM-based maps as reference (**Figure 1A**) as these maps show a clear visuotopic organization for all the CF parameters estimated. Then the same parameters are plotted for all RS scans (**Figures 1B,D**: RS-based derived maps using standard CF model; **Figures 1C**, E: RS-based derived maps using Bayesian CF model). Furthermore, a good level of within-subject reproducibility was observed for each CF parameter estimate for both CF models using RS scans (**Supplementary Table 2**).

In line with the earlier work that introduced the standard CF method (Haak et al., 2013a), we quantified possible differences between the resulting RS-based CF and Bayesian-CF estimates by correlating them against the pRF-derived eccentricity and polar angle parameters that we used as reference (**Table 1**). Eccentricity and polar angle parameters are estimated for each

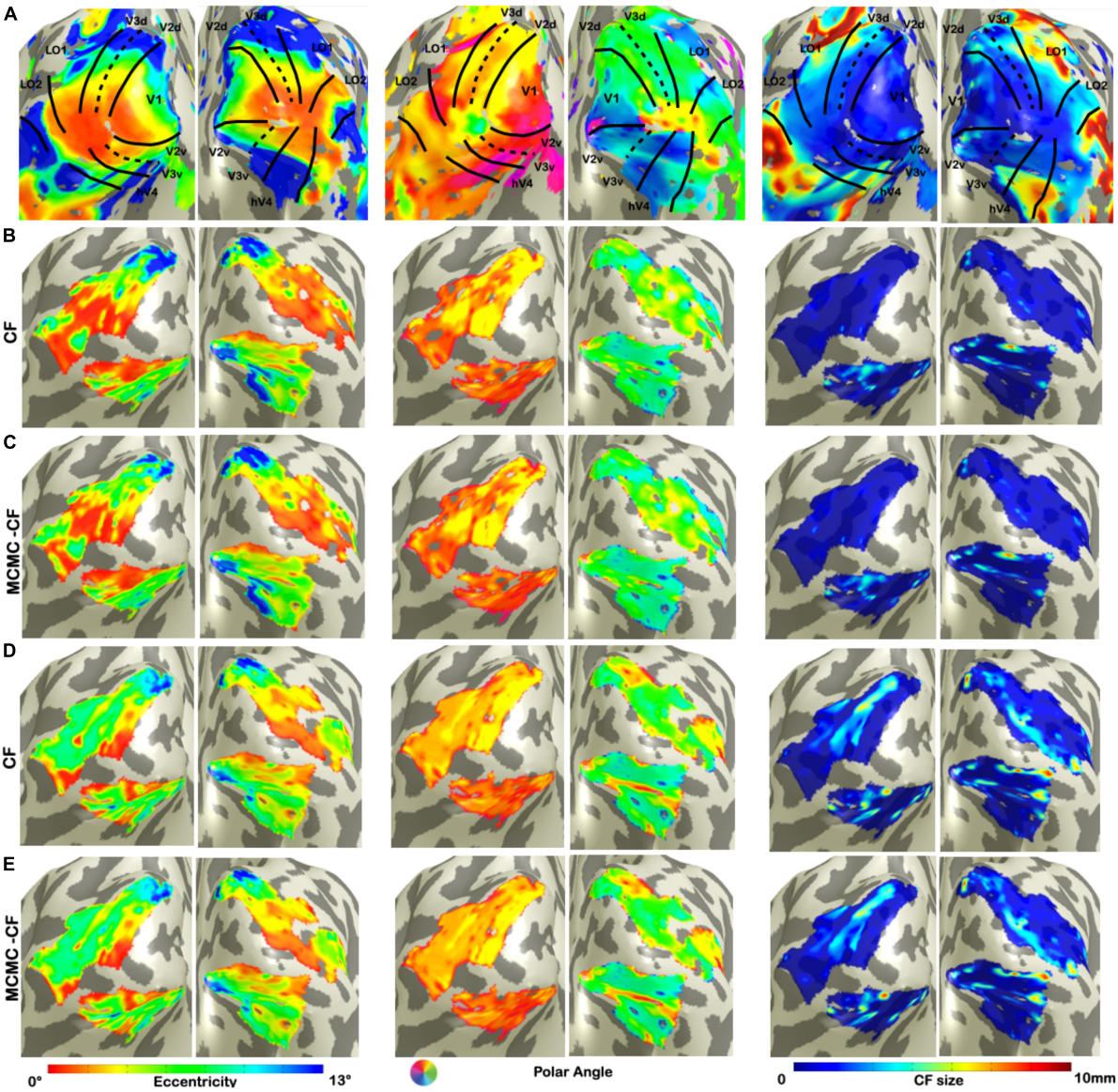

FIGURE 1 | Visualization of CF maps of denoised data for a single participant. From left to right: eccentricity, polar angle, and CF size. **(A)** Corresponds to VFM derived estimates. **(B,C)** Show parameter estimates for the first RS run (RS1) using standard CF and Bayesian CF models, respectively. **(D,E)** Show parameter estimates for the second RS run (RS2) using standard CF and Bayesian CF models, respectively. The fact that **(B,C)** on the one hand, and **(D,E)** on the other, are very comparable is important and indicates that the standard and Bayesian CF models produce highly similar results on RS data.

TABLE 1 | Group level correlation between visual field and resting state maps derived using Bayesian pRF and CF modeling.

Eccentricity									
ROIs	**Standard CF versus pRF**								
	VFM			***RS1***			***RS2***		
	r	***IQR [Q1, Q3]***	***p-value***	***r***	***IQR [Q1, Q3]***	***p-value***	***r***	***IQR [Q1, Q3]***	***p-value***
V1 –> V2	0.86	[0.82, 0.91]	$p < 0.001$	0.44	[0.38, 0.54]	$p < 0.001$	0.57	[0.47, 0.62]	$p < 0.001$
V1 –> V3	0.82	[0.76, 0.87]	$p < 0.001$	0.22	[0.13, 0.34]	$p < 0.001$	0.31	[0.17, 0.43]	$p < 0.001$
V1 -> hV4	0.81	[0.73, 0.83]	$p < 0.001$	0.02	[−0.09, 0.40]	0.0048	0.34	[0.04, 0.46]	$p < 0.001$
V1 -> LO1	0.78	[0.72, 0.81]	$p < 0.001$	0.07	[−0.13, 0.24]	0.0018	0.15	[0.04, 0.3]	0.0021
V1 -> LO2	0.63	[0.43, 0.75]	$p < 0.001$	−0.06	[−0.27, 0.17]	0.0154	0.08	[−0.04, 0.27]	0.0567
ROIs	**Bayesian CF versus pRF**								
	VFM			***RS1***			***RS2***		
	r	***IQR [Q1, Q3]***	***p-value***	***r***	***IQR [Q1, Q3]***	***p-value***	***r***	***IQR [Q1, Q3]***	***p-value***
V1 –> V2	0.86	[0.82, 0.91]	$p < 0.001$	0.48	[0.34, 0.57]	$p < 0.001$	0.58	[0.51, 0.63]	$p < 0.001$
V1 –> V3	0.82	[0.77, 0.87]	$p < 0.001$	0.25	[0.09, 0.43]	$p < 0.001$	0.3	[0.16, 0.41]	$p < 0.001$
V1 -> hV4	0.79	[0.73, 0.84]	$p < 0.001$	0.08	[−0.16, 0.35]	0.0085	0.28	[0.06, 0.40]	$p < 0.001$
V1 -> LO1	0.78	[0.72, 0.82]	$p < 0.001$	0	[−0.17, 0.28]	0.0667	0.24	[0.10 0.43]	$p < 0.001$
V1 -> LO2	0.65	[0.54, 0.76]	$p < 0.001$	−0.03	[−0.25, 0.18]	0.0641	0.09	[−0.02, 0.38]	0.2264
Polar Angle									
ROIs	**Standard CF versus pRF**								
	VFM			***RS1***			***RS2***		
	r	***IQR [Q1, Q3]***	***p-value***	***r***	***IQR [Q1, Q3]***	***p-value***	***r***	***IQR [Q1, Q3]***	***p-value***
V1 –> V2	0.92	[0.85, 0.93]	$p < 0.001$	0.64	[0.41, 0.82]	$p < 0.001$	0.78	[0.178, 0.84]	$p < 0.001$
V1 –> V3	0.84	[0.78, 0.89]	$p < 0.001$	0.17	[−0.05, 0.82]	0.002	0.26	[−0.53, 0.49]	$p < 0.001$
V1 -> hV4	0.79	[0.51, 0.92]	$p < 0.001$	−0.29	[−0.62, 0.66]	$p < 0.001$	0.54	[−0.31, 0.77]	$p < 0.001$
V1 -> LO1	0.79	[0.55, 0.89]	$p < 0.001$	0.68	[0.34, 0.76]	$p < 0.001$	0.56	[−0.11, 0.72]	$p < 0.001$
V1 -> LO2	0.72	[0.46, 0.76]	$p < 0.001$	0.49	[−0.23, 0.68]	0.0046	0.62	[−0.46, 0.76]	$p < 0.001$
ROIs	**Bayesian CF versus pRF**								
	VFM			***RS1***			***RS2***		
	r	***IQR [Q1, Q3]***	***p-value***	***r***	***IQR [Q1, Q3]***	***p-value***	***r***	***IQR [Q1, Q3]***	***p-value***
V1 –> V2	0.92	[0.87, 0.93]	$p < 0.001$	0.62	[0.40, 0.85]	$p < 0.001$	0.83	[0.39, 0.87]	$p < 0.001$
V1 –> V3	0.84	[0.70, 0.92]	$p < 0.001$	0.17	[−0.03, 0.68]	$p < 0.001$	0.17	[−0.36, 0.48]	$p < 0.001$
V1 -> hV4	0.79	[0.51, 0.92]	$p < 0.001$	−0.34	[−0.55, 0.17]	$p < 0.001$	0.54	[−0.02, 0.71]	$p < 0.001$
V1 -> LO1	0.82	[0.55, 0.90]	$p < 0.001$	0.35	[0.10, 0.64]	0.0045	0.52	[−0.08, 0.79]	$p < 0.001$
V1 -> LO2	0.67	[0.51, 0.82]	$p < 0.001$	0.24	[−0.22, 0.76]	0.0021	0.3	[−0.35, 0.83]	$p < 0.001$

Correlations coefficients were computed in order to assess the level of agreement between the eccentricity (Pearson's correlation) and polar angle (circular correlation) estimates obtained by using standard CF and Bayesian CF models and the ones derived by the pRF. We used the VFM-based pRF estimates as reference as stimuli driven and they further show a clear visuotopic organization for all parameters. Correlation, p-values and interquartile range values were estimated at single subject level and then concatenated across all participants.

single participant and then concatenated across participants to calculate the Spearman's correlation and circular correlation, respectively. Overall a good agreement was found for V1 > V2 and V1 > V3 areas using both CF models. Negative or almost zero correlation values can be observed for CF estimates between distant visual areas (i.e., V1 > LO1, V1 > LO2).

To check the possible influence of the denoise procedure applied to RS data, the same quantification analysis was computed on non-denoised RS data. Similar results were observed indicating that the ICA-AROMA denoise procedure on RS-fMRI data did not influence the final CF outcomes. A complete overview of these analyses is reported in

TABLE 2 | Test-retest evaluation between RS scans.

Eccentricity				
ROIs	***CF standard***		***Bayesian CF***	
	ICC (r)	***IQR [Q1, Q3]***	***ICC (r)***	***IQR [Q1, Q3]***
V1 –> V2	0.9661	[0.943, 0.983]	0.9061	[0.844, 0.948]
V1 –> V3	0.2072	[0.073,0.462]	0.193	[0.074, 0.313]
V1 -> hV4	0.1045	[−0.012, 0.426]	−0.006	[−0.065, 0.503]
V1 -> LO1	0.0909	[−0.109, 0.343]	−0.0194	[−0.225, 0.235]
V1 -> LO2	0.1036	[−0.184, 0.604]	0.0413	[−0.244, 0.221]
Polar Angle				
ROIs	***CF standard***		***Bayesian CF***	
	ICC (r)	***IQR [Q1, Q3]***	***ICC (r)***	***IQR [Q1, Q3]***
V1 –> V2	0.9295	[0.874, 0.976]	0.8717	[0.720, 0.941]
V1 –> V3	0.3365	[0.179, 0.495]	0.2997	[0.075, 0.463]
V1 -> hV4	−0.027	[−0.081, 0.157]	−0.0583	[−0.209, 0.067]
V1 -> LO1	0.0732	[−0.106, 0.536]	0.1944	[−0.053, 0.48]
V1 -> LO2	0.4057	[0.137, 0.734]	0.2635	[0.064, 0.6036]
CF size				
ROIs	***CF standard***		***Bayesian CF***	
	ICC (r)	***IQR [Q1, Q3]***	***ICC (r)***	***IQR [Q1, Q3]***
V1 –> V2	0.2939	[0.168, 0.396]	0.2192	[0.061, 0.344]
V1 –> V3	0.0214	[−0.029, 0.139]	0.0335	[−0.077, 0.201]
V1 -> hV4	−0.0533	[−0.131, 0.147]	0.0717	[−0.042, 0.156]
V1 -> LO1	−0.0308	[−0.153, 0.049]	−0.0292	[−0.166, 0.076]
V1 -> LO2	−0.075	[−0.144, −0.017]	−0.1147	[−0.141, −0.007]

For eccentricity, polar angle, and CF size estimates obtained by using the standard CF and the Bayesian CF models. Intraclass correlation coefficients (ICC) were computed across all participants and for each ROI separately. Median and interquartile range are computed across the group.

Supplementary Material (**Supplementary Figure 1** and **Supplementary Table 1**).

Test-Retest Reliability

To estimate test-retest reliability between the two RS scans, we selected the 5% most active voxels and computed the ICC score for each parameter estimate obtained using both CF and Bayesian CF model. For completeness, the relation between ICC and chosen threshold is displayed in **Supplementary Figure 4**. A positive ICC value is reported for V1 > V2 using both models. For higher order visual areas this ICC value gradually drops for all parameters **Table 2**.

Assessing Uncertainty in RS-fMRI Data

In order to estimate a voxel-wise uncertainty value associated to each CF parameter, we computed a quantile analysis of the posterior distribution for each participant. Then, for illustrative purposes, we projected on a smoothed 3D mesh the uncertainty estimates obtained for a single participant (**Figure 2**), where V1 is the source region and V2, V3, hV4, LO1, and LO2 were the target regions; VFM-based CF maps were used as reference (**Figure 2A**). An increased uncertainty in beta estimate in RS1- and RS2-based CF maps was observed compared to VFM-based CF maps but not for CF size. Interestingly, no clear uncertainty-related visuotopic organization was found either for VFM or RS data. Furthermore, we evaluated the possible dependency between the Bayesian parameter estimates and the corresponding (posterior) uncertainty by computing the cross-correlation coefficient between these estimates (**Table 3**). In line with the findings reported in Bornmann (2013), Invernizzi et al. (2020) for VFM data, a weak correlation exists between beta, sigma parameter estimates and their respective uncertainties obtained on RS-data (**Table 3**). Again, this indicates that uncertainty is an additional, independent parameter, but this time obtained from resting-state data.

Bayesian CF Thresholding Application

To evaluate the goodness of the corrected beta-thresholding method in the voxel selection on RS data, we compared the model VE, each CF parameter and the uncertainty associated, respectively (**Figure 3**, CF size and **Supplementary Figure 2**, beta parameter). Both thresholds: VE is higher than 15% and the FWE corrected effect size (>95% **Figure 3A**; for more details, see Invernizzi et al. (2020) are indicated. Based on a direct comparison of FWE *beta*-corrected threshold (CI) to the standard VE of the model (**Figures 3B,C**), the 95% FWE CI-based threshold proved to be more conservative. Note that it is not straightforward to identify a point at which the two threshold definitions will be equivalent.

This threshold was then used to compare the relation between RS-based CF size and VFM-derived eccentricity. **Figure 4** shows that RS-based CF size does not increase with eccentricity within the early visual areas. While it is possible to notice an increase of CF size values with eccentricity only for the later visual areas (LO1 and LO2), especially in RS2. However, no significant differences were found between RS1 and RS2 scans in areas along the visual hierarchy.

DISCUSSION

In this study, we show that 3T RS-fMRI data is suitable for estimating local functional connectivity between visual cortical areas. Furthermore, we observed a good level of agreement between the standard and Bayesian (MCMC) CF models. This indicates that also the latter tool is suitable for studying the cortico-cortical properties of brains at rest. The obtained CF estimates are qualitatively similar to those previously observed for 7T RS-fMRI data. This further supports that sensitive estimations and associated uncertainties can be derived from 3T RS-fMRI data. Finally, we show that a FWE-corrected threshold can be used as a complementary threshold to the standard VE to increase the reliability of estimates. This indicates that both stimulus-driven and RS-based CF modeling are suitable approaches for use in patient- or single-case studies. Below, we discuss our findings in more detail.

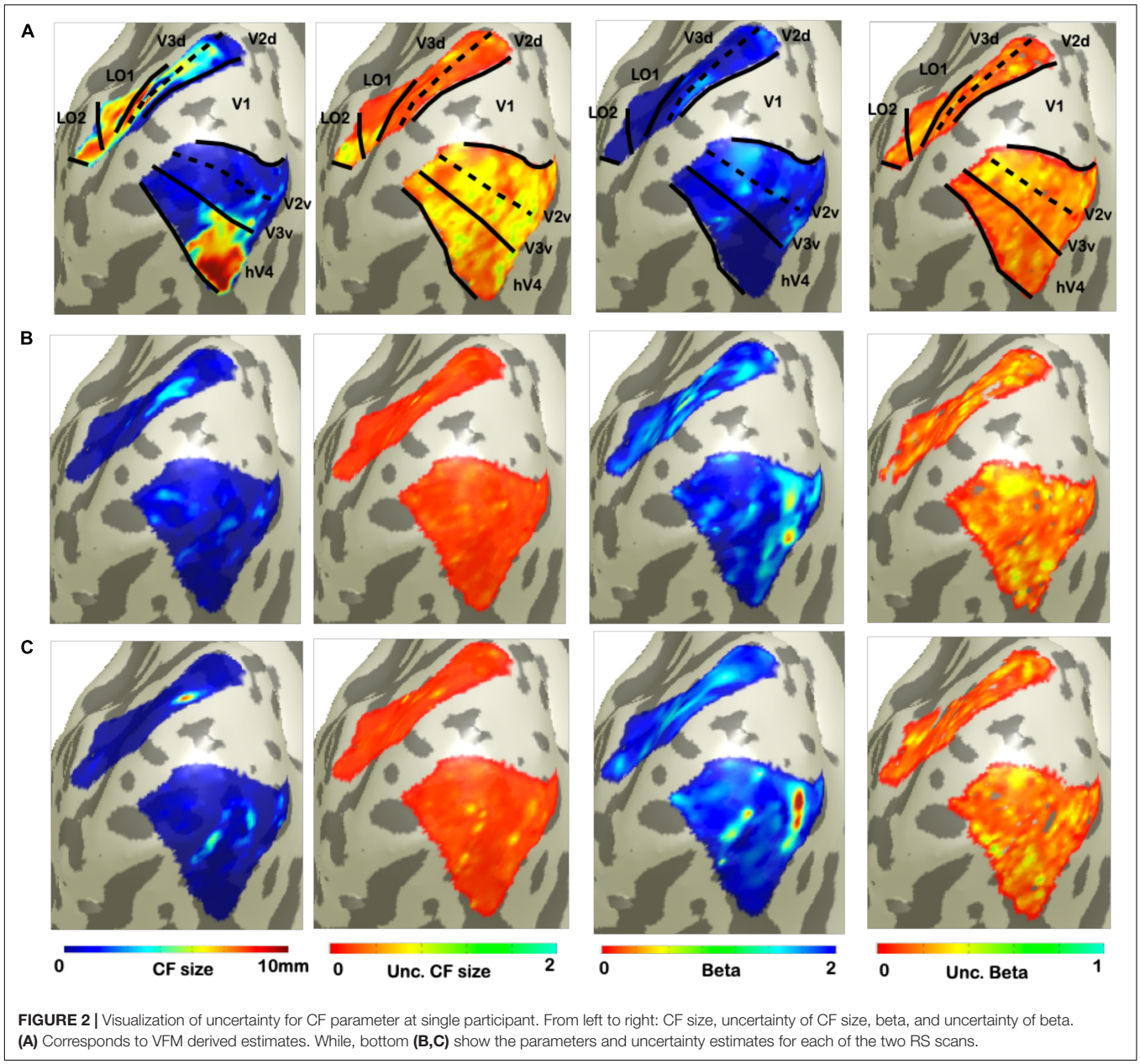

FIGURE 2 | Visualization of uncertainty for CF parameter at single participant. From left to right: CF size, uncertainty of CF size, beta, and uncertainty of beta. **(A)** Corresponds to VFM derived estimates. While, bottom **(B,C)** show the parameters and uncertainty estimates for each of the two RS scans.

TABLE 3 | Dependency between Bayesian CF parameters and uncertainties for both RS scan at group level.

	V1 > V2		V1 > V3		V1 > hV4		V1 > LO1		V1 > LO2	
RS1	***CF size***	***Beta***	***CF size***	***Beta***	***CF size***	***Beta***	***CF size***	***Beta***	***CF size***	***Beta***
Unc. CF size	0.06	−0.01	0.11	0.04	0.1	0.07	0.15	0.1	0.1	0.09
Unc. Beta	−0.03	0.01	−0.01	0.01	−0.04	0.01	−0.03	−0.12	−0.01	−0.01
RS2	***CF size***	***Beta***	***CF size***	***Beta***	***CF size***	***Beta***	***CF size***	***Beta***	***CF size***	***Beta***
Unc. CF size	0.08	−0.08	0.06	−0.05	0.04	−0.02	0.03	0.02	−0.02	−0.06
Unc. Beta	0.01	−0.01	0.01	−0.02	0.01	−0.03	−0.03	−0.04	−0.02	0.04

Cross-correlations were computed between the estimated Bayesian CF parameters and the uncertainty derived from them. Only the CF parameters directly estimated using the model (CF size and beta) are included in this analysis. CF size, beta, and their associated uncertainties were estimated at single participant level and then concatenated across all participants.

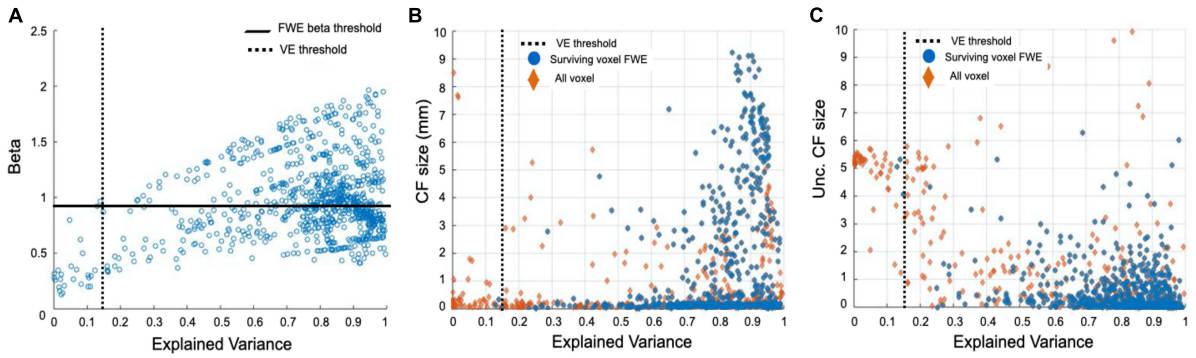

FIGURE 3 | Comparison of thresholding approaches at a single participant level for V1 > V2 connectivity based on RS1 data. In **Panel (A)** the FWE *beta*-corrected thresholds obtained with both 95% CI and the standard VE of the model are shown. A direct comparison between the FWE threshold and the standard VE is presented in **Panels (B,C)**. Since we are interested in testing this FWE-corrected threshold in different conditions, CF size ∼0 which are discarded. In **Panel (B)** the relation between VE and the Bayesian CF size is presented for all voxels (orange diamonds). Blue dots indicate the voxels surviving the 95% CI FWE beta-threshold. The standard VE threshold is not applied but indicated by a black dotted line. In **Panel (C)**, the relation between VE and the uncertainty associated with the CF size is presented. Note that high uncertainty can be associated with voxels with a high VE.

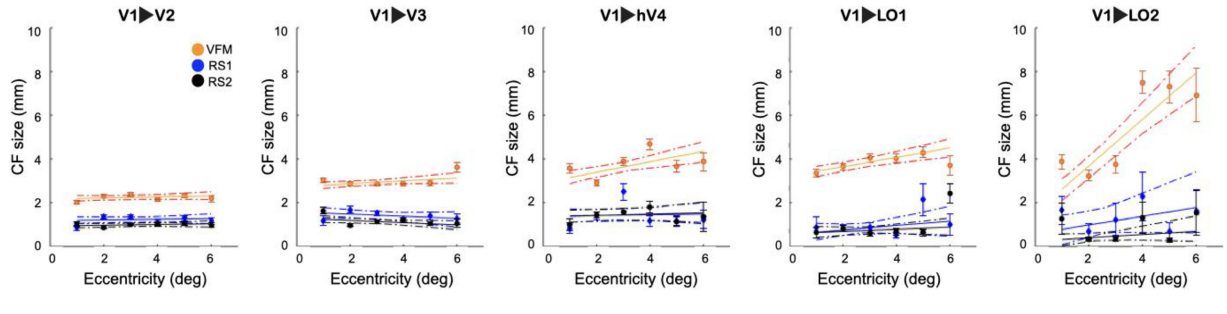

FIGURE 4 | Connective field size as a function of VFM- based eccentricity for RS and VFM scans. For both RS and VFM scans, eccentricity was binned in intervals of 1° and a linear fit was applied. The average CF size was calculated only for voxels that survived the FWE 95%CI threshold. Each dot indicates the mean of the CF size in each bin. The dashed lines correspond to the 95% bootstrap confidence interval of the linear fit. For reference, the VFM data is included.

Comparable CF Estimates Based on Resting-State and Visual Field Mapping at 3T fMRI

The CF method was previously used to reveal relevant aspects of resting-state brain activity using high-resolution 7T-fMRI. Crucially, in this study, we have extended the CF approach and assessed its performance at a lower-field strength (3T-fMRI). Higher magnetic fields can increase the signal-to-noise ratio, the tissue specificity and the spatial resolution of fMRI recordings. However, 3T scanners are much more abundant and more often used in clinical research than 7T ones. Our present findings indicate that, despite the limited resolution of metabolism-sensitive measurements such as fMRI for determining the contribution of neuronal activity to hemodynamic signals, it is still possible to study the aggregate neuronal population properties at 3T using CF approaches. A good level of agreement was found between the CF and Bayesian CF maps estimated from RS and those estimated based on VFM for all CF parameters in the early visual areas (**Figure 1** and **Table 1** – V1 > V2, V1 > V3). Our quantitative and qualitative results are in agreement with those presented previously (Haak et al., 2013b; Gravel et al., 2014; Invernizzi et al., 2020). Qualitatively, we find that the CF maps obtained at 3T are in fair agreement to those obtained at 7T (Gravel et al., 2014, **Figure 1**). Moreover, while we observed variability in the CF maps estimated for different RS scans, this was also observed previously at 7T Gravel et al. (2014).

Thus, RS-derived CF maps at least partly reflect the functional topographic organization revealed by pRF mapping — regardless of the lower spatial resolution and signal-to-noise ratio afforded by 3T-fMRI. While higher magnetic field strengths allow for an enhanced spatiotemporal resolution, the temporal resolution of fMRI is limited by the hemodynamic response to neuronal activity, not by the magnetic field strength. This suggests that the spatially weighted temporal correlations, as captured by the CF method, suffice to reveal the underlying retinotopically organized connectivity between areas.

Examining the relationship between CF size and pRF eccentricity revealed that RS-derived CF size did not increase with eccentricity, neither within individual areas nor throughout the visual hierarchy (**Figures 2**, **4**). In contrast, for VFM, we did find increased CF sizes at higher pRF eccentricities (**Supplementary Figure 3**). This was most pronounced for

higher-order visual area LO2. The same trend was observed in previous results obtained at 7T (Gravel et al., 2014).

In addition, we investigated whether spatial structure could be observed in the uncertainty information, which could potentially be due to large-scale network interactions, physiological processes or measurement noise. In order to do so, we compared the uncertainties associated with CF size, effect size (beta) in the different conditions (**Figure 2** and **Table 3**). However, neither in the VFM nor in the RS based uncertainty maps did we observe a clear visuotopic organization (**Figure 2**). Moreover, for the RS data, we find only weak correlations between the CF size and beta and their corresponding uncertainties (correlation <0.25). This is similar to what we observed previously for VFM data (Invernizzi et al., 2020). Therefore, we conclude that, given these rather weak (co)dependencies, the uncertainties can be treated as additional and independent CF parameters describing the RS state data.

The Effect Size as a New Approach for Voxel-Wise Thresholding of RS Data

The Bayesian variant of CF modeling, in addition to the uncertainties for the CF parameters, provides also a parameter beta describing effect size (β). This parameter can be used to threshold data in a voxel-wise manner similar to the estimated Variance Explained (VE). Since VE indicates the goodness of fit for the model, the current standard approach is to threshold voxels based on the VE of the model for both VFM and RS data (Haak et al., 2013b; Gravel et al., 2014; Halbertsma et al., 2019). However, a high VE does not always correspond to a low uncertainty in the parameter estimates (Thielen et al., 2019). As previously shown for VFM data, beta thresholding provides an alternative thresholding approach (Invernizzi et al., 2020). Here, we show that a FWE-corrected *beta* threshold based on the 95% CI also provides a valid approach for RS data and compares favorably to VE thresholding (**Figure 3** and **Supplementary Figure 2**). However, some thought should be given before applying it to RS data. On the one hand, *beta* thresholding is more sensitive in the selection of voxels compared to the standard VE. Given that RS data is inherently more noisy than VFM data and this might affect the applicability of *beta*-thresholding for this type of scan. On the other, a marked advantage of the FWE *beta*-thresholding approach is that it is participant-specific (Invernizzi et al., 2020). Therefore, using it ensures minimizing the loss of individual participant data and is expected to be especially useful when the Bayesian CF framework is applied to RS data acquired in clinical populations (e.g., with a lesioned visual pathway or brain neurodegeneration). In general, we conclude that FWE *beta*-thresholding is a useful complementary approach to the standard VE thresholding for both VFM and RS data.

Relationship Between Resting State Signals and Functional Architecture

Recent studies have shown that indirect measures of intrinsic neuronal activity, such as spontaneous BOLD fluctuations recorded during RS, can still reflect the organization of the neuroanatomical connectivity that characterizes early visual cortical areas. These studies have allowed the assessment of both fine-grained within- and between- area interactions. This observed spatial specificity in spontaneous BOLD fluctuations can only emerge if these are anchored in the topographically organized architecture of the visual system, as has been shown on multiple occasions (Biswal et al., 1995; Baseler et al., 1999; Azzopardi and Cowey, 2001; Haak et al., 2013b). However, the neuronal and physiological basis of these BOLD patterns is still unclear. Whether spontaneous fMRI activity reflects the consequences of local population spiking activity, sub-threshold neuronal activity (Logothetis et al., 2001; Shi et al., 2017), or metabolic relationships between neurons and astrocytes (e.g., neurovascular coupling) is still a matter of debate (O'Herron et al., 2016; Pang et al., 2017). It is possible that retinotopically organized inter-areal BOLD coupling patterns reflect intrinsic activity in distant cortical areas, sharing similar selectivity in visual field positions which is likely due to "hard wired," i.e., white matter bundle coupling. Alternatively, these patterns may reflect the footprint of slow fluctuations that traverse the brain like "waves" (Logothetis and Wandell, 2004; Carandini et al., 2015). Recent studies have unified these contrasting views by showing that both global fluctuations, in the form of propagating hemodynamic waves, and transient local coactivations are necessary for setting the spatial structure of hemodynamic functional connectivity (Pisauro et al., 2013; Matsui et al., 2016). Taken together, these studies point to the multiple roles that neuroanatomical, physiological and vascular factors play in shaping spontaneous RS activity in a way that gives rise to visuotopically organized fluctuations in the BOLD signal. The similar visual field position selectivity revealed by RS- and VFM-derived CF maps, suggest a shared neuroanatomical origin.

Limitations and Future Directions

Here, we qualitatively compared local functional connectivity at different magnetic field strengths obtained in different participants. For a direct comparison, the 3T and 7T derived results should ideally be obtained in the same participants. However, in our view, the differences in the acquisition protocols are minor and were no reason to burden a new cohort of participants to obtain new scans. Nevertheless, while we indeed report a good level of agreement between the CF estimates obtained using the RS and VFM scans, future studies should consider using identical MR parameters for the VFM and RS scans. Moreover, such future studies could investigate the correlations in the temporal and spatial domain in the cortex extending the Bayesian CF model to capture distinct dynamics in functional connectivity, and their relationship to different cognitive and behavioral states, both in health and disease. Furthermore, such studies could also consider the influence of high frequency fluctuations (above 0.1 Hz) in the spontaneous BOLD signal (Chen and Glover, 2015) on CF parameter estimates. Finally, the stimulus-agnostic and eye-movement independent character of the CF analysis invites applying the present approach also to other cortical regions, such as those involved in auditory, somatosensory, or motor processing (Knapen, 2020).

CONCLUSION

We have shown that CF modeling is a suitable tool to characterize and quantify the local functional connectivity of visual cortical areas during resting state at 3T. Moreover, the CF modeling at 3T provides qualitatively similar results to those previously observed at 7T, indicating that this lower, yet much more commonly available, field strength would be sufficient for characterizing the brains of patients and individual cases. Finally, we show that our novel Bayesian CF modeling approach provides additional and independent parameters such as uncertainty and effect size that, in principle, can be used to compare the local functional connectivity over different conditions, models and/or groups and assess the statistical significance of the modeling.

DATA AVAILABILITY STATEMENT

Data will be made available under request. Requests to access these datasets should be directed to the corresponding author: a.invernizzi@umcg.nl.

ETHICS STATEMENT

The studies involving human participants were reviewed and approved by the UMCG. The patients/participants provided their written informed consent to participate in this study.

AUTHOR CONTRIBUTIONS

AI, NG, KH, RR, and FC conceptualized and designed the study. AI performed the data analysis and visualization. AI and NG wrote and finalized the manuscript. KH, RR, and FC supervised the study and revised the final draft of the manuscript. All authors read and approved the final manuscript.

FUNDING

FC and AI received funding from the European Union's Horizon 2020 Research and Innovation Programme under the Marie Skłodowska-Curie grant agreement no. 661883 (EGRET cofund). AI received additional funding from the Graduate School of Medical Sciences (GSMS), University of Groningen, Netherlands. KH gratefully acknowledges funding from the Netherlands Organisation for Scientific Research (NWO grant no. 016.Veni.171.068). The funding organizations had no role in the design, conduct, analysis, or publication of this research. NG received funding from the Chilean National Commission for Scientific and Technological Research (CONICYT) and the Graduate School of Medical Sciences (GSMS) of the University Medical Center Groningen (UMCG).

ACKNOWLEDGMENTS

We want to thank Barbara Nordhjem for data collection and Hinke N. Halbertsma for data collection and preprocessing (manual segmentation and ROI definitions).

SUPPLEMENTARY MATERIAL

The Supplementary Material for this article can be found online at: https://www.frontiersin.org/articles/10.3389/fnins.2021.625309/full#supplementary-material

Supplementary Figure 1 | Visualization of CF maps of non-denoised and denoised RS data for a single subject. From left to right: eccentricity, polar angle and CF size. **(A)** corresponds to VFM derived estimates. It is reported to serve as reference for estimates obtained using RS data. **(B,D)** show CF parameters for each RS run before applying ICA-AROMA denoising procedure. While **(C,E)** show CF estimates for RS1 and RS2 after applying the denoised procedure.

Supplementary Figure 2 | Comparison of thresholding approaches on a single subject level in V1 > V2 area using RS1 data. In **(A)** the relation between VE and the beta parameter is presented for all the voxels (orange diamonds) and only for the ones surviving the 95% CI FWE beta-threshold (blue dots). The standard VE threshold is not applied but indicated by a black dotted line. In **(B)** the relation between VE and the uncertainty associated with beta is presented.

Supplementary Figure 3 | Connective field size as a function of pRF eccentricity for RS scans. For standard and Bayesian CF models, eccentricity was binned in intervals of 1° and a linear fit was applied. The CF size was initially weighted with variance explained higher than 0.15. Each dot and triangle indicate the mean of the CF size for each bin. While the dashed lines correspond to the 95% bootstrap confidence interval of the linear fit. In **(A)** CF models were applied to RS1 scan while, in **(B)** to RS2 scan.

Supplementary Figure 4 | Evaluation of different VE thresholds on ICC. In order to evaluate a viable VE threshold applied on the test-retest analysis, we evaluate the influence of using five different% of strongest activated voxels based on VE (1%, 5%, 10%, 25%, and 50%) on the final ICC (r) across ROIs **(A–E)**. Each participant is represented by a colored lines.

Supplementary Table 1 | Correlation between non-denoised and denoised CF maps obtained from RS data at group level. To estimate and compare the level of agreement between not-denoised and denoised CF maps that were obtained from RS1 and RS2 scans by using the standard CF model, we computed the Pearson's correlations for the eccentricity (*rho*) and the circular correlation for the polar angle (*theta*) parameters. In order to compute the correlation scores, eccentricity and polar angle parameters were estimated at single subject level and then concatenated across all participants.

Supplementary Table 2 | Within-subject variability of CF parameter estimates. For standard and Bayesian CF models, we estimated the coefficient of variation to evaluate the within-subject reproducibility of eccentricity and polar angle estimates for both RS scans. The coefficient of variation is reported for each visual area and for each participant.

REFERENCES

Azzopardi, P., and Cowey, A. (2001). Motion Discrimination in Cortically Blind Patients. *Brain A J. Neurol.* 124(Pt 1), 30–46. doi: 10.1093/brain/124.1.30

Baseler, H. A., Gouws, A., Haak, K. V., Racey, C., Crossland, M. D., Tufail, A., et al. (2011). Large-Scale Remapping of Visual Cortex Is Absent in Adult Humans with Macular Degeneration. *Nat. Neurosci.* 14, 649–655. doi: 10.1038/nn.2793

Baseler, H. A., Morland, A. B., and Wandell, B. A. (1999). Topographic Organization of Human Visual Areas in the Absence of Input from Primary Cortex. *J. Neurosci.* 19, 2619–2627. doi: 10.1523/JNEUROSCI.19-07-02619.1999

Biswal, B., Yetkin, F. Z., Haughton, V. M., and Hyde, J. S. (1995). Functional Connectivity in the Motor Cortex of Resting Human Brain Using Echo-Planar MRI. *Magnetic Resonan. Med.* 34, 537–541. doi: 10.1002/mrm.1910340409

Bornmann, L. (2013). How to Analyze Percentile Citation Impact Data Meaningfully in Bibliometrics: The Statistical Analysis of Distributions, Percentile Rank Classes, and Top-Cited Papers. *J. Am. Soc. Inform. Sci. Technol.* 64, 587–595. doi: 10.1002/asi.22792

Brainard, D. H. (1997). The Psychophysics Toolbox. *Spatial Vis.* 10, 433–436. doi: 10.1163/156856897X00357

Carandini, M., Shimaoka, D., Rossi, L. F., Sato, T. K., Benucci, A., and Knopfel, T. (2015). Imaging the Awake Visual Cortex with a Genetically Encoded Voltage Indicator. *J. Neurosci.* 35, 53–63. doi: 10.1523/jneurosci.0594-14.2015

Carvalho, J., Invernizzi, A., Ahmadi, K., Hoffmann, M. B., Renken, R. J., and Cornelissen, F. W. (2020). Micro-Probing Enables Fine-Grained Mapping of Neuronal Populations Using fMRI. *NeuroImage* 209:116423. doi: 10.1016/j.neuroimage.2019.116423

Chen, J. E., and Glover, G. H. (2015). BOLD Fractional Contribution to Resting-State Functional Connectivity above 0.1 Hz. *NeuroImage* 107, 207–218. doi: 10.1016/j.neuroimage.2014.12.012

Chib, S. (2011). "Introduction to Simulation and MCMC Methods," in *The Oxford Handbook of Bayesian Econometrics*, eds G. Koop, J. Geweke, and H. K. van Dijk (Oxford: Oxford University Press), doi: 10.1093/oxfordhb/9780199559084.013.0006

Dumoulin, S. O., and Wandell, B. A. (2008). Population Receptive Field Estimates in Human Visual Cortex. *NeuroImage* 39, 647–660. doi: 10.1016/j.neuroimage.2007.09.034

Fischl, B. (2012). FreeSurfer. *NeuroImage* 62, 774–781. doi: 10.1016/j.neuroimage.2012.01.021

Gravel, N., Harvey, B., Nordhjem, B., Haak, K. V., Dumoulin, S. O., Renken, R., et al. (2014). Cortical Connective Field Estimates from Resting State fMRI Activity. *Front. Neurosci.* 8:339. doi: 10.3389/fnins.2014.00339

Gravel, N., Renken, R. J., Harvey, B. M., Deco, G., Cornelissen, F. W., and Gilson, M. (2020). Propagation of BOLD Activity Reveals Task-Dependent Directed Interactions Across Human Visual Cortex. *Cereb. Cortex* 30, 5899–5914. doi: 10.1093/cercor/bhaa165

Haak, K. V., Cornelissen, F. W., and Morland, A. B. (2012). Population Receptive Field Dynamics in Human Visual Cortex. *PLoS One* 7:e37686. doi: 10.1371/journal.pone.0037686

Haak, K. V., Morland, A. B., and Cornelissen, F. W. (2013a). Connective Field Estimates in the Cortical Lesion Project Zone of Individuals with Macular Degeneration. *J. Vis.* 13, T11–T11. doi: 10.1167/13.15.11

Haak, K. V., Winawer, J., Harvey, B. M., Renken, R., Dumoulin, S. O., Wandell, B. A., et al. (2013b). Connective Field Modeling. *NeuroImage* 66, 376–384. doi: 10.1016/j.neuroimage.2012.10.037

Halbertsma, H. N., Haak, K. V., and Cornelissen, F. W. (2019). Stimulus- and Neural-Referred Visual Receptive Field Properties Following Hemispherectomy: A Case Study Revisited. *Neural Plasticity* 2019:6067871. doi: 10.1155/2019/6067871

Invernizzi, A., Haak, K. V., Carvalho, J. C., Renken, R. J., and Cornelissen, F. W. (2020). "Bayesian Connective Field Modeling: A Markov Chain Monte Carlo Approach," in *Conference: OHBM 2019* (Rome: OHBM), doi: 10.1101/2020.09.03.281162

Knapen, T. (2020). Visual Topographic Organization in Human Hippocampus Revealed by Connective Field Modelling during Naturalistic Vision and Resting State. *J. Vis.* 20, 984–984. doi: 10.1167/jov.20.11.984

Lancaster, G., Dmytro, I., Aleksandra, P., Valentina, T., and Aneta, S. (2018). Surrogate Data for Hypothesis Testing of Physical Systems. *Phys. Rep.* 748, 1–60. doi: 10.1016/j.physrep.2018.06.001

Liu, J., Nordman, D. J., and Meeker, W. Q. (2016). The Number of MCMC Draws Needed to Compute Bayesian Credible Bounds. *Am. Statist.* 70, 275–284. doi: 10.1080/00031305.2016.1158738

Logothetis, N. K., and Wandell, B. A. (2004). Interpreting the BOLD Signal. *Annu. Rev. Physiol.* 66, 735–769. doi: 10.1146/annurev.physiol.66.082602.092845

Logothetis, N. K., Pauls, J., Augath, M., Trinath, T., and Oeltermann, A. (2001). Neurophysiological Investigation of the Basis of the fMRI Signal. *Nature* 412, 150–157. doi: 10.1038/35084005

Matsui, T., Murakami, T., and Ohki, K. (2016). Transient Neuronal Coactivations Embedded in Globally Propagating Waves Underlie Resting-State Functional Connectivity. *Proc. Natl. Acad. Sci. U S A.* 113, 6556–6561. doi: 10.1073/pnas.1521299113

McGraw, K. O., and Wong, S. P. (1996). Forming Inferences about Some Intraclass Correlation Coefficients. *Psychol. Methods* 1, 30–46. doi: 10.1037/1082-989x.1.1.30

Nestares, O., and Heeger, D. J. (2000). Robust Multiresolution Alignment of MRI Brain Volumes. *Magnetic Resonan. Med.* 43, 705–715.

O'Herron, P., Chhatbar, P. Y., Levy, M., Shen, Z., Schramm, A. E., Lu, Z., et al. (2016). Neural Correlates of Single-Vessel Haemodynamic Responses in Vivo. *Nature* 534, 378–382. doi: 10.1038/nature17965

Pang, J. C., Robinson, P. A., Aquino, K. M., and Vasan, N. (2017). Effects of Astrocytic Dynamics on Spatiotemporal Hemodynamics: Modeling and Enhanced Data Analysis. *NeuroImage* 147, 994–1005. doi: 10.1016/j.neuroimage.2016.10.023

Pelli, D. G. (1997). The VideoToolbox Software for Visual Psychophysics: Transforming Numbers into Movies. *Spatial Vis.* 10, 437–442. doi: 10.1163/156856897X00366

Perinetti, G. (2018). StaTips Part IV: Selection, Interpretation and Reporting of the Intraclass Correlation Coefficient. *South Eur. J. Orthodontics Dentofacial Res.* 5:17434. doi: 10.5937/sejodr5-17434

Pisauro, M. A., Dhruv, N. T., Carandini, M., and Benucci, A. (2013). Fast Hemodynamic Responses in the Visual Cortex of the Awake Mouse. *J. Neurosci.* 33, 18343–18351. doi: 10.1523/JNEUROSCI.2130-13.2013

Polimeni, J. R., and Uludağ, K. (2018). Neuroimaging with Ultra-High Field MRI: Present and Future. *NeuroImage* 168, 1–6. doi: 10.1016/j.neuroimage.2018.01.072

Prabhakaran, G. T., Carvalho, J., Invernizzi, A., Kanowski, M., Renken, R. J., Cornelissen, F. W., et al. (2020). Foveal pRF Properties in the Visual Cortex Depend on the Extent of Stimulated Visual Field. *NeuroImage* 222:117250.

Pruim, R. H. R., Mennes, M., Buitelaar, J. K., and Beckmann, C. F. (2015). Evaluation of ICA-AROMA and Alternative Strategies for Motion Artifact Removal in Resting State fMRI. *NeuroImage* 112, 278–287.

Räth, C., and Monetti, R. (2009). Surrogates with Random Fourier Phases. *Topics Chaotic Syst.* Preprint. doi: 10.1142/9789814271349_0031

Schreiber, T., and Schmitz, A. (1996). Improved Surrogate Data for Nonlinearity Tests. *Phys. Rev. Lett.* 77, 635–638. doi: 10.1103/physrevlett.77.635

Shi, Z., Wu, R., Yang, P., Wang, F., Wu, T., Mishra, A., et al. (2017). High Spatial Correspondence at a Columnar Level between Activation and Resting State fMRI Signals and Local Field Potentials. *Proc. Natl. Acad. Sci. U S A.* 114, 5253–5258.

Shoukri, M. M., Colak, D., Kaya, N., and Donner, A. (2008). Comparison of Two Dependent within Subject Coefficients of Variation to Evaluate the Reproducibility of Measurement Devices. *BMC Med. Res. Methodol.* 8:24. doi: 10.1186/1471-2288-8-24

Thielen, J., Güçlü, U., Güçlütürk, Y., Ambrogioni, L., Bosch, S. E., and van Gerven, M. A. J. (2019). DeepRF: Ultrafast Population Receptive Field Mapping with Deep Learning. *Cold Spring Harbor Lab.* 2019:732990. doi: 10.1101/732990

van der Kolk, A. G., Hendrikse, J., Zwanenburg, J. J. M., Visser, F., and Luijten, P. R. (2013). Clinical Applications of 7T MRI in the Brain. *Eur. J. Radiol.* 134:7. doi: 10.1016/j.ejrad.2011.07.007

Winawer, J., Horiguchi, H., Sayres, R. A., Amano, K., and Wandell, B. A. (2010). Mapping hV4 and Ventral Occipital Cortex: The Venous Eclipse. *J. Vis.* 10:1. doi: 10.1167/10.5.1

Zeidman, P., Silson, E. H., Schwarzkopf, D. S., Baker, C. I., and Penny, W. (2018). Bayesian Population Receptive Field Modelling. *NeuroImage* 180(Pt A), 173–187. doi: 10.1016/j.neuroimage.2017.09.008

Conflict of Interest: The authors declare that the research was conducted in the absence of any commercial or financial relationships that could be construed as a potential conflict of interest.

frontiers in Neuroscience

ORIGINAL RESEARCH
published: 20 July 2021
doi: 10.3389/fnins.2021.704079

Parietal Lobe Reorganization and Widespread Functional Connectivity Integration in Upper-Limb Amputees: A rs-fMRI Study

*Bingbo Bao[1†], Haifeng Wei[1†], Pengbo Luo[1], Hongyi Zhu[1], Wencheng Hu[1], Yi Sun[1], Junjie Shen[1], Tianhao Zhu[1], Junqing Lin[1], Tengli Huang[1], Jing Li[2], Zhibin Wang[2], Yuehua Li[2] and Xianyou Zheng[1]**

[1] Department of Orthopedic Surgery, Shanghai Jiao Tong University Affiliated Sixth People's Hospital, Shanghai, China, [2] Institute of Diagnostic and Interventional Radiology, Shanghai Jiao Tong University Affiliated Sixth People's Hospital, Shanghai, China

OPEN ACCESS

Edited by:
Yajun Ma,
University of California, San Diego, United States

Reviewed by:
Amy Kuceyeski,
Cornell University, United States
Yi Zhao,
Indiana University, United States

***Correspondence:**
Xianyou Zheng
zhengxianyou@126.com

† These authors have contributed equally to this work

Specialty section:
This article was submitted to Brain Imaging Methods, a section of the journal Frontiers in Neuroscience

Received: 01 May 2021
Accepted: 21 June 2021
Published: 20 July 2021

Citation:
Bao B, Wei H, Luo P, Zhu H, Hu W, Sun Y, Shen J, Zhu T, Lin J, Huang T, Li J, Wang Z, Li Y and Zheng X (2021) Parietal Lobe Reorganization and Widespread Functional Connectivity Integration in Upper-Limb Amputees: A rs-fMRI Study. Front. Neurosci. 15:704079. doi: 10.3389/fnins.2021.704079

The right parietal lobe plays an important role in body image, and disorders of body image emerge after lesions in the parietal lobe or with parietal lobe epilepsy. Body image disorder also often accompanies upper-limb amputation, in which the patient misperceives that their missing limb is still part of their body. Cortical reorganization is known to occur after upper-limb amputation, but it is not clear how widespread and to what degree functional connectivity (FC) is reorganized post-amputation, nor whether such changes might be related to misperceptions of body image. Twenty-four subjects who had a traumatically upper-limb amputees (ULAs) and 24 age-matched healthy controls (HCs) underwent resting-state functional magnetic resonance imaging (rs-fMRI) scans. Regions of interest (ROIs) in the right superior parietal gyrus (SPG_R) and right inferior parietal lobule (IPL_R) were defined using BrainNet Viewer. We calculated the amplitude of low-frequency fluctuations (ALFF) in ROIs and correlated the ROI mean amplitude of low-frequency fluctuations (mALFF) and mean scores on the phantom limb sensation (PLS) scale and beck depression index (BDI). We also calculated ROIs and whole-brain FC. Compared to the HC group, we observed significantly increased activation (mALFF) in ROIs of the ULA group. Moreover, correlation analyses revealed a significant positive correlation between ROI mALFF and scores on the PLS. There was a significant negative correlation between the SPG_R mALFF and BDI scores. Seed-based, whole-brain FC analysis revealed that FC in the ULA group significantly decreased in many brain regions across the entire brain. The right parietal lobe appears to be involved in some aspect of body awareness and depression in amputation patients. Upper-limb amputation results not only in reorganization in the local brain area formerly representing the missing limb, but also results in more widespread reorganization through FC changes in whole brain.

Keywords: amputation, body image disorder, phantom sensation, phantom pain, functional magnetic resonance imaging, functional connectivity, ALFF

INTRODUCTION

Limb amputation is an important health issue affecting the quality of life of untold numbers of people worldwide (Pomares et al., 2018). In the United States, for example, the number of limb amputees continues to increase, mostly due to increases in the number of traumatic injuries resulting from traffic accidents and natural disasters, and amputations related to diabetes and malignant tumors of limbs (Varma et al., 2014). This increasing trend can be seen worldwide, with 1.5 amputations being performed per 1000 people. Although amputation can save lives, the risk of many types of medical complications remains. Moreover, sensory disorders and psychological problems can be present (Armstrong et al., 2019).

Phantom limb pain (PLP), residual limb pain (RLP), and phantom limb sensation (PLS) are the most common clinical complications of amputations (Woodhouse, 2005; Kaur and Guan, 2018; Stover and Prahlow, 2020). Recent studies indicate that 60–80% of amputees experience phantom pain and approximately 80–100% experience phantom sensation (Jensen et al., 1983; Urits et al., 2019). Faced with such high incidences of complications, much basic research has focused on better understanding quality-of-life reducing complications, especially those involving PLP. Theories explaining PLP mainly involve peripheral, central, and supraspinal mechanisms (Flor, 2002; Flor et al., 2006). Despite various useful treatments for PLP (Erlenwein et al., 2021), it still cannot be completely resolved clinically and thus continues to seriously affect amputees' quality of life.

Another consequence of upper-limb amputations is body image disorder. Body image disorder, or disturbance, refers to several different conditions in which a person's body image mismatches reality; that is, the patient feels extreme anxiety and fear associated with an imagined or minor physical flaw, which significantly impedes normal, everyday functioning. Body image disorder comprises several different body disturbances recognized by the DSM-V, including body dysmorphic disorder and muscle dysmorphia, among others. Basic perceptual functions of patients are normal, but the existence of their own body parts, their spatial position, and the relationship between each part are distorted (Demirdel and Ülger, 2021). Amputees often suffer from body image disorders. For example, even though their limb is absent, they perceive that their limb still is present. This kind of disturbance in body image has been linked to various negative psychosocial outcomes, ones involving perceptual, affective, cognitive, evaluative, and behavioral disturbances (McDonald et al., 2014; Luza et al., 2020).

Many studies have investigated the reorganization of the nervous system after amputation, but usually from the perspective of understanding PLS. PLS may be the result of ongoing neuroplasticity (Mercier et al., 2006; Di Pino et al., 2009). Other studies have reported strong correlational relationships between PLS and the degree of cortical reorganization (Wheaton, 2017). A separate line of research on body image disorders shows that the right parietal cortex is prominently involved in the disorder. The right parietal cortex represents a higher-order convergence zone of somatosensory, visual, and vestibular input that is critical for sensorimotor integration (Wolpert et al., 1998). This integration of sensory information with motor intention and actions represents the core of a unified sense of the body in space (Tsakiris, 2010). We are unaware of any relevant research on whether brain remodeling in the parietal lobe after amputation might be related to body image disorders in upper-limb amputees (ULAs).

Resting-state functional magnetic resonance imaging (rs-fMRI) is a promising tool for analyzing brain function remodeling and functional connectivity (FC). rs-fMRI studies represent a significant approach for researching different diseases and disorders at the brain-network level (Smitha et al., 2017). rs-fMRI does not require participants to perform any complex sensorimotor task; it monitors intrinsic activity within the brain, in the absence of any sensory or cognitive stimulus. Resting-state FC analysis has been used to study network-level reorganization of FC following arm amputation, and has revealed reduced FC between neocortical areas associated with the missing hand and the sensorimotor network in amputees (Makin et al., 2015).

Since PLS are manifested in an incorporeal body part, they can be regarded as one type of body image disorder, one that is closely related to changes in the right parietal lobe (Sadibolova et al., 2019). Prompted by the above considerations, we predict that the right parietal lobe in ULAs will undergo changes in plasticity and FC integration, which might be detected with rs-fMRI and network analysis (Smitha et al., 2017). Therefore, the aim of the present study was to characterize right parietal lobe plasticity following upper-limb amputation and to determine its relationship to the phenomenology of PLS.

MATERIALS AND METHODS

Participants

Characteristics of participating subjects are summarized in **Table 1**. Twenty-four individuals (19 male and 5 female) with acquired unilateral upper-limb amputation (mean age ± SD: 44.67 ± 8.33; 15 patients with amputations on the right side) were recruited through the department of orthopedic surgery of a large metropolitan tier 1 hospital in China between October 2020 and December 2020. Thirteen amputations occurred above the elbow and 11 occurred below the elbow. All the patients underwent amputation following a traumatic injury. Exclusion criteria were the following: (1) upper-limb amputation along with another part of the body; (2) history of neurological disease, diabetes, or previous neurotrauma; (3) presence of neurological or psychiatric disorders; (4) elapsed time between amputation and MRI scanning was <3 months; (5) history of psychotropic drug use or (6) MRI contraindication. Twenty-four limb-intact individuals matched for age (mean age, range in years); education; and sex served as healthy controls (HCs). These participants were recruited from the local community. All subjects were right-handed, as assessed by the Chinese version of the Edinburgh Handedness Inventory (Yang et al., 2018). Each participant was informed of the purpose and methods of the study, and each signed a written informed consent to participate. The study was approved by the ethics committee

TABLE 1 | Demographic and clinical characteristics of participating upper-limb amputees.

Subject no.	Age/sex	Side/level of amputation	Education (years)	Time*	RLP†	PLP‡	PLS§	BDI	BAI
1	29/M	L/AEA	7	38	1	2	7	2	3
2	44/F	R/BEA	12	36	0	1	4	1	7
3	41/M	L/AEA	9	32	6	4	9	1	1
4	41/M	L/BEA	9	30	1	1	1	5	21
5	38/M	R/AEA	9	34	2	3	10	3	4
6	56/M	L/BEA	0	43	6	6	8	22	33
7	48/F	R/AEA	8	32	6	6	4	13	9
8	42/M	R/AEA	2	47	1	1	5	7	28
9	52/M	R/AEA	8	26	7	6	3	33	46
10	41/M	L/AEA	9	18	5	8	6	17	17
11	54/M	L/AEA	5	264	5	5	9	1	8
12	59/M	R/AEA	10	5	0	3	7	9	2
13	47/M	L/BEA	12	26	1	0	4	12	3
14	42/M	L/BEA	8	46	0	0	2	6	4
15	50/M	R/AEA	8	348	0	2	8	2	1
16	39/M	R/BEA	7	60	0	0	10	4	15
17	44/M	R/BEA	12	48	1	1	6	4	5
18	45/F	R/AEA	3	7	3	7	3	4	27
19	37/M	R/BEA	22	4	5	7	10	3	5
20	40/M	R/AEA	12	48	7	5	8	17	11
21	27/M	R/BEA	15	51	1	0	4	2	0
22	60/F	R/BEA	3	300	3	2	7	19	22
23	43/M	L/AEA	8	252	2	0	10	1	1
24	53/F	R/BEA	8	432	0	0	6	6	4

M, male; F, female; R, right; L, left; AEA, above the elbow; BEA, below the elbow; RLP, residual limb pain; PLP, phantom limb pain; PLS, phantom limb sensation; Chinese version of BDI, beck depression index, 0 = Not at All to 63 = severe; Chinese version of BAI, Beck anxiety inventory, 0 = Not at All to 63 = severe.

**Elapsed time in months from amputation.*

†Residual limb pain, 0 = none to 10 = worst imaginable at time of MRI.

‡Phantom limb pain, 0 = none to 10 = worst imaginable at time of MRI.

§Phantom Limb Sensations, 0 = none to 10 = worst imaginable at time of MRI.

of our institution and performed according to international standards (World Medical Association., 2013).

Clinical Assessments

Clinical assessments were done before fMRI scanning. An adapted questionnaire for upper limb amputation was used to collect information about amputation-related variables. The adaptations assessed the level of amputation, side of amputation, elapsed time (months) since amputation, previous treatment approaches, and whether they were effective or not. We also assessed RLP; PLP; and the frequency, quality, and type of PLS. Pain was measured with a visual analog scale assessment tool, on which self-reported pain is scored on a scale from 0 (no pain) to 10 (worst imaginable pain). As a visual indicator of pain, this scale was also color-coded with a gradient of green (at 0) to red (at 10). Participants were asked to rate the presence and intensity of pain related to PLP. Similar scales were used to assess RLP, stump pain, and PLS, and non-painful sensations. Depression and anxiety, respectively, was evaluated using the Chinese versions of the Beck Depression Index (BDI) and Beck Anxiety Index (BAI).

MRI Scanning and Image Acquisition

For image acquisition of functional and structural data, we used a Siemens 3.0-T MRI scanner (MAGNETOM Prisma; Siemens Healthcare GmbH, Erlangen, Germany) equipped with a 64-channel phased-array head coil. Rs-fMRI data were collected via simultaneous multi-slice MRI technology for a total of 240 volumes (288 s). The following parameters were used: repetition time (TR) = 1200 ms; echo time (TE) = 39 ms; flip angle = 52°; matrix = 88 × 88; field of view = 100 mm; slice thickness = 2.4 mm; 56 slices with a voxel size = 2.4 mm × 2.4 mm × 3.0 mm. During the resting-state scan, subjects were asked to relax with their eyes closed and not to think of anything in particular. In addition, for each participant we acquired high-resolution T1-weighted structural images using a magnetization-prepared rapid gradient echo (MPRAGE) pulse sequence. The following parameters were used: TR = 2300 ms; TE = 2.46 ms; flip angle = 8°; matrix = 256 × 256; thickness = 1.0 mm; 176 slices with a voxel size = 1 mm × 1 mm × 1 mm.

Data Preprocessing

Preprocessing was performed using Statistical Parametric Mapping (SPM12[1]) implemented in MATLAB R2013b (MathWorks Inc., Natick, MA, United States). To allow the signal to reach equilibrium and the participants to adapt to the scanner noise, data collection began after 10 images

[1]http://www.fil.ion.ucl.ac.uk/spm

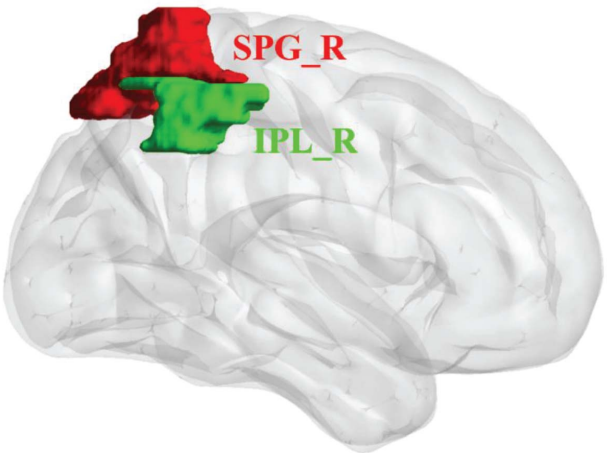

FIGURE 1 | Regions of interest (ROIs) for network analysis of rs-fMRI data of upper-limb amputees (ULA) and healthy control (HC) subjects.
Three-dimensional rendering showing the approximate locations of ROIs (colored patches) in parietal cortex. SPG_R, right superior parietal gyrus (red); IPL_R, right inferior parietal lobule (green).

were collected; thus, these first 10 scans of each subject were discarded. The remaining 230 images of each subject were co-registered to the individual anatomical data sets after the anterior commissure had been manually defined as the reference point. For all subjects, the translation or rotation parameters did not exceed ±2.5 mm or ±2.5°, respectively. To further reduce the effects of confounding factors, including signals from white matter and cerebrospinal fluid, the mean time series of all voxels across the whole brain were removed from the data via linear regression. The resulting maps were spatially normalized into a standard stereotaxic space at a resolution of 3 mm × 3 mm × 3 mm using an echo-planar imaging template. After normalization, the images were smoothed using the full width at half maximum of the Gaussian kernel of 6 mm to decrease spatial noise.

Seed Selection Using mALFF and FC Analyses

We analyzed the mean amplitude of low-frequency fluctuations (mALFF) and FC to define body image disturbance-related brain regions in patients with upper-extremity amputations. We selected two cortical areas from a freely available atlas of regions defined by correlated activation patterns (Shirer et al., 2012). These regions of interest (ROIs) were the right superior parietal gyrus (SPG_R) and right inferior parietal lobule (IPL_R). Two ROIs of cortical regions were visualized with BrainNet Viewer (Xia et al., 2013; **Figure 1**).

Before calculating the amplitude of low-frequency fluctuations (ALFF) value in our participants' ROIs, all subject-level data were preprocessed to remove any signal variations and noise using the detrend and nuisance covariate regression features of the Resting-State fMRI Data Analysis Toolkit plus V1.2 (RESTplus V1.2[2] (Song et al., 2011). The data were detrended to reduce low-frequency drift. Linear regression of the global mean signal, head motion parameters, cerebrospinal fluid signal, and white matter signal was performed to remove the effects of nuisance covariates. We calculated the mALFF value of all the subjects' ROIs (SPG_R and IPL_R). Next, we extracted the mALFF value of each subject's ROIs and correlated it with the subject's clinical scale scores.

Before calculating ROIs and whole-brain FC, all subject-level data were preprocessed with detrend, nuisance covariate regression, and band-pass filter. The data were detrended to reduce low-frequency drift. Linear regression of global mean signal, head motion parameters, cerebrospinal fluid signal, and white matter signal was executed to remove the effects of nuisance covariates. The data were processed with a temporal band-pass filter (0.01–0.08 Hz) to reduce low-frequency drift and high-frequency physiological noise. Then, FC analysis was performed using the Resting-State fMRI Data Analysis Toolkit plus V1.2 (Song et al., 2011). Based on the literature and the ALFF results, SPG_R and IPL_R were defined as the FC ROI. Next, we performed seed-based whole-brain voxel-wise FC analysis by computing the temporal correlation between the mean time series of the ROIs and the time series of each voxel within the brain. Pearson correlation coefficient maps were created for each individual subject, and these were converted to z-values using the Fisher z transformation.

Statistical Analysis

Analysis of Demographic and Clinical Characteristics

After validating the normality assumption, two-tailed two sample t-tests and chi-square tests (only for sex) were performed to compare the demographic and clinical data from the two groups (SPSS 24.0; SPSS, Inc., Chicago, IL, United States). Significance level was set at $p < 0.05$.

Analyses of ROIs mALFF

Independent sample t-tests were used for comparing differences of mALFF between ULA and HC groups. Significance thresholds for t-tests were set at $p < 0.05$; thresholds were corrected with the AlphaSim module of Analysis of Functional NeuroImages (AFNI) software[3] (Cox, 1996). The results were viewed with bspmview, a graphical user interface for overlaying, thresholding, and visualizing 3D statistical neuroimages in MATLAB. The specific anatomical location of the brain regions with statistical significance in the Montreal Neurological Institute (MNI) atlas template was also determined in bspmview. mALFF values were represented by t-values: $t > 0$ indicated increased functional activity and $t < 0$ indicated decreased functional activity.

Relationships Between mALFF and Clinical Characteristics

To quantify the relationship between mALFF values of ROIs and clinical variables, correlational analyses were performed between

[2]http://restfmri.net/forum/rest_v12
[3]https://afni.nimh.nih.gov/

TABLE 2 | Statistical comparison of participants' demographic and clinical characteristics.

Characteristic	ULA (n = 24)	HC (n = 24)	t-Value or $\chi 2$	p-Value
Age (mean ± SD)	44.67 ± 8.33	44.88 ± 12.03	−0.07	0.945
Education (year; mean ± SD)	8.58 ± 4.52	8.04 ± 6.05	0.352	0.727
Sex (male/female)	5/19	11/13	3.375	0.066
Elapsed time since amputation (month; mean ± SD)	92.79 ± 123.34	–		–
Age at amputation (year; mean ± SD)	37.13 ± 10.18	–		–
Side of amputation left/right (no.)	9/15	–		–
Amputation above/below elbows (no.)	13/11	–		–

ULA, upper-limb amputees; HC, healthy controls.

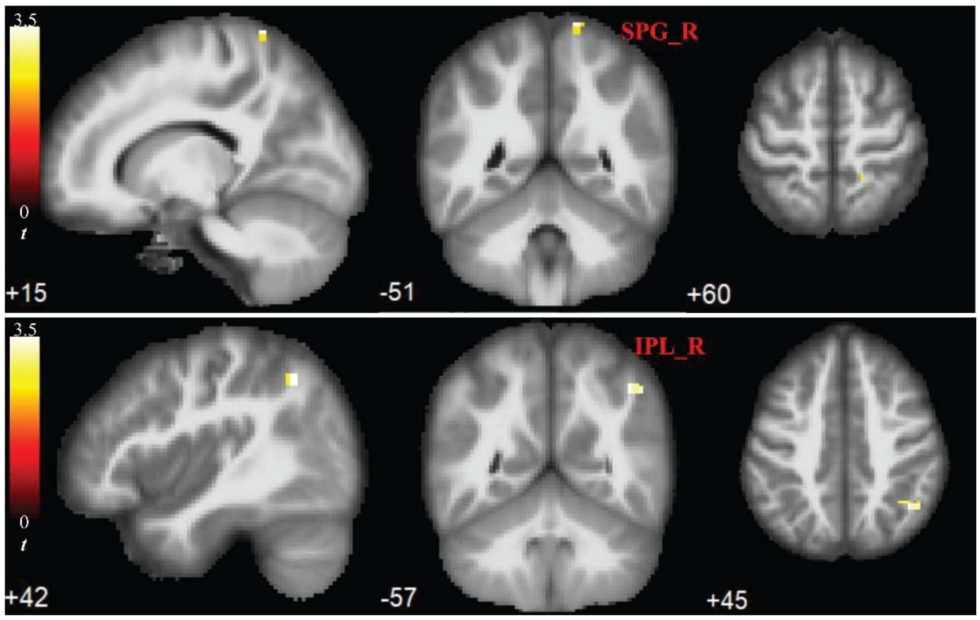

FIGURE 2 | Significant increases in rs-fMRI activity of right parietal lobe months after upper-limb amputation. ROIs showing significant differences in mean amplitude of low-frequency fluctuations (mALFFs) in SPG_R and IPL_R (ULA vs. HC subjects; $p < 0.05$; AlphaSim corrected cluster). MRI slices of patients in transverse, frontal, and axial planes with color-coded t-values overlaid. Color-coded scale indicates increasing positive t-values toward yellow. SPG_R, right superior parietal gyrus; IPL_R, right inferior parietal lobule; ULA, upper-limb amputee; HC, healthy control.

the mALFF values of ROIs and RLP, PLP, PLS, BDI, and BAI scores in ULAs. A two-tailed partial correlation analysis was used after controlling for age, sex, educational level as confounding variables and used multiple comparisons to correct p-values ($p < 0.05$).

Analyses of FC

For seed-based whole-brain voxel-wise connectivity, two-tailed two-sample t-tests were performed to evaluate group-related differences between the ULAs and the HCs. Significance threshold for t-tests was set at $p < 0.01$ (AlphaSim corrected). The covariates of age, sex, and educational level were controlled. These statistical analyses were carried out with the SPM12 toolbox.[4]

[4]https://www.fil.ion.ucl.ac.uk/spm/

RESULTS

Demographic and Clinical Characteristics

Table 2 shows the demographic and clinical characteristics of ULA and HC participants. No significant group differences were observed regarding age, sex, or education ($p > 0.05$).

ROIs mALFF

Compared to the HC group, the ULA group showed a significant increase in mALFF values of both the SPG_R and IPL_R ($p < 0.05$; AlphaSim corrected cluster; see **Figure 2**).

Correlations Between ROIs mALFF and Clinical Characteristics

Correlational analyses identified a significant positive correlation between the mALFF values of IPL_R and PLS scores of the

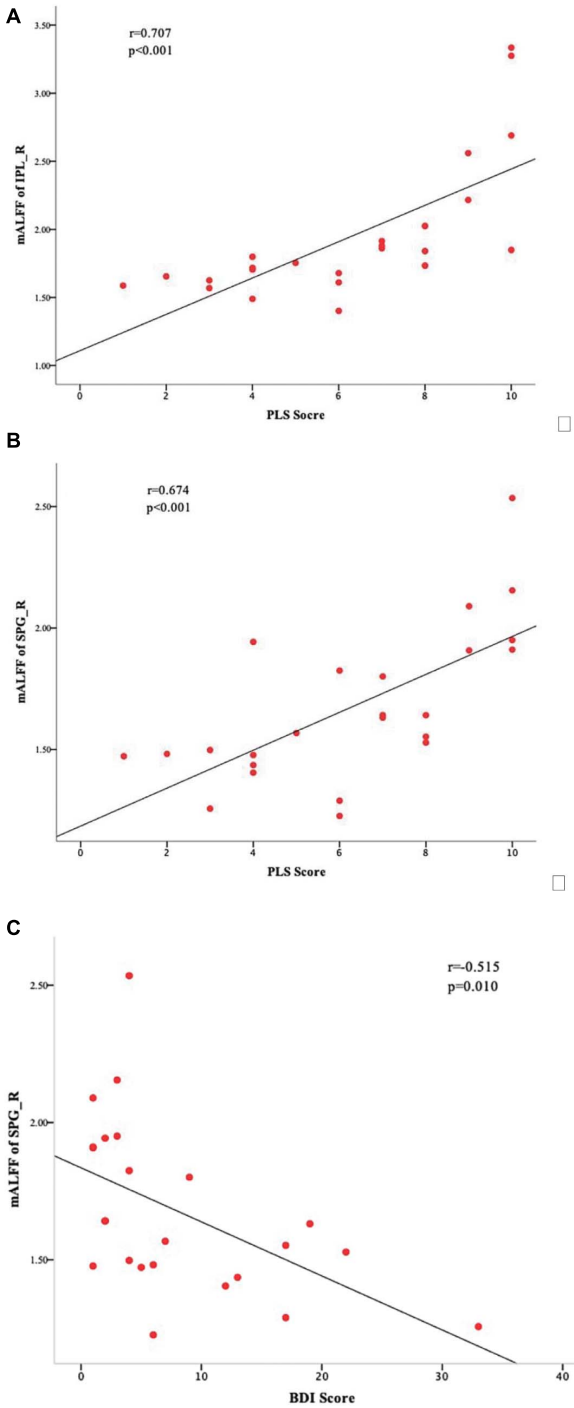

FIGURE 3 | Sensory and emotional disturbances after upper-limb amputation. Correlations between ULA participants' mALFF values in the ROIs and their clinical characteristics. **(A)** Scatter plot and statistically significant linear relationship between mALFF values of IPL_R and PLS scores ($r = 0.707$; $p < 0.001$). **(B)** Scatter plot and statistically significant linear relationship between mALFF values of SPG_R and PLS scores ($r = 0.674$; $p < 0.001$). **(C)** Scatter plot and statistically significant linear relationship between mALFF values of SPG_R and BDI score ($r = -0.515$, $p = 0.01 < 0.05$). SPG_R, right superior parietal gyrus; IPL_R, right inferior parietal lobule; PLS: phantom limb sensation; ULA, upper-limb amputee.

TABLE 3 | Decreased functional connectivity in ULA participants with seed region in the IPL_R*.

Brain region	Cluster size (voxels)	Peak coordinates (*x*/*y*/*z*; MNI)			*t*-Value
Temporal_Mid_R	238	57	−39	−3	−4.370
Temporal_Sup_R		45	−15	−6	−2.899
Cerebelum_L	102	−27	−63	−57	−4.354
Precentral_L	282	−33	−15	60	−3.961
Paracentral_Lobule_L		−18	−27	69	−3.113
Insula_L	430	−42	12	−9	−3.957
Temporal_Sup_L		−60	−15	12	−3.624
Lingual_R	157	21	−93	−12	−3.826
Occipital_Inf_R		42	−93	−6	−3.758
Cerebelum_L	154	−24	−78	−21	−3.493
Precentral_R	176	57	−6	48	−3.753
Frontal_Mid_R		45	12	54	−3.387

**Compared with functional connectivity of HC group ($p < 0.01$; AlphaSim corrected; voxels > 100); MNI, Montreal Neurological Institute coordinate system.*

ULA group ($r = 0.707$, $p < 0.001$; **Figure 3A**), and a significant positive correlation between the mALFF values of SPG_R and PLS scores of the ULA group ($r = 0.674$, $p < 0.001$; **Figure 3B**). The analyses also identified a significant negative correlation between the mALFF values of SPG_R and BDI scores of the ULA group ($r = -0.515$, $p = 0.01 < 0.05$; **Figure 3C**).

Seed-Based Whole-Brain FC

Comparison of the brain connectivity maps of ULAs and HCs revealed significantly decreased FC between the IPL_R seed and many brain regions in the ULA group ($p < 0.01$; AlphaSim corrected cluster; see **Table 3** and **Figure 4**). In the ULA group, we also observed decreased FC between the SPG_R and many brain regions ($p < 0.01$; AlphaSim corrected cluster; see **Table 4** and **Figure 5**).

DISCUSSION

PLP and PLS are essentially illusions, misinterpreted perceptions that the limb is still present after it has been amputated. Approximately 41–76% of limb amputees report persistent PLP and PLS (Ahmed et al., 2017). This condition can be considered to be a type of body image disorder, since a coherent body image is absent (Casale et al., 2009). Due to the loss of afferent and efferent nerves in amputees, extensive cortical remodeling occurs. This plasticity represents one of the key mechanisms that lead to PLP and PLS (Makin and Flor, 2020).

The reorganization in the cerebral cortex after limb amputation is sensorimotor in nature (MacIver et al., 2008) and is believed to originate from post-amputation changes in callosal connections (Giummarra et al., 2007) or from "unmasking" of latent brain circuits that arise from permanent changes in synaptic structure (Ramachandran and Rogers-Ramachandran, 2000). Although many ULAs report PLP and PLS, non-painful phantom sensation that is related to cortical reorganization in amputees is controversial (Flor et al., 2006).

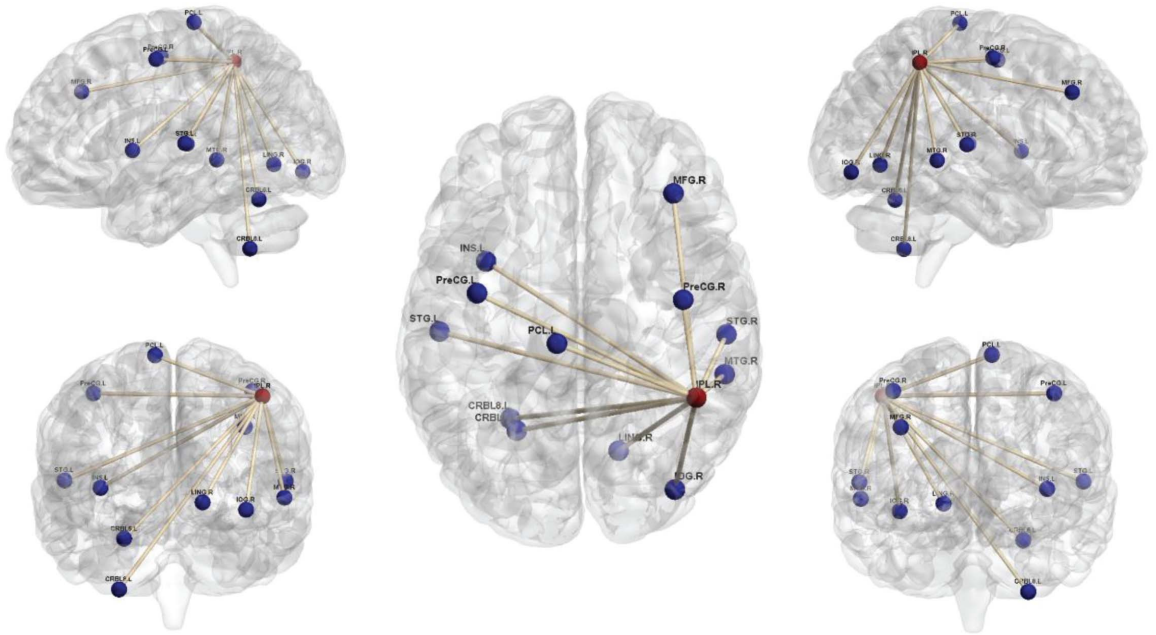

FIGURE 4 | Seed-based functional connectivity maps of right inferior parietal lobe (IPL_R) in ULAs based on rs-fMRI. Compared to HC subjects, ULA subjects showed decreased functional connectivity between the seed region in the IPL_R and various brain regions ($p < 0.01$; AlphaSim corrected; voxels > 100). ULA, upper-limb amputee; HC, healthy control.

The aim of the present study was to determine whether right parietal lobe plasticity following upper-limb amputation is related to aspects of PLS and body image.

Traditionally, body image disorders have been associated with damage to the convexity of the right parietal lobe posterior to the post-central gyrus (area S1) (Roth, 1949). The posterior parietal lobe is divided into the superior posterior gyrus (SPG) and inferior posterior lobules (area IPL) (Berlucchi and Vallar, 2018). Since the right SPG receives inputs from the dorsal visual stream (S1 and S2), the premotor cortex, and M1 (Van Essen et al., 2019), it seemed reasonable that the right SPG is strategically positioned to integrate disparate sensory inputs to construct a dynamic body image (Felleman and Van Essen, 1991). Therefore, we speculate that the disruption in body image after upper-limb amputation might be related to right parietal lobe remodeling.

Our rs-fMRI results revealed that the mALFF values of the ULA group were increased in both the SPG_R and IPL_R regions compared to those of the HC group. ALFF represents the intensity of local brain activity. Thus, we conclude that right parietal lobe activity increases after upper-limb amputation. This finding is consistent with related research (Flor et al., 2000; Foell et al., 2014). Increased activity in the right parietal lobe may represent functional compensation related to limb deficiencies.

Xenomelia is another kind of body image disorder that is often accompanied by the patient's desire to self-amputate a healthy limb (McGeoch et al., 2011). Several studies confirm that reduced function of the right parietal lobe underlies this type of mental illness (McGeoch et al., 2011; Hilti et al., 2013). It is interesting that these two conditions – xenomelia and PLS – may be accounted for by opposite processes: A functional decrease in the right parietal lobe is correlated with a xenomelia patient's desire to amputate a healthy limb, whereas a functional increase in the right parietal lobe is correlated with an amputee's PLS. Both conditions are body disorders. Our present correlation analyses revealed a significantly positive correlation between

TABLE 4 | Decreased functional connectivity in ULA participants with seed region in the SPG_R*.

Brain region	Cluster size (voxels)	Peak coordinates (*x*/*y*/*z*; MNI)			*t*-Value
Temporal_Inf_L	1152	−45	−30	−27	−4.963
Frontal_Inf_Tri_L		−57	24	9	−4.794
Temporal_Pole_Mid_L		−48	12	−30	−4.751
Temporal_Sup_L	358	−54	−42	15	−4.670
Temporal_Mid_L		−63	−42	−6	−3.747
Frontal_Sup_L	598	−27	−9	69	−4.669
Postcentral_L		−45	−33	63	−4.217
Precentral_L		−45	−12	60	−4.048
Lingual_R	571	27	−72	0	−4.363
Fusiform_R		27	−51	−15	−3.825
Occipital_Inf_R		36	−87	−15	−3.619
Lingual_L	464	−9	−90	−18	−4.258
Postcentral_R	180	69	−12	27	−4.016
Temporal_Mid_R	308	63	−45	6	−4.004
Temporal_Inf_R		69	−39	−21	−3.619
Temporal_Sup_R		48	−54	21	−3.451
Frontal_Sup_Medial_R	111	12	51	45	−3.722

**Compared with functional connectivity of HC group ($p < 0.01$; AlphaSim corrected; voxels > 100); MNI, Montreal Neurological Institute coordinate system.*

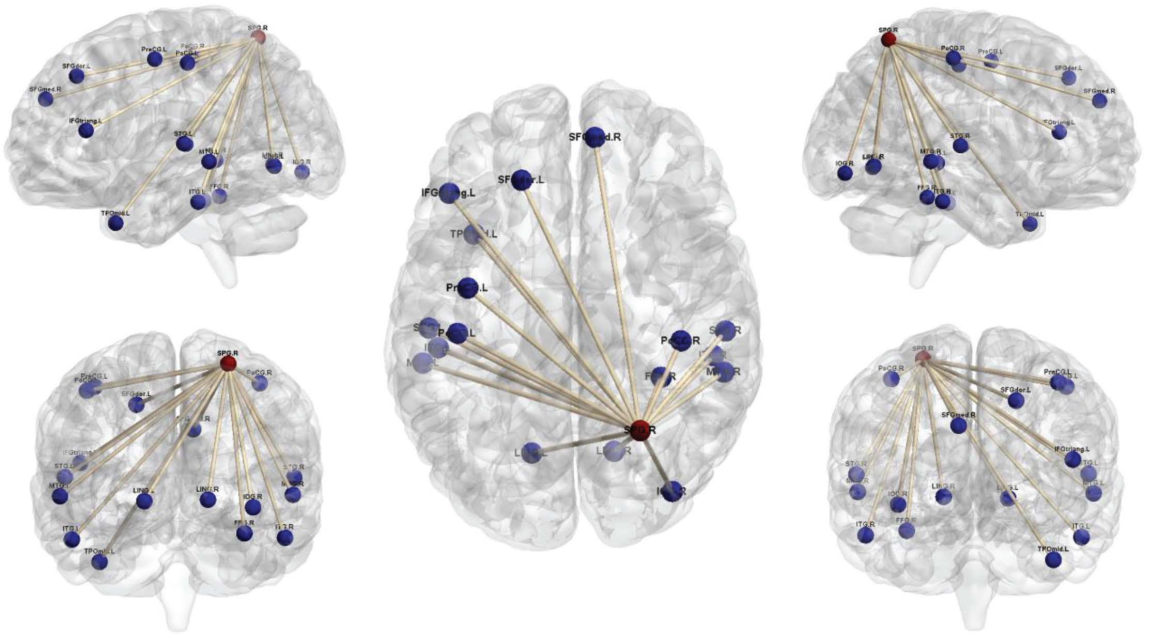

FIGURE 5 | Seed-based functional connectivity maps of right superior parietal lobe (SPG_R) in ULAs based on rs-fMRI. Compared to HC subjects, ULA subjects showed decreased functional connectivity between the seed region in the SPG_R and various brain regions ($p < 0.01$; AlphaSim corrected; voxels > 100). ULA, upper-limb amputee; HC, healthy control.

mALFF values in IPL_R and SPG_R with PLS scores in the ULA group. We can infer that there may be a certain relationship between abnormal activation of the right parietal lobe and PLS. Thus, the function of the right parietal lobe after upper-limb amputation appears to dramatically change, affecting the quality of life of amputees.

Two different brain regions that are anatomically connected are more likely to be functionally connected (Smitha et al., 2017). With the assistance of linear temporal correlation, FC analyses using rs-fMRI data can establish that two spatially separate ROIs are connected functionally. These kind of data make it possible to analyze and understand the occurrence and development of a brain disorder to some extent (Park et al., 2018).

Through seed-based whole-brain FC calculations we found that IPL_R and SPG_R regions in ULAs exhibit decreased functional connections with many areas throughout the brain, including lingual area, precentral area, frontal area, insula area, among others (**Figures 4**, **5**). Related studies on post-amputation changes corroborate our finding that remodeling of brain function is not limited only to local sensorimotor areas in the brain that represent the respective limb (Makin et al., 2015; Zhang et al., 2018; Molina-Rueda et al., 2019). How might these widespread changes be manifest behaviorally?

Amputee patients with a body image disorder often have reduced sensorimotor function, emotional disorders, and compromised social skills (Ko et al., 2015). The present study showed that the occipital lobe, which is involved in the expression of body image disorders, has varying degrees of reduced FC with brain areas that control sensorimotor functions and brain areas that are involved in depression and social emotions. Thus, upper-limb amputation is more than simply removal of a limb. When we did correlation analyses, we found that there are significant negative correlations between the mALFF values of SPG_R and BDI scores in amputees (see **Figure 3C**). We speculate that the depression scores may be related to a reduction in functional connections between SPG_R and frontal areas, because the dorsolateral superior frontal gyrus is the most important brain area associated with depression. These findings have important implications for rehabilitation. When aiming to improve remodeling of local brain areas related to the missing limb representation, it is also important to consider how to maintain FC of more remote brain areas involved in other cognitive and emotional functions affected indirectly by the amputation.

Our study has certain limitations that should be considered when interpreting the results. First, there was a limited number of subjects due to difficulty in recruiting ULAs. Of course, in future studies, more efforts will be made to recruit more upper limb amputees, so that the time and length of amputation can be effectively and reliably controlled. Second, selection bias may be present, because amputees self-selected to participate, meaning that this cooperation may relate to higher social adaptability. Third, physiological noise, such as respiratory and heartbeat fluctuations, may have influenced the stability of the rs-fMRI signals during scanning. However, we have no reason to believe that this variable would be systematically distributed to either the experimental or control group. Taken together, these limitations mean that large-scale longitudinal studies are needed for studying

resting-state brain function in brain regions of patients with upper-limb amputation.

CONCLUSION

Our investigation of the functional organization of parietal lobes in ULAs suggests that post-amputation reorganization is a complex phenomenon that includes functional reorganization in local areas of the respective cortical limb representations and in the degree of FC across wide areas of the brain. With further research, these results provide a reference for directing postoperative rehabilitation of not only upper-limb amputation patients but also perhaps a "road map" for investigations of other types of amputation.

DATA AVAILABILITY STATEMENT

The raw data supporting the conclusions of this article will be made available by the authors, without undue reservation.

ETHICS STATEMENT

The studies involving human participants were reviewed and approved by Ethics Committee of Affiliated Sixth People's Hospital of Shanghai Jiao Tong University of China (approval no. 2017-034). The patients/participants provided their written informed consent to participate in this study.

AUTHOR CONTRIBUTIONS

XZ was responsible for study design and manuscript revision. BB and HW were responsible for data collection and analysis. BB was responsible for manuscript writing. All authors critically reviewed the content of the manuscript and read and approved the final manuscript.

FUNDING

This study was supported by Shanghai Municipal Education Commission-Gaofeng Clinical Medicine Grant (grant number 20161429) and National Natural Science Foundation of China (grant number 81974331).

REFERENCES

Ahmed, A., Bhatnagar, S., Mishra, S., Khurana, D., Joshi, S., and Ahmad, S. M. (2017). Prevalence of phantom limb pain, stump pain, and phantom limb sensation among the amputated cancer patients in India: a prospective, observational study. *Indian J. Palliat. Care* 23, 24–35. doi: 10.4103/0973-1075.197944

Armstrong, T. W., Williamson, M. L. C., Elliott, T. R., Jackson, W. T., Kearns, N. T., and Ryan, T. (2019). Psychological distress among persons with upper extremity limb loss. *Br. J. Health Psychol.* 24, 746–763. doi: 10.1111/bjhp.12360

Berlucchi, G., and Vallar, G. (2018). The history of the neurophysiology and neurology of the parietal lobe. *Handb. Clin. Neurol.* 151, 3–30. doi: 10.1016/b978-0-444-63622-5.00001-2

Casale, R., Alaa, L., Mallick, M., and Ring, H. (2009). Phantom limb related phenomena and their rehabilitation after lower limb amputation. *Eur. J. Phys. Rehabil. Med.* 45, 559–566.

Cox, R. W. (1996). AFNI: software for analysis and visualization of functional magnetic resonance neuroimages. *Comput. Biomed. Res.* 29, 162–173. doi: 10.1006/cbmr.1996.0014

Demirdel, S., and Ülger, Ö (2021). Body image disturbance, psychosocial adjustment and quality of life in adolescents with amputation. *Disabil. Health J.* 101068. doi: 10.1016/j.dhjo.2021.101068

Di Pino, G., Guglielmelli, E., and Rossini, M. (2009). Neuroplasticity in amputees: main implications on bidirectional interfacing of cybernetic hand prostheses. *Prog. Neurobiol.* 88, 114–126. doi: 10.1016/j.pneurobio.2009.03.001

Erlenwein, J., Diers, M., Ernst, J., Schulz, F., and Petzke, F. (2021). Clinical updates on phantom limb pain. *Pain Rep.* 6:e888. doi: 10.1097/pr9.0000000000000888

Felleman, D. J., and Van Essen, D. C. (1991). Distributed hierarchical processing in the primate cerebral cortex. *Cereb. Cortex* 1, 1–47. doi: 10.1093/cercor/1.1.1

Flor, H. (2002). Phantom-limb pain: characteristics, causes, and treatment. *Lancet Neurol.* 1, 182–189. doi: 10.1016/s1474-4422(02)00074-1

Flor, H., Mühlnickel, W., Karl, A., Denke, C., Grüsser, S., Kurth, R., et al. (2000). A neural substrate for nonpainful phantom limb phenomena. *Neuroreport* 11, 1407–1411. doi: 10.1097/00001756-200005150-00011

Flor, H., Nikolajsen, L., and Staehelin Jensen, T. (2006). Phantom limb pain: a case of maladaptive CNS plasticity? *Nat. Rev. Neurosci.* 7, 873–881. doi: 10.1038/nrn1991

Foell, J., Bekrater-Bodmann, R., Diers, M., and Flor, H. (2014). Mirror therapy for phantom limb pain: brain changes and the role of body representation. *Eur. J. Pain* 18, 729–739. doi: 10.1002/j.1532-2149.2013.00433.x

Giummarra, M. J., Gibson, S. J., Georgiou-Karistianis, N., and Bradshaw, J. L. (2007). Central mechanisms in phantom limb perception: the past, present and future. *Brain Res. Rev.* 54, 219–232. doi: 10.1016/j.brainresrev.2007.01.009

Hilti, L. M., Hänggi, J., Vitacco, D. A., Kraemer, B., Palla, A., Luechinger, R., et al. (2013). The desire for healthy limb amputation: structural brain correlates and clinical features of xenomelia. *Brain* 136(Pt 1), 318–329. doi: 10.1093/brain/aws316

Jensen, T. S., Krebs, B., Nielsen, J., and Rasmussen, P. (1983). Phantom limb, phantom pain and stump pain in amputees during the first 6 months following limb amputation. *Pain* 17, 243–256. doi: 10.1016/0304-3959(83)90097-0

Kaur, A., and Guan, Y. (2018). Phantom limb pain: a literature review. *Chin. J. Traumatol.* 21, 366–368. doi: 10.1016/j.cjtee.2018.04.006

Ko, C. Y., Chang, Y., Kim, S. B., Kim, S., Kim, G., Ryu, J., et al. (2015). Evaluation of physical and emotional responses to vibrotactile stimulation of the forearm in young adults, the elderly, and transradial amputees. *Physiol. Behav.* 138, 87–93. doi: 10.1016/j.physbeh.2014.10.021

Luza, L. P., Ferreira, E. G., Minsky, R. C., Pires, G. K. W., and da Silva, R. (2020). Psychosocial and physical adjustments and prosthesis satisfaction in amputees: a systematic review of observational studies. *Disabil. Rehabil. Assist. Technol.* 15, 582–589. doi: 10.1080/17483107.2019.1602853

MacIver, K., Lloyd, D. M., Kelly, S., Roberts, N., and Nurmikko, T. (2008). Phantom limb pain, cortical reorganization and the therapeutic effect of mental imagery. *Brain* 131(Pt 8), 2181–2191. doi: 10.1093/brain/awn124

Makin, T. R., Filippini, N., Duff, E. P., Tracey, I., and Johansen-Berg, H. (2015). Network-level reorganisation of functional connectivity following arm amputation. *Neuroimage* 114, 217–225. doi: 10.1016/j.neuroimage.2015.02.067

Makin, T. R., and Flor, H. (2020). Brain (re)organisation following amputation: implications for phantom limb pain. *Neuroimage* 218:116943. doi: 10.1016/j.neuroimage.2020.116943

McDonald, S., Sharpe, L., and Blaszczynski, A. (2014). The psychosocial impact associated with diabetes-related amputation. *Diabet. Med.* 31, 1424–1430. doi: 10.1111/dme.12474

McGeoch, P. D., Brang, D., Song, T., Lee, R. R., Huang, M., and Ramachandran, V. S. (2011). Xenomelia: a new right parietal lobe syndrome. *J. Neurol. Neurosurg. Psychiatry* 82, 1314–1319. doi: 10.1136/jnnp-2011-300224

Mercier, C., Reilly, K. T., Vargas, C. D., Aballea, A., and Sirigu, A. (2006). Mapping phantom movement representations in the motor cortex of amputees. *Brain* 129(Pt 8), 2202–2210. doi: 10.1093/brain/awl180

Molina-Rueda, F., Navarro-Fernández, C., Cuesta-Gómez, A., Alguacil-Diego, I. M., Molero-Sánchez, A., and Carratalá-Tejada, M. (2019). Neuroplasticity modifications following a lower-limb amputation: a systematic review. *PM R* 11, 1326–1334. doi: 10.1002/pmrj.12167

Park, H. J., Friston, K. J., Pae, C., Park, B., and Razi, A. (2018). Dynamic effective connectivity in resting state fMRI. *Neuroimage* 180(Pt B), 594–608. doi: 10.1016/j.neuroimage.2017.11.033

Pomares, G., Coudane, H., Dap, F., and Dautel, G. (2018). Epidemiology of traumatic upper limb amputations. *Orthop. Traumatol. Surg. Res.* 104, 273–276. doi: 10.1016/j.otsr.2017.12.014

Ramachandran, V. S., and Rogers-Ramachandran, D. (2000). Phantom limbs and neural plasticity. *Arch. Neurol.* 57, 317–320. doi: 10.1001/archneur.57.3.317

Roth, M. (1949). Disorders of the body image caused by lesions of the right parietal lobe. *Brain* 72, 89–111. doi: 10.1093/brain/72.1.89

Sadibolova, R., Ferrè, E. R., Linkenauger, S. A., and Longo, M. R. (2019). Distortions of perceived volume and length of body parts. *Cortex* 111, 74–86. doi: 10.1016/j.cortex.2018.10.016

Shirer, W. R., Ryali, S., Rykhlevskaia, E., Menon, V., and Greicius, M. D. (2012). Decoding subject-driven cognitive states with whole-brain connectivity patterns. *Cereb. Cortex* 22, 158–165. doi: 10.1093/cercor/bhr099

Smitha, K. A., Akhil Raja, K., Arun, K. M., Rajesh, P. G., Thomas, B., Kapilamoorthy, T. R., et al. (2017). Resting state fMRI: a review on methods in resting state connectivity analysis and resting state networks. *Neuroradiol. J.* 30, 305–317. doi: 10.1177/1971400917697342

Song, X. W., Dong, Z. Y., Long, X. Y., Li, S. F., Zuo, X. N., Zhu, C. Z., et al. (2011). REST: a toolkit for resting-state functional magnetic resonance imaging data processing. *PLoS One* 6:e25031. doi: 10.1371/journal.pone.0025031

Stover, G., and Prahlow, N. (2020). Residual limb pain: an evidence-based review. *NeuroRehabilitation* 47, 315–325. doi: 10.3233/nre-208005

Tsakiris, M. (2010). My body in the brain: a neurocognitive model of body-ownership. *Neuropsychologia* 48, 703–712. doi: 10.1016/j.neuropsychologia.2009.09.034

Urits, I., Seifert, D., Seats, A., Giacomazzi, S., Kipp, M., Orhurhu, V., et al. (2019). Treatment strategies and effective management of phantom limb-associated pain. *Curr. Pain Headache Rep.* 23:64. doi: 10.1007/s11916-019-0802-0

Van Essen, D. C., Donahue, C. J., Coalson, T. S., Kennedy, H., Hayashi, T., and Glasser, M. F. (2019). Cerebral cortical folding, parcellation, and connectivity in humans, nonhuman primates, and mice. *Proc. Natl. Acad. Sci. U.S.A.* 116, 26173–26180. doi: 10.1073/pnas.1902299116

Varma, P., Stineman, M. G., and Dillingham, T. R. (2014). Epidemiology of limb loss. *Phys. Med. Rehabil. Clin. N. Am.* 25, 1–8. doi: 10.1016/j.pmr.2013.09.001

Wheaton, L. A. (2017). Neurorehabilitation in upper limb amputation: understanding how neurophysiological changes can affect functional rehabilitation. *J. Neuroeng. Rehabil.* 14:41. doi: 10.1186/s12984-017-0256-8

Wolpert, D. M., Goodbody, S. J., and Husain, M. (1998). Maintaining internal representations: the role of the human superior parietal lobe. *Nat. Neurosci.* 1, 529–533. doi: 10.1038/2245

Woodhouse, A. (2005). Phantom limb sensation. *Clin. Exp. Pharmacol. Physiol.* 32, 132–134. doi: 10.1111/j.1440-1681.2005.04142.x

World Medical Association. (2013). World Medical Association declaration of Helsinki: ethical principles for medical research involving human subjects. *Jama* 310, 2191–2194. doi: 10.1001/jama.2013.281053

Xia, M., Wang, J., and He, Y. (2013). BrainNet Viewer: a network visualization tool for human brain connectomics. *PLoS One* 8:e68910. doi: 10.1371/journal.pone.0068910

Yang, N., Waddington, G., Adams, R., and Han, J. (2018). Translation, cultural adaption, and test-retest reliability of Chinese versions of the Edinburgh handedness inventory and waterloo footedness questionnaire. *Laterality* 23, 255–273. doi: 10.1080/1357650x.2017.1357728

Zhang, J., Zhang, Y., Wang, L., Sang, L., Li, L., Li, P., et al. (2018). Brain functional connectivity plasticity within and beyond the sensorimotor network in lower-limb amputees. *Front. Hum. Neurosci.* 12:403. doi: 10.3389/fnhum.2018.00403

Conflict of Interest: The authors declare that the research was conducted in the absence of any commercial or financial relationships that could be construed as a potential conflict of interest.

frontiers in Neuroscience

ORIGINAL RESEARCH
published: 13 September 2021
doi: 10.3389/fnins.2021.742102

Effective Connectivity of Right Amygdala Subregions Predicts Symptom Improvement Following 12-Week Pharmacological Therapy in Major Depressive Disorder

Yang Xiao[1,2,3], Lei Zhao[1,2,3], Donglin Wang[1,2,3], Shao-Wei Xue[1,2,3]*, Zhonglin Tan[4], Zhihui Lan[1,2,3], Changxiao Kuai[1,2,3], Yan Wang[1,2,3], Hanxiaoran Li[1,2,3], Chenyuan Pan[1,2,3], Sufen Fu[1,2,3] and Xiwen Hu[4]*

[1] Center for Cognition and Brain Disorders, The Affiliated Hospital of Hangzhou Normal University, Hangzhou, China, [2] Institutes of Psychological Sciences, Hangzhou Normal University, Hangzhou, China, [3] Zhejiang Key Laboratory for Research in Assessment of Cognitive Impairments, Hangzhou, China, [4] Affiliated Mental Health Center and Hangzhou Seventh People's Hospital, Zhejiang University School of Medicine, Hangzhou, China

OPEN ACCESS

Edited by:
Yajun Ma,
University of California, San Diego, United States

Reviewed by:
Jing Xu,
Shanghai International Studies University, China
Yayan Yin,
Capital Medical University, China

***Correspondence:**
Donglin Wang
wangdl@hznu.edu.cn
Shao-Wei Xue
xuedrm@126.com

Specialty section:
This article was submitted to Brain Imaging Methods, a section of the journal Frontiers in Neuroscience

Received: 15 July 2021
Accepted: 13 August 2021
Published: 13 September 2021

Citation:
Xiao Y, Zhao L, Wang D, Xue S-W, Tan Z, Lan Z, Kuai C, Wang Y, Li H, Pan C, Fu S and Hu X (2021) Effective Connectivity of Right Amygdala Subregions Predicts Symptom Improvement Following 12-Week Pharmacological Therapy in Major Depressive Disorder. Front. Neurosci. 15:742102. doi: 10.3389/fnins.2021.742102

The low rates of treatment response still exist in the pharmacological therapy of major depressive disorder (MDD). Exploring an optimal neurological predictor of symptom improvement caused by pharmacotherapy is urgently needed for improving response to treatment. The amygdala is closely related to the pathological mechanism of MDD and is expected to be a predictor of the treatment. However, previous studies ignored the heterogeneousness and lateralization of amygdala. Therefore, this study mainly aimed to explore whether the right amygdala subregion function at baseline can predict symptom improvement after 12-week pharmacotherapy in MDD patients. We performed granger causality analysis (GCA) to identify abnormal effective connectivity (EC) of right amygdala subregions in MDD and compared the EC strength before and after 12-week pharmacological therapy. The results show that the abnormal EC mainly concentrated on the frontolimbic circuitry and default mode network (DMN). With relief of the clinical symptom, these abnormal ECs also change toward normalization. In addition, the EC strength of right amygdala subregions at baseline showed significant predictive ability for symptom improvement using a regularized least-squares regression predict model. These findings indicated that the EC of right amygdala subregions may be functionally related in symptom improvement of MDD. It may aid us to understand the neurological mechanism of pharmacotherapy and can be used as a promising predictor for symptom improvement in MDD.

Keywords: amygdala, major depressive disorder, subregion, lateralization, granger causality analysis, treatment

INTRODUCTION

Major depressive disorder (MDD) is a widespread and serious mental disease with a range of depressive symptoms and impaired emotional functions as its symbolic features (Hasin et al., 2018; Tottenham et al., 2021). While pharmacological antidepressant therapy is clearly effective, the treatment response is always low and is often hindered by several unsuccessful trials (Saveanu et al., 2015; Kautzky et al., 2021). Considering that treatment prescription based on clinical experience exerts negative effects on occupation, social relationships, and physical health of patients, it is critical that we identify a reliable biological predictor of pharmacotherapy to improve clinical outcome and reduce medical costs (Lam et al., 2016; Fonseka et al., 2018).

Altered functional activities of amygdala were involved in clinical symptoms of MDD, including emotional perception, memory, and reaction, as reported by some meta-analyses (Sergerie et al., 2008; Diener et al., 2012; Miller et al., 2015). As the core of the emotional circuitry in the brain, the amygdala plays a key role in the pathway among emotional feelings and responses (LeDoux, 2000). Various neuroimaging studies have focused on ascertaining the relationship between the functional changes of the amygdala and the changes of clinical symptoms in MDD patients (Arnone, 2019). According to a facial emotion recognition paradigm-based functional magnetic resonance imaging (fMRI) study, MDD patients showed low reactivity in amygdala compared to controls at baseline and increased toward "normalization" after treatment (Ruhé et al., 2012). A resting-state fMRI (R-fMRI) study also reported that antidepressant treatment changed the amygdala abnormal functional connectivity (FC) in adolescents with MDD (Cullen et al., 2016). Notably, these literatures suggested that changes of the amygdala functions may signify neural changes behind pharmacotherapy in MDD, but they ignored the heterogeneousness and lateralization of amygdala (Sah et al., 2003).

Based on cytoarchitectonic characteristics, some researchers (LeDoux, 2000, 2007; Amunts et al., 2005) suggest that the amygdala is composed of three subdivisions: centromedial amygdala (CM), laterobasal amygdala (LB), and superficial amygdala (SF). Recent neurobiological studies have revealed that these three amygdala subregions may have unique connectivity and distinct functional profiles (McGaugh, 2004; Hofmann and Straube, 2019; Michely et al., 2020). The LB subregion is usually viewed as the sensory interface of the amygdala, which is responsible for receiving the sensory input from the thalamus and auditory cortex, mainly including the auditory inputs (LeDoux, 2003). The CM is regarded as the output regions, which play an important role in generating the behavior response for emotion stimulation (Phelps and LeDoux, 2005). It has been found that the SF in the amygdala has connections with the hypothalamus, frontal cortex, and hippocampus and appears to regulate the visceral function related to emotional stimulation (Price, 2003). A study of amygdala subregion function demonstrated that both LB-prefrontal cortex and CM/SF-brainstem connectivity abnormalities exist in MDD (Tang et al., 2019). In another study, MDD exhibited dysfunctional amygdala subregions to frontal cortex circuitry, but no difference was found when using the whole amygdala as seeds (Qiu et al., 2018). These finding indicates that the amygdala has partially separated information processing between amygdala subregions, and it is necessary to divide the amygdala into different subregions. On the other hand, a growing body of studies have emphasized the different roles for the right and left amygdala in emotion processing; that is, there is a lateralized activity pattern of the amygdala (Baas et al., 2004). For instance, some researchers suggested that the right amygdala may be more involved in the analysis of visual information, and it will be activated more strongly when visual stimulation appeared (Markowitsch, 1998). Moreover, the right amygdala is faster, shallower, and more automated than the left amygdala in processing information (Baas et al., 2004). The right amygdala may be the first to participate in emotional analysis and then quickly becomes habituated for negative stimulation (Wright et al., 2001). The main function of habituation is to limit the use of attention resources to stimulations; impaired habitual function will easily lead to depression-related sustained negative emotions and thinking rumination due to a number of negative emotional experiences that cannot be habituated (Wright et al., 2001). Intriguingly, previous studies have revealed more effect on the right amygdala after treatment, hence implying the clinical potential of the right amygdala in therapy (Suslow et al., 2010). To some extent, the aforementioned findings indicate that the analysis of right amygdala subregions is more promising for elucidating the mechanisms of pharmacotherapy.

Effective connectivity (EC) is an effective technique to characterize the brain information flow in the interacting brain regions; furthermore, EC can detect the direction of information and describe the casual influences exerted among different brain regions, which have facilitated the identification of abnormal intrinsic brain activity in various neurological and neuropsychiatric diseases (Deshpande and Hu, 2012). Granger causality analysis (GCA) is a popular method to estimate EC using responses from time-series data in different regions to infer the direction and intensity of the causal influence of regional neural activity (Goebel et al., 2003; Hamilton et al., 2011). Prior studies in MDD treatment have taken advantage of the GCA technique to investigate the effect of electroconvulsive therapy (ECT), and the result indicated that the amygdala subregion EC can be used as a predictor of the treatment effect of ECT (Wang et al., 2017). The information flow of amygdala subregions may underlie the clinical symptom improvement of MDD. Exploring MDD symptom improvement caused by pharmacotherapy in EC of amygdala subregions is clinically meaningful and provides directional information of brain function, which cannot be detected by FC. However, very few studies investigate whether the EC of right amygdala subregions at baseline can predict medication efficacy.

Here, we have three aims: (1) to determine the abnormal EC of right amygdala subregions in MDD patients; (2) to explore the relationship between the variance in EC and symptom improvement before and after 12-week pharmacological treatment using longitudinal analysis; and (3) to predict symptom improvement using the EC strength of right amygdala subregions at baseline. As far as we know, few studies have

focused on the subregions of the right amygdala and using the GCA to investigate whether the EC can effectively predict the symptom improvement in MDD patients. Given some previous evidence in the analysis of the amygdala implicating that the function of the amygdala is linked with antidepressant interventions (Fonseka et al., 2018), we thus hypothesized that pharmacotherapy would normalize the abnormalities in EC of right amygdala subregions, and right amygdala subregion-based EC strength at baseline is able to predict the symptom improvement of MDD patients after 12-week pharmacotherapy.

MATERIALS AND METHODS

Participants and Study Design

A total of 70 MDD patients (age: 26.93 ± 9.14 years, 21 males/49 females) and 43 sex- and age-matched healthy controls (HCs) (age: 29.42 ± 12.56 years, 16 males/27 females) were recruited from the Department of Psychiatry of Hangzhou Seventh People's Hospital and the Department of Psychiatry at The Affiliated Hospital of Hangzhou Normal University. More detailed information of the participants was summarized in **Table 1**. All patients were interviewed by certified psychiatrists, and 24-item Hamilton Rating Scale for Depression (HAMD) was used to assess the severity of depression symptoms. All patients met the following exclusion criteria: (1) currently pregnant or lactating; (2) serious suicidal tendency; (3) severe medical or neurological illness; (4) material dependence, including tobacco, alcohol, or other psychoactive substances; or (5) metallic implants or other contraindications to MRI. All the research procedures were carried out in accordance with the Helsinki Declaration of Ethical Principles and approved by the local Institutional Review Boards of Hangzhou Normal University. All subjects provided written informed IRB-approved consent before participating.

TABLE 1 | Demographic data and group differences.

Characteristics	MDD (Mean ± SD)	HC (Mean ± SD)	$t/\chi 2$ value	p-value
Sex (M/F)	70 (21/49)	43 (16/27)	0.63	0.43[a]
Age (years)	26.93 ± 9.14	29.42 ± 12.56	−1.22	0.23[b]
HAMD scores	28.06 ± 6.67 (70)	11.41 ± 7.09	11.76	<0.001[b]
Before pharmacotherapy	27.78 ± 6.70 (36)			
After pharmacotherapy	11.42 ± 7.09 (36)			
Durations of illness (months)	7.56 ± 12.74			
On-medication (n patients)				
SSRIs	36			

MDD, major depressive disorder; HC, healthy control; SD, standard deviation; M, male; F, female; HAMD, 24-item Hamilton Rating Scale for Depression; SSRIs, selective serotonin reuptake inhibitors.

[a] *The p-value was obtained by a chi-square test.*

[b] *The p-value was obtained by a two-tailed two-sample t-test.*

The study design flowchart is shown in **Figure 1**. The assessment of MDD patients included R-fMRI neural and scale symptom assessment in the current study. Before pharmacotherapy, all patients with MDD and HCs completed resting-state fMRI scan and HAMD scale to get the time series of each voxel in the whole brain and HAMD scores; meanwhile, we used GCA to calculate the EC between the time series of three amygdala subregions and whole brain voxels, and to explore the abnormal EC of right amygdala subregions in the MDD group through between-group comparison. After pretests, MDD patients then began to receive antidepressant treatment with typical selective serotonin reuptake inhibitors (SSRIs). The medication doses were prescribed and adjusted by the treating clinicians according to routine clinical practice and followed the recommended dose ranges. It is worth nothing that we chose the same kind of drugs (SSRIs) to reduce the heterogeneity of antidepressant drugs, which are recognized and close to homogeneous interventions in scientific research. After 12 weeks of treatment, the remaining 36 (51.43%) of the 70 MDD patients were invited to return to enter another identical fMRI scan and HAMD scale; the EC strength and HAMD scores of the MDD group were obtained again, and we performed a longitudinal analysis to explore the changes of EC strength and HAMD scores in pre- and post-test of treatment, respectively. Finally, we used the voxel-wise EC strength of between right amygdala subregions at baseline to predict symptom improvement, which was defined as the changes of HAMD scores (HAMD scores in pre-test – HAMD scores in post-test), through a regularized least-squares regression using the Least Absolute Shrinkage and Selection Operator (LASSO) algorithms-based machine learning approach, and Spearman's rank correlation analysis was used to evaluate the model predictive power. The HC participants did not take any medicine and received only one fMRI scanning.

Image Acquisition and Preprocessing

Baseline imaging data for 70 MDD patients and 43 HCs were collected before pharmacotherapy to determine neural alterations in depressed individuals, and follow-up images of 36 (51.43%) MDD patients were acquired after 12-week pharmacological therapy. Baseline and follow-up imaging data were obtained by a Siemens MAGNETOM Allegra syngo 3.0T MR Scanner (Siemens AG, Medical Solutions, Erlangen, Germany) at the Center for Cognition and Brain Disorders at Hangzhou Normal University. Functional images were collected by using a T2*-weighted gradient-recalled echo-planar-imaging (EPI) sequence, which has the following parameters: 33 axial slices with a slice thickness = 3 mm, repetition time (TR) = 2,000 ms, echo time (TE) = 30 ms, field of view (FOV) = 220 mm × 220 mm, flip angle = 90°, matrix = 64 × 64, and number of total volumes = 240. A high-resolution T1-weighted structural image in the sagittal orientation is obtained by using magnetization-prepared rapid gradient echo (MPRAGE) sequence. The participants were told to relax with their eyes closed but not fall asleep, and keep motionless during the scanning as much as possible.

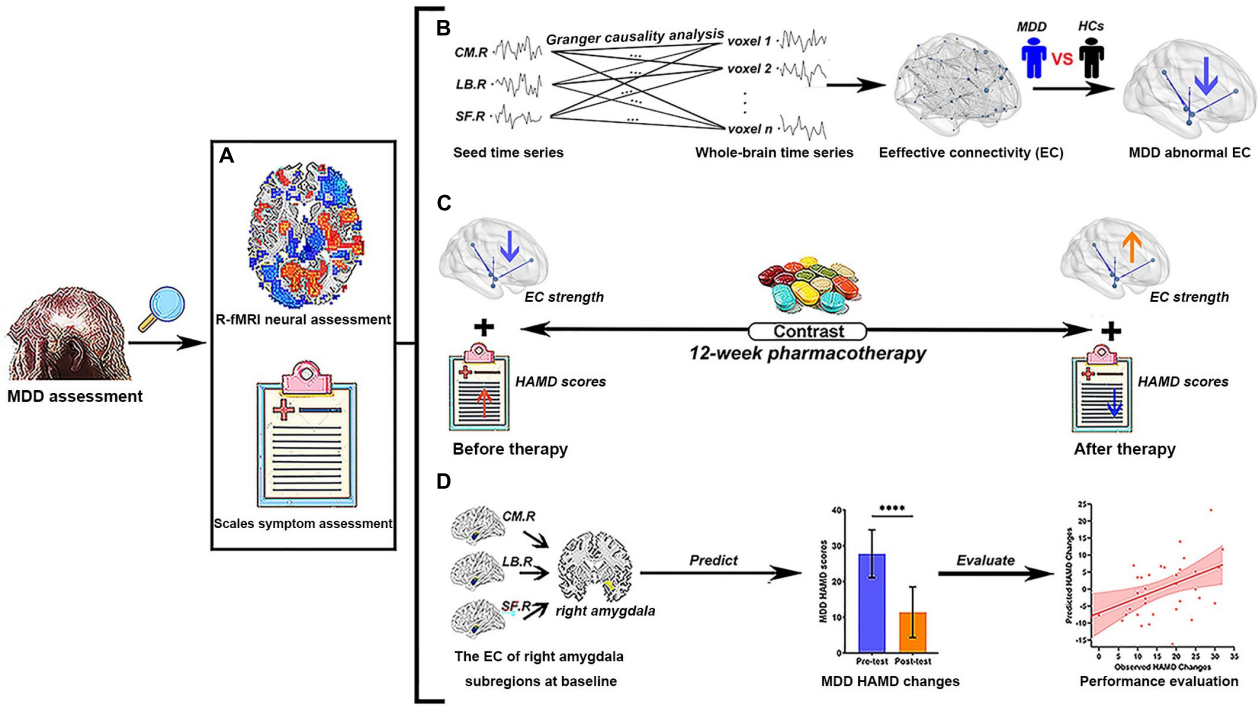

FIGURE 1 | Study flowchart of current research. **(A)** Two different MDD assessment methods were used in the present study. **(B)** The EC analysis of right amygdala subregions using Granger causality analysis. We explore abnormal right amygdala subregion-based EC in MDD patients by the comparison of R-fMRI data between MDD and HCs. **(C)** The contrast of the variance of EC strength and the changes of HAMD scores of MDD patients before and after pharmacotherapy, respectively. **(D)** The voxel-wise EC strength of right amygdala subregions at baseline is taken as feature sets to predict the changes of HAMD scores in MDD patients. The Spearman's rank correlation between predicted HAMD scores changes and observed HAMD scores changes is used to evaluate the prediction power of current predictors. MDD, major depressive disorder; HC, healthy controls; R-fMRI, resting-state functional magnetic resonance imaging; CM, centromedial amygdala; LB, basolateral amygdala; SF, superficial amygdala; EC, effective connectivity; HAMD, 24-item Hamilton Rating Scale for Depression; L, left hemisphere; R, right hemisphere. Different color arrows indicate the change direction of studied indicators compared with the previous stage: cool colors indicate decrease and warm colors indicate increase. $^{****}p < 0.0001$.

The preprocessing of image data was conducted using a combination of the DPABI software[1] (Yan et al., 2016) and a custom code written in MATLAB (The MathWorks, Inc., Natick, MA, United States). The first 10 functional volumes were discarded to stabilize the scanner signals and ensure that the participants adapt themselves to the circumstances. The remaining 230 images were performed by slice timing correction and then realigned to the first volume for head motion correction. The head motion information is recorded by estimating the translations in each direction and the rotations in angular motion about each axis for each of the consecutive volumes. All participants exhibited a maximum displacement of less than 2.5 mm in the x, y, or z directions and an angular motion of less than 2.5° for each axis. To further control the confounding influence of head motion, the framewise displacement (FD) across time points was calculated for further analysis (Power et al., 2012). The residual effects of Friston-24 motion parameters and signals of white matter and cerebrospinal fluid were controlled by linear regression. The corrected images were normalized into standard Montreal Neurological Institute space (resampling voxel size = 3 mm × 3 mm × 3 mm). The images were smoothed with a 6-mm full-width at half-maximum Gaussian kernel. To reduce the effect of the physiological artifacts, we removed several sources of nuisance signals [six motion parameters, white matter signal, and cerebrospinal fluid (CSF) signal] from the smoothed images through linear regression. After band-pass filtering (0.01–0.1 Hz), the "scrubbing" cut method was employed to remove the "bad" time points using Piecewise Cubic Hermite interpolation, and the threshold is 0.5 mm (Liao et al., 2018).

[1]http://www.rfmri.org/

Effective Connectivity Analysis of Right Amygdala Subregions

Following some existing literatures, we defined three right amygdala subregions by using cytoarchitectonically defined probabilistic maps and select the masks of regions of interest (ROIs), including CM, LB, and SF as provided within the SPM Anatomy toolbox. All ROI masks of amygdala subregions will serve as the seeds for subsequent EC analysis. The detailed locations of the selected ROIs are shown in **Figure 2A**. The right amygdala subregions were showed using the BrainNet Viewer package (Xia et al., 2013).

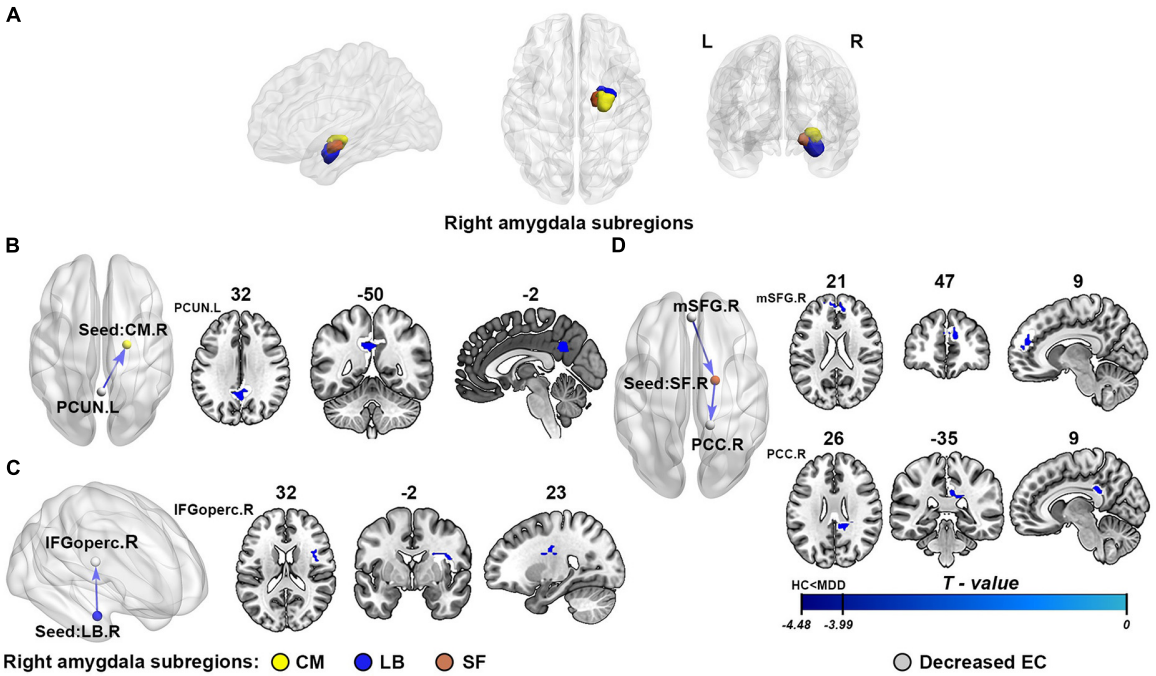

FIGURE 2 | The results of effective connectivity analysis of right amygdala subregions. **(A)** The subregions of the right amygdala: the centromedial amygdala (CM; yellow), laterobasal amygdala (LB; purple), and superficial amygdala (SF; red). **(B–D)** Represent the illustration of the abnormal effective connectivity of MDD in three different right amygdala subregions, respectively: CM, LB, and SF. The cool color arrows indicate significant decreased information flow of target brain regions in MDD. The gray indicates the specific abnormal brain regions, and the yellow/purple/red represents right CM/LB/SF, respectively. EC, effective connectivity; CM, centromedial amygdala; LB, basolateral amygdala; SF, superficial amygdala; PCUN, precuneus; IFGoperc, opercular part of inferior frontal gyrus; mSFG, medial superior frontal gyrus; PCC, posterior cingulate cortex; L, left hemisphere; R, right hemisphere.

In order to acquire the resting-state EC map of each subregion of the right amygdala, the GCA method was used to describe the EC. The GCA is a method based on multiple linear regression, which is used to study whether the current value of time series Y is correctly predicted by a past value of another time series X, and if the combination of the time series X and Y past value could more accurately estimate the time series Y current value than the time series Y past value alone, then time series X has a Granger casual influence on series time Y (Roebroeck et al., 2005). In the present study, voxel-wise GCA was implemented by the DynamicBC toolbox (Liao et al., 2014). The time series of the three right amygdala subregions was defined as the seed time series X, and the time series Y represents the time series of the rest of brain voxels. The residual-based GCA model was carried out to investigate the EC between amygdala subregions and each voxel of the whole brain. Finally, residual-based F was normalized to a Z score using a custom code written in MATLAB for each voxel to improve the normality of F for further statistical analysis (Zang et al., 2012).

Predictive Model Definition and Evaluation

To explore whether the effective connectivity of right amygdala subregions might serve as useful predictors for symptom improvement in MDD, a regularized least-squares regression using LASSO algorithms combining with a nested cross-validation predicted model was employed. We repeatedly analyzed our current data using two different cross-validation strategies, leave-one-out cross-validation (LOOCV) and 10-fold cross-validation (10-fold CV), for internal validation, and added it to the predicted model to improve robustness and repeatability of our conclusions. The predicted model was carried out by using MATLAB; the dependent variable is the HAMD changes, and the independent variables included the EC between one right amygdala subregion and all voxels in the other two subregions at baseline. The LASSO regularization uses the method based on the L1 constraint to perform the selection of correlated variables and prevent unimportant features from resulting in an overfitting problem (Witten and Tibshirani, 2011), and the cross-validation strategy was adopted to improve the generalization ability of the model. The model was fit to the relationship between the EC strength of right amygdala subregions and HAMD changes in each feature set of n participants (where n is the number of participants, n = 36 in this study), which was repeated k times (where k is the number of the fold in cross-validation, including 36 and 10 in the current study). In each cross-validation fold, we set the values of alpha = 1 and use the internal 10-fold CV to select the best LASSO regularization parameter lambda (λ), which controls the number of features selected, and calculated the predicted HAMD changes of the left-out

subject. After the cross-validation, the predicted HAMD changes were achieved, and a Spearman's rank correlation between observed HAMD changes and predicted HAMD changes was used to evaluate the model predictive performance. The non-parametric p-value was calculated based on 10,000 permutation tests.

Statistical Analysis

In baseline MDD patients and HCs, through independent-sample t-test and regressed covariates of age, sex, and head motion, the differences of EC strength in right amygdala subregions between MDD and HC groups were examined. To reduce the type I error, the family-wise error (FWE) correction was conducted using the Gaussian random field (GRF) theory, and the significance threshold of FWE correction was set to $p < 0.001$ at the voxel level and FWE correction at the cluster level to $p < 0.0167$ (0.05/3) through Bonferroni correction.

To obtain the symptom change after pharmacotherapy, we utilized paired-sample t-test to compare the HAMD scores of MDD patients in before and after treatment, and the threshold for significance was set as $p < 0.05$. The HAMD scores of these patients will be used as an index to evaluate the clinical symptom improvement of MDD. Paired-sample t-test was also used to assess the variance of abnormal EC strength in right amygdala subregions found in between-group comparison before and after pharmacotherapy. The statistical threshold was set at $p = 0.05$ and using false discovery rate (FDR) correction for multiple comparisons.

To further determine whether the neural changes are related to symptom improvement and make further analysis meaningful, we performed Pearson's r correlation analysis between the variance of abnormal EC strength and HAMD score changes in the MDD group. The significance level threshold was set at $p < 0.05$.

TABLE 2 | Brain regions with significant differences in right amygdala subregions seeded-EC between MDD and HC.

Seed region	Anatomical region	Cluster size (voxels)	Peak *T*-value	MNI (XYZ) coordinates
Right CM				
Input regions	PCUN.L	55	−3.99	0, −54, 33
Right LB				
Output regions	IFGoperc.R	48	−4.48	39, 0, 21
Right SF				
Input regions	mSFG.R	41	−3.99	9, 48, 21
Output regions	PCC.R	48	−4.41	15, −42, 27

The statistical threshold used the GRF theory [single-tailed, voxel-level p < 0.001, cluster-level p < 0.0167 (0.05/3, Bonferroni correction)]. MNI, Montreal Neurological Institute; CM, centromedial amygdala; LB, basolateral amygdala; SF, superficial amygdala; PCUN, precuneus; IFGoperc, opercular part of inferior frontal gyrus; mSFG, medial superior frontal gyrus; PCC, posterior cingulate cortex; L, left hemisphere; R, right hemisphere.

RESULTS

Effective Connectivity Analysis

As shown in **Figure 2** and **Table 2**, compared with the healthy controls, the patients with MDD showed attenuation of EC strength, mainly including three inhibitory pathways: (1) from the left precuneus (PCUN) to the right CM, (2) from the right LB to the right opercular part of the inferior frontal gyrus (IFGoperc), and (3) from the right medial superior frontal gyrus (mSFG) to the right SF to the right posterior cingulate cortex (PCC). There were no significant between-group differences in the causal outflow from the right CM to other brain regions and the causal inflow from other brain regions to the right LB.

Longitudinal EC Analyses Following 12-Week Pharmacotherapy

In the MDD group, 36 (51.42%) patients completed both before and after treatment clinical assessment and MRI scanning. The primary clinical symptom improvement was assessed by 24-item HAMD scores before and after 12-week pharmacological treatment. Following antidepressant treatment, the results showed that the symptom of MDD has a significant improvement ($t = 11.764$, $p < 0.0001$, paired-sample t-test) after the pharmacotherapy.

The longitudinal results showed the variance of EC strength between pre- and post-test of pharmacotherapy. As shown in **Figure 3A**, through paired-sample t-test, we have found that all abnormal EC of right amygdala subregions had a normalizing effect after treatment. The EC from the right LB to the right IFGoperc ($t = 2.444$, $p = 0.020$) and the EC from the right SF to the right PCC ($t = 2.639$, $p = 0.012$) showed significant differences in pretest and post-test. The variance of EC strength in the remaining connectivity approached significance, which is the EC from the left PCUN to the right CM ($t = 1.942$, $p = 0.060$) and from the right mSFG to the right SF ($t = 1.941$, $p = 0.060$), respectively.

Correlation analysis between the variance of mean EC strength and HAMD score changes is illustrated in **Figure 3B**. We found that improvement in symptoms after 12-week treatment was significantly correlated with the variance of mean EC strength in the EC from the left PCUN to the right CM ($r = -0.357$, $p = 0.038$) and the EC from the right mSFG to the right SF ($r = -0.358$, $p = 0.032$). There was no significant correlation in the EC from the right LB to the right IFGoperc ($r = -0.144$, $p = 0.402$) and the EC from the right SF to the right PCC ($r = -0.203$, $p = 0.234$), but the change direction of them is still consistent with the change direction of symptom improvement.

Predictive Accuracy

Based on the EC of right amygdala subregions at baseline as features, the predicted model yielded significant prediction power. As **Figure 4** shows, the model analysis revealed that the EC in right amygdala subregions exhibited excellent performance in predicting symptom improvement in MDD patients; the

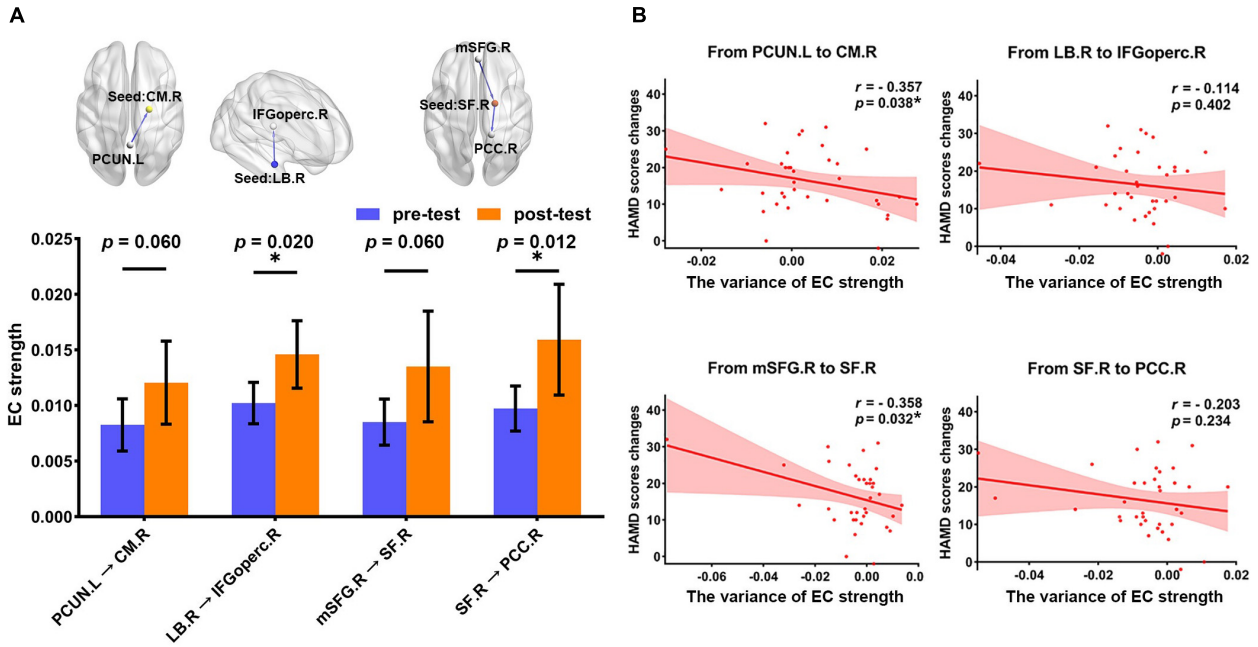

FIGURE 3 | The association of the changes in two different assessment methods between pre- and post-test of pharmacotherapy. **(A)** The histogram shows the variance in the EC strength between pre- and post-test of pharmacotherapy (FDR correction at $p < 0.05$), including the EC from the left PCUN to the right CM ($t = 1.942$, $p = 0.060$), the EC from the right LB to the right IFGoperc ($t = 2.444$, $p = 0.020$), the EC from the right mSFG to the right SF ($t = 1.941$, $p = 0.060$), and the EC from the right SF to the right PCC ($t = 2.639$, $p = 0.012$). *$p < 0.05$. **(B)** Scatter plots for the relationship between HAMD scores changes and the variance of EC strength. The significant correlation was found in the EC from the left PCUN to the right CM ($r = -0.357$, $p = 0.038$) and the EC from the right mSFG to the right SF ($r = -0.358$, $p = 0.032$). *$p < 0.05$. EC, effective connectivity; PCUN, precuneus; CM, centromedial amygdala; LB, basolateral amygdala; IFGoperc, opercular part of inferior frontal gyrus; mSFG, medial superior frontal gyrus; SF, superficial amygdala; PCC, posterior cingulate cortex; HAMD, 24-item Hamilton Rating Scale for Depression; L, left hemisphere; R, right hemisphere.

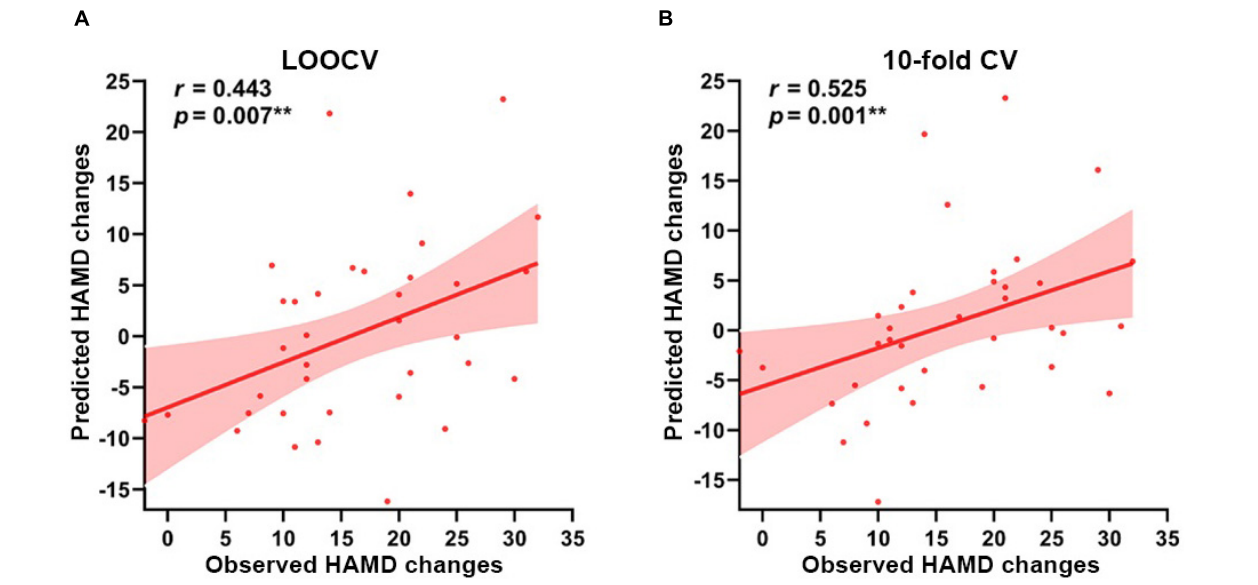

FIGURE 4 | Prediction results based on the EC of right amygdala subregions at baseline for symptom improvement. Scatter plots show the Spearman's rank correlations between the observed HAMD scores changes and predicted HAMD scores changes of all participants in **(A)** LOOCV: $r = 0.443$, permutation $p = 0.007$, and **(B)** 10-fold CV: $r = 0.525$, permutation $p = 0.001$, respectively. **$p < 0.01$. LOOCV, Leave-one-out cross-validation; 10-fold CV, 10-fold cross-validation; HAMD, 24-item Hamilton Rating Scale for Depression.

predicted HAMD changes had a Spearman's rank correlation of $r = 0.443$ with the observed HAMD changes with a nested LOOCV (permutation $p = 0.007$), and Spearman's rank correlation is $r = 0.525$ in a nested 10-fold CV (permutation $p = 0.001$).

DISCUSSION

In the current study, we investigated the abnormal EC patterns of right amygdala subregions in MDD based on GCA. Three abnormal EC pathways of right amygdala subregions were identified in baseline MDD patients. With the relief of symptoms, these abnormal connections are also normalized following 12-week pharmacological therapy, and correlation analysis results revealed that the variance of EC strength is related to the change of HAMD scores. More importantly, individual depressive symptom improvement can be predicted using the EC of right amygdala subregions at baseline.

Abnormal Effective Connectivity

The GCA provided a new tool for exploring the EC, and emerging reports have suggested that GCA can effectively identify the directed functional interactions between brain regions (Chen et al., 2009). We found the abnormal EC of depressed individuals mainly in three significant inhibitory pathways, that is, from the left PCUN to the right CM, from the right LB to the right opercular part of IFG, and from the right mSFG to the right SF to the right PCC. These abnormal brain regions provided preliminary evidence for the neural substrate of clinical symptom, which promotes further analysis.

Previous evidence suggested that the mSFG plays an important role in emotional processing and response and has been implicated in some emotional disorders (Phan et al., 2003). For example, our previous research found that the FC between mSFG and medial orbitofrontal cortex (mOFC) subregions is correlated with anxiety in healthy male adults (Xue et al., 2018). The activity of the mSFG is related to the amygdala, which suggested that the extent of coupling between the mSFG and the amygdala associated with emotional response to negative scenes (Wu et al., 2016). The SF of the amygdala is also considered to be involved in social and affective information processing (Adolphs, 2008). The finding of inhibitory connection from the mSFG to the SF supported the existing theories suggesting that the neural mechanism of depression has extensive involvement within frontolimbic circuitry (Lai, 2019). Besides, our results also found that the function of PCC is inhibited by the right SF, and the right CM is inhibited by the PCUN in MDD patients. The PCC and the adjacent PCUN are the main components of the default mode network (DMN), a network of brain regions that are more active when the brain is at rest. A large number of neuroimaging studies pointed out that the DMN is closely associated with neuropathological mechanism of MDD (Kaiser et al., 2015). Consistent with our results, the abnormal connectivity between the amygdala and the PCC or the PCUN has been found in different MDD populations (Cullen et al., 2016). Furthermore, similar to the function of the right amygdala, the PCC and the PCUN also have the advantages in visual imaging processing (Shen et al., 2015). Due to the fact that the right CM mediates behavioral responses to potentially harmful stimuli, taken together, one interpretation of our findings is that the damage of frontolimbic circuitry may inhibit the normal function of the DMN in emotional processing for external stimulus, and then inhibiting the CM nucleus of the right amygdala makes correct emotional responses and cannot habituate from a negative emotional stimulus up to wrong emotional responses, such as sustaining negative emotions and thinking rumination. Additionally, the IFG is involved in relaying top-down cognitive inputs, which was shown to be involved in the updating of task representations and to be activated commonly in multiple cognitive tasks (Derrfuss et al., 2005; Hampshire et al., 2010). The IFG has connected with the limbic system and played a key role in cognitive-emotional integration and continuous behavioral monitoring (Gao et al., 2016). We speculated that the LB nucleus of the right amygdala, as the input region, may be due to inadequate high-level cognitive guidance, resulting in lower-level emotional cognitive processing disorders.

Longitudinal EC Analyses Following 12-Week Pharmacotherapy

The normalization of aberrant right amygdala subregions connectivity may indicate that the EC of right amygdala subregions correlated with the depressive symptoms. The longitudinal analyses following 12-week pharmacotherapy revealed that the depressive symptoms and hypoconnectivities of right amygdala subregions were ameliorated with pharmacotherapy; in other words, the pharmacotherapy may relief the symptom of depression by improving the right amygdala subregion brain function. This claim echoed previous studies, which revealed that the pharmacological treatment improved the SF nucleus function for emotion and social information processing and the ability of the CM nucleus to make correct emotion responses (Phan et al., 2003). Another study suggested that pharmacological antidepressant effects can be measured in terms of some increase of frontolimbic connectivity and that these effects were most clearly demonstrated by the change of amygdala connections (Chen et al., 2008). Considering that mSFG and IFGoperc are part of frontolimbic circuitry and are critical for the pathological mechanism of MDD, SSRIs therapy may, in part, improve depressive symptoms by restoring the connectivity between the amygdala and these regions. Some analyses exploring the improvement of symptom predictors for pharmacotherapy have found the potential of the PCC as predictive of improved response (Rizvi et al., 2013). Lower baseline EC between the CM and the PCC exhibited increased strength after treatment in our study, which implies that this connectivity was associated with treatment response to SSRIs.

Correlation analysis further supports our conclusion, which shows that depressive symptom improvement is associated with the change of brain function or neuroplasticity. The relationship between MDD improvement and the PCUN component of the DMN has been identified, which is consistent with previous reports of the DMN being associated with symptom

improvement (Fonseka et al., 2018). The PCUN and the PCC located in the midline cortical regions of the DMN mediate self-referential processing; they may have excessive involvement in information processing in MDD (Li et al., 2013). What is more, SSRI selective altered intrinsic regional DMN connectivity has also been found in previous research (van de Ven et al., 2013). The result of paired-sample *t*-test between before and after treatment shows that the EC of the IFGoperc and the PCC with right amygdala subregions was reconfigured under the influence of treatment, although no significant corrections were found there, which is related to the mechanism of pharmacotherapy. MDD is a complex mental disease, which involves a variety of abnormal brain functions (Furey et al., 2013). The HAMD score only reflects the part of clinical symptoms in MDD patients, and there are still many potential abnormalities in MDD that may be changed by treatment. In addition, due to the internal heterogeneity of mental illness itself and the influence of external environment, the clinical diagnosis is often not as detailed as research projects (Gao et al., 2018). Some hidden anomalies that are not related to the HAMD scores in MDD could be found by objective brain imaging measurements. This is because the function of the human brain, which is characterized by complex spatial structure, may have some complex non-linear relationship with clinical scores that cannot be found in correlation analysis (Cohen et al., 2020). Therefore, their changes are still meaningful for better understanding of the neural mechanism of MDD treatment. These results indicated that right amygdala subregion function was suggested to be relevant to characterize the neurobiology of antidepressant medications and may be useful in guiding treatment selection in future studies.

Predictive Power of Effective Connectivity

There is no doubt that the etiopathogenesis of depression has its biological basis (Ge et al., 2020). It is important to identify the neurobiological mechanisms of pharmacotherapy in MDD, so that this knowledge can be applied to improve clinical treatment. Great progress has been made in the study of human brain dysfunction caused by depression or MDD using MRI (Dosenbach et al., 2010). However, whether these human brain functional indicators contain enough information to help us predict the therapeutic improvement remains a big unknown. Along this line, many studies try to explore useful therapeutic predictors using difference MRI neuroimaging makers and machine-learning algorithms (Jiang et al., 2018). For example, a previous study indicated that the right amygdala was associated with MDD, and the right amygdala connectivity predicted the psychotherapy improvement in depressed adolescents (Straub et al., 2017). In our study, our results also demonstrated the predictive ability of EC of right amygdala subregions at baseline for symptom improvement after 12-week pharmacological therapy in MDD. Consistent with our hypothesis, these findings are suggestive of the fact that right amygdala subregion-seeded EC may aid in understanding mechanisms of pharmacotherapy in MDD and holds the promise for future research to improve the clinical outcomes. Since emotional dysfunctions are the main symptom of MDD, it makes sense to predict the symptom improvement from the amygdala at baseline, and many studies have discovered the potential of the amygdala as a predictor for pharmacotherapy (Furey et al., 2013; Williams et al., 2015). Moreover, the correlation between roles of the right amygdala for visual emotional stimuli and MDD symptoms improvement is supported by some studies (Furey et al., 2013; Szczepanik et al., 2016).

Employing internal validation procedures, we built our predictive models based on two different cross-validation methods. Encouragingly, the results are robust and still support our conclusion. From the methodological principle of GCA, the "scrubbing" in data preprocessing removes the "bad" time points and may affect the evaluation results of GCA. We thus repeated all analyses without "scrubbing" in the preprocessing analysis. Our findings were similar, and the model maintains good prediction performance. The high reproducibility shows the feasibility of the EC in the right amygdala subregions for predicting the symptom improvement of MDD. Predictive data mining has become very popular in neuroimaging research, especially in the study of mental diseases (Meng et al., 2017). The ultimate purpose of neuroimaging diagnosis is to predict the symptom of patients, and our results strengthen the role of the amygdala in the pathophysiology of MDD and its importance in model mood dysregulation and as a new therapeutic target.

Limitation

Several limitations warrant further consideration. First, the number of participants was small, and not all subjects have completed the pre- and post-test, which may limit the statistical power in finding the abnormal EC brain regions and challenge our results. Therefore, a larger number of sample sizes and measures to prevent the loss of subjects are needed in further studies. Second, there is internal heterogeneity of SSRIs in the pharmacological drugs among patients for the current dataset. However, only the baseline data of R-fMRI have been used to predict the symptom improvement, and these data are not related to heterogeneous pharmacotherapy. Consistent with our dataset and previous studies on the prediction of the MDD symptom improvement treated with heterogenous antidepressant drugs, neuroimaging markers also perform effective predictive capacity (Shen et al., 2015), and a large-sample study shows that there are only subtle differences between different pharmacological treatment modalities (Stassen et al., 2007). Nevertheless, to control the heterogeneity of therapy medicine is needed for future research. Third, the dosages of drugs could affect the experimental results. As the longitudinal study leads to the loss of participant data, only 15 of the 36 participants in our remaining data have complete information about the dosages of drugs. We repeated our analysis by using the EC in right amygdala subregions of these 15 subjects as features and incorporate the drug dose as a covariant in the predicted model. Fortunately, the EC of right amygdala subregions still significant predict the symptom improvement. The high reproducibility of our findings indicated the reliability of right amygdala subregions-based predictor for treatment outcomes, but a more complete

large sample size should be used to verify this conclusion in future research. Finally, the current study revealed that the EC in right amygdala subregions significantly predicts the symptom improvement of MDD patients after 12-week pharmacological therapy. However, apart from the treatment improvement after 12-week pharmacotherapy, an important topic in the future is whether the symptom improvement of other treatment courses can be predicted.

CONCLUSION

The current study demonstrated the abnormal right amygdala subregion-seeded EC, and the results mainly concentrated in the frontolimbic circuits and the DMN. The longitudinal analysis found that the symptom improvement caused by antidepressant medications is associated with the change of mean EC strength of right amygdala subregions in MDD patients. Importantly, the EC in right amygdala subregions at baseline significantly predicts the symptom improvement of pharmacotherapy. The function of right amygdala subregions may contribute to a better understanding of the neurobiological mechanism of pharmacotherapy. Meanwhile, these results also provided new supporting evidence for the application of neuroimaging techniques in the treatment outcome prediction and thus guide more individualized treatment for MDD patients.

DATA AVAILABILITY STATEMENT

The raw data supporting the conclusions of this article will be made available by the authors, without undue reservation.

ETHICS STATEMENT

The studies involving human participants were reviewed and approved by the Institutional Review Boards of Hangzhou Normal University. The patients/participants provided their written informed consent to participate in this study.

AUTHOR CONTRIBUTIONS

YX, DW, and S-WX had full access to all of the data in the study and take responsibility. S-WX, YX, DW, and ZT proposed the study concept and designed the experiments. YX, S-WX, and LZ drafted the manuscript. YX, S-WX, LZ, and ZL modified the manuscript for important intellectual content. YX, CK, HL, and CP were responsible for statistical analysis. DW and S-WX obtained funding. YX, XH, SF, and YW were responsible for administrative, technical, or material support. All authors participated in acquisition, analysis, or interpretation of data and contributed to the article and approved the final manuscript.

FUNDING

This work was supported by the Key Medical Disciplines of Hangzhou, the Natural Science Foundation of Zhejiang Province (LY17H180007), the National Natural Science Foundation of China (81271503), and Hangzhou Medical Key Discipline and the cultivation project of the province-leveled preponderant characteristic discipline in the College of Education (18JYXK036) of Hangzhou Normal University.

ACKNOWLEDGMENTS

The authors thank the teachers and students who assisted in the experiment and data collection.

REFERENCES

Adolphs, R. (2008). Fear, faces, and the human amygdala. *Curr. Opin. Neurobiol.* 18, 166–172. doi: 10.1016/j.conb.2008.06.006

Amunts, K., Kedo, O., Kindler, M., Pieperhoff, P., Mohlberg, H., Shah, N. J., et al. (2005). Cytoarchitectonic mapping of the human amygdala, hippocampal region and entorhinal cortex: intersubject variability and probability maps. *Anat. Embryol. (Berl.).* 210, 343–352. doi: 10.1007/s00429-005-0025-5

Arnone, D. (2019). Functional MRI findings, pharmacological treatment in major depression and clinical response. *Prog. Neuropsychopharmacol. Biol. Psychiatry* 91, 28–37. doi: 10.1016/j.pnpbp.2018.08.004

Baas, D., Aleman, A., and Kahn, R. S. (2004). Lateralization of amygdala activation: a systematic review of functional neuroimaging studies. *Brain Res. Brain Res. Rev.* 45, 96–103. doi: 10.1016/j.brainresrev.2004.02.004

Chen, C. H., Suckling, J., Ooi, C., Fu, C. H., Williams, S. C., Walsh, N. D., et al. (2008). Functional coupling of the amygdala in depressed patients treated with antidepressant medication. *Neuropsychopharmacology* 33, 1909–1918. doi: 10.1038/sj.npp.1301593

Chen, H., Yang, Q., Liao, W., Gong, Q., and Shen, S. (2009). Evaluation of the effective connectivity of supplementary motor areas during motor imagery using granger causality mapping. *Neuroimage* 47, 1844–1853. doi: 10.1016/j.neuroimage.2009.06.026

Cohen, A. D., Chen, Z., Parker Jones, O., Niu, C., and Wang, Y. (2020). Regression-based machine-learning approaches to predict task activation using resting-state fMRI. *Hum. Brain Mapp.* 41, 815–826. doi: 10.1002/hbm.24841

Cullen, K. R., Klimes-Dougan, B., Vu, D. P., Westlund Schreiner, M., Mueller, B. A., Eberly, L. E., et al. (2016). Neural correlates of antidepressant treatment response in adolescents with major depressive disorder. *J. Child Adolesc. Psychopharmacol.* 26, 705–712. doi: 10.1089/cap.2015.0232

Derrfuss, J., Brass, M., Neumann, J., and von Cramon, D. Y. (2005). Involvement of the inferior frontal junction in cognitive control: meta-analyses of switching and Stroop studies. *Hum. Brain Mapp.* 25, 22–34. doi: 10.1002/hbm.20127

Deshpande, G., and Hu, X. (2012). Investigating effective brain connectivity from fMRI data: past findings and current issues with reference to granger causality analysis. *Brain Connect.* 2, 235–245. doi: 10.1089/brain.2012.0091

Diener, C., Kuehner, C., Brusniak, W., Ubl, B., Wessa, M., and Flor, H. (2012). A meta-analysis of neurofunctional imaging studies of emotion and cognition in major depression. *Neuroimage* 61, 677–685. doi: 10.1016/j.neuroimage.2012.04.005

Dosenbach, N. U., Nardos, B., Cohen, A. L., Fair, D. A., Power, J. D., Church, J. A., et al. (2010). Prediction of individual brain maturity using fMRI. *Science* 329, 1358–1361. doi: 10.1126/science.1194144

Fonseka, T. M., MacQueen, G. M., and Kennedy, S. H. (2018). Neuroimaging biomarkers as predictors of treatment outcome in major depressive disorder. *J. Affect. Disord.* 233, 21–35. doi: 10.1016/j.jad.2017.10.049

Furey, M. L., Drevets, W. C., Hoffman, E. M., Frankel, E., Speer, A. M., and Zarate, C. A. Jr. (2013). Potential of pretreatment neural activity in the visual cortex during emotional processing to predict treatment response to scopolamine in major depressive disorder. *JAMA Psychiatry* 70, 280–290. doi: 10.1001/2013.jamapsychiatry.60

Gao, Q., Zou, K., He, Z., Sun, X., and Chen, H. (2016). Causal connectivity alterations of cortical-subcortical circuit anchored on reduced hemodynamic response brain regions in first-episode drug-naïve major depressive disorder. *Sci. Rep.* 6:21861. doi: 10.1038/srep21861

Gao, S., Calhoun, V. D., and Sui, J. (2018). Machine learning in major depression: from classification to treatment outcome prediction. *CNS Neurosci. Ther.* 24, 1037–1052. doi: 10.1111/cns.13048

Ge, R., Downar, J., Blumberger, D. M., Daskalakis, Z. J., and Vila-Rodriguez, F. (2020). Functional connectivity of the anterior cingulate cortex predicts treatment outcome for rTMS in treatment-resistant depression at 3-month follow-up. *Brain Stimul.* 13, 206–214. doi: 10.1016/j.brs.2019.10.012

Goebel, R., Roebroeck, A., Kim, D. S., and Formisano, E. (2003). Investigating directed cortical interactions in time-resolved fMRI data using vector autoregressive modeling and granger causality mapping. *Magn. Reson. Imaging* 21, 1251–1261. doi: 10.1016/j.mri.2003.08.026

Hamilton, J. P., Chen, G., Thomason, M. E., Schwartz, M. E., and Gotlib, I. H. (2011). Investigating neural primacy in major depressive disorder: multivariate granger causality analysis of resting-state fMRI time-series data. *Mol. Psychiatry* 16, 763–772. doi: 10.1038/mp.2010.46

Hampshire, A., Chamberlain, S. R., Monti, M. M., Duncan, J., and Owen, A. M. (2010). The role of the right inferior frontal gyrus: inhibition and attentional control. *Neuroimage* 50, 1313–1319. doi: 10.1016/j.neuroimage.2009.12.109

Hasin, D. S., Sarvet, A. L., Meyers, J. L., Saha, T. D., Ruan, W. J., Stohl, M., et al. (2018). Epidemiology of adult DSM-5 major depressive disorder and its specifiers in the United States. *JAMA Psychiatry* 75, 336–346. doi: 10.1001/jamapsychiatry.2017.4602

Hofmann, D., and Straube, T. (2019). Resting-state fMRI effective connectivity between the bed nucleus of the stria terminalis and amygdala nuclei. *Hum. Brain Mapp.* 40, 2723–2735. doi: 10.1002/hbm.24555

Jiang, R., Abbott, C. C., Jiang, T., Du, Y., Espinoza, R., Narr, K. L., et al. (2018). SMRI Biomarkers predict electroconvulsive treatment outcomes: accuracy with independent data sets. *Neuropsychopharmacology* 43, 1078–1087. doi: 10.1038/npp.2017.165

Kaiser, R. H., Andrews-Hanna, J. R., Wager, T. D., and Pizzagalli, D. A. (2015). Large-scale network dysfunction in major depressive disorder: a meta-analysis of resting-state functional connectivity. *JAMA Psychiatry* 72, 603–611. doi: 10.1001/jamapsychiatry.2015.0071

Kautzky, A., Möller, H. J., Dold, M., Bartova, L., Seemüller, F., Laux, G., et al. (2021). Combining machine learning algorithms for prediction of antidepressant treatment response. *Acta Psychiatr. Scand.* 143, 36–49. doi: 10.1111/acps.13250

Lai, C. H. (2019). The neural markers of MRI to differentiate depression and panic disorder. *Prog. Neuropsychopharmacol. Biol. Psychiatry* 91, 72–78. doi: 10.1016/j.pnpbp.2018.04.013

Lam, R. W., McIntosh, D., Wang, J., Enns, M. W., Kolivakis, T., Michalak, E. E., et al. (2016). Canadian network for mood and anxiety treatments (CANMAT) 2016 clinical guidelines for the management of adults with major depressive disorder: section 1. disease burden and principles of care. *Can. J. Psychiatry* 61, 510–523. doi: 10.1177/0706743716659416

LeDoux, J. (2003). The emotional brain, fear, and the amygdala. *Cell. Mol. Neurobiol.* 23, 727–738. doi: 10.1023/a:1025048802629

LeDoux, J. (2007). The amygdala. *Curr. Biol.* 17, R868–R874. doi: 10.1016/j.cub.2007.08.005

LeDoux, J. E. (2000). Emotion circuits in the brain. *Annu. Rev. Neurosci.* 23, 155–184. doi: 10.1146/annurev.neuro.23.1.155

Li, B., Liu, L., Friston, K. J., Shen, H., Wang, L., Zeng, L. L., et al. (2013). A treatment-resistant default mode subnetwork in major depression. *Biol. Psychiatry* 74, 48–54. doi: 10.1016/j.biopsych.2012.11.007

Liao, W., Li, J., Duan, X., Cui, Q., Chen, H., and Chen, H. (2018). Static and dynamic connectomics differentiate between depressed patients with and without suicidal ideation. *Hum. Brain Mapp.* 39, 4105–4118. doi: 10.1002/hbm.24235

Liao, W., Wu, G. R., Xu, Q., Ji, G. J., Zhang, Z., Zang, Y. F., et al. (2014). DynamicBC: a MATLAB toolbox for dynamic brain connectome analysis. *Brain Connect.* 4, 780–790. doi: 10.1089/brain.2014.0253

Markowitsch, H. J. (1998). Differential contribution of right and left amygdala to affective information processing. *Behav. Neurol.* 11, 233–244. doi: 10.1155/1999/180434

McGaugh, J. L. (2004). The amygdala modulates the consolidation of memories of emotionally arousing experiences. *Annu. Rev. Neurosci.* 27, 1–28. doi: 10.1146/annurev.neuro.27.070203.144157

Meng, X., Jiang, R., Lin, D., Bustillo, J., Jones, T., Chen, J., et al. (2017). Predicting individualized clinical measures by a generalized prediction framework and multimodal fusion of MRI data. *Neuroimage* 145(Pt B), 218–229. doi: 10.1016/j.neuroimage.2016.05.026

Michely, J., Rigoli, F., Rutledge, R. B., Hauser, T. U., and Dolan, R. J. (2020). Distinct processing of aversive experience in amygdala subregions. *Biol. Psychiatry Cogn. Neurosci. Neuroimaging* 5, 291–300. doi: 10.1016/j.bpsc.2019.07.008

Miller, C. H., Hamilton, J. P., Sacchet, M. D., and Gotlib, I. H. (2015). Meta-analysis of functional neuroimaging of major depressive disorder in youth. *JAMA Psychiatry* 72, 1045–1053. doi: 10.1001/jamapsychiatry.2015.1376

Phan, K. L., Taylor, S. F., Welsh, R. C., Decker, L. R., Noll, D. C., Nichols, T. E., et al. (2003). Activation of the medial prefrontal cortex and extended amygdala by individual ratings of emotional arousal: a fMRI study. *Biol. Psychiatry* 53, 211–215. doi: 10.1016/s0006-3223(02)01485-3

Phelps, E. A., and LeDoux, J. E. (2005). Contributions of the amygdala to emotion processing: from animal models to human behavior. *Neuron* 48, 175–187. doi: 10.1016/j.neuron.2005.09.025

Power, J. D., Barnes, K. A., Snyder, A. Z., Schlaggar, B. L., and Petersen, S. E. (2012). Spurious but systematic correlations in functional connectivity MRI networks arise from subject motion. *Neuroimage* 59, 2142–2154. doi: 10.1016/j.neuroimage.2011.10.018

Price, J. L. (2003). Comparative aspects of amygdala connectivity. *Ann. N. Y. Acad. Sci.* 985, 50–58. doi: 10.1111/j.1749-6632.2003.tb07070.x

Qiu, L., Xia, M., Cheng, B., Yuan, L., Kuang, W., Bi, F., et al. (2018). Abnormal dynamic functional connectivity of amygdalar subregions in untreated patients with first-episode major depressive disorder. *J. Psychiatry Neurosci.* 43, 262–272. doi: 10.1503/jpn.170112

Rizvi, S. J., Salomons, T. V., Konarski, J. Z., Downar, J., Giacobbe, P., McIntyre, R. S., et al. (2013). Neural response to emotional stimuli associated with successful antidepressant treatment and behavioral activation. *J. Affect. Disord.* 151, 573–581. doi: 10.1016/j.jad.2013.06.050

Roebroeck, A., Formisano, E., and Goebel, R. (2005). Mapping directed influence over the brain using granger causality and fMRI. *Neuroimage* 25, 230–242. doi: 10.1016/j.neuroimage.2004.11.017

Ruhé, H. G., Booij, J., Veltman, D. J., Michel, M. C., and Schene, A. H. (2012). Successful pharmacologic treatment of major depressive disorder attenuates amygdala activation to negative facial expressions: a functional magnetic resonance imaging study. *J. Clin. Psychiatry* 73, 451–459. doi: 10.4088/JCP.10m06584

Sah, P., Faber, E. S., Lopez De Armentia, M., and Power, J. (2003). The amygdaloid complex: anatomy and physiology. *Physiol. Rev.* 83, 803–834. doi: 10.1152/physrev.00002.2003

Saveanu, R., Etkin, A., Duchemin, A. M., Goldstein-Piekarski, A., Gyurak, A., Debattista, C., et al. (2015). The international study to predict optimized treatment in depression (iSPOT-D): outcomes from the acute phase of antidepressant treatment. *J. Psychiatr. Res.* 61, 1–12. doi: 10.1016/j.jpsychires.2014.12.018

Sergerie, K., Chochol, C., and Armony, J. L. (2008). The role of the amygdala in emotional processing: a quantitative meta-analysis of functional neuroimaging studies. *Neurosci. Biobehav. Rev.* 32, 811–830. doi: 10.1016/j.neubiorev.2007.12.002

Shen, Y., Yao, J., Jiang, X., Zhang, L., Xu, L., Feng, R., et al. (2015). Sub-hubs of baseline functional brain networks are related to early improvement following two-week pharmacological therapy for major depressive disorder. *Hum. Brain Mapp.* 36, 2915–2927. doi: 10.1002/hbm.22817

Stassen, H. H., Angst, J., Hell, D., Scharfetter, C., and Szegedi, A. (2007). Is there a common resilience mechanism underlying antidepressant drug response?

Evidence from 2848 patients. *J. Clin. Psychiatry* 68, 1195–1205. doi: 10.4088/jcp.v68n0805

Straub, J., Metzger, C. D., Plener, P. L., Koelch, M. G., Groen, G., and Abler, B. (2017). Successful group psychotherapy of depression in adolescents alters fronto-limbic resting-state connectivity. *J. Affect. Disord.* 209, 135–139. doi: 10.1016/j.jad.2016.11.024

Suslow, T., Konrad, C., Kugel, H., Rumstadt, D., Zwitserlood, P., Schöning, S., et al. (2010). Automatic mood-congruent amygdala responses to masked facial expressions in major depression. *Biol. Psychiatry* 67, 155–160. doi: 10.1016/j.biopsych.2009.07.023

Szczepanik, J., Nugent, A. C., Drevets, W. C., Khanna, A., Zarate, C. A. Jr., and Furey, M. L. (2016). Amygdala response to explicit sad face stimuli at baseline predicts antidepressant treatment response to scopolamine in major depressive disorder. *Psychiatry Res. Neuroimaging* 254, 67–73. doi: 10.1016/j.pscychresns.2016.06.005

Tang, S., Li, H., Lu, L., Wang, Y., Zhang, L., Hu, X., et al. (2019). Anomalous functional connectivity of amygdala subregional networks in major depressive disorder. *Depress. Anxiety* 36, 712–722. doi: 10.1002/da.22901

Tottenham, N., Weissman, M. M., Wang, Z., Warner, V., Gameroff, M. J., Semanek, D. P., et al. (2021). Depression risk is associated with weakened synchrony between the amygdala and experienced emotion. *Biol. Psychiatry Cogn. Neurosci. Neuroimaging* 6, 343–351. doi: 10.1016/j.bpsc.2020.10.011

van de Ven, V., Wingen, M., Kuypers, K. P., Ramaekers, J. G., and Formisano, E. (2013). Escitalopram decreases cross-regional functional connectivity within the default-mode network. *PLoS One* 8:e68355. doi: 10.1371/journal.pone.0068355

Wang, J., Wei, Q., Bai, T., Zhou, X., Sun, H., Becker, B., et al. (2017). Electroconvulsive therapy selectively enhanced feedforward connectivity from fusiform face area to amygdala in major depressive disorder. *Soc. Cogn. Affect. Neurosci.* 12, 1983–1992. doi: 10.1093/scan/nsx100

Williams, L. M., Korgaonkar, M. S., Song, Y. C., Paton, R., Eagles, S., Goldstein-Piekarski, A., et al. (2015). Amygdala reactivity to emotional faces in the prediction of general and medication-specific responses to antidepressant treatment in the randomized iSPOT-D trial. *Neuropsychopharmacology* 40, 2398–2408. doi: 10.1038/npp.2015.89

Witten, D. M., and Tibshirani, R. (2011). Penalized classification using Fisher's linear discriminant. *J. R. Stat. Soc. Ser. B Stat. Methodol.* 73, 753–772. doi: 10.1111/j.1467-9868.2011.00783.x

Wright, C. I., Fischer, H., Whalen, P. J., McInerney, S. C., Shin, L. M., and Rauch, S. L. (2001). Differential prefrontal cortex and amygdala habituation to repeatedly presented emotional stimuli. *Neuroreport* 12, 379–383. doi: 10.1097/00001756-200102120-00039

Wu, Y., Li, H., Zhou, Y., Yu, J., Zhang, Y., Song, M., et al. (2016). Sex-specific neural circuits of emotion regulation in the centromedial amygdala. *Sci. Rep.* 6:23112. doi: 10.1038/srep23112

Xia, M., Wang, J., and He, Y. (2013). BrainNet viewer: a network visualization tool for human brain connectomics. *PLoS One* 8:e68910. doi: 10.1371/journal.pone.0068910

Xue, S. W., Lee, T. W., and Guo, Y. H. (2018). Spontaneous activity in medial orbitofrontal cortex correlates with trait anxiety in healthy male adults. *J. Zhejiang Univ. Sci. B* 19, 643–653. doi: 10.1631/jzus.B1700481

Yan, C. G., Wang, X. D., Zuo, X. N., and Zang, Y. F. (2016). DPABI: data processing & analysis for (resting-state) brain imaging. *Neuroinformatics* 14, 339–351. doi: 10.1007/s12021-016-9299-4

Zang, Z. X., Yan, C. G., Dong, Z. Y., Huang, J., and Zang, Y. F. (2012). Granger causality analysis implementation on MATLAB: a graphic user interface toolkit for fMRI data processing. *J. Neurosci. Methods* 203, 418–426.

Conflict of Interest: The authors declare that the research was conducted in the absence of any commercial or financial relationships that could be construed as a potential conflict of interest.

Publisher's Note: All claims expressed in this article are solely those of the authors and do not necessarily represent those of their affiliated organizations, or those of the publisher, the editors and the reviewers. Any product that may be evaluated in this article, or claim that may be made by its manufacturer, is not guaranteed or endorsed by the publisher.

frontiers in Neuroscience

ORIGINAL RESEARCH
published: 16 September 2021
doi: 10.3389/fnins.2021.731596

Altered Variability and Concordance of Dynamic Resting-State fMRI Indices in Patients With Attention Deficit Hyperactivity Disorder

Feiling Lou[1†], Jiejie Tao[1†], Ronghui Zhou[1], Shuangli Chen[1], Andan Qian[1], Chuang Yang[2], Xiangwu Zheng[1], Bicheng Chen[3], Zhishan Hu[4] and Meihao Wang[1*]*

[1] Department of Radiology, The First Affiliated Hospital of Wenzhou Medical University, Wenzhou, China, [2] Department of Psychiatry, The First Affiliated Hospital of Wenzhou Medical University, Wenzhou, China, [3] Key Laboratory of Diagnosis and Treatment of Severe Hepato-Pancreatic Diseases of Zhejiang Province, Zhejiang Provincial Top Key Discipline in Surgery, The First Affiliated Hospital of Wenzhou Medical University, Wenzhou, China, [4] State Key Laboratory of Cognitive Neuroscience and Learning, Beijing Normal University, Beijing, China

OPEN ACCESS

Edited by:
Xiaopeng Song, Harvard Medical School, United States

Reviewed by:
Shao-Wei Xue, Affiliated Hospital of Hangzhou Normal University, China
Zhijun Yao, Lanzhou University, China

***Correspondence:**
Zhishan Hu
huzhishan@me.com
Meihao Wang
wzwmh@wmu.edu.cn

[†] These authors have contributed equally to this work

Specialty section:
This article was submitted to Brain Imaging Methods, a section of the journal Frontiers in Neuroscience

Received: *27 June 2021*
Accepted: *26 August 2021*
Published: *16 September 2021*

Citation:
Lou F, Tao J, Zhou R, Chen S, Qian A, Yang C, Zheng X, Chen B, Hu Z and Wang M (2021) Altered Variability and Concordance of Dynamic Resting-State fMRI Indices in Patients With Attention Deficit Hyperactivity Disorder. Front. Neurosci. 15:731596. doi: 10.3389/fnins.2021.731596

Objective: Attention deficit hyperactivity disorder (ADHD) is a commonly diagnosed neuropsychiatric disorder in children, which is characterized by inattention, hyperactivity and impulsivity. Using resting-state functional magnetic resonance imaging (R-fMRI), the alterations of static and dynamic characteristics of intrinsic brain activity have been identified in patients with ADHD. Yet, it remains unclear whether the concordance among indices of dynamic R-fMRI is altered in ADHD.

Methods: R-fMRI scans obtained from 50 patients with ADHD and 28 healthy controls (HC) were used for the current study. We calculated the regional dynamic changes in brain activity indices using the sliding-window method and compared the differences in variability of these indices between ADHD patients and HCs. Further, the concordance among these dynamic indices was calculated and compared. Finally, the relationship between variability/concordance of these indices and ADHD-relevant clinical test scores was investigated.

Results: Patients with ADHD showed decreased variability of dynamic amplitude of low-frequency fluctuation (dALFF) in the left middle frontal gyrus and increased one in right middle occipital gyrus, as compared with the HCs. Besides, ADHD patients showed decreased voxel-wise concordance in the left middle frontal gyrus. Further, lower voxel-wise concordance in ADHD's left middle frontal gyrus was associated with more non-perseverative errors in Wisconsin Card Sorting Test, which reflects worse cognitive control.

Conclusion: Our findings suggest that variability and concordance in dynamic brain activity may serve as biomarkers for the diagnosis of ADHD. Further, the decreased voxel-wise concordance is associated with deficit in cognitive control in ADHD patients.

Keywords: ADHD, resting-state fMRI, temporal dynamics, concordance, variability

INTRODUCTION

Attention deficit hyperactivity disorder (ADHD) is characterized by inattention, hyperactivity and impulsivity. It is one of the most commonly diagnosed childhood neurodevelopmental disorder, whose prevalence in school-age children and adolescents is estimated at 7.2% (Thomas et al., 2015). This disorder seriously affects these children's academic performance and social skills and causes immense burden for their families.

Maladaptive in the intrinsic brain activity of ADHD was frequently reported in previous studies. Many of these findings were derived from resting-state functional magnetic resonance imaging (R-fMRI), which measures the blood oxygen level dependent (BOLD) signal without task or stimulation and further characterizes the spatiotemporal organization of brain activities (Forster et al., 1998; Fox and Raichle, 2007). In specific, multiple R-fMRI indices have been developed to depict the intrinsic BOLD signal. For example, amplitude of low frequency fluctuation (ALFF) characterizes the intensity of local activity of brain spontaneous activity (Zang et al., 2007; Zou et al., 2008); Regional homogeneity (ReHo) measures the consistency of regional neural activity (Zang et al., 2004); Degree centrality (DC) describes the association between a local area with the whole brain (Buckner et al., 2009; Zuo et al., 2012); Voxel mirror homotopic connectivity (VMHC) represents the functional connectivity between each pair of symmetrical interhemispheric voxels (Zuo et al., 2010). Global signal connectivity (GSC) is described as the correlation between local voxels and global signal (Hahamy et al., 2014; Power et al., 2017).

These R-fMRI indices have been used to characterize the maladaptive brain functions in patients with ADHD. For example, children with ADHD exhibited increased ALFF in the occipital cortex and globus pallidus (An et al., 2013; Li et al., 2014), and decreased one in the left orbitofrontal cortex and ventral superior frontal gyrus (Li et al., 2014), showing hyperactive visual processing and hypoactive frontal control. Meanwhile, increased ReHo was reported in the bilateral lingual and fusiform gyri and right dorsal anterior cingulate cortices, and decreased ReHo in the bilateral ventral medial prefrontal cortex, cerebellum and right middle frontal gyrus, and right precuneus (An et al., 2013), which again indicated deficit in frontal lobe. In addition, the increased ReHo in right dorsal anterior cingulate cortex and left lingual gyrus, and the decreased ReHo in right cerebellum were associated with higher ADHD symptom scores in the ADHD group (An et al., 2013). Meantime, decreased DC was observed in the head of the right pallidum, caudate and putamen and in the left postcentral cortex (Di Martino et al., 2013), as well as right posterior cingulate gyrus and frontoparietal network (Jiang et al., 2019). Also, it was found that children with ADHD exhibited increased DC in the cerebellar anterior lobe, cingulate gyrus and middle occipital cortex, and increased VMHC in bilateral superior frontal, middle occipital, and cerebellar anterior lobes (Jiang et al., 2019). The findings above have proven that the R-fMRI indices can successfully capture the dysfunctions in the brains of ADHD patients.

Although these studies provided insights into the neural basis of ADHD, they failed to capture the dynamic changes in brain activities. Recent evidence demonstrated the temporal dynamic in brain activity patterns (Hutchison et al., 2013; Allen et al., 2014) and found that the alterations in these patterns were associated with neurological and psychiatric disorders. For example, patients with generalized anxiety disorder (GAD) exhibited increased variability in dynamic ALFF (dALFF) across wide spread brain regions (Cui et al., 2020). Meanwhile, patients with major depressive disorder (MDD) showed decreased variability in dALFF in the emotion network (Li et al., 2019). As for patients with ADHD, one study reported that they showed decreased mean value and variability in dynamic ReHo in the parietal lobe, compared to the healthy control group (Kim et al., 2018).

In addition, the concordance, i.e., temporal and spatial coupling, among multiple dynamic brain activity indices shows stable individual difference (Yan et al., 2017). Studies revealed that patients with psychiatric disorders exhibited decreased concordance in brain activity indices. For example, patients with schizophrenia showed decreased volume-wise concordance in whole gray matter and reduced voxel-wise concordance in multiple brain regions. Moreover, these concordance changes were negatively correlated with their onset age (Zhu et al., 2018). For MDD patients, reduced concordance was found in a wide range of brain regions, and the reduction was associated with impaired prospective memory and sustained attention (Zhu et al., 2019). Considering the tight relationship between the concordance of R-fMRI indices and mental disorders, the concordance may also underpin the ADHD. However, little has been done to explore this potential biomarker.

The current study aimed to bridge this gap. In specific, we compared the variability of dynamic R-fMRI indices and concordance among them between patients with ADHD and healthy controls, and further correlated the variability/concordance with the clinical test scores. Based on the results of previous studies, we hypothesized that ADHD patients would exhibit abnormalities in dynamic brain activity and its concordance, and this concordance would be related to its clinical manifestations. Our study may enhance the understanding of the neural mechanism underlying ADHD.

MATERIALS AND METHODS

Participants

Fifty-eight drug-naïve ADHD patients were recruited from the Out-patient Clinic of the First Affiliated Hospital of Wenzhou Medical University. Meanwhile, 31 healthy controls matched in gender, age and IQ were recruited from local schools. The diagnosis of ADHD was performed by three experienced psychiatrists according to the Fifth Edition of the Diagnostic and Statistical Manual of Mental Disorders (DSM-V). For all the participants, the exclusion criteria were: (1) conduct disorder, oppositional defiant disorder, or any other psychotropic disorder besides ADHD; (2) history of major neurological or physical illness; (3) current or history use of psychotropic drugs; (4) intelligence quotient (IQ) lower than 80; (5) MR scanning contraindications. This study was approved by the

Ethics Committee of the First Affiliated Hospital of Wenzhou Medical University. All participants were well informed and written informed consent was obtained before the test.

Behavior and Cognition Assessment

The revised version of Conners' Parent Rating Scale (CPRS) (Conners et al., 1998) was used to assess children's behavioral problems, including conduct problems, study problems, psychosomatic disorders, impulse hyperactivity, anxiety, and hyperactivity.

The computerized Wisconsin Card Sorting Test (WCST) (Feldstein et al., 1999) was used to assess the executive function, including cognitive flexibility, working memory, continuous attention, and response inhibition. In specific, patients were required to match two cards according to the color, shape or quantity. After 10 trials of correct matching, one completed session was counted and the rule would be changed. The task was ended if the participants complete six sessions or 128 trials. The perseverative errors (at least two successive errors) and non-perseverative errors were counted. Note that non-perseverative errors were counted as the difference between the total number of errors and the number of perseverative errors.

MRI Data Acquisition

Images were acquired in a 3T GE Sigma HDX 3.0 scanner (GE Healthcare, United States) with the following parameters: repetition time (TR) = 2,000 ms, echo time (TE) = 30 ms, 31 axial slices, slice thickness = 4 mm, slice gap = 0.2 mm, flip angle = 90°, matrix size = 64 × 64, field of view (FOV) = 192 × 192 mm, and 240 volumes. High-spatial-resolution T1-weighted 3D images were obtained axially using the following parameters:162 axial slices, repetition time (TR) = 7,200 ms, echo time (TE) = 2.2 ms, flip angle = 7°, section thickness = 1 mm, gap = 0, field of view (FOV) = 256 × 256 mm, data matrix = 256 × 256. During the scanning, sponge earplugs were used to reduce scanner noise, and foam cushions were used to minimize head movement. The subjects were required to be relax, stay still, close their eyes, and stay awake.

Data Preprocessing

Data Processing and Analysis for Brain Imaging (DPABI) (Yan et al., 2016) was used for data preprocessing: (1) the first 10 volumes were eliminated to enable subjects to adapt to the scanning environment and the magnetic field to be stable; (2) slice timing correction; (3) head motion correction (subjects were excluded from further analysis if their maximal head motion exceeded 3 mm displacement or 3°of rotation, 8 ADHD patients and 3 HCs were therefore excluded, leaving 50 ADHD patients and 28 HCs); (4) structural image alignment, aligning the individual T1-weighted image to the average functional image through six-degree-of-freedom linear transformation; (5) structural image segmentation, which divides the structural image into gray matter, white matter and cerebrospinal fluid; (6) nuisance covariates regression, including the Friston-24 motion parameters, white matter signals, cerebrospinal fluid signals and linear drift. Note that the multiple direction motion parameters and the mean frame-wise displacement (FD) of each subject were calculated to evaluate and compare the head motion, results were listed in **Table 1** and **Supplementary Table 1**; (7) based on the segmented images, the individual space was transformed to the MNI space using the DARTEL (diffeomorphic anatomical registration through exponentiated lie algebra) tool, and the resampled voxel size is 3 mm × 3 mm × 3 mm.

Dynamic R-fMRI Indices Calculation

R-fMRI indices were calculated with following procedures:

ALFF (Zang et al., 2007; Zou et al., 2008). After Fourier transform of time series of a voxel, ALFF takes the mean amplitude of a specific frequency range (0.01–0.08 Hz) as the intensity of local activity of the voxel.

ReHo (Zang et al., 2004). The Kendall's coefficient of concordance between the time series of a given voxel and the time series of its closest voxel.

DC (Buckner et al., 2009; Zuo et al., 2012). In this study, we calculate the Pearson correlation coefficient between the time course of each voxel and the time course of every other voxel in the whole brain. For each voxel, DC denotes the sum of connections that showed a correlation coefficient exceeding 0.25 (Buckner et al., 2009; Yan et al., 2017). Correlations below this threshold were considered mainly caused by signal noise. Meanwhile, it has been proven that different threshold selection from 0.1 to 0.3 did not significantly change the network structure (Buckner et al., 2009). The obtained DC values were converted to Z-scores by subtracting the global mean DC and dividing by the SD of the whole brain DC, the obtained voxel-wise DC map.

VMHC (Zuo et al., 2010). Function images were transformed into a symmetric space. Then, Pearson's correlation coefficients between time series from homologous brain regions were calculated (VMHC). Finally, the VMHC maps were transformed by Fisher Z-transformation for subsequent analysis.

TABLE 1 | Clinical and demographic characteristics of ADHD patients and HCs.

Characteristics	ADHD (*N* = 50)	HC (*N* = 28)	Statistics	*P*-value
Age	8.26 ± 1.93	8.93 ± 1.46	$t = -1.596$	0.115
Gender (male/female)	(43/7)	(20/8)	$\chi^2 = 2.454$	0.117
Head motion (FD) (mm)	0.105 ± 0.069	0.093 ± 0.054	$t = 0.791$	0.432
Full-scale IQ	116.94 ± 17.45	122.43 ± 13.84	$t = -1.430$	0.157
Conners' Parent Rating Scale				
Conduct problem	1.23 ± 0.51	0.39 ± 0.33	$t = 8.869$	<0.001***
Study problem	1.93 ± 0.68	0.64 ± 0.62	$t = 8.217$	<0.001***
Psychosomatic	0.41 ± 0.35	0.15 ± 0.24	$t = 3.859$	<0.001***
Impulsive–hyperactive	1.70 ± 0.63	0.52 ± 0.50	$t = 8.441$	<0.001***
Anxiety	0.49 ± 0.47	0.35 ± 0.29	$t = 1.646$	0.104
Hyperactivity index	1.62 ± 0.54	0.50 ± 0.40	$t = 9.457$	<0.001***
Wisconsin Card Sorting Test				
Perseverative errors	16.20 ± 9.24	12.00 ± 5.55	$t = 2.506$	0.014*
Non-perseverative errors	13.62 ± 6.30	14.75 ± 4.96	$t = -0.818$	0.416

*$P < 0.05$; ***$P < 0.001$.

GSC (Hahamy et al., 2014; Power et al., 2017). BOLD signals from all the voxels were averaged as the global signal. Pearson correlation coefficients between each voxel time course and the global signal were calculated to get the GSC maps, finally The GSC maps included in the subsequent analysis were Fisher Z-transformed.

In particular, dynamics of these R-fMRI indices were analyzed using Temporal Dynamic Analysis (TDA) toolkits based on DPABI (Yan et al., 2016). Specifically, R-fMRI indices mentioned above were computed with the hamming windows (window length = 32 TR, window step = 4 TR, generating 50 windows). Previous studies have revealed that even a window length ranged from 30 to 60 s is able to capture dynamic functional connectivity fluctuations and different window lengths do not yield significantly different results (Preti et al., 2017). Also, previous studies have demonstrated that the step size does not dramatically affect the variance of dynamic properties of R-fMRI (Liao et al., 2019). Therefore, we used a window length of 32 TR (64 s) and a step size of 4 TR (8 s) (Yang et al., 2020). More importantly, different window length (48 TR/64 TR) were used to validate our results (see **Supplementary Materials**). The R-fMRI indices mentioned above were prefixed with a *d* to indicate the dynamic indices. For example, dALFF represents dynamic ALFF. Further, the standard deviation (SD) of each index across the time series from each voxel was calculated and normalized across the voxels to measure the variability in these dynamic R-fMRI indices. Finally, the normalized SD maps of each dynamic R-fMRI index were smoothed (FWHM = 4 mm) to improve the signal-to-noise ratio.

Concordance Analysis

The concordance of five dynamic R-fMRI indices (ALFF, ReHo, DC, VMHC, and GSC) were calculated. In specific, volume-wise and voxel-wise concordance was measured by Kendall's W among these indices (Yan et al., 2017). The volume-wise concordance (spatial concordance) was calculated in two steps. First, compute the Kendall's W of the five indices across voxels for each window. Second, the dynamic volume-wise concordance was computed as the averaged Kendall's W across all time windows for each participant. The voxel-wise concordance (temporal concordance) was measured by the Kendall's W of the five indices across all time windows. By doing this, each voxel (voxel-wise) was assigned a concordance value. These voxel-wise concordance maps were then smoothed (FWHM = 4 mm) for subsequent analyses. Thus, for each participant, they got one volume-wise concordance value and N (*N* = number of voxels) voxel-wise concordance values.

Importantly, we validated the results with the window length of 48 and 64 TR.

Statistical Analysis

We compared age, IQ, ADHD-relevant clinical variables between ADHD patients and healthy controls using two-sample *t*-tests. Meanwhile, gender distributions were compared using chi-square test. These statistical analyses were performed with SPSS 23.0.

The dynamic R-fMRI indices and voxel-wise concordance were compared using two-sample *t*-test, and the whole-brain gray mask was applied, and the results were corrected by multiple comparisons using Gaussian random field theory (GRF, voxel-wise $p < 0.001$, cluster-wise $p < 0.05$, two-tailed). Meanwhile, the volume-wise concordance was compared using analysis of covariance (ANCOVA). Further, Pearson or Spearman partial correlation was used to quantify the associations between dynamic indices and ADHD-relevant clinical test scores. Note that the age, gender, IQ, and head motions are controlled as covariates.

RESULTS

Clinical and Demographic Characteristics

The characteristics of samples were summarized in **Table 1**. In particular, the ADHD group and the HCs group showed no significant differences in age, gender, head motion, or IQ. As measured by CPRS, ADHD patients exhibited significantly higher hyperactive and impulsive, and had more serious behavior and learning problems. In Wisconsin Card Sorting Test, the number of perseverative errors in ADHD group was higher than that in HC group ($P = 0.014$).

Alterations of Variability in ADHD

Compared with HCs, the ADHD group exhibited increased dALFF variability in right middle occipital gyrus and decreased dALFF variability in left middle frontal gyrus (GRF, voxel-wise $p < 0.001$, cluster-wise $p < 0.05$, two-tailed; see **Table 2** and **Figure 1**). No significant between-group difference was found for the dynamics of other R-fMRI indices.

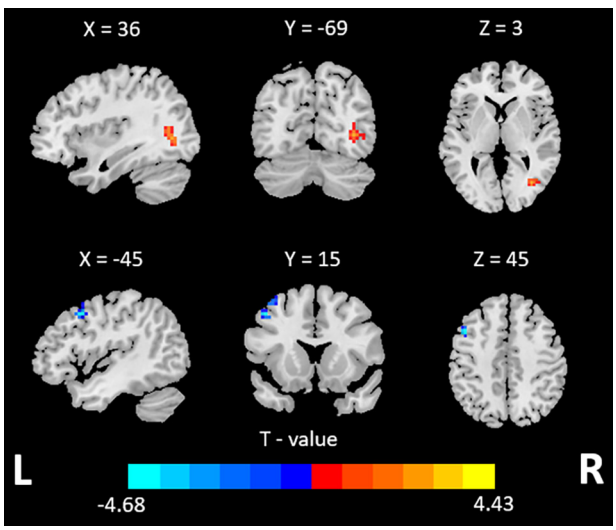

FIGURE 1 | Brain regions showing different dALFF variability between the ADHD and HCs.

TABLE 2 | Brain regions with significant differences in R-fMRI dynamic indices (SD) between ADHD patients and HCs.

Measurements	Brain regions	MNI coordinates (x, y, z)			Voxels	Peak *t*-values	*P*-value (cluster-lever)
dALFF	Right middle occipital gyrus	36	−69	0.3	45	4.43	0.002
	Left middle frontal gyrus	−45	15	45	36	−4.68	0.005

Alterations of Volume-Wise and Voxel-Wise Concordance in ADHD

The ANCOVA results indicated no significant differences in volume-wise concordance between the ADHD group and HC group. However, ADHD patients showed decreased voxel-wise concordance in left middle frontal gyrus (GRF, voxel-wise $p < 0.001$, cluster-wise $p < 0.05$, two-tailed; see **Table 3** and **Figure 2**).

Negative Correlation With the Non-perseverative Errors

No significant correlations were found between the CPRS scores and altered dALFF variability for the ADHD group. However, the abnormal voxel-wise concordance of the left middle frontal was negatively correlated with the non-perseverative errors in WCST of patients with ADHD (Pearson partial correlation, $r = -0.367$, $p = 0.012$; see **Figure 3**). Meanwhile, we found no correlation between left middle frontal voxel-wise concordance and non-persistent errors in HC group (Pearson partial correlation, $r = 0.099$, $p = 0.646$; see **Figure 3**).

Validation of the Results

The validation results with the window length of 48 and 64 TR showed good agreement with the results mentioned above (**Supplementary Tables 2–5** and **Supplementary Figures 1–6**).

DISCUSSION

Abnormality in intrinsic brain activities is tightly associated with ADHD. This study systematically compared the dynamic changes in resting-state brain activities of patients with ADHD with HCs. Specifically, we calculated the temporal variability, spatial and temporal concordance of dynamic R-fMRI indices including ALFF, ReHo, DC, VMHC, and GSC in both groups. These properties were then compared between groups and correlated with the clinical variables, in which both the alterations and correlations were identified.

Altered Variability in Occipital and Frontal Gyrus

Specifically, for the variability, ADHD patients exhibited increased dALFF variability in right middle occipital gyrus and decreased one in left middle frontal gyrus, which may reflect the hyper-activation in visual cortex and hypo-activation in frontal cortex. This is consistent with a previous study in which decreased ReHo was found in frontal and increased ReHo and ALFF was found in visual cortex (An et al., 2013).

The development of the frontal lobe is essential for the acquisition, execution and control of a wide range of functions (Rosch and Mostofsky, 2019). And frontal lobe is a component of the brain region of the cognitive-attention network (cingulate-frontal lobe-parietal lobe), these areas are typically involved in cognitive, attentional, executive function, response inhibition, motor control, and working memory (Bush, 2011). Deficits in frontal lobe can lead to a series of developmental disorders like ADHD, and increase the psychopathological vulnerability. Many studies have revealed that the structural and functional abnormalities in the frontal lobe of patients with ADHD (Albajara Sáenz et al., 2019). For example, the volume of gray matter (Shaw et al., 2011) and the ALFF (Yang et al., 2011) in the middle frontal gyrus was decreased in ADHD patients. One previous study also exhibited decreased functional connectivity between right middle frontal gyrus and whole brain, and the decreased was associated with lower IQ (Shaw and Sudre, 2021). Consistent with the previous studies, we also observed decreased dALFF variability in middle frontal gyrus. The decreased dALFF variability indicated abnormal temporal fluctuations of brain activity in this region. Such an abnormal pattern may underlie the deficit in cognitive control of patients with ADHD, and the failure in cognitive control plays a key role in the main symptoms of ADHD.

Structural and functional alterations in occipital were also reported in previous studies. For example, reduced gray matter volume in the right middle occipital gyrus (Wang L. J.

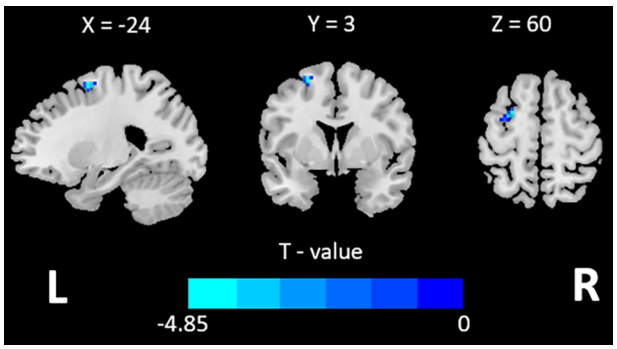

FIGURE 2 | Brain region showing different voxel-wise concordance between the ADHD and HCs.

TABLE 3 | Brain region with decreased voxel-wise concordance in ADHD.

Brain Regions	MNI Coordinates (x, y, z)			Voxels	Peak *t*-values	*P*-value (Cluster-lever)
Left middle frontal gyrus	−24	3	60	40	−4.85	0.002

et al., 2020) and hyper-activation of occipital lobe function was found in ADHD (Tian et al., 2008; Icer et al., 2019), indicating that atypical visual processing may play a key role. Previous study also reported that the decreased connectivity between the frontal cortex and visual cortex was associated with increased severity in ADHD symptoms (Wang M. et al., 2020). Meanwhile, the interaction between the dorsal attention network and visual cortex is important for maintaining attention (Shulman et al., 2009). These findings suggest that brain activities in frontal and occipital regions and their interactions may play a key role in ADHD, which awaits further investigation.

Altered Concordance in Left Middle Frontal Gyrus

Alterations in concordance among the dynamic R-fMRI indices were also identified in patients with ADHD. A recent study found that R-fMRI regional indices was high concordant in brain cortical and subcortical areas across the time window (Yan et al., 2017), and the voxel-wise concordance reflects homogeneity between these indices. Several studies on schizophrenia or MDD have found abnormal voxel-wise concordance in multiple brain regions (Zhu et al., 2018, 2019). These findings suggest that the concordance of dynamic indices may be an important biomarker for neuropsychiatric disorders. In our study, ADHD patients exhibited decreased voxel-wise concordance in the left middle frontal, which was consistent with the decreased dALFF variability in middle frontal gyrus, indicating maladaptive in frontal lobe.

Correlation Between Concordance of Frontal Gyrus and Executive Function

In addition, we found that the voxel-wise concordance change in left middle frontal gyrus was negatively correlated with non-perseverative errors in WCST of ADHD group. Whereas, we did not find a correlation between them in the HCs. WCST is widely used to assess executive function, including cognitive flexibility, working memory, continuous attention and response inhibition (Godinez et al., 2012). Non-perseverative error measures the difficulties in working memory, sustained attention, and response inhibition (Barceló, 1999; Barceló and Knight, 2002; Godinez et al., 2012). Furthermore, non-perseverative errors have been found to be associated with frontal lobe function in patients with ADHD (Qian et al., 2018). However, no significant difference in non-perseverative errors was found between ADHD patients and healthy controls. This may due to the relatively small sample size, which might induce more variance and undermine the difference between these two groups. Nevertheless, this implies that the concordance in left middle frontal gyrus can be a sensitive biomarker that can capture the changes in non-preservative errors in ADHD patients.

Clinical Applications

Our findings highlighted the role of frontal lobe in the neuropathological mechanism of ADHD, and demonstrated that concordance of R-fMRI indices can serve as a biomarker to indicate the deficit in frontal lobe. To date, the diagnosis of ADHD is still based on symptom scores from clinical interviews, which can be subjective and can be influenced by many factors, such as the experience, stereotype, and cultural differences. Neuropsychiatric biomarkers can help to build a standard and objective diagnosis system, which can benefit the patients. R-fMRI is among the neuropsychiatric tools that have the potential to find the biomarkers (Abi-Dargham and Horga, 2016). Such biomarkers, combined with the rapidly developed machine learning algorithms, researchers are able to precisely classify the ADHD from healthy control (Du et al., 2018). R-fMRI indices such as ReHo (Wang et al., 2013) and functional connectivity (Fair et al., 2012) have been frequently used by these researchers. Functional concordance incorporates features from multiple metrics, which are fully explored in the current study, can also be used to train the machine learning models,

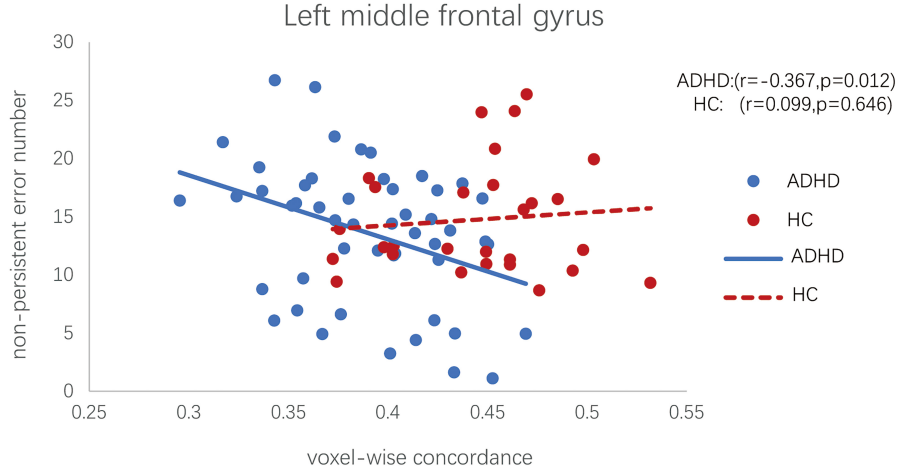

FIGURE 3 | Scatter plot of the voxel-wise concordance in the left middle frontal and the non-perseverative errors in WCST of patients with ADHD. (Pearson partial correlation scatter diagram, controlling for effects of head motion, age, IQ, and gender).

and thereby can promote the accuracy of classification and prediction of ADHD.

Further, the behavioral dysfunction may be too subtle to be measured, just like the non-perseverative errors that failed to be capture by the current study. However, as mentioned above, the R-fMRI indices as proposed by the current study are able to evaluated the maladaptive of brain functions.

Limitations

This study has several limitations. First, no significant differences were found among some dynamic indices, which may be due to the relatively small sample size. A larger sample size is needed to validate the alterations in dynamic brain function in ADHD and examine the relationship between dynamic variables and psychological data. Second, the current study only focus on the BOLD signal from gray matter. However, previous studies have demonstrated the white matter signals also provide valuable information (Peer et al., 2017; Ding et al., 2018; Li et al., 2020a,b). Hence, further studies are need to explore the altered variability and concordance of white matter signals in patients with ADHD. Third, this study used a variety of indices to reflect different patterns of dynamic spontaneous brain activity, but the seed-based functional connectivity analysis (FC) and independent component analysis (ICA) were not included in the analysis, this is because ICA may be biased by component selection and FC may be biased by seed definition. In future studies, more supplementary R-fMRI indices should be considered, which may help to describe the spontaneous brain activity more thoroughly and understand its underlying physiological processes more deeply.

CONCLUSION

The current study investigated the variability and concordance of a range of commonly used R-fMRI indices in ADHD. We found that patients with ADHD exhibited increased dALFF variability in right middle occipital gyrus and decreased dALFF variability in left middle frontal gyrus. Meanwhile, we found that voxel-wise concordance of a series of R-fMRI indices in patients with ADHD was decreased in frontal lobe, and a greater decrease was related to worse WSCT performance. These findings suggest that dynamic analysis and functional concordance may provide new insights into the neuropathological mechanism of ADHD.

DATA AVAILABILITY STATEMENT

The raw data supporting the conclusions of this article will be made available by the authors, without undue reservation.

ETHICS STATEMENT

The studies involving human participants were reviewed and approved by the Ethics Committee of the First Affiliated Hospital of Wenzhou Medical University. Written informed consent to participate in this study was provided by the participants' legal guardian/next of kin.

AUTHOR CONTRIBUTIONS

FL and JT analyzed the data and wrote the manuscript. RZ analyzed the data. SC and AQ collected the MRI data. CY, XZ, and BC evaluated the subjects. ZH and MW designed and supervised the experiment, and finalized the manuscript. All authors reviewed the manuscript and made significant contribution to this manuscript.

FUNDING

This work was supported by the Wenzhou Municipal Science and Technology Bureau, China (grant No. Y20180185), the Medical Health Science and Technology Project of Zhejiang Provincial Health Commission (grant No. 2019KY102), the National Natural Science Foundation of China (62007002), and the China Postdoctoral Science Foundation (2020M670189).

ACKNOWLEDGMENTS

We thank the First Affiliated Hospital of Wenzhou Medical University for its support. And we also thank all the volunteers for their participations.

SUPPLEMENTARY MATERIAL

The Supplementary Material for this article can be found online at: https://www.frontiersin.org/articles/10.3389/fnins.2021.731596/full#supplementary-material

REFERENCES

Abi-Dargham, A., and Horga, G. (2016). The search for imaging biomarkers in psychiatric disorders. *Nat. Med.* 22, 1248–1255. doi: 10.1038/nm.4190

Albajara Sáenz, A., Villemonteix, T., and Massat, I. (2019). Structural and functional neuroimaging in attention-deficit/hyperactivity disorder. *Dev. Med. Child Neurol.* 61, 399–405.

Allen, E. A., Damaraju, E., Plis, S. M., Erhardt, E. B., Eichele, T., and Calhoun, V. D. (2014). Tracking whole-brain connectivity dynamics in the resting state. *Cereb. Cortex* 24, 663–676. doi: 10.1093/cercor/bhs352

An, L., Cao, Q. J., Sui, M. Q., Sun, L., Zou, Q. H., Zang, Y. F., et al. (2013). Local synchronization and amplitude of the fluctuation of spontaneous brain activity in attention-deficit/hyperactivity disorder: a resting-state fMRI study. *Neurosci. Bull.* 29, 603–613. doi: 10.1007/s12264-013-1353-8

Barceló, F. (1999). Electrophysiological evidence of two different types of error in the Wisconsin Card Sorting Test. *Neuroreport* 10, 1299–1303. doi: 10.1097/00001756-199904260-00027

Barceló, F., and Knight, R. T. (2002). Both random and perseverative errors underlie WCST deficits in prefrontal patients. *Neuropsychologia* 40, 349–356. doi: 10.1016/s0028-3932(01)00110-5

Buckner, R. L., Sepulcre, J., Talukdar, T., Krienen, F. M., Liu, H., Hedden, T., et al. (2009). Cortical hubs revealed by intrinsic functional connectivity: mapping, assessment of stability, and relation to Alzheimer's disease. *J. Neurosci.* 29, 1860–1873. doi: 10.1523/jneurosci.5062-08.2009

Bush, G. (2011). Cingulate, frontal, and parietal cortical dysfunction in attention-deficit/hyperactivity disorder. *Biol. Psychiatry* 69, 1160–1167. doi: 10.1016/j.biopsych.2011.01.022

Conners, C. K., Sitarenios, G., Parker, J. D., and Epstein, J. N. (1998). The revised Conners' Parent Rating Scale (CPRS-R): factor structure, reliability, and criterion validity. *J. Abnorm. Child Psychol.* 26, 257–268.

Cui, Q., Sheng, W., Chen, Y., Pang, Y., Lu, F., Tang, Q., et al. (2020). Dynamic changes of amplitude of low-frequency fluctuations in patients with generalized anxiety disorder. *Hum. Brain Mapp.* 41, 1667–1676. doi: 10.1002/hbm.24902

Di Martino, A., Zuo, X. N., Kelly, C., Grzadzinski, R., Mennes, M., Schvarcz, A., et al. (2013). Shared and distinct intrinsic functional network centrality in autism and attention-deficit/hyperactivity disorder. *Biol. Psychiatry* 74, 623–632. doi: 10.1016/j.biopsych.2013.02.011

Ding, Z., Huang, Y., Bailey, S. K., Gao, Y., Cutting, L. E., Rogers, B. P., et al. (2018). Detection of synchronous brain activity in white matter tracts at rest and under functional loading. *Proc. Natl. Acad. Sci. U.S.A.* 115, 595–600. doi: 10.1073/pnas.1711567115

Du, Y., Fu, Z., and Calhoun, V. D. (2018). Classification and prediction of brain disorders using functional connectivity: promising but challenging. *Front. Neurosci.* 12:525. doi: 10.3389/fnins.2018.00525

Fair, D. A., Nigg, J. T., Iyer, S., Bathula, D., Mills, K. L., Dosenbach, N. U., et al. (2012). Distinct neural signatures detected for ADHD subtypes after controlling for micro-movements in resting state functional connectivity MRI data. *Front. Syst. Neurosci.* 6:80. doi: 10.3389/fnsys.2012.00080

Feldstein, S. N., Keller, F. R., Portman, R. E., Durham, R. L., Klebe, K. J., and Davis, H. P. (1999). A comparison of computerized and standard versions of the Wisconsin Card Sorting Test. *Clin. Neuropsychol.* 13, 303–313. doi: 10.1076/clin.13.3.303.1744

Forster, B. B., MacKay, A. L., Whittall, K. P., Kiehl, K. A., Smith, A. M., Hare, R. D., et al. (1998). Functional magnetic resonance imaging: the basics of blood-oxygen-level dependent (BOLD) imaging. *Can. Assoc. Radiol. J.* 49, 320–329.

Fox, M. D., and Raichle, M. E. (2007). Spontaneous fluctuations in brain activity observed with functional magnetic resonance imaging. *Nat. Rev. Neurosci.* 8, 700–711. doi: 10.1038/nrn2201

Godinez, D. A., Friedman, N. P., Rhee, S. H., Miyake, A., and Hewitt, J. K. (2012). Phenotypic and genetic analyses of the Wisconsin Card Sort. *Behav. Genet.* 42, 209–220. doi: 10.1007/s10519-011-9502-1

Hahamy, A., Calhoun, V., Pearlson, G., Harel, M., Stern, N., Attar, F., et al. (2014). Save the global: global signal connectivity as a tool for studying clinical populations with functional magnetic resonance imaging. *Brain Connect.* 4, 395–403. doi: 10.1089/brain.2014.0244

Hutchison, R. M., Womelsdorf, T., Allen, E. A., Bandettini, P. A., Calhoun, V. D., Corbetta, M., et al. (2013). Dynamic functional connectivity: promise, issues, and interpretations. *Neuroimage* 80, 360–378. doi: 10.1016/j.neuroimage.2013.05.079

Icer, S., Gengec Benli, S., and Ozmen, S. (2019). Differences in brain networks of children with ADHD: whole–brain analysis of resting–state fMRI. *Int. J. Imaging Syst. Technol.* 29, 645–662. doi: 10.1002/ima.22348

Jiang, K. H., Yi, Y., Li, L., Li, H. X., Shen, H. J., Zhao, F. Q., et al. (2019). Functional network connectivity changes in children with attention-deficit hyperactivity disorder: a resting-state fMRI study. *Int. J. Dev. Neurosci.* 78, 1–6. doi: 10.1016/j.ijdevneu.2019.07.003

Kim, J. I., Yoo, J. H., Kim, D., Jeong, B., and Kim, B. N. (2018). The effects of GRIN2B and DRD4 gene variants on local functional connectivity in attention-deficit/hyperactivity disorder. *Brain Imaging Behav.* 12, 247–257. doi: 10.1007/s11682-017-9690-2

Li, F., He, N., Li, Y., Chen, L., Huang, X., Lui, S., et al. (2014). Intrinsic brain abnormalities in attention deficit hyperactivity disorder: a resting-state functional MR imaging study. *Radiology* 272, 514–523. doi: 10.1148/radiol.14131622

Li, J., Biswal, B. B., Meng, Y., Yang, S., Duan, X., Cui, Q., et al. (2020a). A neuromarker of individual general fluid intelligence from the white-matter functional connectome. *Transl. Psychiatry* 10:147.

Li, J., Chen, H., Fan, F., Qiu, J., Du, L., Xiao, J., et al. (2020b). White-matter functional topology: a neuromarker for classification and prediction in unmedicated depression. *Transl. Psychiatry* 10:365.

Li, J., Duan, X., Cui, Q., Chen, H., and Liao, W. (2019). More than just statics: temporal dynamics of intrinsic brain activity predicts the suicidal ideation in depressed patients. *Psychol. Med.* 49, 852–860. doi: 10.1017/s0033291718001502

Liao, W., Li, J., Ji, G. J., Wu, G. R., Long, Z., Xu, Q., et al. (2019). Endless fluctuations: temporal dynamics of the amplitude of low frequency fluctuations. *IEEE Trans. Med. Imaging* 38, 2523–2532. doi: 10.1109/tmi.2019.2904555

Peer, M., Nitzan, M., Bick, A. S., Levin, N., and Arzy, S. (2017). Evidence for functional networks within the human brain's white matter. *J. Neurosci.* 37, 6394–6407. doi: 10.1523/jneurosci.3872-16.2017

Power, J. D., Plitt, M., Laumann, T. O., and Martin, A. (2017). Sources and implications of whole-brain fMRI signals in humans. *Neuroimage* 146, 609–625. doi: 10.1016/j.neuroimage.2016.09.038

Preti, M. G., Bolton, T. A. W., and Van De Ville, D. (2017). The dynamic functional connectome: state-of-the-art and perspectives. *Neuroimage* 160, 41–54. doi: 10.1016/j.neuroimage.2016.12.061

Qian, A., Tao, J., Wang, X., Liu, H., Ji, L., Yang, C., et al. (2018). Effects of the 2-repeat allele of the DRD4 gene on neural networks associated with the prefrontal cortex in children With ADHD. *Front. Hum. Neurosci.* 12:279. doi: 10.3389/fnhum.2018.00279

Rosch, K. S., and Mostofsky, S. (2019). Development of the frontal lobe. *Handb. Clin. Neurol.* 163, 351–367.

Shaw, P., Gilliam, M., Liverpool, M., Weddle, C., Malek, M., Sharp, W., et al. (2011). Cortical development in typically developing children with symptoms of hyperactivity and impulsivity: support for a dimensional view of attention deficit hyperactivity disorder. *Am. J. Psychiatry* 168, 143–151. doi: 10.1176/appi.ajp.2010.10030385

Shaw, P., and Sudre, G. (2021). Adolescent attention-deficit/hyperactivity disorder: understanding teenage symptom trajectories. *Biol. Psychiatry* 89, 152–161. doi: 10.1016/j.biopsych.2020.06.004

Shulman, G. L., Astafiev, S. V., Franke, D., Pope, D. L., Snyder, A. Z., McAvoy, M. P., et al. (2009). Interaction of stimulus-driven reorienting and expectation in ventral and dorsal frontoparietal and basal ganglia-cortical networks. *J. Neurosci.* 29, 4392–4407. doi: 10.1523/jneurosci.5609-08.2009

Thomas, R., Sanders, S., Doust, J., Beller, E., and Glasziou, P. (2015). Prevalence of attention-deficit/hyperactivity disorder: a systematic review and meta-analysis. *Pediatrics* 135, e994–e1001.

Tian, L., Jiang, T., Liang, M., Zang, Y., He, Y., Sui, M., et al. (2008). Enhanced resting-state brain activities in ADHD patients: a fMRI study. *Brain Dev.* 30, 342–348. doi: 10.1016/j.braindev.2007.10.005

Wang, L. J., Li, S. C., Kuo, H. C., Chou, W. J., Lee, M. J., Chou, M. C., et al. (2020). Gray matter volume and microRNA levels in patients with attention-deficit/hyperactivity disorder. *Eur. Arch. Psychiatry Clin. Neurosci.* 270, 1037–1045.

Wang, M., Hu, Z., Liu, L., Li, H., Qian, Q., and Niu, H. (2020). Disrupted functional brain connectivity networks in children with attention-deficit/hyperactivity disorder: evidence from resting-state functional near-infrared spectroscopy. *Neurophotonics* 7:015012.

Wang, X., Jiao, Y., Tang, T., Wang, H., and Lu, Z. (2013). Altered regional homogeneity patterns in adults with attention-deficit hyperactivity disorder. *Eur. J. Radiol.* 82, 1552–1557. doi: 10.1016/j.ejrad.2013.04.009

Yan, C. G., Wang, X. D., Zuo, X. N., and Zang, Y. F. (2016). DPABI: data processing & analysis for (resting-state) brain imaging. *Neuroinformatics* 14, 339–351. doi: 10.1007/s12021-016-9299-4

Yan, C. G., Yang, Z., Colcombe, S. J., Zuo, X. N., and Milham, M. P. (2017). Concordance among indices of intrinsic brain function: insights from inter-individual variation and temporal dynamics. *Sci. Bull.* 62, 1572–1584. doi: 10.1016/j.scib.2017.09.015

Yang, H., Wu, Q., Guo, L., Li, Q., Long, X., Huang, X., et al. (2011). Abnormal spontaneous brain activity in medication-naïve ADHD children: a resting state fMRI study. *Neurosci. Lett.* 502, 89–93. doi: 10.1016/j.neulet.2011.07.028

Yang, Y., Peng, G., Zeng, H., Fang, D., Zhang, L., Xu, S., et al. (2020). Effects of the *SNAP25* on integration ability of brain functions in children with ADHD. *J. Atten. Disord.* doi: 10.1177/1087054720964561

Zang, Y., Jiang, T., Lu, Y., He, Y., and Tian, L. (2004). Regional homogeneity approach to fMRI data analysis. *Neuroimage* 22, 394–400. doi: 10.1016/j.neuroimage.2003.12.030

Zang, Y. F., He, Y., Zhu, C. Z., Cao, Q. J., Sui, M. Q., Liang, M., et al. (2007). Altered baseline brain activity in children with ADHD revealed by resting-state functional MRI. *Brain Dev.* 29, 83–91. doi: 10.1016/j.braindev.2006.07.002

Zhu, J., Zhang, Y., Zhang, B., Yang, Y., Wang, Y., Zhang, C., et al. (2019). Abnormal coupling among spontaneous brain activity metrics and cognitive deficits in major depressive disorder. *J. Affect. Disord.* 252, 74–83. doi: 10.1016/j.jad.2019.04.030

Zhu, J., Zhu, D. M., Qian, Y., Li, X., and Yu, Y. (2018). Altered spatial and temporal concordance among intrinsic brain activity measures in schizophrenia. *J. Psychiatr. Res.* 106, 91–98. doi: 10.1016/j.jpsychires.2018.09.015

Zou, Q. H., Zhu, C. Z., Yang, Y., Zuo, X. N., Long, X. Y., Cao, Q. J., et al. (2008). An improved approach to detection of amplitude of low-frequency fluctuation (ALFF) for resting-state fMRI: fractional ALFF. *J. Neurosci. Methods* 172, 137–141. doi: 10.1016/j.jneumeth.2008.04.012

Zuo, X. N., Ehmke, R., Mennes, M., Imperati, D., Castellanos, F. X., Sporns, O., et al. (2012). Network centrality in the human functional connectome. *Cereb. Cortex* 22, 1862–1875. doi: 10.1093/cercor/bhr269

Zuo, X. N., Kelly, C., Di Martino, A., Mennes, M., Margulies, D. S., Bangaru, S., et al. (2010). Growing together and growing apart: regional and sex differences in the lifespan developmental trajectories of functional homotopy. *J. Neurosci.* 30, 15034–15043. doi: 10.1523/jneurosci.2612-10.2010

Conflict of Interest: The authors declare that the research was conducted in the absence of any commercial or financial relationships that could be construed as a potential conflict of interest.

Publisher's Note: All claims expressed in this article are solely those of the authors and do not necessarily represent those of their affiliated organizations, or those of the publisher, the editors and the reviewers. Any product that may be evaluated in this article, or claim that may be made by its manufacturer, is not guaranteed or endorsed by the publisher.

frontiers in Neuroscience

ORIGINAL RESEARCH
published: 20 October 2021
doi: 10.3389/fnins.2021.768418

A Quantitative Data-Driven Analysis Framework for Resting-State Functional Magnetic Resonance Imaging: A Study of the Impact of Adult Age

*Xia Li[1], Håkan Fischer[2,3], Amirhossein Manzouri[2], Kristoffer N. T. Månsson[2,4] and Tie-Qiang Li[1,5,6]**

[1] Institute of Informatics Engineering, China Jiliang University, Hangzhou, China, [2] Department of Psychology, Stockholm University, Stockholm, Sweden, [3] Stockholm University Brain Imaging Centre, Stockholm, Sweden, [4] Centre of Psychiatry Research, Department of Clinical Neuroscience, Karolinska Institutet, Stockholm, Sweden, [5] Department of Clinical Science, Intervention, and Technology, Karolinska Institute, Solna, Sweden, [6] Department of Medical Radiation and Nuclear Medicine, Karolinska University Hospital, Solna, Sweden

OPEN ACCESS

Edited by:
Xiaopeng Song, Harvard Medical School, United States

Reviewed by:
Yameng Gu, The Pennsylvania State University (PSU), United States
Faruque Reza, Universiti Sains Malaysia Health Campus, Malaysia

***Correspondence:**
Tie-Qiang Li
tie-qiang.li@ki.se

Specialty section:
This article was submitted to Brain Imaging Methods, a section of the journal Frontiers in Neuroscience

Received: *31 August 2021*
Accepted: *28 September 2021*
Published: *20 October 2021*

Citation:
Li X, Fischer H, Manzouri A, Månsson KNT and Li TQ (2021) A Quantitative Data-Driven Analysis Framework for Resting-State Functional Magnetic Resonance Imaging: A Study of the Impact of Adult Age. Front. Neurosci. 15:768418. doi: 10.3389/fnins.2021.768418

The objective of this study is to introduce a new quantitative data-driven analysis (QDA) framework for the analysis of resting-state fMRI (R-fMRI) and use it to investigate the effect of adult age on resting-state functional connectivity (RFC). Whole-brain R-fMRI measurements were conducted on a 3T clinical MRI scanner in 227 healthy adult volunteers (N = 227, aged 18–76 years old, male/female = 99/128). With the proposed QDA framework we derived two types of voxel-wise RFC metrics: the connectivity strength index and connectivity density index utilizing the convolutions of the cross-correlation histogram with different kernels. Furthermore, we assessed the negative and positive portions of these metrics separately. With the QDA framework we found age-related declines of RFC metrics in the superior and middle frontal gyri, posterior cingulate cortex (PCC), right insula and inferior parietal lobule of the default mode network (DMN), which resembles previously reported results using other types of RFC data processing methods. Importantly, our new findings complement previously undocumented results in the following aspects: (1) the PCC and right insula are anti-correlated and tend to manifest simultaneously declines of both the negative and positive connectivity strength with subjects' age; (2) separate assessment of the negative and positive RFC metrics provides enhanced sensitivity to the aging effect; and (3) the sensorimotor network depicts enhanced negative connectivity strength with the adult age. The proposed QDA framework can produce threshold-free and voxel-wise RFC metrics from R-fMRI data. The detected adult age effect is largely consistent with previously reported studies using different R-fMRI analysis approaches. Moreover, the separate assessment of the negative and positive contributions to the RFC metrics can enhance the RFC sensitivity and clarify some of the mixed results in the literature regarding to the DMN and sensorimotor network involvement in adult aging.

Keywords: quantitative data-driven analysis (QDA), resting-state functional magnetic resonance imaging (R-fMRI), resting-state functional connectivity (RFC), connectivity strength index (CSI), connectivity density index (CDI), adult age

INTRODUCTION

Among the different analysis approaches for resting-state fMRI (R-fMRI) data, the anatomic region-of-interest (ROI)-based, and data-driven independent component analysis (ICA) methods are probably the most commonly used (Tyszka et al., 2014). Resting-state functional connectivity (RFC) results from the ROI-based and ICA derived methods are generally similar but conceptually different. The quantitative relationship between ROI-based and ICA derived measures of RFC has been investigated with computer simulation and experiment approaches (Joel et al., 2011; Rosazza et al., 2012). In theory, the ROI-based RFC measures can be shown to be the sum of the ICA derived RFC both for the within and between networks (Joel et al., 2011; Rosazza et al., 2012).

With ROI-based analysis the brain is first parcellated into predefined anatomical regions, the mean time course for each ROI is then determined. By calculating the temporal correlations in a pairwise fashion between the defined ROIs, for each R-fMRI dataset a correlation coefficient matrix of the ROIs can be obtained for further statistical assessment. Therefore, specific connectivity between specific regions is explicitly tested in a model-driven framework by using the average time courses of the selected ROIs as a temporal model. Since the RFC patterns do not necessarily coincide precisely with the atlas-based ROI definition, all voxels within predefined ROIs are not necessarily a part of the network-of-interest and functionally connected. This can potentially affect the accuracy and sensitivity of the ROI-based analysis (Song et al., 2016). On the other hand, ICA can reveal dynamics and spatially distributed brain networks in a data-driven fashion without the need of a temporal model. Beside motor and sensory networks, ICA studies have identified the brain networks involved in attentional control (Lawrence et al., 2003), including the task-dependent (Vossel et al., 2014) dorsal and ventral lateral attention networks (DAN and VAN), the task-independent (Raichle et al., 2001; Buckner et al., 2008) default mode network (DMN), and the salience network (SN), which was postulated to be the switching control network for the up-regulation of attention networks and the downregulation of the DMN (Menon and Uddin, 2010). The dynamic interactions between the DAN, VAN, DMN, and SN networks are believed to be the key for understanding the function and dysfunction efficient attention allocation for task performance.

Despite the growing consensus regarding the ICA-derived intrinsic RFC networks in the healthy brain with stable spatial components reproduced across studies (Damoiseaux et al., 2006; Smith et al., 2009; Allen et al., 2011), the precise number of independent components (NIC), as a prerequisite input parameter for ICA, is not known *a priori*. NIC can substantially influence the ICA outcomes (Wang and Li, 2015). Moreover, there is lack of gold standard for the selection of meaningful components to exclude non-interesting noise resources, such as ventricular, vascular, susceptibility, or motion-related artifacts (Wang and Li, 2013).

In this study we refined further of our quantitative data-driven analysis (QDA) framework based on the time course of individual voxel inside the brain. The QDA approach is data-driven as ICA and can generate two types of quantitative RFC metrics for each voxel inside the brain without the need for specifying a particular threshold, model or mode. Since it uses the time course of each voxel within the brain as the reference seed in turn to compute voxel-wise whole-brain correlational coefficient matrix, the size of the correlation matrix is equal to the number of voxels inside the brain. It is typical $N > 10^4$ for whole-brain R-fMRI datasets with 4 mm voxel size. To facilitate further statistical assessment of the whole-brain correlation matrix, we derive two types of voxel-wise RFC metrics from the correlation matrix, namely the connectivity strength index (CSI) and connectivity density index (CDI). CSI and CDI provide general connectivity metrics of strength and density for the local voxel with the rest of brain, respectively. These metrics can be used for straightforward statistical comparison to assess differences between groups and longitudinal changes of individuals. This is a basic requirement for radiological diagnosis in clinical practice.

Several voxel-based RFC metrics have been proposed in the literature. Among other things, the regional homogeneity (Zang et al., 2004; Meier et al., 2017; Reynolds et al., 2017), measures of low frequency oscillation including the amplitude of low frequency fluctuations (ALFF) and the fractional ALFF (Yang et al., 2007; Zang et al., 2007; Zou et al., 2008; Sun et al., 2016; Zhang X.D. et al., 2016; Pan et al., 2017), measurements of complexity, such as the Hurst exponent (Hayasaka and Laurienti, 2010; He, 2011; Ciuciu et al., 2014), and brain entropy (de Araujo et al., 2003; Zhao et al., 2010; Jia et al., 2017; Viol et al., 2017) have been used for studying the RFC in normal and diseased brains. These methods have yielded interesting results. However, there remains still some methodological issues to be addressed, such as the arbitrariness in the selection of cut-off frequency (Yang et al., 2007; Zang et al., 2007; Zou et al., 2008; Sun et al., 2016; Zhang X.D. et al., 2016; Pan et al., 2017), loss of information (Hayasaka and Laurienti, 2010; He, 2011; Ciuciu et al., 2014), and computation difficulty (de Araujo et al., 2003; Zhao et al., 2010; Jia et al., 2017; Viol et al., 2017). These technical difficulties may have contributed to the inconsistent findings in the published literature. Moreover, the different RFC metrics portray different aspects of R-fMRI signal and may have different sensitivities to the physiological activities and pathological abnormality (Golestani et al., 2017; Reynolds et al., 2017).

Both ICA and ROI-based approaches have previously been applied to study age-related changes in RFC (Bluhm et al., 2008; Biswal et al., 2010; Weissman-Fogel et al., 2010; Zuo et al., 2010; Dennis and Thompson, 2014; Alarcon et al., 2015; Zhang C. et al., 2016). Numerous studies have confirmed that reduced RFC in healthy aging in the DMN is correlated with cognitive deficit (Damoiseaux et al., 2008; Biswal et al., 2010; Campbell et al., 2013; Ferreira and Busatto, 2013; Scheinost et al., 2015). There is accumulating evidence to support the notion that elderly adults typically have reduced RFC across most parts of the DMN, particularly in the dorsal medial prefrontal cortex (mPFC) and the ventral and posterior cingulate cortex (PCC; Campbell et al., 2013; Scheinost et al., 2015). However, in the reported literature there is also considerable variability concerning age-related RFC differences in the limbic and other DMN subsystems. For example, some studies have found age-related RFC reduction

in the hippocampal (Damoiseaux et al., 2008; Campbell et al., 2013; Scheinost et al., 2015) and subcortical regions (Ystad et al., 2010), whereas others reported either no significant decline or elevated RFC in some of the specific hippocampal (Pasquini et al., 2015) and DMN regions (Salami et al., 2014; Damoiseaux et al., 2016). The discrepancies in the reported findings among the different R-fMRI studies may reflect not only variability in the sample characteristics, but also diversity in the data processing methods for deriving the different RFC metrics for connectivity of specific pathways.

The main objective of this study is to develop a QDA framework to analyze R-fMRI data and derive quantitative, model-free, and threshold-free RFC metrics, which are optimally sensitive to physiological and pathological changes in the central nervous systems. We used the proposed metrics to assess if and how adult age in healthy subjects influences these RFC metrics.

EXPERIMENTAL AND METHODS

Participants

A total of 227 volunteers (aged 18–76 years, male/female = 99/128) completed the study and were recruited into the study through the local media advertisement in the Stockholm region. All participants were right-handed, and native Swedish speakers with normal or corrected-to-normal vision. They all reported being free of a history of neurological, psychiatric, and cardiovascular diseases. None of the participants reported any use of psychotropic drugs. Each subject signed informed consent before completing the magnetic resonance imaging (MRI) examination protocol. They were financially compensated for their participation. The regional ethics committee approved the study protocol 2014/1982-31/1, which was conducted in line with the declaration of Helsinki.

Magnetic Resonance Imaging Data Acquisition Protocol

The MRI data acquisition was conducted on a whole-body 3T clinical MRI scanner (Magnetom Trio, Siemens Medical Solutions, Erlangen, Germany) equipped with a 32-channel phased-array receiving head coil. All data was acquired at Karolinska University Hospital, Huddinge, Stockholm, between noon and 5:00 PM. The MRI data acquisition protocol included the following scanning sessions: (1) 3-plane localizer; (2) Conventional clinical MRI scans including 3D T1-weighted MPRAGE, T2 and FLAIR scans; and (3) A session of 375 s long R-fMRI measurements. The main acquisition parameters for the R-fMRI data included the following: TE/TR 35/2,500 ms, flip angle = 90°, 34 slices of 3.5 mm thick, FOV = 225 mm, matrix size = 76 × 76, data acquisition acceleration with GRAPPA parallel imaging method (iPAT = 2), and 150 dynamic timeframes. The T1-weighted MPRAGE images used for co-registration with functional images were acquired with the following parameters: TR = 1,900 ms, TE = 2.52 ms, FA = 9 degrees, FOV = 256, voxel size 1 mm × 1 mm × 1 mm. The acquisition parameters for the FLAIR image were the following: TE/TR = 89/9,000 ms, flip angle = 130°; inversion time (TI) = 2,500 ms, slice thickness = 4.0 mm, and FOV = 199 × 220 mm. An experienced radiologist inspected both the FLAIR and T1-weighted images for potential signs of neuropathology.

We used foam patting to fix each subject's head carefully in the head coil to reduce involuntary head motions. During the R-fMRI data acquisition the participants were instructed to focus their sight on a white cross in black background projected on a screen installed in front of their eyes. The subjects were also instructed to not think about anything particular during the R-fMRI session.

Resting-State Functional Magnetic Resonance Imaging Data Pre-processing

The R-fMRI datasets underwent a preprocessing procedure, which has been described elsewhere in details (Li et al., 2021) and was performed with AFNI (Version Debian-16.2.07~dfsg.1-3~nd14.04+1, http://afni.nimh.nih.gov/afni) and FSL[1] programs with a bash wrapper shell (Wang and Li, 2013, 2015). After temporal de-spiking, six-parameter rigid body image registration was performed for motion correction. The average volume for each motion-corrected time series was used to generate a brain mask to minimize the inclusion of the extra-cerebral tissues. Spatial normalization to the standard MNI template was performed using a 12-parameter affine transformation and a mutual-information cost function. During the affine transformation the imaging data were also re-sampled to isotropic resolution using a Gaussian kernel with 4 mm full width at half maximum (FWHM). The co-registered average image volume for the cohort has 28,146 non-zero voxels inside the brain and was used to generate the average brain mask for the preprocessed whole-brain R-fMRI data with 4 mm spatial resolution. Nuisance signal removal was performed by voxel-wise regression using 14 regressors based on the motion correction parameters, average signal of the ventricles and their 1st order derivatives. After baseline trend removal up to the third order polynomial, effective band-pass filtering was performed using low-pass filtering at 0.08 Hz. Local Gaussian smoothing up to FWHM = 4 mm was performed using an eroded gray matter mask (Wang and Li, 2015).

Pearson's correlation coefficients (CC) were computed between the time courses of all pairs of voxels inside the brain, leading to a whole-brain functional connectivity matrix for each subject. This computation was performed for all voxels located within the brain mask, which was generated by overlapping the registered brains of all participants. This brain mask contained 28,146 voxels and each voxel inside the brain was used as the seed voxel in turn. Therefore, the size of the CC matrix size is 28,146 × 28,146. Each row or column of the CC matrix corresponds to the CC image volume for the seed voxel with the rest of the brain. That is the connectivity map for the seed voxel. As schematically illustrated in **Figure 1**, based on the CC histogram for each row of the matrix we derived the following two types of

[1]http://www.fmrib.ox.ac.uk/fsl

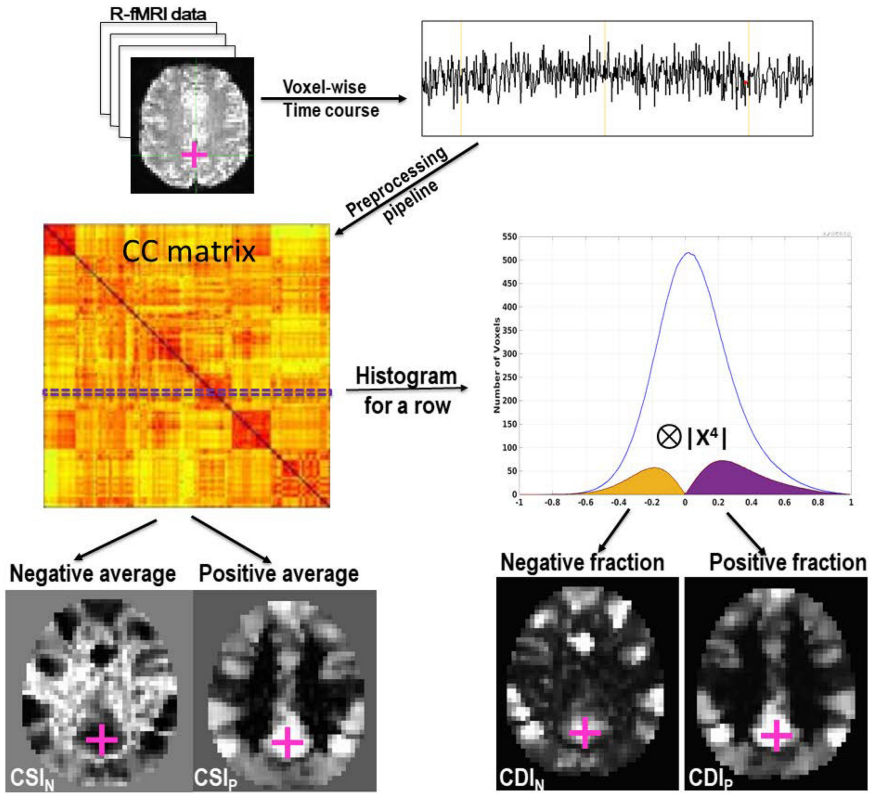

FIGURE 1 | A schematic overview to illustrate the QDA framework. With QDA the time course of each voxel is used in turn to compute the whole-brain CC matrix. For each row of the CC matrix, we compute a CC histogram with 200 evenly binned intervals within [−1, 1]. The histogram shown in the graph is the cohort's average CC histogram for a voxel within the PCC as marked with the cross. Two types of RFC images are derived from the CC matrix: (1) CSI_P and CSI_N whose voxel values are the averages of the positives and negatives in each row of the CC matrix, respectively. (2) CDI_P and CDI_N whose voxel values are the positive and negative parts of the convolution between the CC histogram and the kernel, respectively.

threshold-free voxel-wise RFC metrics: the CSI and CDI. As we are interested in systematically investigating all relevant synchronized activities in the whole brain, we quantify the negative and positive portions of the CC histogram separately to avoid information cancelation, sensitivity reduction, and statistical interference. From here on, the subscripts "N" and "P" are used to indicate the negative and positive portions of the RFC metrics, respectively. The metrics without subscripts refer to the mixed measures without distinction of the negative and position correlations.

As shown in **Figure 1**, the voxel value for the CSI_P and CSI_N are defined as the averages of the positives and negatives in each row of the CC matrix, respectively. That is

$$CSI_P = \left(\sum_{CC>0} CC_{row}\right)/np \tag{1}$$

$$CSI_N = \left(\sum_{CC<0} CC_{row}\right)/nn \tag{2}$$

Where CC_{row} refers to a row in the CC matrix. *np* and *nn* refer to the number of positive and negative correlation coefficients in a row of the CC matrix, respectively. The voxel values for CDI are defined as the convolution between the CC histogram and a kernel function. That is

$$CDI = Hist\,(CC_{row}) \otimes kernel \tag{3}$$

The CDI_P and CDI_N correspond to the positive and negative portions of the convolution defined in Eq. (3), respectively. To facilitate statistical comparison it is useful to transform the raw RFC metrics into standard *Z*-score using the following formula:

$$Z = (RFC - u)/\sigma \tag{4}$$

Where μ and σ are the mean and standard deviation of the corresponding RFC metrics, respectively. For optimization of the CDI sensitivity, we investigated 6 different kernel functions including

$$k_{i=1,2,\ldots,4} = \left|x^i\right|, \tag{5}$$

$$k_5 = \left|\sin^2(\pi/2x)\right|, \tag{6}$$

$$k_6 = step(|x| - 0.3), \tag{7}$$

where $x \subset [-1,1]$ corresponds to the interval of the correlation coefficients. The kernels are also graphically depicted in **Figure 2**.

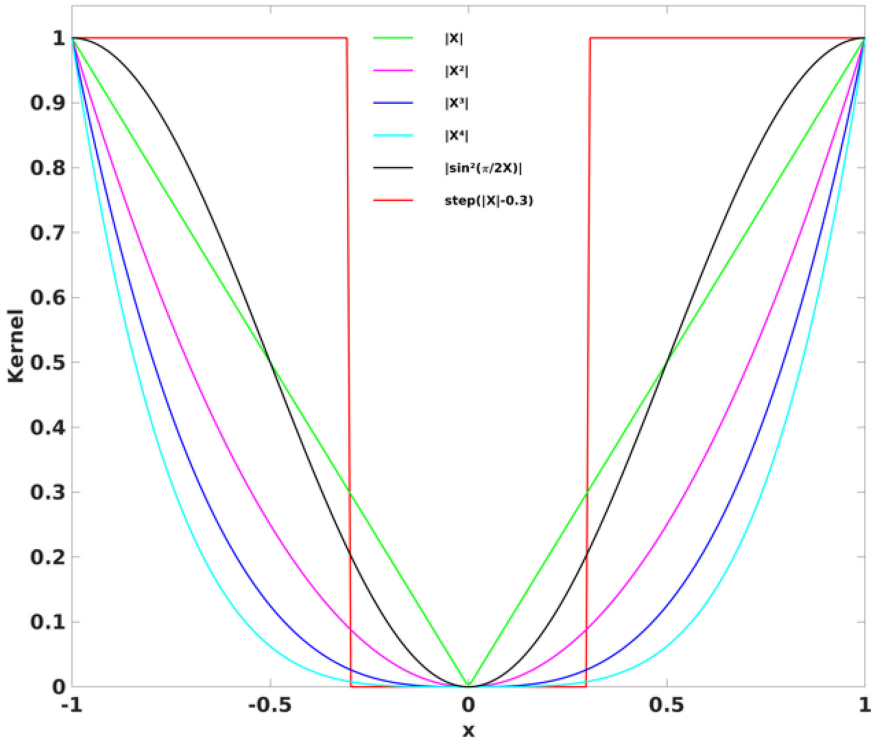

FIGURE 2 | The six different kernel functions investigated in the study to derive the CDI_P and CDI_N metrics. The widely used threshold method can be considered as the case for the square-well kernel function (k_6).

The kernel should weight the higher correlation coefficients more than the lower ones. The widely used threshold approach can be considered as the case of the square-well kernel function k_6. For illustration, an arbitrary threshold of 0.3 was used here. The CSI metrics can also be considered as a special case of CDI corresponding to a kernel of the sign function.

Statistical Analyses

To investigate if and how the RFC metrics are influenced by heathy aging for the studied cohort we performed voxel-wise linear regression analyses of the CSI and CDI metrics versus the subject's age, while gender was treated as a covariate by using the AFNI program 3dRegAna to extract the regression parameter β and linear coefficient r. The statistical significance was assessed by using a two-step approach. Firstly, we imposed a voxel-wise threshold $p < 0.001$ (uncorrected corresponding t-score ≥ 3.34) to form the initial cluster candidates. Secondly, we performed permutation simulations without assuming a particular form of probability distribution for the voxel values in the statistic images to identify the brain ROI out of the initially detected clusters at family-wise error rate $p \leq 0.05$. Using the detected ROIs as masks, the mean values of the RFC metrics for each ROI were evaluated and plotted against the subjects' age. Besides linear regression analysis with age, we performed also verification using two-sample t-test between the young and elderly subgroups. For this, we selected all subjects aged 18–30 years as the young subgroup ($n = 124$, males/females = 51/73), and all subjects aged 64–76 years as the elderly subgroup ($n = 76$, males/females = 35/41). To keep sufficient age gap between the young and elderly subgroups the remaining 27 subjects in the age range of 31–63 years old were excluded from the t-test. In the selection of subgroups we attempted to minimize the number of excluded subjects with intermediate ages, maximize the age gap between the subgroups, and keep similar number of subjects and age ranges. It should be emphasized that all 227 subjects were included in the regression analysis.

RESULTS

The Quantitative Data-Driven Analysis Framework

The CC histogram for each seed voxel in the brain is dependent on its location in the brain (see **Supplementary Materials**). **Figure 3** shows the average CC histogram of the cohort for a seed voxel in the PCC as illustrated by the cross in **Figure 1**. The histogram is somewhat asymmetric and shifted toward the positive side. This is quite typical at least for voxels within gray matter. Selecting different threshold values along the histogram allows us to examine the RFC networks of different connection strengths associated with the selected seed voxel. As shown in **Figure 3**, at high negative threshold (**Figures 3A,B**) we observe the DMN. At low negative threshold, we observe its association with cerebral spinal fluid (CSF) space and white

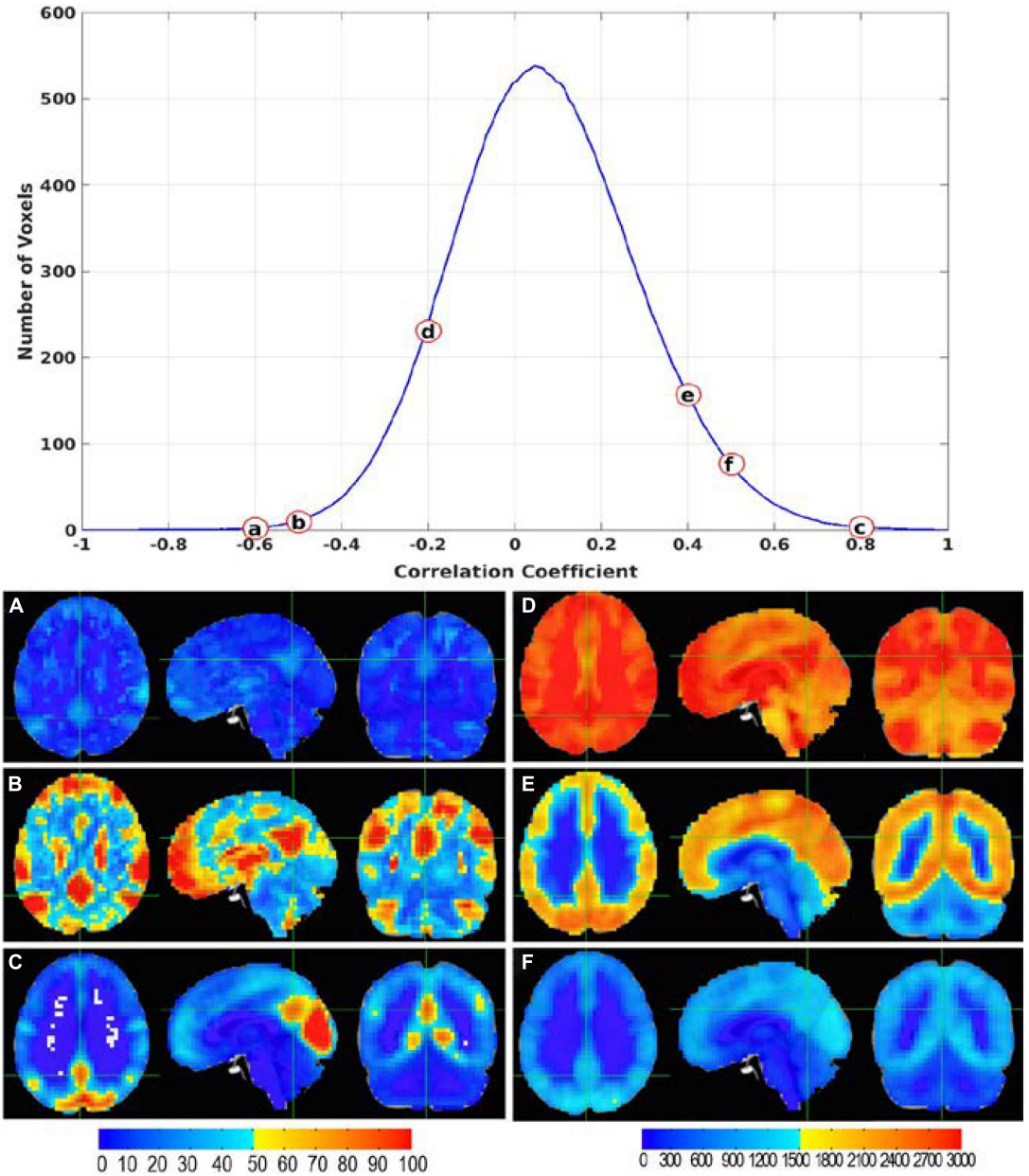

FIGURE 3 | The average CC histogram of the cohort for a seed voxel in the posterior cingulate cortex (PCC) as indicated by the green cross. Selecting different threshold values along the histogram allows us to examine the functional connection networks of different strengths **(A–F)** associated with the seed voxel in the PCC.

matter (**Figure 3D**). At moderately high positive threshold, the PCC voxel is not only a part of the DMN, but also connected to most of the cortical gray matter (**Figures 3E,F**). At high positive threshold, the PCC voxel is associated with the posterior portion of the DMN and the visual cortex (**Figure 3C**). The visual cortex looks relatively bright at high threshold indicating a relatively high number of voxels are associated with the visual network or voxels within the visual cortex are associated with each other at high threshold criterion. The idea of the QDA framework is to avoid the arbitrary threshold and optimize the contribution of meaningful informatics to the quantitative RFC metrics.

Figure 4 shows an axial slice of CDI_P and CDI_N images for a typical R-fMRI dataset (from a 36 year old male subject). Multiple brain regions depict high CDI_P including the bilateral mPFC, superior and middle temporal gyri (MTG), inferior and superior parietal lobule, precuneus and PCC. These regions have been described as RFC hubs implying their important role in neural signaling and communication across the brain (Buckner et al., 2009; Tomasi and Volkow, 2011). On the other hand, the PCC, insula cortex. White matter and CSF regions have high CDI_N metric. The contrast and intensity variations across each row in **Figure 4** demonstrate that selection of the kernel

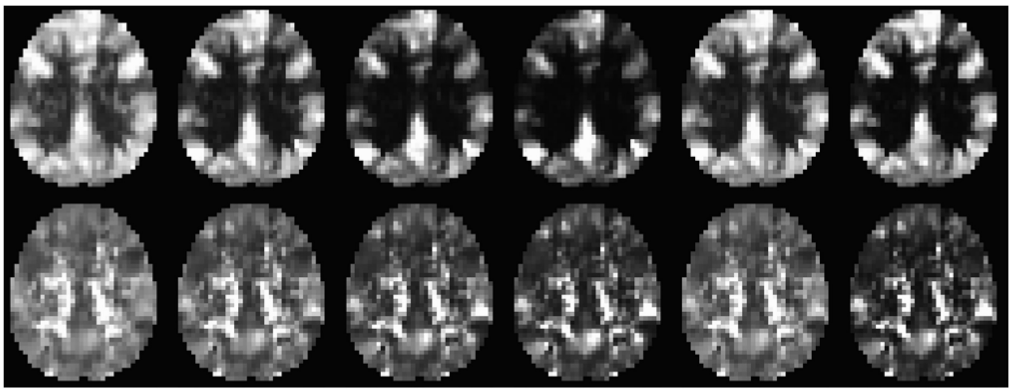

FIGURE 4 | An axial slice of the CDI_P (upper row) and CDI_N (lower row) metrics derived from a typical R-fMRI dataset (a male subject of 36 year's age). The images from left to right depict the results for the following 6 kernel functions $|x|$, $|x^2|$, $|x^3|$, $|x^4|$, $\sin^2(\pi/2x)$, and $\text{step}(|x| - 0.3)$, respectively.

function can optimize the contrast and signal-to-noise ratio of the CDI metrics.

Resting-State Functional Connectivity Changes Associated With the Adult Age

The linear regression results for the CSI, CSI_N, and CSI_P data versus subjects' age are summarized in **Figure 5** and **Table 1**. The corresponding results for the CDI, CDI_N, and CDI_P are shown in **Figure 6** and **Table 2**. The CSI metric without separation of the negative and positive correlations shows decline of the functional connectivity strength with age in the superior and middle prefrontal gyrus (MFG) and increase of connectivity strength in the precuneus and right inferior parietal lobule (r-IPL). The more specifically defined CSI_N and CSI_P metrics are more sensitive to the adult age effect and the detected brain volumes with significant aging effect are nearly tripled compared with that for the CSI metric. With CSI_N and CSI_P we also observe a more intricate pattern of change with the adult age, which are summarized as follows:

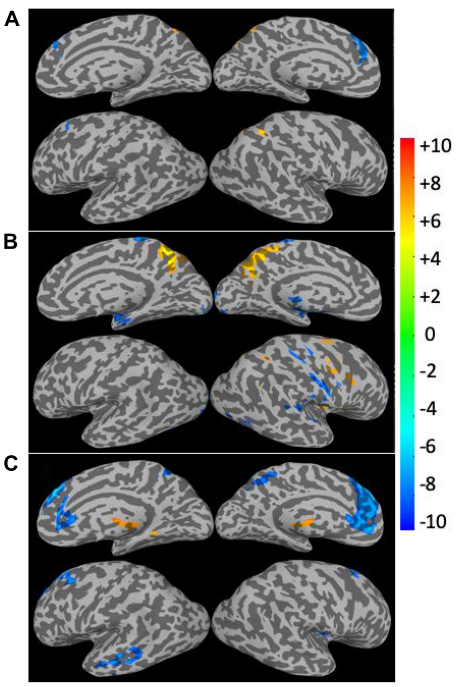

FIGURE 5 | Brain regions with significant correlation ($p < 0.05$, corrected) between the connectivity strength metrics and the subject's age. The results for the CSI **(A)**, CSI_N **(B)**, and CSI_P **(C)** are depicted separately. The Color bar shows the *t*-score level.

(1) The CSI_P shows mainly decline trend with adult age (negative β and *r*) in the extended DMN including superior and MFG, PCC, bilateral insula cortex and left middle temporal gyrus (l-MTG) except for putamen where upregulation of CSI_P was observed.
(2) The CSI_N depicts a more complicated pattern of dependence on adult age. The negative connectivity strength was reduced (positive β and *r*) with adult age in the PCC, right insula cortex and IPL, while enhancement (negative β and *r*) was detected in the sensorimotor network (paracentral lobule, bilateral postcentral gyri), bilateral parahippocampal cortices (PHC), and right superior temporal gyrus.
(3) There are two brain regions where both the CSI_N and CSI_P demonstrated significant reduction trend with adult age, which were detected by applying the logical "AND" operation to the regression results for the CSI_P and CSI_N. As shown in **Table 2** and **Figure 7**, the two overlapping ROIs in the PCC and r-insula cortex depict significant down-regulation of CSI_P and CSI_N metrics with the subjects' age.

To study the specific connectivity associated with the two ROIs defined by the overlap between the CSI_N and CSI_P metrics, we computed Pearson's correlation maps for the time courses of the seeds as defined by the overlapping ROIs depicted in **Figure 7A**. As expected, the associated RFC network for the PCC ROI is obviously the well-known DMN and include

TABLE 1 | The brain regions where the connectivity strength metrics are significantly ($p < 0.05$) correlated with the subjects' ages.

RFC	Voxel	X_{cm}	Y_{cm}	Z_{cm}	β (10^3)	*r*	*p*	Annotation
CSI	239	+2.1	+63.0	+47.9	9.50	0.459	<0.01	Precuneus
	152	+3.4	−47.3	+30.1	−9.72	−0.389	<0.01	Superior and MFG
	62	−38.5	+55.3	−35.5	9.57	0.354	<0.01	R-IPL
CSI_N	237	+0.0	+53.1	+27.3	12.29	0.413	<0.01	PCC
	171	−42.6	−10.4	+11.0	12.36	0.411	<0.01	R-insula cortex
	161	−2.3	+28.2	+59.4	−11.05	−0.371	<0.01	Paracentral lobule
	153	−49.1	+47.6	+41.2	11.62	0.441	<0.01	R-IPL
	133	−39.8	+25.7	+55.5	−10.99	−0.325	<0.01	R-postcentral gyrus
	75	−27.3	−3.8	−34.0	−9.99	−0.450	<0.01	R-PHC
	67	−56.8	+14.6	+5.9	−9.28	−0.400	<0.01	R-STG
	58	+18.4	+0.4	−18.9	−9.36	−0.441	<0.01	L-PHC
	56	+42.0	+25.9	+57.1	−10.38	−0.309	<0.01	L-postcentral gyrus
	713	+2.0	−45.4	+23.6	−10.37	−0.487	<0.01	Superior and MFG
CSI_P	157	−1.1	+14.7	−17.8	7.96	0.506	<0.01	Putamen
	110	+55.7	+13.1	−19.5	−9.49	−0.433	<0.01	L-MTG
	75	+2.7	+48.5	+31.1	−9.01	−0.336	<0.01	PCC
	53	−40.0	−8.7	+0.8	−8.48	−0.361	<0.01	R-insula cortex
	52	+45.1	−10.5	−8.9	−8.36	−0.376	<0.01	L-insula cortex
CSI_N CSI_P	70	+2.8	+49.0	+31.0	14.15	0.374	<0.01	PCC (CSI_N)
					13.37	0.362	<0.01	PCC (CSI_P)
	34	−40.8	−10.0	+0.0	−9.04	−0.334	<0.01	R-Insula cortex (CSI_N)
					−8.63	−0.336	<0.01	R-Insula cortex (CSI_P)

The volume, center of mass coordinates in MNI space, regression parameter (β), linear correlation coefficient (r), statistical significance (p), and anatomic annotations are specified. The default is bilateral, while R and L- indicate the right and left hemisphere of the brain, respectively. CSINP indicates the overlapping results between CSIN and CSIP.

4 negatively correlated brain regions, which are the bilateral IPL and insula cortices (see **Figure 7B**). On the other hand, the associated RFC network for the insula ROI includes the PCC and bilateral precuneus as the negatively correlated brain regions (**Figure 7C**) **Figure 8**. Shows the anti-correlated brain regions between the above 2 RFC networks as obtained by multiplying the two correlation maps with each other and applying negative threshold at CC $\leq (-0.5)$. The mutually inclusive anti-correlation between the PCC and the right insular cortex explains why both CSI_P and CSI_N metrics in these regions depict declines with the adult age.

Figure 9 shows the ROI average of the CSI_N and CSI_P metrics in the PCC and right insula cortex as a function of the subject's age. With normal aging, both the CSI_P and CSI_N are reduced in these brain regions (overlap shown in **Figure 7A**). Therefore, the PCC and right insula are particularly sensitive to the adult age effect. However, the aging effect is barely detectable by the unseparated CSI metric (see **Table 1**).

As expected, the CDI_P and CDI_N metrics derived by using the different kernels differ in their sensitivity in detecting the adult age effect. **Figure 10A** shows the detected brain volumes where the CDI_P and CDI_N metrics are significantly associated with the adult age. The sensitivity difference of the kernels is also manifested in the regression parameter β which are detailed in **Table 3** and **Figure 10B**. To compare the similarity of the detected aging effects among the CDI metrics of different kernels, we assessed the joint overlapping brain regions detected by the different CDI_N and CDI_P metrics of different kernels. The observed overall trends of RFC enhancement or decline with age are quite similar. The joint overlapping volumes for the CDI_P and CDI_N metrics of different kernels are 733 and 671 voxels, respectively. Moreover, there is also a reasonable anatomic consistency between the results of the connectivity strength metrics and connectivity density metrics. As detailed in **Tables 2**, **3**, the anatomical locations of the joint overlapping regions for the different CDI_P metrics match those for the 3 largest ROIs identified by the CSI_P results (see **Table 1**). Similarly, the brain regions of the joint overlapping for the different CDI_N metrics are largely the same as those identified by the CSI_N data (see **Table 1**). However, it should be noted that the β parameters for the CDI_N and CSI_N have opposite signs even through the trend of change with the adult age is the same. This is because the negative connectivity strength (CSI_N) is negative in nature, while the connectivity density corresponding to the negative correlation (CDI_N) is always positive. Therefore, the enhancement of the negative connectivity strength (CSI_N) with age (for example in the sensorimotor network) corresponds to a negative β, while the connectivity density result corresponds to a positive β value.

DISCUSSION

Effects of Adult Age on Resting-State Functional Connectivity

Age is an important risk factor for declines of neural cognitive functions and pathology of neurodegenerative diseases. It is also

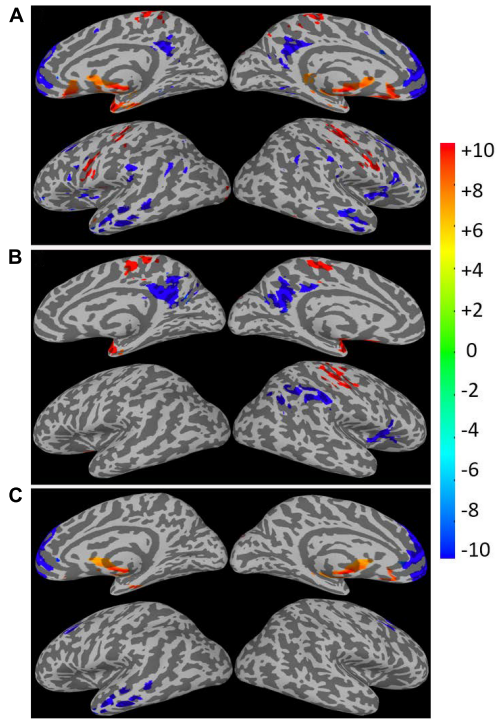

FIGURE 6 | Brain regions with significant correlation ($p < 0.05$, corrected) between the connectivity strength metrics and the subject's age. The results for the CDI **(A)**, CDI_N **(B)**, and CDI_P **(C)** are depicted separately. The Color bar shows the *t*-score level.

a complex metric difficult to precisely interpret the involved physiology. Healthy individuals of similar age may have quite different vascular and brain-health status. It follows that age is not a single strongest predictor for the RFC in the brain. This is likely to be the reason why the linear regressions of the RFC metrics with the adult age depict substantial scatters and relative low correlation coefficients. The impact of the potential confounds and pre-processing strategies that can mitigate them have been extensively investigated in the published literature (Bluhm et al., 2008; Biswal et al., 2010; Weissman-Fogel et al., 2010; Zuo et al., 2010; Dennis and Thompson, 2014; Alarcon et al., 2015; Zhang C. et al., 2016; Geerligs et al., 2017; Hussein et al., 2020). Here we focus on comparing our findings in the context of documented literature results, particularly the adult age effect in the DMN, dorsal attention network (DAN), sensorimotor network, and subcortical brain regions.

With QDA, we found support for RFC decline with advancing adult age in multiple brain regions of the DMN and DAN, including superior and MFG, PCC, MTG, and IPL. Age-related RFC decrements in the DMN and DAN have previously been reported in numerous R-fMRI studies using ROI and ICA based analysis (Buckner et al., 2008; Damoiseaux et al., 2008; Dennis and Thompson, 2014; Scheinost et al., 2015; Luo et al., 2020). Our findings regarding to the RFC changes in the DMN are overall in agreement with previous reported results (Damoiseaux et al., 2008, 2016; Koch et al., 2010; Ystad et al., 2010; Williams, 2013; Lu et al., 2014; Persson et al., 2014, 2015; Salami et al., 2014). Besides the DMN and DAN, normal aging was associated with RFC increase in the sensorimotor, subcortical network, and para-hippocampal cortex. This has also been reported previously (Persson et al., 2015, 2016; Damoiseaux et al., 2016; Geerligs et al., 2017; Hussein et al., 2020; Luo et al., 2020). We didn't find significant age-related RFC declines in precuneus and specific sub-regions of the hippocampal cortex as reported in previous studies (Salami et al., 2014; Damoiseaux et al., 2016). Since we assessed the negative and positive correlation separately, this may allow us to detect more intricate age-related RFC changes in the brain. To illustrate this point, we analyzed further the 3 ROIs with significant correlation between the CSI and the subject's age. As shown in **Tables 1**, **4** and **Figure 11**, the detected ROI in the precuneus depicted significant positive linear correlation between CSI and the subject's age ($\beta = 9.50 \times 10^{-3}$, $r = 0.459$), even though the CSI_P and CSI_N in the same ROI showed only a slight (not significant) increment and decrement with age, respectively, i.e., contribution from a low-significant CSI_P increment and a non-significant CSI_N decrement resulted in a highly significant increment trend in the CSI metric. With the same line of reasoning, we can explain why the MFG ROI detected by the CSI metric is much smaller than that detected by the CSI_P metric, because the decremental trend in the CSI_P metric was partially canceled by the CSI_N contribution. This can also explain why we didn't detect significant CSI decrement with the adult age in the PCC and R-insula, because both the CSI_P and CSI_N metrics exhibited significant decremental trends with age and their contributions annulled each other. Therefore, it is important to pay attention to the precise definition of the RFC when comparing the results of different studies.

Both CSI_P ($r = 0.506$, see **Table 1**) and CDI_P ($r = 0.577$, see **Table 2**) showed age-related enhancement Caudate/putamen and the association are quite strong. This finding based on QDA approach are consistent with previous reports (Manza et al., 2015; Rieckmann et al., 2018) from ROI-based studies aimed to investigate the aging effect on specific functional connectivity of in the striatum-cortical system. It is well known that the striatum-somatomotor connection is primarily associated with motor performance, especially the "automatic" performance of already learned movements. It has been reported that posterior putamen and pallidum decreases in connectivity to left somatomotor cortex with age (Manza et al., 2015). This provides a reasonable explanation for the commonly observed motor deficits as in elderly subjects. There is also growing evidence support the notion that striatum-cortical connectivity is potentially important for memory function at older age. Intriguingly, this is related to the enhanced RFC with age in the putamen/caudate. Several studies have reported that increased striatum functional connectivity in older adults typically reflects less negative connectivity between two regions belonging to different networks, and the increased connectivity is often negatively associated with cognitive performance (Rieckmann et al., 2018). Therefore, better understanding the RFC change with

TABLE 2 | The brain regions where the connectivity strength metrics are significantly ($p < 0.05$) correlated with the subjects' ages.

RFC	Voxel	X_{cm}	Y_{cm}	Z_{cm}	β (10^3)	r	$p(10^{-3})$	Annotation
CDI	736	+0.7	−45.4	+24.2	6.511	0.603	<0.01	Superior amd MFG
	663	−6.0	+5.6	−19.3	−13.43	−0.469	<0.01	Caudate/putamen
	100	+0.7	+48.4	+30.8	−14.14	−0.325	<0.01	Precuneus
	99	+56.3	+16.8	−16.2	−11.04	−0.412	<0.01	L-ITG
	86	−45.9	−10.2	+6.6	−10.81	−0.387	<0.01	R-insular cortex
	63	−2.7	+33.0	+66.3	11.48	0.306	<0.01	r-postcentral gyrus
	49	−58.3	+15.3	−16.8	−10.83	−0.408	<0.01	R-ITG
CDI_N	243	−0.0	+52.4	+29.9	−14.78	−0.381	<0.01	PCC
	124	−2.3	+28.5	+58.3	11.49	0.354	<0.01	Primary motor cortex
	98	−48.4	+47.3	+42.1	−14.41	−0.426	<0.01	R-IPL
	96	−40.1	+25.2	+55.8	12.09	0.327	<0.01	R-postcentral gyrus
	85	+20.5	−2.2	−20.7	10.52	0.423	<0.01	L-piriform cortex
	83	−44.3	−13.1	+3.1	−16.74	−0.375	<0.01	R-insular cortex
	56	−27.3	−6.6	−31.4	10.12	0.403	<0.01	R-fusiform gyrus
	54	+40.8	+25.1	+57.6	10.00	0.302	<0.01	L-postcentral gyrus
	39	+38.1	−12.3	+4.2	−13.85	−0.381	<0.01	L-insular cortex
	37	+57.0	+9.2	+30.8	10.72	0.315	<0.01	L-postcentral gyrus
	36	+47.6	+19.1	+6.2	8.68	0.376	<0.01	L-STG
	36	−7.6	−14.3	+40.1	−11.73	−0.349	<0.01	ACC
	31	−47.2	+21.0	+8.2	8.32	0.382	<0.01	R-STG
	804	+2.0	−45.3	+24.8	−13.14	−0.476	<0.01	Superior and MFG
	485	+1.1	+8.*r*05	−5.0	5.69	0.577	<0.01	Caudate/putamen
CDI_P	92	+55.9	+14.2	−18.2	−10.23	−0.400	<0.01	L-ITG
	50	−30.2	−9.1	−33.3	7.53	0.388	<0.01	R-ITG
	30	+0.6	+46.2	+33.2	−12.87	−0.303	<0.01	PCC
CDI_NCDI	23	−28.7	−8.5	−32.1	10.81	0.372	<0.01	R-parahippocampal (CDI_N)
					7.186	0.376	<0.01	R-parahippocampal (CDI_P)
	23	+0.2	+47.2	+33.3	−17.27	−0.330	<0.01	PCC (CDI_N)
					−12.96	−0.303	<0.01	PCC (CDI_P)

The volume, center of mass coordinates in MNI space, regression parameter (β), linear correlation coefficient (r), statistical significance (p), and anatomic annotations are specified. The default is bilateral, while R and L- indicate the right and left hemisphere of the brain, respectively. CDI_{NP} indicates the overlapping results between CDI_N and CDI_P.

adult age in the striatum-cortical system can be potentially useful for assessing motor as well cognitive functions in elderly subjects.

Methodological Issues

The QDA framework proposed in the study is a voxel-wise and data-driven approach. It has the following two unique features: (1) It can avoid confounding caused by the cancelation of the negative and positive correlations by assessing the negative and positive portions of the CC histogram separately; (2) It derives different RFC metrics based on the connectivity strength and density by utilizing the concept of convolutions with different kernels. The metrics weight all the correlations of a given voxel with the rest of the brain according to the amplitudes of the correlation coefficients and disregard the anatomical distance between the correlation pairs. This permits a comprehensive characterization of the intrinsic activities of each voxel without the use of an arbitrary threshold. The QDA approach can encapsulate the widely used threshold approach as a special case of the square-well kernel function. The widely used degree centrality corresponds precisely this square-well kernel situation which adopts a somewhat arbitrary threshold and every connection above the threshold are weighted equally. Even the CSI metrics can be encapsulated under the convolution concept for a special kernel of the sign function. This provides a unified view for RFC and can facilitate its further optimization. The QDA framework uses the time course of each voxel within the brain as the seed reference to compute voxel-wise whole-brain correlational coefficient matrix. For whole-brain R-fMRI data acquired at 4 mm spatial resolution, the correlational coefficient matrix is in the order of 10^5 and is currently not practical for direct visualization and statistic assessment. Particularly, when data are acquired with higher spatial resolution, e.g., 2 mm, the matrix size is increased by 8×8 times. Therefore, for data reduction, we derived two types of voxel-wise RFC metrics from the correlational coefficient matrix without the need for specifying a particular seed, threshold, model, or mode. As their names indicated, CSI and CDI are aimed to capture the local (voxel) connectivity strength and density with rest of brain, respectively. The QDA metrics can assess the general connectivity with the rest of the brain without specifying a specific path or network. The QDA method does not highlight the specific

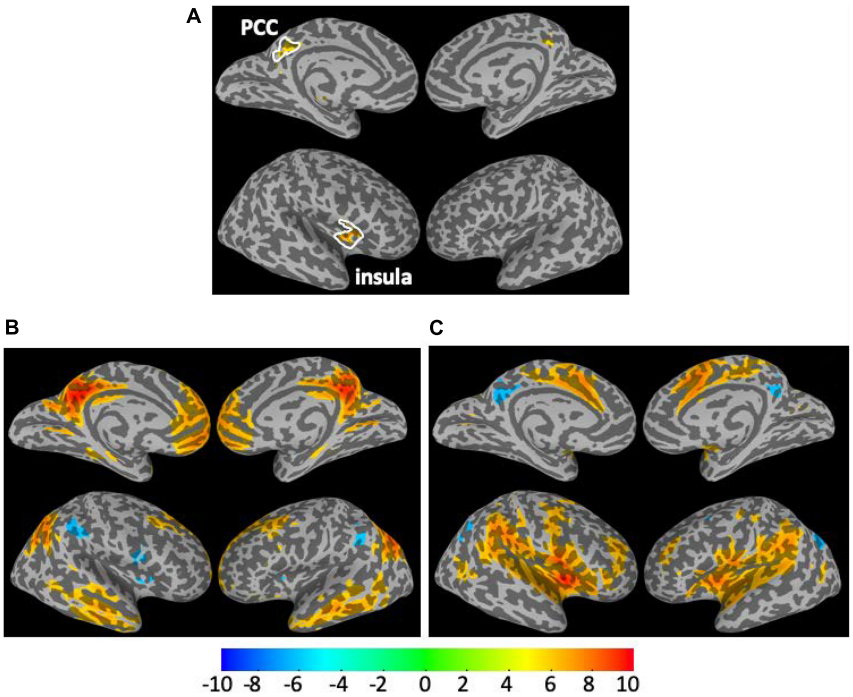

FIGURE 7 | The overlapping ROIs in the PCC and right insula cortex where both the CSI_P and CSI_N metrics depict significant decline with the adult age **(A)**. The one sample *t*-test maps for the Pearson's correlation maps associated the seeds defined as the overlapping ROI in the PCC **(B)** and insula cortex **(C)**.

connectivity changes between selected brain regions. The precise neural correlate of R-fMRI signal is currently not well understood (Hyder and Rothman, 2010). However, it is reasonable to assume that the R-fMRI signal fluctuations indirectly reflect the slow modulations of neuronal activities at rest. Furthermore, the sigmoid function has been widely accepted as the logistic function of neuronal activation instead of a square-well. With current status of knowledge, we cannot identify a convolution kernel to reveal a particular feature of the neurophysiology. However, we can attempt to optimize the kernel to reduce bias and improve sensitivity of the RFC metrics to pathophysiological changes.

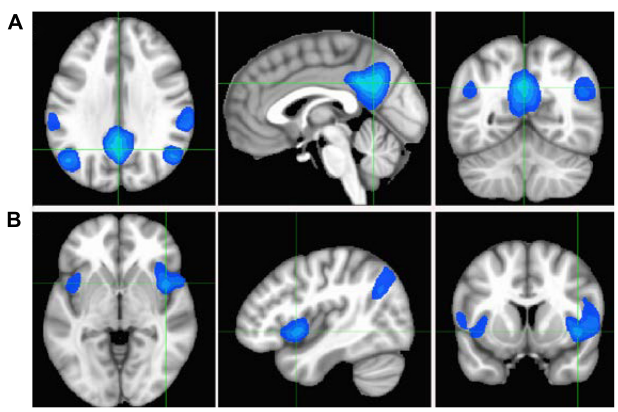

FIGURE 8 | Cross-sectional display of the anti-correlation network associated with the PCC **(A)** and insula **(B)** seeds as derived by multiplying the correlation maps shown in **Figures 7B,C** and applying a negative threshold at CC ≤ (−0.5). The crossing points of green lines depict the center of mass for PCC and insula ROIs.

The current results based on the QDA framework should be interpreted in the context of some technical and biological limitations. Firstly, at a TR of 2,500 ms, the cardiac and respiratory fluctuation effects might be aliased into the low frequency R-fMR signal fluctuations. The regression up-to the 1st order derivative of the head motions and lowpass filtering could not eliminate the effects of these physiological noises (Muschelli et al., 2014; Pruim et al., 2015; Bright et al., 2017; Parkes et al., 2018). Thus, these aliasing effects could reduce the specificity of the RFC metrics, or even might further confound the detected RFC differences between the young and elderly subgroups. With the more up-to-date acquisition techniques, such as multi-band simultaneous acquisition of multiple slices and compress-sensing with high under-sampling factor, it is possible to use a shorter TR (e.g., 500 ms) and higher spatial resolution for the data acquisition. Therefore, these physiological effects may be further mitigated.

Secondly, the resting state is associated with spontaneous thoughts and cognitive processing, we cannot exclude the possibility that differences in spontaneous thoughts may exist between the young and elderly subjects (Wu et al., 2007). However, considering the overall consistency of our results with the previous studies, particularly the results from the longitudinal studies (Fjell et al., 2014; Ng et al., 2016; Staffaroni et al., 2018; Li Q. et al., 2020), it is unlikely that these differences have major

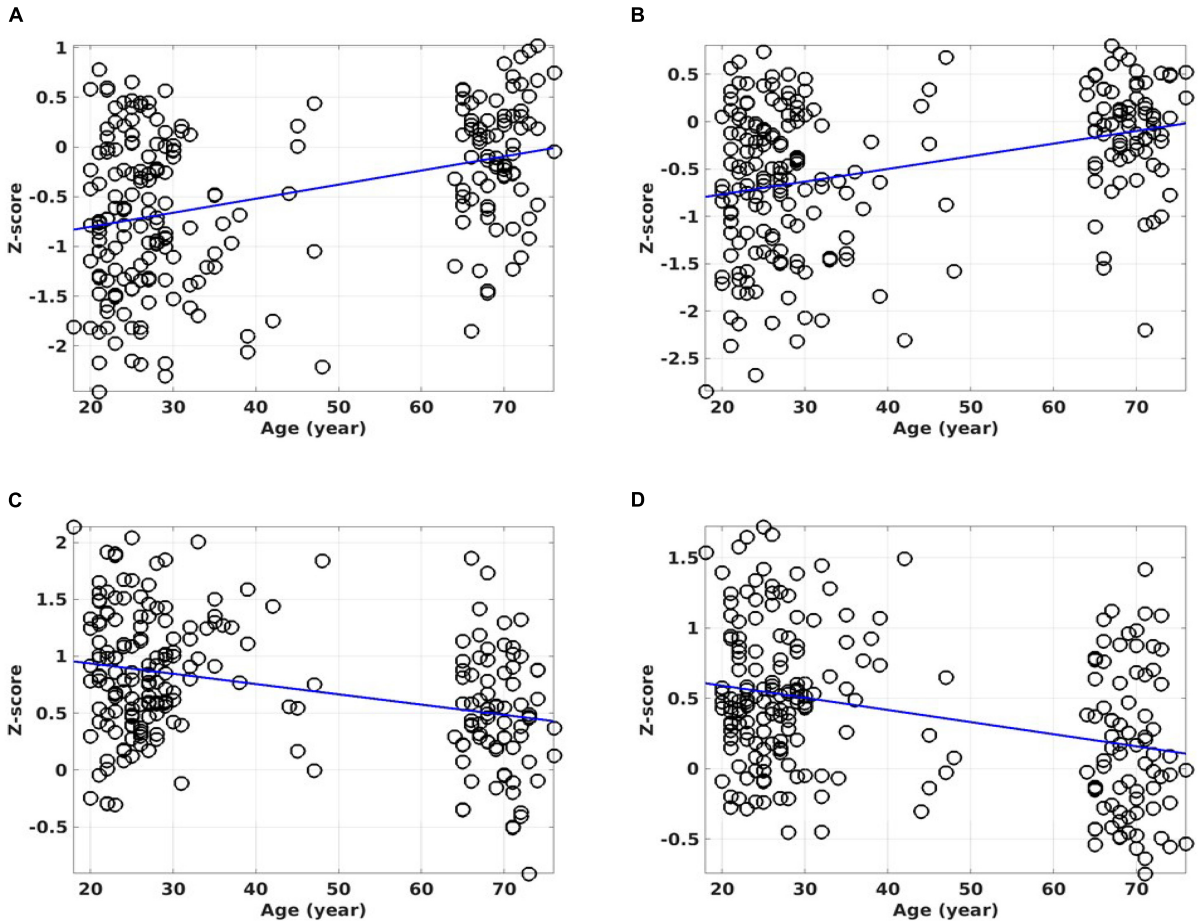

FIGURE 9 | Scattered plots of the regression against age for the overlapping results between the CSI_N and the CSI_P metrics (see the bottom rows of **Table 1**). The ROI average of the CSI_N metric against the subject's age for the overlapping ROI in the PCC **(A)**. The ROI average for the CSI_N metric against the subject's age for the overlapping ROI in the right insula cortex **(B)**. The ROI average for the CSI_P metric against the subject's age for the overlapping ROI in the PCC **(C)**. The ROI average for the CSI_P metric against the subject's age for the overlapping ROI in the insula cortex **(D)**. The lines show the linear regression results of the RFC metrics against the subject's ages.

influence on our findings. These initial findings encourage the future use of QDA as a tool to analyze longitudinal R-fMRI data aimed to develop a comprehensive understanding of age- or pathology-related brain functional changes.

Thirdly, the generalizability, or external validity issue should be considered. This is due to the non-random recruitment procedures and relying on a sample of convenience. The sample size used in this study ($N = 227$) is moderate, includes unbalanced young and elderly subgroups reflecting the difficulties to recruit elderly healthy subjects. The ages of the participants range from young to old adulthood (reflecting the age of participants in most neuroimaging studies). The age-related RFC differences observed in this study were relatively small but quite robust. However, the results from this cross-sectional study of the cohort cannot distinguish whether the RFC changes in the brain regions are due to gradual changes throughout the adulthood or a more sudden change at later stage in life.

Fourthly, the R-fMRI data were acquired under open-eye condition. Recent studies indicate that opening versus closing eyes at resting-state results in RFC difference between V1 with DMN and SNs (Costumero et al., 2020). This may explain why we did not detect significant RFC change with age in the visual cortex.

Negative Cross Correlation in White Matter and Cerebral Spinal Fluid

As discussed above negative correlation is an important fraction of the CC histogram irrespective of the tissue type and anatomical location of the voxel in question. In the published literature, there is also a rapid growing interest in studying the negative correlations between the voxels (Fox et al., 2009; Weissenbacher et al., 2009; Bianciardi et al., 2011; Schwarz and McGonigle, 2011; Gonzalez-Castillo et al., 2012; Gopinath et al., 2015; Liu et al., 2015; Spreng et al., 2016; Chen et al., 2020). It is clear that the negative portion of the CC histogram is more dominant for voxels in CSF (Gruszecki et al., 2018) and white matter (McColgan et al., 2017; Gore et al., 2019;

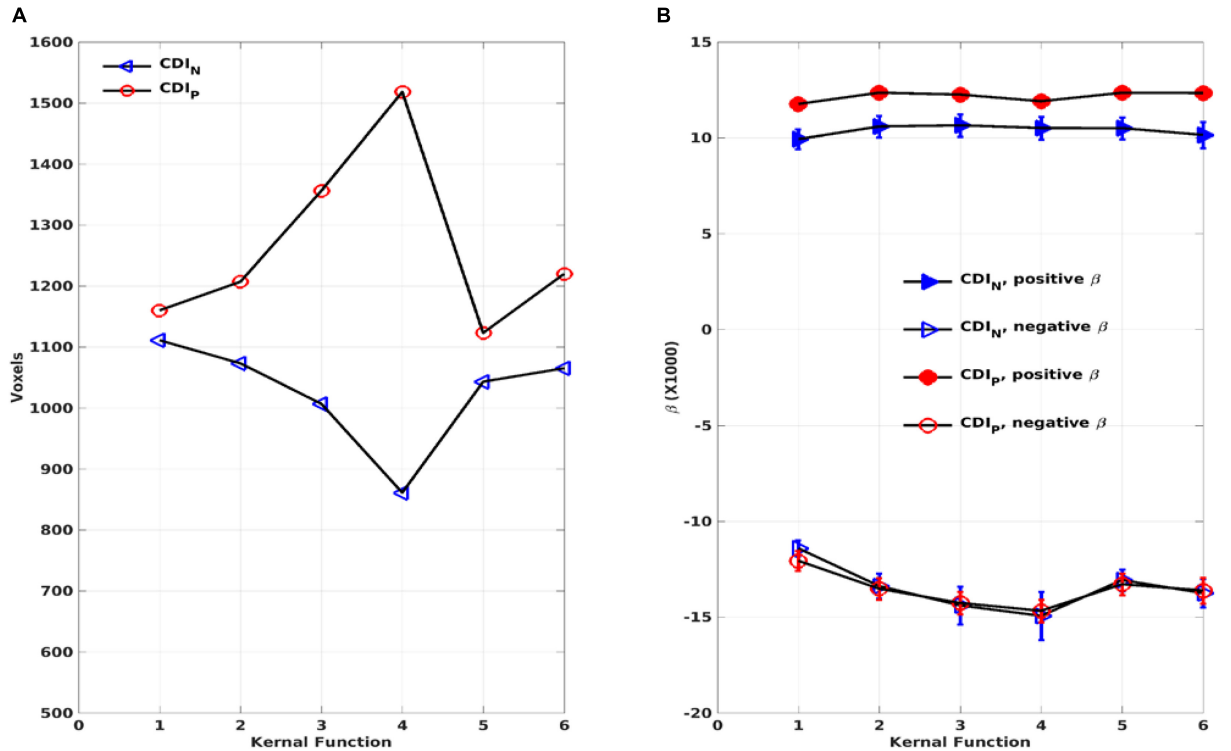

FIGURE 10 | The total volumes of the detected brain regions with significant correlation ($p < 0.05$, corrected) between the connectivity density index (CDI_P and CDI_N) and the subject's age as a function of the kernels **(A)**. The average regression parameter β for the detected brain regions as a function of the kernels **(B)**. The negative and positive correlations were assessed separately.

TABLE 3 | The joint overlapping brain regions where the connectivity density metrics of different kernels are all significantly ($p < 0.05$) correlated with the subjects' ages.

RFC	Voxel	X_{cm}	Y_{cm}	Z_{cm}	β (10^3)	r	$p(10^{-3})$	Notations
CDI_N	216	+0.1	+51.9	+29.2	−13.81	−0.376	<0.01	PCC
	103	+0.5	+28.2	+57.6	12.16	0.366	<0.01	Paracentral lobule
	92	−48.2	+47.0	+42.1	−13.32	−0.431	<0.01	R-IPL
	72	−38.7	+26.2	+57.2	11.91	0.326	<0.01	R-post central gyrus
	44	+21.2	−4.7	−20.6	9.95	0.430	<0.01	L-PHC
	38	−41.9	−12.4	+5.0	−15.16	−0.374	<0.01	R-insula cortex
	29	+20.8	−4.0	−20.0	8.75	0.371	<0.01	L-STG
	29	−1.5	−14.4	+39.5	−11.66	−0.355	<0.01	Anterior cingulate cortex
	28	+44.0	+24.1	+57.1	10.37	0.297	<0.01	L-post central gyrus
	20	−45.2	+18.4	+9.6	9.20	0.364	<0.01	R-STG
CDI_P	567	+4.2	−46.9	+24.8	−12.20	−0.480	<0.01	Superior and MFG
	136	−9.4	+21.2	−22.3	8.53	0.452	<0.01	Putamen
	30	+57.0	+15.8	−15.8	−10.09	−0.387	<0.01	L-MTG

The volume, center of mass coordinates in MNI space, and anatomic annotations, regression parameters (β), linear correlation coefficient (r), statistical significance (p), and anatomic annotations are specified. The default is bilateral, while R and L- indicate the right and left hemisphere of the brain, respectively. CDI_N and CDI_P indicate the joint overlaps among the CDI_N and CDI_P metrics of the different kernels, respectively. The β, r, and p are the average results for the 6 different kernels.

Wu et al., 2019; Li M. et al., 2020). However, the negative portion cannot be ignored even for voxels in the gray matter (see **Supplementary Materials**). To avoid confound caused by inappropriate preprocessing pipelines, we have carefully tested and updated our preprocessing pipeline. We did not implement the global signal regression (GSR) which removes the mean signal averaged over the entire brain. GSR removal via linear regression is one of the most controversial procedures in the analysis of R-fMRI data (Fox et al., 2009; Weissenbacher et al., 2009). On one hand, the global mean signal contains variance associated with respiratory, scanner-, and motion-related artifacts. Its removal by GSR can improve various quality control metrics, which enhances the anatomical specificity of RFC networks, and increase the explained behavioral variance. On the other hand, GSR alters the distribution of regional signal correlations in the brain, can induce artefactual anti-correlation patterns, may remove real

TABLE 4 | The linear regression results for the 3 ROIs with significant correlation between CSI and the subject's age.

ROI	CSI_P			CSI_N			CSI		
	$\beta \times 10^3$	*r*	*p*	$\beta \times 10^3$	*r*	*p*	$\beta \times 10^3$	*r*	*p*
Precuneus	4.93	0.283	< 0.01	3.17	0.175	0.07	9.50	0.459	<0.01
MFG	−11.46	−0.441	< 0.01	3.77	0.136	0.11	−9.72	−0.389	<0.01
R-IPL	0.73	0.031	0.61	8.03	0.299	< 0.01	9.57	0.354	<0.01

The CSI_P and CSI_N results are based on the masks determined solely by the CSI results.

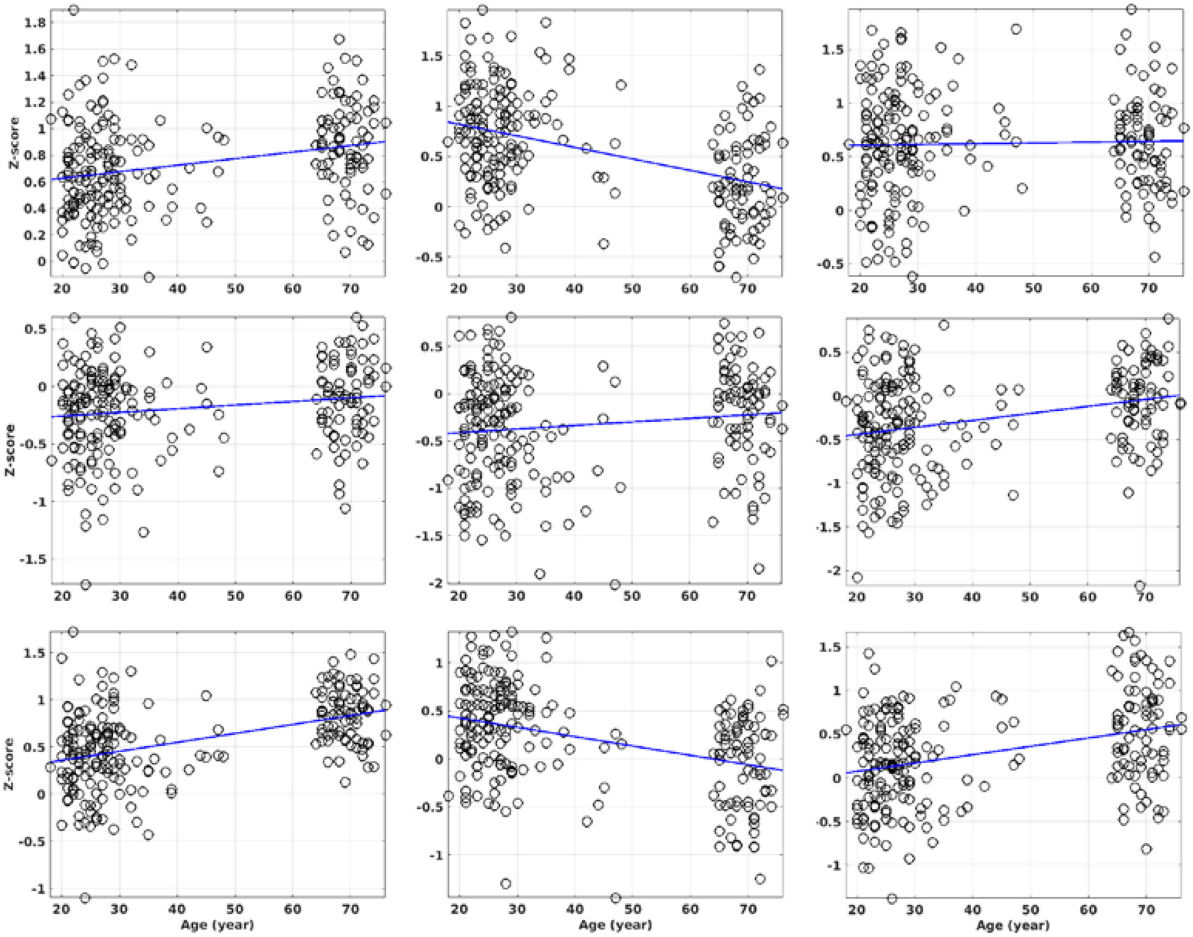

FIGURE 11 | The ROI average of the CSI_P, CSI_N, and CSI metrics against the subject's age for the 3 ROIs with significant correlation between CSI and the subject's age. The details of the regression results are summarized in **Table 4**. The columns 1 to 3 are the results for the ROIs in the precuneus, MFG, and R-IPL, respectively. The rows 1 to 3 are the results for the CSI_P, CSI_N and CSI metrics, respectively. The ROI masks are solely based on the CSI metric only.

neural signal, and can distort RFC metrics. The brain masked "global signal" is usually misunderstood, because it is not "global" and its variance contains dominant contributions from different domains of the voxels with temporally coherent signal variation.

To limit the study in a reasonable scope, in the discussion of the adult age effect on RFC we focused on gray matter and did not discuss white matter and CSF related issues. However, it should be pointed out that aging effects in white matter (McColgan et al., 2017; Gore et al., 2019; Wu et al., 2019; Li M. et al., 2020) and CSF (Sakka et al., 2011; Gruszecki et al., 2018) are also worth exploring. There is indeed a rapid growing interest in these arenas in published literature (Sakka et al., 2011; McColgan et al., 2017; Gruszecki et al., 2018; Gore et al., 2019; Wu et al., 2019; Li M. et al., 2020), particularly in the context of the age effect for the glymphatic system.

CONCLUSION

The proposed QDA framework can provide data-driven, threshold-free and voxel-wise analysis of R-fMRI data and offer a unified view for RFC metrics which can facilitate further

development and optimization of the RFC metrics by choosing appropriate kernel functions. The QDA results for the adult age effect are largely consistent with previously published results based on other analysis methods. Moreover, our new findings based on the separate assessment of the negative and positive correlations can improve the sensitivity of the RFC metrics to physiological changes associated with the advancing adult age and may clarify some of the confounding reports in the literature regarding to the DMN and sensorimotor network involvement in normal aging.

DATA AVAILABILITY STATEMENT

The datasets presented in this study can be found in online repositories. The names of the repository/repositories and accession number(s) can be found below: http://dx.doi.org/10.17632/pt9d2rdv46.1.

ETHICS STATEMENT

The studies involving human participants were reviewed and approved by the regional Ethics Committee in Stockholm and the study protocols included 2012/1511-31/2 and 2014/1982-31/1. The patients/participants provided their written informed consent to participate in this study.

AUTHOR CONTRIBUTIONS

XL: conceptualization and software. HF: project administration, editing, supervision, and funding acquisition. AM: validation and visualization. KM: investigation and data curation. TQL: methodology, formal analysis, and original draft preparation. All authors contributed to the article and approved the submitted version.

FUNDING

This work was supported by China Scholarship Council, Zhejiang Natural Science Foundation of China (No. LY18E070005), Key Research and Development Program of Zhejiang Province (No. 2020C03020), and Stockholm Regional ALF fund and the Joint China-Sweden Mobility program from the Swedish Foundation for International Cooperation Research and Higher Education (Dnr: 495 CH2019-8397).

ACKNOWLEDGMENTS

We would like to acknowledge that the descriptions of the R-fMRI data associated with the study, preprocessing pipeline, and related histogram analysis have recently been published in Data in Brief (www.sciencedirect.com/science/article/pii/S235234092100617X?via%3Dihub).

SUPPLEMENTARY MATERIAL

The Supplementary Material for this article can be found online at: https://www.frontiersin.org/articles/10.3389/fnins.2021.768418/full#supplementary-material

Supplementary Figure 1 | Anatomic locations for 4 different seed voxels of different tissue types including white matter (WM), cerebral spinal fluid (CSF), PCC, and motor cortex (MC). The crossing green lines depict the locations of the cross sections.

Supplementary Figure 2 | The average CC histograms of the cohort for the 4 different seed voxels shown in **Supplementary Figure 1** and **Supplementary Table 1**.

Supplementary Figure 3 | The convolutions of the CC histograms shown in **Supplementary Figure 2** for the 4 different seed voxels located in WM (a), PCC (b), CSF (c), and MC (d).

Supplementary Table 1 | The MNI coordinates for the 4 voxels of different tissue types illustrated in **Supplementary Figure 1**.

REFERENCES

Alarcon, G., Cservenka, A., Rudolph, M. D., Fair, D. A., and Nagel, B. J. (2015). Developmental sex differences in resting state functional connectivity of amygdala sub-regions. *Neuroimage* 115, 235–244. doi: 10.1016/j.neuroimage.2015.04.013

Allen, E. A., Erhardt, E. B., Damaraju, E., Gruner, W., Segall, J. M., Silva, R. F., et al. (2011). A baseline for the multivariate comparison of resting-state networks. *Front. Syst. Neurosci.* 5:2. doi: 10.3389/fnsys.2011.00002

Bianciardi, M., Fukunaga, M., van Gelderen, P., de Zwart, J. A., and Duyn, J. H. (2011). Negative BOLD-fMRI signals in large cerebral veins. *J. Cereb. Blood Flow Metab.* 31, 401–412. doi: 10.1038/jcbfm.2010.164

Biswal, B. B., Mennes, M., Zuo, X. N., Gohel, S., Kelly, C., Smith, S. M., et al. (2010). Toward discovery science of human brain function. *Proc. Natl. Acad. Sci. U.S.A.* 107, 4734–4739. doi: 10.1073/pnas.0911855107

Bluhm, R. L., Osuch, E. A., Lanius, R. A., Boksman, K., Neufeld, R. W., Theberge, J., et al. (2008). Default mode network connectivity: effects of age, sex, and analytic approach. *Neuroreport* 19, 887–891. doi: 10.1097/WNR.0b013e328300ebbf

Bright, M. G., Tench, C. R., and Murphy, K. (2017). Potential pitfalls when denoising resting state fMRI data using nuisance regression. *Neuroimage* 154, 159–168. doi: 10.1016/j.neuroimage.2016.12.027

Buckner, R. L., Andrews-Hanna, J. R., and Schacter, D. L. (2008). The brain's default network: anatomy, function, and relevance to disease. *Ann. N. Y. Acad. Sci.* 1124, 1–38. doi: 10.1196/annals.1440.011

Buckner, R. L., Sepulcre, J., Talukdar, T., Krienen, F. M., Liu, H., Hedden, T., et al. (2009). Cortical hubs revealed by intrinsic functional connectivity: mapping, assessment of stability, and relation to Alzheimer's disease. *J. Neurosci.* 29, 1860–1873. doi: 10.1523/JNEUROSCI.5062-08.2009

Campbell, K. L., Grigg, O., Saverino, C., Churchill, N., and Grady, C. L. (2013). Age differences in the intrinsic functional connectivity of default network subsystems. *Front. Aging Neurosci.* 5:73. doi: 10.3389/fnagi.2013.00073

Chen, J. E., Lewis, L. D., Chang, C., Tian, Q., Fultz, N. E., Ohringer, N. A., et al. (2020). Resting-state "physiological networks". *Neuroimage* 213:116707. doi: 10.1016/j.neuroimage.2020.116707

Ciuciu, P., Abry, P., and He, B. J. (2014). Interplay between functional connectivity and scale-free dynamics in intrinsic fMRI networks. *Neuroimage* 95, 248–263. doi: 10.1016/j.neuroimage.2014.03.047

Costumero, V., Bueicheku, E., Adrian-Ventura, J., and Avila, C. (2020). Opening or closing eyes at rest modulates the functional connectivity of V1 with default and salience networks. *Sci. Rep.* 10: 9137. doi: 10.1038/s41598-020-66100-y

Damoiseaux, J. S., Beckmann, C. F., Arigita, E. J., Barkhof, F., Scheltens, P., Stam, C. J., et al. (2008). Reduced resting-state brain activity in the "default network" in normal aging. *Cereb. Cortex* 18, 1856–1864. doi: 10.1093/cercor/bhm207

Damoiseaux, J. S., Viviano, R. P., Yuan, P., and Raz, N. (2016). Differential effect of age on posterior and anterior hippocampal functional connectivity. *Neuroimage* 133, 468–476. doi: 10.1016/j.neuroimage.2016.03.047

Damoiseaux, J., Rombouts, S., Barkhof, F., Scheltens, P., Stam, C., Smith, S., et al. (2006). Consistent resting-state networks across healthy subjects. *Proc. Natl. Acad. Sci. U.S.A.* 103:13848.

de Araujo, D. B., Tedeschi, W., Santos, A. C., Elias, J. Jr., Neves, U. P., and Baffa, O. (2003). Shannon entropy applied to the analysis of event-related fMRI time series. *Neuroimage* 20, 311–317.

Dennis, E. L., and Thompson, P. M. (2014). Functional brain connectivity using fMRI in aging and Alzheimer's disease. *Neuropsychol Rev.* 24, 49–62. doi: 10.1007/s11065-014-9249-6

Ferreira, L. K., and Busatto, G. F. (2013). Resting-state functional connectivity in normal brain aging. *Neurosci. Biobehav. Rev.* 37, 384–400. doi: 10.1016/j.neubiorev.2013.01.017

Fjell, A. M., McEvoy, L., Holland, D., Dale, A. M., Walhovd, K. B., and Alzheimer's Disease Neuroimaging Initiative (2014). What is normal in normal aging? Effects of aging, amyloid and Alzheimer's disease on the cerebral cortex and the hippocampus. *Prog. Neurobiol.* 117, 20–40. doi: 10.1016/j.pneurobio.2014.02.004

Fox, M. D., Zhang, D., Snyder, A. Z., and Raichle, M. E. (2009). The global signal and observed anticorrelated resting state brain networks. *J. Neurophysiol.* 101, 3270–3283. doi: 10.1152/jn.90777.2008

Geerligs, L., Tsvetanov, K. A., Cam, C., and Henson, R. N. (2017). Challenges in measuring individual differences in functional connectivity using fMRI: the case of healthy aging. *Hum. Brain Mapp.* 38, 4125–4156. doi: 10.1002/hbm.23653

Golestani, A. M., Kwinta, J. B., Khatamian, Y. B., and Chen, J. J. (2017). The effect of low-frequency physiological correction on the reproducibility and specificity of resting-state fMRI metrics: functional connectivity, ALFF, and ReHo. *Front. Neurosci.* 11:546. doi: 10.3389/fnins.2017.00546

Gonzalez-Castillo, J., Saad, Z. S., Handwerker, D. A., Inati, S. J., Brenowitz, N., and Bandettini, P. A. (2012). Whole-brain, time-locked activation with simple tasks revealed using massive averaging and model-free analysis. *Proc. Natl. Acad. Sci. U.S.A.* 109, 5487–5492. doi: 10.1073/pnas.1121049109

Gopinath, K., Krishnamurthy, V., Cabanban, R., and Crosson, B. A. (2015). Hubs of anticorrelation in high-resolution resting-state functional connectivity network architecture. *Brain Connect.* 5, 267–275. doi: 10.1089/brain.2014.0323

Gore, J. C., Li, M., Gao, Y., Wu, T. L., Schilling, K. G., Huang, Y., et al. (2019). Functional MRI and resting state connectivity in white matter – a mini-review. *Magn. Reson. Imaging* 63, 1–11. doi: 10.1016/j.mri.2019.07.017

Gruszecki, M., Lancaster, G., Stefanovska, A., Neary, J. P., Dech, R. T., Guminski, W., et al. (2018). Human subarachnoid space width oscillations in the resting state. *Sci. Rep.* 8:3057. doi: 10.1038/s41598-018-21038-0

Hayasaka, S., and Laurienti, P. J. (2010). Comparison of characteristics between region-and voxel-based network analyses in resting-state fMRI data. *Neuroimage* 50, 499–508. doi: 10.1016/j.neuroimage.2009.12.051

He, B. J. (2011). Scale-free properties of the functional magnetic resonance imaging signal during rest and task. *J. Neurosci.* 31, 13786–13795. doi: 10.1523/JNEUROSCI.2111-11.2011

Hussein, A., Matthews, J. L., Syme, C., Macgowan, C., MacIntosh, B. J., Shirzadi, Z., et al. (2020). The association between resting-state functional magnetic resonance imaging and aortic pulse-wave velocity in healthy adults. *Hum. Brain Mapp.* 41, 2121–2135. doi: 10.1002/hbm.24934

Hyder, F., and Rothman, D. L. (2010). Neuronal correlate of BOLD signal fluctuations at rest: err on the side of the baseline. *Proc. Natl. Acad. Sci. U.S.A.* 107, 10773–10774. doi: 10.1073/pnas.1005135107

Jia, Y., Gu, H., and Luo, Q. (2017). Sample entropy reveals an age-related reduction in the complexity of dynamic brain. *Sci. Rep.* 7:7990. doi: 10.1038/s41598-017-08565-y

Joel, S. E., Caffo, B. S., van Zijl, P. C., and Pekar, J. J. (2011). On the relationship between seed-based and ICA-based measures of functional connectivity. *Magn. Reson. Med.* 66, 644–657. doi: 10.1002/mrm.22818

Koch, W., Teipel, S., Mueller, S., Buerger, K., Bokde, A. L., Hampel, H., et al. (2010). Effects of aging on default mode network activity in resting state fMRI: does the method of analysis matter? *Neuroimage* 51, 280–287. doi: 10.1016/j.neuroimage.2009.12.008

Lawrence, N. S., Ross, T. J., Hoffmann, R., Garavan, H., and Stein, E. A. (2003). Multiple neuronal networks mediate sustained attention. *J. Cogn. Neurosci.* 15, 1028–1038.

Li, M., Gao, Y., Gao, F., Anderson, A. W., Ding, Z., and Gore, J. C. (2020). Functional engagement of white matter in resting-state brain networks. *Neuroimage* 220:117096. doi: 10.1016/j.neuroimage.2020.117096

Li, Q., Dong, C., Liu, T., Chen, X., Perry, A., Jiang, J., et al. (2020). Longitudinal changes in whole-brain functional connectivity strength patterns and the relationship with the global cognitive decline in older adults. *Front. Aging Neurosci.* 12:71. doi: 10.3389/fnagi.2020.00071

Li, X., Fischer, H., Manzouri, A., Mansson, K. N. T., and Li, T. Q. (2021). Dataset of whole-brain resting-state fMRI of 227 young and elderly adults acquired at 3T. *Data Brief* 38:107333. doi: 10.1016/j.dib.2021.107333

Liu, Y., Huang, L., Li, M., Zhou, Z., and Hu, D. (2015). Anticorrelated networks in resting-state fMRI-BOLD data. *Biomed. Mater. Eng.* 26 Suppl 1, S1201–S1211. doi: 10.3233/BME-151417

Lu, T., Aron, L., Zullo, J., Pan, Y., Kim, H., Chen, Y., et al. (2014). REST and stress resistance in ageing and Alzheimer's disease. *Nature* 507, 448–454. doi: 10.1038/nature13163

Luo, N., Sui, J., Abrol, A., Lin, D., Chen, J., Vergara, V. M., et al. (2020). Age-related structural and functional variations in 5,967 individuals across the adult lifespan. *Hum. Brain Mapp.* 41, 1725–1737. doi: 10.1002/hbm.24905

Manza, P., Zhang, S., Hu, S., Chao, H. H., Leung, H. C., and Li, C. R. (2015). The effects of age on resting state functional connectivity of the basal ganglia from young to middle adulthood. *Neuroimage* 107, 311–322.

McColgan, P., Gregory, S., Razi, A., Seunarine, K. K., Gargouri, F., Durr, A., et al. (2017). White matter predicts functional connectivity in premanifest Huntington's disease. *Ann. Clin. Transl. Neurol.* 4, 106–118. doi: 10.1002/acn3.384

Meier, T. B., Bellgowan, P. S. F., and Mayer, A. R. (2017). Longitudinal assessment of local and global functional connectivity following sports-related concussion. *Brain Imaging Behav.* 11, 129–140. doi: 10.1007/s11682-016-9520-y

Menon, V., and Uddin, L. Q. (2010). Saliency, switching, attention and control: a network model of insula function. *Brain Struct. Funct.* 214, 655–667.

Muschelli, J., Nebel, M. B., Caffo, B. S., Barber, A. D., Pekar, J. J., and Mostofsky, S. H. (2014). Reduction of motion-related artifacts in resting state fMRI using aCompCor. *Neuroimage* 96, 22–35. doi: 10.1016/j.neuroimage.2014.03.028

Ng, K. K., Lo, J. C., Lim, J. K. W., Chee, M. W. L., and Zhou, J. (2016). Reduced functional segregation between the default mode network and the executive control network in healthy older adults: a longitudinal study. *Neuroimage* 133, 321–330. doi: 10.1016/j.neuroimage.2016.03.029

Pan, P., Zhu, L., Yu, T., Shi, H., Zhang, B., Qin, R., et al. (2017). Aberrant spontaneous low-frequency brain activity in amnestic mild cognitive impairment: a meta-analysis of resting-state fMRI studies. *Ageing Res. Rev.* 35, 12–21. doi: 10.1016/j.arr.2016.12.001

Parkes, L., Fulcher, B., Yucel, M., and Fornito, A. (2018). An evaluation of the efficacy, reliability, and sensitivity of motion correction strategies for resting-state functional MRI. *Neuroimage* 171, 415–436. doi: 10.1016/j.neuroimage.2017.12.073

Pasquini, L., Scherr, M., Tahmasian, M., Meng, C., Myers, N. E., Ortner, M., et al. (2015). Link between hippocampus' raised local and eased global intrinsic connectivity in AD. *Alzheimers Dement* 11, 475–484. doi: 10.1016/j.jalz.2014.02.007

Persson, N., Ghisletta, P., Dahle, C. L., Bender, A. R., Yang, Y., Yuan, P., et al. (2014). Regional brain shrinkage over two years: individual differences and effects of pro-inflammatory genetic polymorphisms. *Neuroimage* 103, 334–348. doi: 10.1016/j.neuroimage.2014.09.042

Persson, N., Ghisletta, P., Dahle, C. L., Bender, A. R., Yang, Y., Yuan, P., et al. (2016). Regional brain shrinkage and change in cognitive performance over two years: the bidirectional influences of the brain and cognitive reserve factors. *Neuroimage* 126, 15–26. doi: 10.1016/j.neuroimage.2015.11.028

Persson, N., Wu, J., Zhang, Q., Liu, T., Shen, J., Bao, R., et al. (2015). Age and sex related differences in subcortical brain iron concentrations among healthy adults. *Neuroimage* 122, 385–398. doi: 10.1016/j.neuroimage.2015.07.050

Pruim, R. H. R., Mennes, M., van Rooij, D., Llera, A., Buitelaar, J. K., and Beckmann, C. F. (2015). ICA-AROMA: a robust ICA-based strategy for

removing motion artifacts from fMRI data. *Neuroimage* 112, 267–277. doi: 10.1016/j.neuroimage.2015.02.064

Raichle, M. E., MacLeod, A. M., Snyder, A. Z., Powers, W. J., Gusnard, D. A., and Shulman, G. L. (2001). A default mode of brain function. *Proc. Natl. Acad. Sci. U.S.A.* 98, 676–682.

Reynolds, B. B., Stanton, A. N., Soldozy, S., Goodkin, H. P., Wintermark, M., and Druzgal, T. J. (2017). Investigating the effects of subconcussion on functional connectivity using mass-univariate and multivariate approaches. *Brain Imaging Behav.* 12, 1332–1345. doi: 10.1007/s11682-017-9790-z

Rieckmann, A., Johnson, K. A., Sperling, R. A., Buckner, R. L., and Hedden, T. (2018). Dedifferentiation of caudate functional connectivity and striatal dopamine transporter density predict memory change in normal aging. *Proc. Natl. Acad. Sci. U.S.A.* 115, 10160–10165.

Rosazza, C., Minati, L., Ghielmetti, F., Mandelli, M. L., and Bruzzone, M. G. (2012). Functional connectivity during resting-state functional MR imaging: study of the correspondence between independent component analysis and region-of-interest-based methods. *AJNR Am. J. Neuroradiol.* 33, 180–187. doi: 10.3174/ajnr.A2733

Sakka, L., Coll, G., and Chazal, J. (2011). Anatomy and physiology of cerebrospinal fluid. *Eur. Ann. Otorhinolaryngol. Head Neck Dis.* 128, 309–316. doi: 10.1016/j.anorl.2011.03.002

Salami, A., Pudas, S., and Nyberg, L. (2014). Elevated hippocampal resting-state connectivity underlies deficient neurocognitive function in aging. *Proc. Natl. Acad. Sci. U.S.A.* 111, 17654–17659. doi: 10.1073/pnas.1410233111

Scheinost, D., Finn, E. S., Tokoglu, F., Shen, X., Papademetris, X., Hampson, M., et al. (2015). Sex differences in normal age trajectories of functional brain networks. *Hum. Brain Mapp.* 36, 1524–1535. doi: 10.1002/hbm.22720

Schwarz, A. J., and McGonigle, J. (2011). Negative edges and soft thresholding in complex network analysis of resting state functional connectivity data. *Neuroimage* 55, 1132–1146. doi: 10.1016/j.neuroimage.2010.12.047

Smith, S. M., Fox, P. T., Miller, K. L., Glahn, D. C., Fox, P. M., Mackay, C. E., et al. (2009). Correspondence of the brain's functional architecture during activation and rest. *Proc. Natl. Acad. Sci. U.S.A.* 106, 13040–13045. doi: 10.1073/pnas.0905267106

Song, X., Panych, L. P., and Chen, N. K. (2016). Data-driven and predefined ROI-based quantification of long-term resting-state fMRI reproducibility. *Brain Connect.* 6, 136–151. doi: 10.1089/brain.2015.0349

Spreng, R. N., Stevens, W. D., Viviano, J. D., and Schacter, D. L. (2016). Attenuated anticorrelation between the default and dorsal attention networks with aging: evidence from task and rest. *Neurobiol. Aging* 45, 149–160. doi: 10.1016/j.neurobiolaging.2016.05.020

Staffaroni, A. M., Brown, J. A., Casaletto, K. B., Elahi, F. M., Deng, J., Neuhaus, J., et al. (2018). The longitudinal trajectory of default mode network connectivity in healthy older adults varies as a function of age and is associated with changes in episodic memory and processing speed. *J. Neurosci.* 38, 2809–2817. doi: 10.1523/JNEUROSCI.3067-17.2018

Sun, Y., Dai, Z., Li, Y., Sheng, C., Li, H., Wang, X., et al. (2016). Subjective cognitive decline: mapping functional and structural brain changes-a combined resting-state functional and structural MR imaging study. *Radiology* 281, 185–192. doi: 10.1148/radiol.2016151771

Tomasi, D., and Volkow, N. D. (2011). Functional connectivity hubs in the human brain. *Neuroimage* 57, 908–917. doi: 10.1016/j.neuroimage.2011.05.024

Tyszka, J. M., Kennedy, D. P., Paul, L. K., and Adolphs, R. (2014). Largely typical patterns of resting-state functional connectivity in high-functioning adults with autism. *Cereb. Cortex* 24, 1894–1905. doi: 10.1093/cercor/bht040

Viol, A., Palhano-Fontes, F., Onias, H., de Araujo, D. B., and Viswanathan, G. M. (2017). Shannon entropy of brain functional complex networks under the influence of the psychedelic Ayahuasca. *Sci. Rep.* 7:7388. doi: 10.1038/s41598-017-06854-0

Vossel, S., Geng, J. J., and Fink, G. R. (2014). Dorsal and ventral attention systems: distinct neural circuits but collaborative roles. *Neuroscientist* 20, 150–159.

Wang, Y. L., and Li, T. Q. (2013). Analysis of whole-brain resting-state FMRI data using hierarchical clustering approach. *PLoS One* 8:e76315. doi: 10.1371/journal.pone.0076315

Wang, Y., and Li, T. Q. (2015). Dimensionality of ICA in resting-state fMRI investigated by feature optimized classification of independent components with SVM. *Front. Hum. Neurosci.* 9:259. doi: 10.3389/fnhum.2015.00259

Weissenbacher, A., Kasess, C., Gerstl, F., Lanzenberger, R., Moser, E., and Windischberger, C. (2009). Correlations and anticorrelations in resting-state functional connectivity MRI: a quantitative comparison of preprocessing strategies. *Neuroimage* 47, 1408–1416. doi: 10.1016/j.neuroimage.2009.05.005

Weissman-Fogel, I., Moayedi, M., Taylor, K. S., Pope, G., and Davis, K. D. (2010). Cognitive and default-mode resting state networks: do male and female brains "rest" differently? *Hum. Brain Mapp.* 31, 1713–1726. doi: 10.1002/hbm.20968

Williams, S. C. (2013). Alzheimer's disease: mapping the brain's decline. *Nature* 502, S84–S85.

Wu, T., Zang, Y., Wang, L., Long, X., Hallett, M., Chen, Y., et al. (2007). Aging influence on functional connectivity of the motor network in the resting state. *Neurosci. Lett.* 422, 164–168. doi: 10.1016/j.neulet.2007.06.011

Wu, T.-L., Wang, F., Li, M., Schilling, K. G., Gao, Y., Anderson, A. W., et al. (2019). Resting-state white matter-cortical connectivity in non-human primate brain. *NeuroImage* 184, 45–55. doi: 10.1016/j.neuroimage.2018.09.021

Yang, H., Long, X. Y., Yang, Y., Yan, H., Zhu, C. Z., Zhou, X. P., et al. (2007). Amplitude of low frequency fluctuation within visual areas revealed by resting-state functional MRI. *Neuroimage* 36, 144–152. doi: 10.1016/j.neuroimage.2007.01.054

Ystad, M., Eichele, T., Lundervold, A. J., and Lundervold, A. (2010). Subcortical functional connectivity and verbal episodic memory in healthy elderly–a resting state fMRI study. *Neuroimage* 52, 379–388. doi: 10.1016/j.neuroimage.2010.03.062

Zang, Y. F., He, Y., Zhu, C. Z., Cao, Q. J., Sui, M. Q., Liang, M., et al. (2007). Altered baseline brain activity in children with ADHD revealed by resting-state functional MRI. *Brain Dev.* 29, 83–91. doi: 10.1016/j.braindev.2006.07.002

Zang, Y., Jiang, T., Lu, Y., He, Y., and Tian, L. (2004). Regional homogeneity approach to fMRI data analysis. *Neuroimage* 22, 394–400. doi: 10.1016/j.neuroimage.2003.12.030

Zhang, C., Cahill, N. D., Arbabshirani, M. R., White, T., Baum, S. A., and Michael, A. M. (2016). Sex and age effects of functional connectivity in early adulthood. *Brain Connect.* 6, 700–713. doi: 10.1089/brain.2016.0429

Zhang, X. D., Jiang, X. L., Cheng, Z., Zhou, Y., Xu, Q., Zhang, Z. Q., et al. (2016). Decreased coupling between functional connectivity density and amplitude of low frequency fluctuation in non-neuropsychiatric systemic lupus erythematosus: a resting-stage functional mri study. *Mol. Neurobiol.* 54, 5225–5235. doi: 10.1007/s12035-016-0050-9

Zhao, M., Zhou, C., Chen, Y., Hu, B., and Wang, B. H. (2010). Complexity versus modularity and heterogeneity in oscillatory networks: combining segregation and integration in neural systems. *Phys. Rev. E Stat. Nonlin. Soft. Matter. Phys.* 82(4 Pt 2):046225. doi: 10.1103/PhysRevE.82.046225

Zou, Q. H., Zhu, C. Z., Yang, Y., Zuo, X. N., Long, X. Y., Cao, Q. J., et al. (2008). An improved approach to detection of amplitude of low-frequency fluctuation (ALFF) for resting-state fMRI: fractional ALFF. *J. Neurosci. Methods* 172, 137–141. doi: 10.1016/j.jneumeth.2008.04.012

Zuo, X. N., Kelly, C., Di Martino, A., Mennes, M., Margulies, D. S., Bangaru, S., et al. (2010). Growing together and growing apart: regional and sex differences in the lifespan developmental trajectories of functional homotopy. *J. Neurosci.* 30, 15034–15043. doi: 10.1523/JNEUROSCI.2612-10.2010

Conflict of Interest: The authors declare that the research was conducted in the absence of any commercial or financial relationships that could be construed as a potential conflict of interest.

Publisher's Note: All claims expressed in this article are solely those of the authors and do not necessarily represent those of their affiliated organizations, or those of the publisher, the editors and the reviewers. Any product that may be evaluated in this article, or claim that may be made by its manufacturer, is not guaranteed or endorsed by the publisher.

frontiers in Neuroscience

METHODS
published: 11 November 2021
doi: 10.3389/fnins.2021.768602

Cox Regression Based Modeling of Functional Connectivity and Treatment Outcome for Relapse Prediction and Disease Subtyping in Substance Use Disorder

*Tianye Zhai, Hong Gu and Yihong Yang**

Neuroimaging Research Branch, Intramural Research Program, National Institute on Drug Abuse, National Institutes of Health, Baltimore, MD, United States

Functional magnetic resonance imaging (fMRI) has become one of the most widely used noninvasive neuroimaging technique in research of cognitive neurosciences and of neural mechanisms of neuropsychiatric/neurological diseases. A primary goal of fMRI-based neuroimaging studies is to identify biomarkers for brain-behavior relationship and ultimately perform individualized treatment outcome prognosis. However, the concern of inadequate validation and the nature of small sample sizes are associated with fMRI-based neuroimaging studies, both of which hinder the translation from scientific findings to clinical practice. Therefore, the current paper presents a modeling approach to predict time-dependent prognosis with fMRI-based brain metrics and follow-up data. This prediction modeling is a combination of seed-based functional connectivity and voxel-wise Cox regression analysis with built-in nested cross-validation, which has been demonstrated to be able to provide robust and unbiased model performance estimates. Demonstrated with a cohort of treatment-seeking cocaine users from psychosocial treatment programs with 6-month follow-up, our proposed modeling method is capable of identifying brain regions and related functional circuits that are predictive of certain follow-up behavior, which could provide mechanistic understanding of neuropsychiatric/neurological disease and clearly shows neuromodulation implications and can be used for individualized prognosis and treatment protocol design.

Keywords: prediction modeling, fMRI, treatment outcome, Cox regression, functional connectivity, neuromodulation implications

OPEN ACCESS

Edited by:
Fei Du,
Harvard Medical School,
United States

Reviewed by:
Liangsuo Ma,
Virginia Commonwealth University,
United States
Sheng Zhang,
Yale University, United States

***Correspondence:**
Yihong Yang
yihongyang@intra.nida.nih.gov

Specialty section:
This article was submitted to Brain Imaging Methods, a section of the journal Frontiers in Neuroscience

Received: *31 August 2021*
Accepted: *19 October 2021*
Published: *11 November 2021*

Citation:
Zhai T, Gu H and Yang Y (2021) Cox Regression Based Modeling of Functional Connectivity and Treatment Outcome for Relapse Prediction and Disease Subtyping in Substance Use Disorder. Front. Neurosci. 15:768602. doi: 10.3389/fnins.2021.768602

INTRODUCTION

Since the initial demonstration of blood-oxygen-level-dependent (BOLD) signal *in vivo* in early 1990s (Ogawa et al., 1990), functional magnetic resonance imaging (fMRI) has become a noninvasive neuroimaging technique widely used in research of cognitive neurosciences, as well as in understanding of neural mechanisms of neuropsychiatric/neurological diseases. For example, in exploring neurobiological mechanisms of substance use disorder, a highly relapsing chronic brain disease (Dutra et al., 2008; Koob and Volkow, 2016; Volkow et al., 2016) currently without effective

treatments, imaging biomarkers based on both resting-state fMRI (Zhai et al., 2021) and task-evoked fMRI (Luo et al., 2013) have shown prediction validity of relapse to cocaine use following treatment. Such neuroimaging-based studies provide mechanistic understanding of relapse to drug use and suggest neural targets for the development of neuromodulation (e.g., transcranial magnetic stimulation/TMS) treatment protocols.

Over the past three decades, in spite of advances in both imaging acquisition and analysis techniques, which have greatly enhanced our understanding of brain function and dysfunction, two major concerns have been associated with fMRI-based neuroimaging studies that hinder the translation from scientific knowledge to clinical practice. One concern is lack of appropriate validation in fMRI data analyses. A primary goal of fMRI-based neuroimaging research is to identify biomarkers that can be used to establish the relationship between brain and behavior and ultimately perform individualized predictions of health/prognosis outcomes (Gabrieli et al., 2015; Shen et al., 2017). However, the term of "prediction" was often misused when actual results reported were association/correlation that related brain measures with behavioral assessments/treatment outcome within samples being tested (Meng et al., 2017; Shen et al., 2017). A recent review on neuroimaging studies claiming prediction validity using fMRI data indicates that among 100 studies from 2017 to 2019, over 40% claimed prediction without any cross-validation (Poldrack et al., 2020). These in-sample correlational models without proper cross-validation tend to provide inflated prediction accuracy due to overfitting, resulting in difficulties in generalizability (Whelan and Garavan, 2014; Shen et al., 2017). Another concern is the relatively small sample size in fMRI-based neuroimaging studies (Turner et al., 2018; Szucs and Ioannidis, 2020), partially due to the large financial expenses associated with fMRI scanning, as well as difficulties associated with recruiting certain types of patients/participants. Among the 100 studies examined, more than 70% were with a sample size less than 100, and more than 50% were with a sample size less than 50 (Poldrack et al., 2020). The small sample size nature of fMRI-based neuroimaging studies can further intensify the problem of overfitting in prediction analyses (Whelan and Garavan, 2014). Previous studies have suggested the utilization of nested cross-validation in prediction, which has been demonstrated to be able to provide robust and unbiased model performance estimates, and outperform some other commonly used cross-validation methods (such as K-fold cross-validation) especially in applications with small sample sizes (Varma and Simon, 2006; Vabalas et al., 2019).

Therefore, we present here an analytical approach to predict time-dependent follow-up behaviors by imaging metrics from resting-state fMRI and demonstrated the approach in a cohort of treatment-seeking cocaine users. Our prediction modeling is a hybrid of hypothesis-driven and data-driven approaches built upon a combination of seed-based functional connectivity and voxel-wise Cox regression. The seed-based functional connectivity serves as the hypothesis-driven part, which is hypothesis specific (e.g., implication for neuromodulation target selection) and ensures the interpretability of results. The Cox regression was originally introduced for survival analysis (Cox, 1972). Due to the mathematical similarity between survival and the relapse to drug use (time-dependent binary outcome), the Cox regression model is an ideal statistical tool for probing brain—relapse relationship. For example, it has been utilized in predicting cocaine relapse with the brain activation induced by a stop-signal inhibition task as measured by fMRI (Luo et al., 2013). Also utilized under the resting-state, the Cox model yielded high accuracy in predicting cocaine relapse with functional connectivity (Geng et al., 2017). Therefore, we choose the Cox regression model for the study of relapse during follow-up after treatment. The whole prediction modeling pipeline is organized into a nested cross-validation loop. Detailed procedures are described below.

MATERIALS AND EQUIPMENT

The prediction method that we proposed here is based on a voxel-wise Cox regression of resting-state fMRI and treatment outcome. The whole procedure is cross-validated, potentially utilizable on novel patients/subjects to predict their treatment outcome prospectively. Here we list all the materials and equipment that we used to conduct the prediction modeling: A functional magnetic resonance imaging (fMRI) dataset acquired from an MRI scanner and a post-treatment follow-up dataset of relapse to drug use. Tools for image pre-processing and functional connectivity analyses include the AFNI (v17.0.06[1]) and SPM[2] software packages. The computational pipeline of relapse prediction, including voxel-wise Cox regression, prediction model fitting, cross-validation, and *post-hoc* analyses, were developed with Matlab (R2020b, The MathWorks, Inc., Natick, MA, United States).

Methods

Participants and Clinical Assessment Procedures

To demonstrate our relapse prediction modeling, we employed imaging and behavioral data collected from a cohort of 45 treatment-seeking cocaine dependent participants who underwent and completed psychosocial treatment from local residential treatment programs using the Minnesota Model Psychosocial treatment approach (Cook, 1988). Several clinical measurements were assessed including the Inventory of Drug Use Consequences (InDUC) which assess the life problems related to drug use (Tonigan and Miller, 2002), Cocaine Craving Questionnaire (CCQ-Brief), years of cocaine use, days of cocaine use in the past 90 days, and days since last cocaine use. Following discharge from the psychosocial treatment program, participants were followed up for 168 days or until relapse, whichever was earlier. Abstinence was verified by weekly phone interviews and/or in-person urine drug screens. Date of relapse was recorded as the day of drug use or the day of the first missed appointment if lost to follow-up. Participants who failed to maintain abstinence were then discharged from the study. The study was reviewed and approved by the Institutional

[1] http://afni.nimh.nih.gov/afni/

[2] http://www.fil.ion.ucl.ac.uk/spm/software/spm12/

Review Boards of the University of Texas Southwestern Medical Center and the Veterans Administration North Texas Health Care System. Written informed consent was obtained from each participant. Summary of the demographic information of the cohort is presented in **Table 1** (n = 43 after excluding two participants for excessive head motion during fMRI scanning, see section "Computational Pipeline of Relapse Prediction" in the section "Methods"). More detailed information on participants' inclusion/exclusion, treatment/assessment procedures have been described previously (Zhai et al., 2021).

Magnetic Resonance Imaging/Functional Magnetic Resonance Imaging Scanning Parameters

For each participant, a whole-brain BOLD resting-state fMRI dataset of 6 min was acquired from a 3T Philips MRI scanner with an eight-channel radio-frequency coil (Philips Medical Systems, Best, Netherlands). Images were collected in the axial plane parallel to the AC-PC line using a single-shot, echo-planar imaging sequence (TE = 25 ms, TR = 1.7 s, flip angle = 70°, spatial resolution = 3.25 mm × 3.25 mm × 3 mm with no gap). Participants were instructed to keep their heads still and eyes open during the resting-state scan. A high-resolution anatomical T1-weighted image was also acquired from each participant using a 3D magnetization-prepared rapid gradient-echo sequence (TE = 3.8 ms, TR = 8.2 ms, flip angle = 12°, spatial resolution = 1 mm × 1 mm × 1 mm).

Computational Pipeline of Relapse Prediction

The relapse prediction modeling that we developed and demonstrated here was inspired by the connectome-based predictive modeling proposed by Shen et al. (2017). Generally, our methodological pipeline was a combination of seed-based functional connectivity and voxel-wise Cox regression of functional connectivity and treatment outcome in a nested cross-validation fashion, which consisted of six logical elements: (1) image preprocessing; (2) functional connectivity calculation; (3) voxel-wise Cox regression analysis; (4) thresholding and generating composite indices; (5) Cox model fitting for brain-behavior relationship and model evaluation (ROC analysis); and (6) cross validation and permutation test. Procedural steps are illustrated in **Figure 1** and described in details below.

TABLE 1 | Demographic, clinical and head-motion assessments.

	CD cohort (n = 43)
Age	43.42 ± 7.19
Sex (M/F)	38/5
Edu (years)	12.49 ± 2.11
Cocaine use (years)	8.28 ± 5.22
Nicotine use (CPD)	11.42 ± 10.36
Mean head motion (mm)	0.09 ± 0.03

CD, cocaine dependent; Edu, years of education; CPD, cigarettes per day.

The first step was image pre-processing that included: discarding the first five volumes to allow the magnetic resonance signal to reach steady state, slice timing correction (*3dTshift, AFNI*), volume registration (*3dvolreg, AFNI*), polynomial detrending (up to the 3rd order, *3dDetrend, AFNI*) and head motion correction (*3dTproject, AFNI*). Signals from white matter and cerebrospinal fluid (CSF) were treated as a marker of non-neuronal noise and were regressed out (*3dTproject, AFNI*). A band-pass filter was applied to select low-frequency fluctuations between 0.012 and 0.1 Hz (*3dTproject, AFNI*) (Fransson, 2005). The fMRI data were normalized to standard MNI image space and resampled to a 2-mm isotropic resolution (SPM12). Head motion was also evaluated at the frame-by-frame level to further control for image quality using pair-wise displacement calculated based on the Euclidean distance (*1d_tool.py, AFNI*). Volumes with displacement >0.35 mm were censored; participants were excluded if their mean head motion across volumes were greater than 0.2 mm or their percentage of censored volumes exceeding 20%. Two participants were excluded due to head motion exceeding this threshold, leaving 43 participants in the subsequent analytical steps.

Step two was to select a seed or region-of-interest (ROI) based on specific hypothesis and calculate its whole-brain functional connectivity (**Figure 1A**). The dlPFC has been utilized as stimulation target for high frequency rTMS treatment that reduced craving for nicotine and cocaine (Politi et al., 2008; Li et al., 2013; Pripfl et al., 2014). Here, we chose an ROI on the left dlPFC for demonstration due to its promising role in the treatment of cocaine dependence as stimulation target of high frequency rTMS (Terraneo et al., 2016), as well as the high validity in predicting cocaine relapse with its downstream functional circuits (Zhai et al., 2021). Whole-brain functional connectivity maps were obtained by calculating the cross-correlation (CC) between the time series of the seed and that of each voxel in the whole-brain (*3dDeconvolve, AFNI*). The CC maps were then Fisher's Z-transformed with the inverse hyperbolic tangent function $Z = atanh(cc)$ (*3dcalc, AFNI*) as the resting-state functional connectivity (rsFC) maps for subsequent analyses.

Step three was to conduct the voxel-wise Cox regression analysis on the rsFC generated in the previous step and the relapse information (days till relapse) obtained during the follow-up period (**Figure 1B**): $h(X_i,\ t) = h_0(t)e^{\sum_j x_{ij}b_j}$, where X_i is the linear combination of the predictor variables/covariates for the ith participant $h(X_i,\ t)$, is the hazard rate at time t for X_i, $h_0(t)$ is the baseline hazard rate function, and $x_{ij}b_i$ within the exponential term represents the loglinear regression. The voxel-wise beta coefficient maps (beta map) of all participants were obtained in this step (**Figure 1C**), and the whole-brain relative hazard ratio (HR) maps can further be calculated with the exponential of the beta values.

Step four was to generate composite indices. All beta/HR maps were voxel-wisely thresholded at a given threshold (e.g., $p < 0.001$ as demonstrated here). This is an initial thresholding serving the purpose of pre-selection of those voxels with functional connectivity relates to relapse the most, and was arbitrarily chosen based on empirical experience, similarly as demonstrated

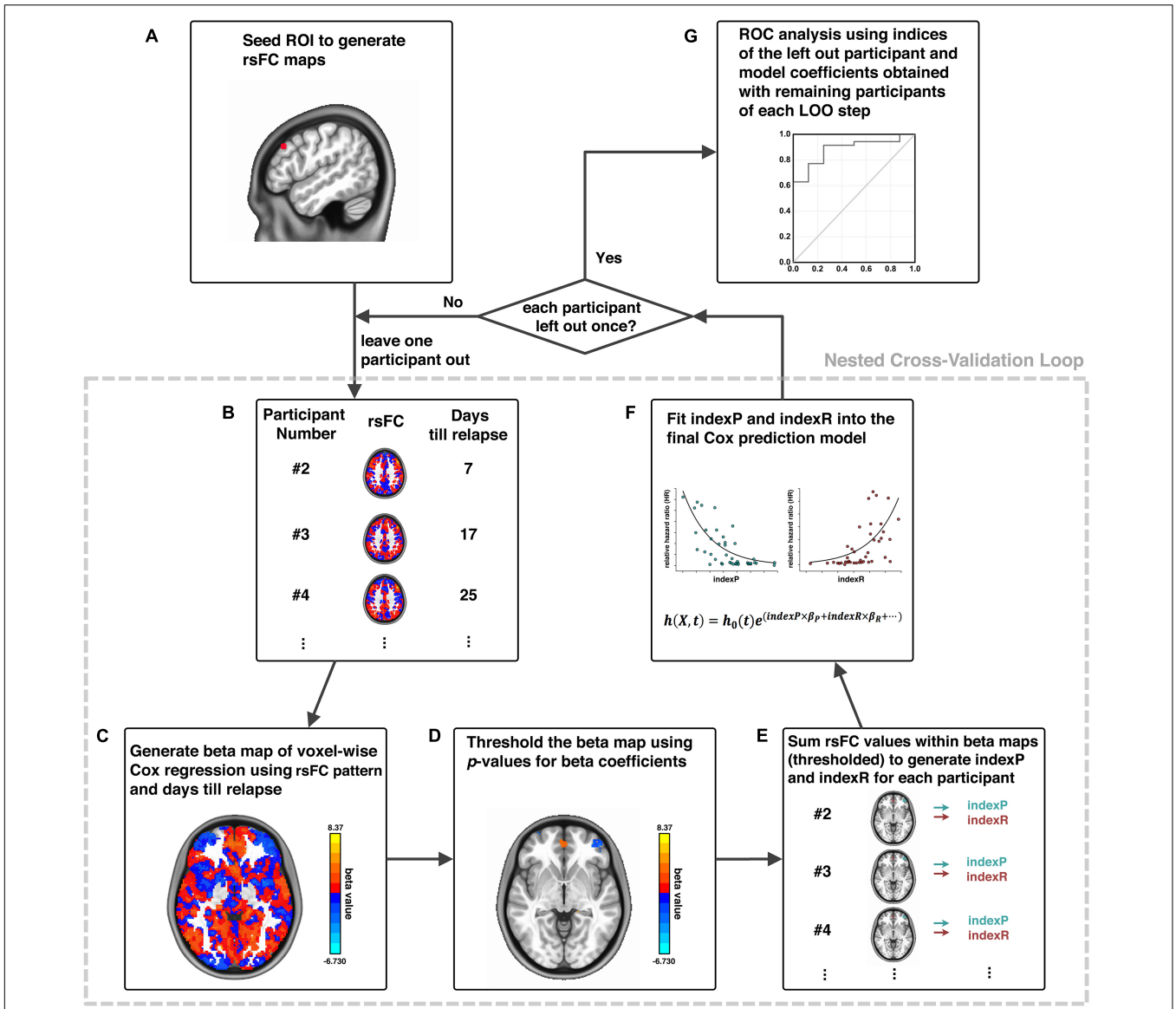

FIGURE 1 | Schematic diagram of analytical pipeline. Illustration of our analytical procedures using one exemplar seed ROI, adapted from Zhai et al. (2021). First, an ROI is selected as a seed **(A)**; the whole-brain rsFC of this seed is calculated for each participant **(B)**; a voxel-wise Cox regression is conducted using rsFC and days until relapse to generate beta maps **(C)**; beta maps of Cox regression is thresholded **(D)**; generation of indexP and indexR by linearly summation of the rsFC values within the thresholded beta maps for the negative and positive beta voxels, respectively **(E)**; construction of the final prediction model by fitting indexP and indexR into the Cox model **(F)**; procedures B to F were organized in a nested cross-validation loop, and after each participant is left out once, an ROC analysis evaluates the final prediction model **(G)**. rsFC, resting-state functional connectivity; ROI, region-of-interest; ROC, Receiver-Operating-Characteristics.

in the connectome-based predictive modeling (Shen et al., 2017). These thresholded beta/HR maps were subsequently used to generate a set of "protective circuits" (voxels with negative beta values/HR value less than 1, indicating less risk of relapse with stronger functional connectivity), and a set of "risk circuits" (voxels with positive beta values/HR value greater than 1, indicating higher risk of relapse with stronger functional connectivity), as well as two composite indices: indexP and indexR by linear summation of functional connectivity from all voxels within the "protective" and the "risk" circuits, respectively (**Figures 1D,E**).

Step five was the final Cox model fitting for brain-behavior relationship using these two composite indices, with age, sex, years of education (edu), daily cigarette use (CPD) and head motion during fMRI scan (HM) as covariates: $h(X_i, t) = h_0(t)e^{(indexP \times \beta_P + indexR \times \beta_R + age \times \beta_A + sex \times \beta_S + edu \times \beta_E + CPD + \beta_C + HM \times \beta_H)}$, (**Figure 1F**), and Receiver-Operating-Characteristic (ROC) analysis for model evaluation (**Figure 1G**). Step three to step five (**Figures 1B–F**) was organized into a nested cross-validation loop, where the voxel-wise Cox regression and thresholding serve the purpose of feature selection, and the final Cox fitting with the two composite indices

works as final model generation. The loop was repeated n times (n equals the number of participants), and each time a new model was developed from scratch with the n-th participant being left out. After the nested cross-validation loop was completed, the thresholds array for the cross-validated ROC analysis for model evaluation was generated with the actual predictor values (i.e., indexR and indexP, as well as other covariates such as age and years of education etc.) of each participant and the model that was generated with this participant being left out (**Figure 1G**).

In the final step, permutation test was performed to determine statistical significance based on empirical distribution determined with the permutation. We repeated the entire analysis 10,000 times, each time with the predictor (composite indices) and outcome (days till relapse) pairs randomly permuted to generate the data/model specific empirical *null* distribution for the area-under-the-curve (AUC) values of the ROC curve. The p-value of the AUC was then derived based on the ranking of the actual AUC value in this empirical *null* distribution.

Furthermore, our prediction modeling can be adapted into different settings based on specific applications. For example, in order to evaluate the prediction potential of our composite indices in early relapse prediction, we generated an early relapse prediction model with the indexP and indexR to predict cocaine relapse at an early follow-up cut-off of 30-day follow-up, as well as an intermediate prediction model with follow-up cut-off at 90-day, using the pipeline described above.

Post-hoc Analyses of Disease Subtyping

We performed several *post-hoc* analyses to further utilize our prediction modeling to explore brain mechanisms of cocaine addiction and to assess individual difference in the brain (functional connectivity) versus behavioral (relapse) relationship. First, we binarized the HR maps of all leave-one-out steps, and then stacked them together to generate a heat map of relapse relevant functional circuits. This heat map was further arbitrarily thresholded based on the majority of leave-one-out steps (e.g., $>$ 85% as demonstrated here) to demonstrate the group-level protective and risk circuits. We then extracted the averaged functional connectivity from each of the 43 participants within the group-level protective and risk circuits as the input for our *post-hoc* analyses, defined as the idxP_ph, and the idxR_ph, respectively, for the protective and risk circuits (note here the suffix "ph" stands for *post-hoc*, to be differentiated from the composite indices "indexP" and "indexR" used in the abovementioned prediction modeling section). Linear regression analysis was conducted to explore the relationship between the idxP_ph and the idxR_ph. To identify potential subtypes of cocaine dependence, we also conducted the k-means clustering in the P-R space (idxP_ph and idxR_ph). The optimal number of clusters was determined by visual inspection with the "elbow criterion" at a cluster number so that adding another cluster only grants minimal returns (variance explained) with the increment of cost (overfitting). The "elbow curve" was depicted as $\sum D_{within}/\sum D_{between}$, where $\sum D_{within}$ is the sum of within cluster distances and $\sum D_{between}$ is the sum of between cluster distances.

(ANTICIPATED) RESULTS

Demographic and Clinical Characterization

The current cohort of 43 participants included five females and 38 males with a mean (SD) age of 43.4 (7.2). **Table 1** lists the demographic information, clinical and head-motion assessments. The clinical characterization of cocaine relapse during the follow-up is illustrated in **Figure 2**; as shown in the Kaplan–Meier curve, during the early relapse at cut-off of 30-day, 22 out of 43 (51.2%) failed to remain abstinent; by the end of the 6-month follow-up period, 35 out of 43 (81.4%) participants had relapsed.

The Predicative Region-of-Interest of Cocaine Relapse

The prediction modeling we proposed here will grant the final results of (1) a specific ROI (e.g., dlPFC) that is identified predictive of certain behavior (e.g., cocaine relapse), with prediction accuracy evaluated with the AUC value of the ROC curve; and (2) a set of protective circuits and risk circuits that are underlying the prediction. In our previous investigation on the dlPFC ROIs across the entire surface area of bilateral dlPFC, three dlPFC loci were identified significantly predictive of cocaine relapse with their corresponding protective and risk functional circuits (Zhai et al., 2021). Here we choose the predictive ROI on the left dlPFC to demonstrate the anticipated results of our prediction modeling pipeline (**Figure 3**). As **Figure 3A** shows, the demonstrative left dlPFC ROI is locate at MNI coordinates of [−48, 30, 34]. **Figure 3B** demonstrates the prediction accuracy of 83.9% as measured by the AUC value of the ROC curve. The statistical significance is confirmed by the p-value of 0.0005 based on the *empirical null-distribution* generated with the permutation test. The predictive ROI associated group-level protective and risk functional circuits are recapped in **Figure 3C**. More detailed descriptions and discussions on these functional circuits can be found in the "predictive ROI-1" section of Zhai et al. (2021). We further tested whether clinical measurements could predict cocaine relapse by utilizing the same prediction modeling method proposed here, and the clinical measurements tested here included the InDUC, CCQ, cocaine use years, days of cocaine use in the past 90 days, and days since last cocaine use. None of these measurements significantly predicted cocaine relapse (see **Supplementary Table 1** for details).

Early and Intermediate Relapse Prediction of the Predictive Region-of-Interest

The composite indices (indexP and indexR) of the protective and risk circuits associated with the predictive ROI can also be used to build other prediction models such as the early and intermediate relapse prediction models. By setting up the cut-off follow-up time at 30 days, an early relapse prediction model (**Figure 4A**) predicted cocaine relapse with a relatively lower, but statistically significant AUC value of 0.714 of its ROC curve. For comparison, we also built an intermediate prediction model (**Figure 4B**) that

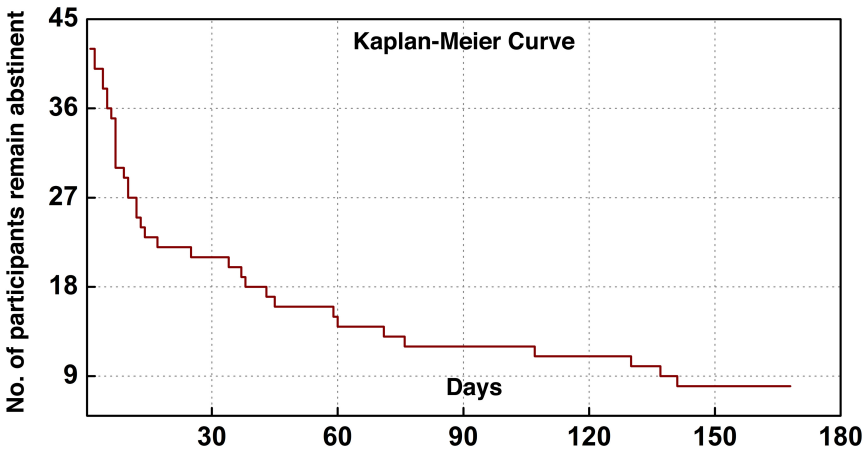

FIGURE 2 | Clinical characterization of cocaine relapse. The Kaplan–Meier curve illustrates the survivorship of participants in terms of maintaining abstinence.

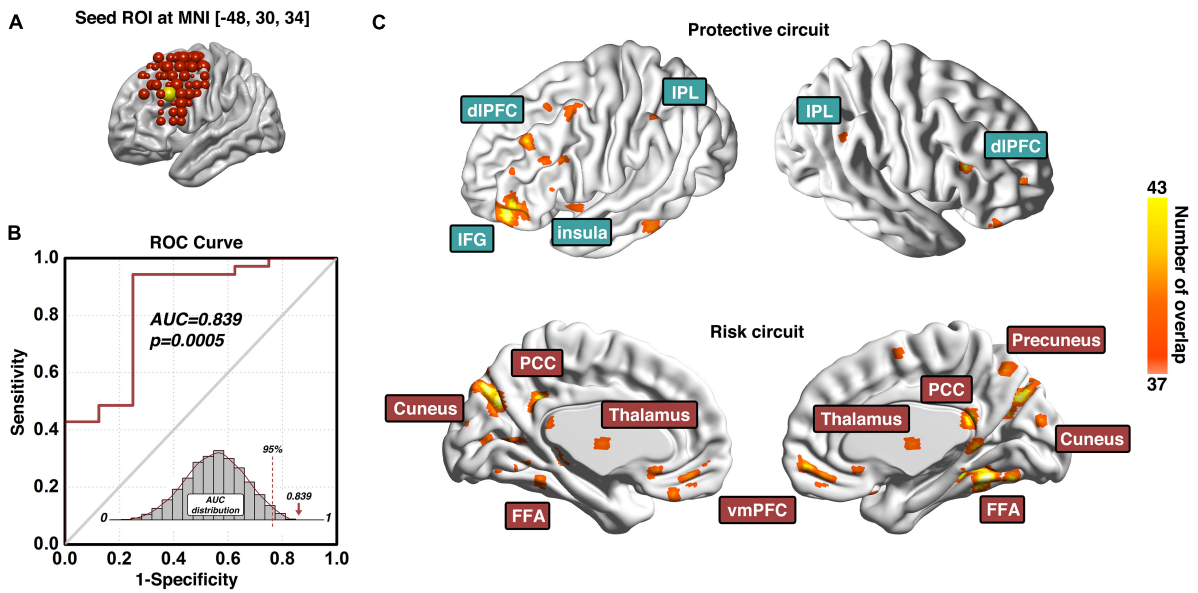

FIGURE 3 | Predictive ROI location, model prediction accuracy, and associated functional circuits. Adapted from Zhai et al. (2021), panel **(A)** shows the location and MNI coordinates of the predictive dlPFC ROI; the prediction accuracy measured with the area-under-the-curve (AUC) of the receiver-operating-characteristic (ROC) curve and its corresponding statistical significance is demonstrated in panel **(B)**; and the functional circuits associated with this dlPFC ROI that were used to generate the composite indexP and indexR for subsequent early relapse prediction is recapped in panel **(C)**. ROI, region-of-interest; ROC, Receiver-Operating-Characteristics; AUC, area-under-the-curve; dlPFC, dorsolateral prefrontal cortex; IPL, inferior parietal lobule; IFG, inferior frontal gyrus; PCC, posterior cingulate cortex; FFA, fusiform face area; vmPFC, ventromedial prefrontal cortex.

was capable of predicting cocaine relapse with an AUC value of 0.833 of its ROC curve by setting the cut-off follow-up time at 90 days. Statistical significance was verified with the permutation test based *empirical null-distribution* curves, which showed *p*-values of 0.0249 and 0.0010 for the early and intermediate relapse prediction models, respectively.

Post-hoc Analyses of Disease Subtyping

For *post-hoc* analyses exploring the protective-risk relationship, we first defined idxP_ph and idxR_ph as the averaged functional connectivity from each of the 43 participants within the group-level protective and risk circuits, respectively (note here the suffix "ph" stands for *post-hoc*, to be differentiated from the composite indices "indexP" and "indexR" used in the prediction modeling section). As **Figure 5A** shows, the *post-hoc* indices idxP_ph and idxR_ph showed significant negative correlation ($R^2 = 0.402$, $p < 0.0001$). For potential subtyping of cocaine use disorder in terms of vulnerability to relapse, we also conducted the *k*-means clustering in the two-dimensional space of (idxP_ph, idxR_ph). **Figure 5B** shows the "elbow curve" depicted as the ratio of the sum of within cluster distances to the sum of

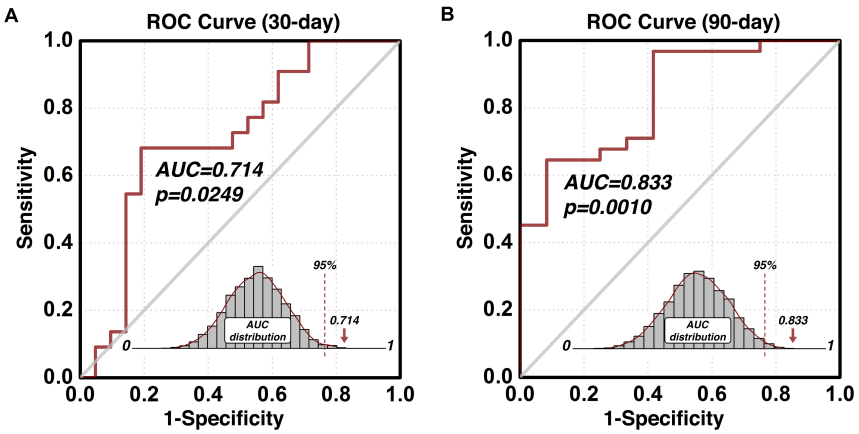

FIGURE 4 | Predict validity of the early and intermediate relapse prediction models. The prediction accuracy using the functional circuits of the identified predictive dlPFC ROI is illustrated in panel **(A)** for the early relapse prediction model where the follow-up cut-off is at 30 days, and in panel **(B)** for the intermediate relapse prediction model where the follow-up cut-off is at 90 days. ROC, Receiver-Operating-Characteristics; AUC, area-under-the-curve; dlPFC, dorsolateral prefrontal cortex; ROI, region-of-interest.

between cluster distances from $k = 2$ to $k = 11$. Here $k = 4$ was selected as the number of clusters as it represents a good balance between the benefit and the cost based on visual inspection of the elbow curve. The clustering result is shown in **Figure 5C**. Each of the four clusters represents a specific subtype of cocaine dependent participants. Cluster I is at the bottom-right corner (green diamond, $n = 7$, median days till relapse = 168 days) of the (idxP_ph, idxR_ph) space, Cluster II at the top-left corner (magenta triangle, $n = 15$, median days till relapse = 7 days), and Cluster III and Cluster IV are in the middle (yellow circle, $n = 11$, median days till relapse = 25 days; and cyan square, $n = 9$, median days till relapse = 60 days). Note here all *post-hoc* analyses conducted in the (idxP_ph, idxR_ph) space were with a sample size of 42, as one participant was excluded since both *post-hoc* indices were beyond the three-standard-deviation range. Corresponding results with this participant included can be seen in **Supplementary Figure 1**.

DISCUSSION

We presented here a modeling approach to predict time-dependent follow-up behaviors by fMRI-based brain metrics, and demonstrated the utility of the approach in predicting relapse to drug use following a psychosocial treatment in a cohort of treatment-seeking cocaine users. This modeling is a combination of seed-based functional connectivity and voxel-wise Cox regression organized in a nested cross-validation fashion, which is suitable for investigation of brain-behavior relationships reliably in patient cohorts with small-to-moderate sample sizes.

Neural Mechanisms and Individual-Level Relapse Prediction

As demonstrated in the prediction of cocaine relapse in **Figure 3**, our proposed modeling method is capable of identifying a prediction model in which functional connectivity of a specific brain region predicts individual's relapse behaviors with high accuracy. The nature of the Cox regression results in two functional brain circuit sets, one protective and one risk that collectively underlie the high prediction validity. As such, these two functional circuits could be considered a system-level neural mechanism of cocaine relapse. The ROC analysis that yielded the high AUC value is within the nested cross-validation framework, which indicates the model's prediction potential on independent participants. Although the proposed model is built upon the 6-month follow-up data, the identified protective and risk functional circuits are also capable of predicting early relapse. As shown in **Figure 4**, using the indices (indexP and indexR) from the same functional circuits derived from the 6-month model, prediction of early relapse (30 day) can also be achieved with a relatively lower but statistically significant prediction accuracy (AUC of 0.714).

Based on the *post-hoc* analyses, the *post-hoc* protective factor (idxP_ph) and the risk factor (idxR_ph) are negatively correlated, suggesting participants with higher protective capability tend to have lower risk factor, and *vice versa.* Further clustering analysis on the (idxP_ph, idxR_ph) space identified four subtypes of cocaine relapse related participants. Subtype I (N = 7) had highest values of the idxP_ph and lowest idxR_ph, and held the longest time till relapse (median of 168 days till relapse). Subtype II ($N = 15$), on the contrary, had lowest values of the idxP_ph and highest idxR_ph, and were all early relapse participants with the shortest time till relapse (median of 7 days till relapse). Subtypes III ($N = 11$) and IV ($N = 9$) fell between the subtypes I and II. Participants in these two subgroups showed similar levels of idxP_ph and idxR_ph with moderate days till relapse (median of 25 and 60 days till relapse, respectively). These results suggest that using the protective and risk indices, potential subtypes may be characterized for novel/independent participants by simply measuring their resting-state fMRI and calculating the values of these fMRI indices. These imaging metrics may be used to guide the design of personalized treatment strategies

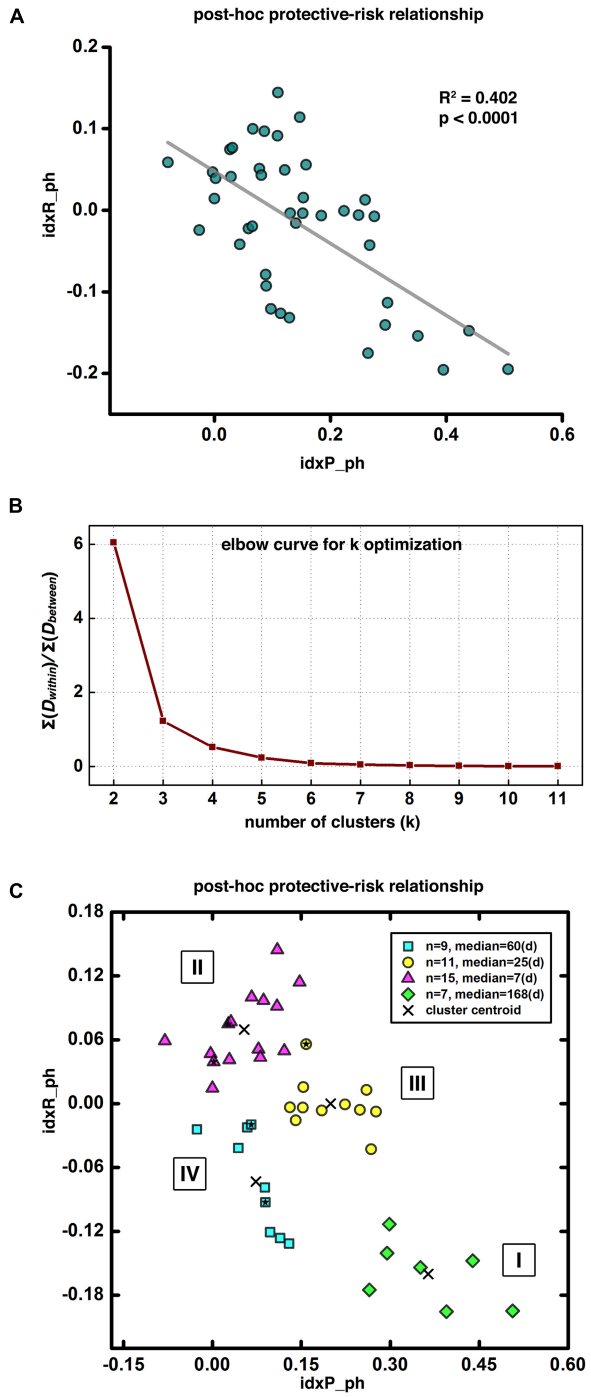

FIGURE 5 | *Post-hoc* results and disease subtyping. Panel **(A)** shows significant negative correlation between the *post-hoc* protective and risk indices. Panel **(B)** demonstrates the "elbow curve" for cluster number selection in clustering analysis for disease subtyping. Panel **(C)** illustrates four potential subtypes of cocaine dependent participants as indicated by our clustering result, Subtype I at the bottom-right corner with longest abstinent days (green diamonds), Subtype II at the top-left corner with the shortest days till relapse (magenta triangles), and Subtypes III and IV in-between with moderated days till relapse (yellow circles and cyan squares). The five solid stars within the corresponding symbol shapes label the five female participants in current demonstrative cohort.

specific to individuals (e.g., to promote the protective circuits for participants with a high risk index but without matched protective index; or to inhibit the risk circuits for participants with a strong, intact protective index).

Neuromodulation Implications

As in our demonstration of relapse prediction, a dlPFC ROI located at MNI coordinates [−48, 30, 34] was found to be highly predictive with its functional circuits (**Figure 3**). The prediction modeling proposed here is capable of identifying brain ROIs, whose functional circuits are closely related to certain behaviors/treatment outcomes. This shows the potential utility of the prediction modeling in selecting brain sites for neuromodulation-based treatment of neuropsychiatric/neurological disorders. In neuromodulation (e.g., TMS) treatment, one of the critical issues is to determine the effective stimulation site. Intuitively, in a direct search among M different brain sites with N participants in each site to evaluate treatment efficacy (a total of M × N participants), a potential optimal stimulation site would be determined by comparing the group outcomes of these M clinical studies. Furthermore, other than the stimulation location, the large parameter space (e.g., frequency, intensity, etc.) makes such clinical investigations impractically costly and time consuming to undertake in a systematic and comprehensive manner, and no such effort has been made in neuropsychiatric disorders other than medication-resistant depression (Fox et al., 2012). An alternative strategy is a two-stage approach combining neuroimaging-based search for relevant brain areas and the actual neuromodulation on these limited and specific sites. In the first stage, imaging data are collected ideally at the baseline and after a traditional treatment (non-neuromodulation, such as psychosocial treatment), and then location-specific imaging measures (e.g., functional connectivity) are identified that are related to treatment outcome. These locations are therefore considered as potential treatment sites. Then in the second stage, these candidate sites are further confirmed for their treatment efficacy with actual neuromodulation. The first stage can be done in a systematic and comprehensive manner covering a large brain area (e.g., dlPFC) while only few most relevant brain locations being tested in the second stage, thus greatly reducing the number needed for neuromodulation-based clinical investigations. Our previous study utilizing this modeling technique investigated 98 ROIs covering the entire surface of the bilateral dlPFC and identified three ROIs predictive of cocaine relapse (Zhai et al., 2021), with one on the left side being spatially proximal to an actual dlPFC stimulation site that showed promising treatment efficacy in a clinical study treating cocaine addiction (Terraneo et al., 2016). This is a perfect example of potential applications of our proposed modeling approach in the first stage for identification of potential effective TMS sites, which can then be used to guide experimental designs in the second stage for validation of these potentially effective TMS targets.

Limitations

Several limitations should be considered regarding our analysis. We have a moderate sample size less than 50, and an unbalanced

sex (five females and 38 males), which makes the dataset less ideal. However, there are practical difficulties associated with research on psychiatric diseases such as addiction, especially with a longitudinal follow-up up to 24 weeks. Combined with proper modeling and validating method, the current dataset is capable of providing at least novel hypothesis (i.e., the identified predictive ROI and its functional circuits) to be further tested clinically (i.e., neuromodulation treatment efficacy). Our sample included only five females and future work should address the possibility of gender differences.

Conclusion

Demonstrated with a treatment-seeking cocaine addiction cohort, we presented here a prediction-modeling method that combines the hypothesis-driven seed-based functional connectivity and the Cox regression-based prediction with built-in nested cross-validation to assess treatment outcome (relapse to drug use). Other than predicting certain behaviors/treatment outcomes at individual level, specific brain regions, as well as their functional circuits, relevant to the behavioral/clinical assessments can also be identified using this modeling method. Functional connectivity of the brain circuits showing protective or risk effect on drug relapse may be used for disease subtyping. Taken together, the prediction modeling method presented here is capable of identifying brain regions and related functional circuits that are predictive of certain behavior/treatment outcome, which clearly shows neuromodulation implications and can be used for individualized prognosis and treatment protocol design.

DATA AVAILABILITY STATEMENT

The data analyzed in this study is subject to the following licenses/restrictions: Raw data associated with the current study contain personally identifiable information that could compromise the privacy of research participants if shared publicly. Codes and derived data supporting the findings of this study are available from the corresponding author contingency of institutional approval, upon reasonable request. Requests to access these datasets should be directed to YY, yihongyang@intra.nida.nih.gov.

ETHICS STATEMENT

The studies involving human participants were reviewed and approved by Institutional Review Boards of the University of Texas Southwestern Medical Center and the Veterans Administration North Texas Health Care System. The patients/participants provided their written informed consent to participate in this study.

AUTHOR CONTRIBUTIONS

TZ, HG, and YY contributed to the manuscript review, revision, and conception and design of the study. YY contributed to the funding/resources acquisition and overall supervision. TZ and HG organized the database. TZ performed the statistical analyses and visualization of the results. TZ wrote the first draft of the manuscript. All authors contributed to the article and approved the submitted version.

FUNDING

This study was supported by the Intramural Research Program of the National Institute on Drug Abuse (NIDA-IRP), NIH (ZIA DA000469).

ACKNOWLEDGMENTS

The authors would like to thank the Substance Abuse Team at the VA North Texas Health Care System, Homeward Bound, Inc., for their assistance, and Nexus Recovery Center for their support in the screening and recruitment of study participants, and Dr. Bryon Adinoff for providing the data.

SUPPLEMENTARY MATERIAL

The Supplementary Material for this article can be found online at: https://www.frontiersin.org/articles/10.3389/fnins.2021.768602/full#supplementary-material

REFERENCES

Cook, C. C. (1988). The Minnesota model in the management of drug and alcohol dependency: miracle, method or myth? Part I. The philosophy and the programme. *Br. J. Addict.* 83, 625–634.

Cox, D. R. (1972). Regression models and life-tables. *J. R. Stat. Soc. Ser. B Methodol.* 34, 187–202. doi: 10.1111/j.2517-6161.1972.tb00899.x

Dutra, L., Stathopoulou, G., Basden, S. L., Leyro, T. M., Powers, M. B., and Otto, M. W. (2008). A meta-analytic review of psychosocial interventions for substance use disorders. *Am. J. Psychiatry* 165, 179–187. doi: 10.1176/appi.ajp.2007.06111851

Fox, M. D., Buckner, R. L., White, M. P., Greicius, M. D., and Pascual-Leone, A. (2012). Efficacy of transcranial magnetic stimulation targets for depression is related to intrinsic functional connectivity with the subgenual cingulate. *Biol. Psychiatry* 72, 595–603. doi: 10.1016/j.biopsych.2012.04.028

Fransson, P. (2005). Spontaneous low-frequency BOLD signal fluctuations: an fMRI investigation of the resting-state default mode of brain function hypothesis. *Hum. Brain Mapp.* 26, 15–29.

Gabrieli, J. D. E., Ghosh, S. S., and Whitfield-Gabrieli, S. (2015). Prediction as a humanitarian and pragmatic contribution from human cognitive neuroscience. *Neuron* 85, 11–26. doi: 10.1016/j.neuron.2014.10.047

Geng, X., Hu, Y., Gu, H., Salmeron, B. J., Adinoff, B., Stein, E. A., et al. (2017). Salience and default mode network dysregulation in chronic cocaine users predict treatment outcome. *Brain* 140, 1513–1524. doi: 10.1093/brain/awx036

Koob, G. F., and Volkow, N. D. (2016). Neurobiology of addiction: a neurocircuitry analysis. *Lancet Psychiatry* 3, 760–773. doi: 10.1016/S2215-0366(16)00104-8

Li, X., Hartwell, K. J., Owens, M., Lematty, T., Borckardt, J. J., Hanlon, C. A., et al. (2013). Repetitive transcranial magnetic stimulation of the dorsolateral prefrontal cortex reduces nicotine cue craving. *Biol. Psychiatry* 73, 714–720. doi: 10.1016/j.biopsych.2013.01.003

Luo, X., Zhang, S., Hu, S., Bednarski, S. R., Erdman, E., Farr, O. M., et al. (2013). Error processing and gender-shared and -specific neural predictors of relapse in cocaine dependence. *Brain* 136, 1231–1244. doi: 10.1093/brain/awt040

Meng, X., Jiang, R., Lin, D., Bustillo, J., Jones, T., Chen, J., et al. (2017). Predicting individualized clinical measures by a generalized prediction framework and multimodal fusion of MRI data. *Neuroimage* 145, 218–229. doi: 10.1016/j.neuroimage.2016.05.026

Ogawa, S., Lee, T. M., Kay, A. R., and Tank, D. W. (1990). Brain magnetic resonance imaging with contrast dependent on blood oxygenation. *Proc. Natl. Acad. Sci. U. S. A.* 87, 9868–9872. doi: 10.1073/pnas.87.24.9868

Poldrack, R. A., Huckins, G., and Varoquaux, G. (2020). Establishment of best practices for evidence for prediction: a review. *JAMA Psychiatry* 77, 534–540. doi: 10.1001/jamapsychiatry.2019.3671

Politi, E., Fauci, E., Santoro, A., and Smeraldi, E. (2008). Daily sessions of transcranial magnetic stimulation to the left prefrontal cortex gradually reduce cocaine craving. *Am. J. Addict.* 17, 345–346. doi: 10.1080/10550490802139283

Pripfl, J., Tomova, L., Riecansky, I., and Lamm, C. (2014). Transcranial magnetic stimulation of the left dorsolateral prefrontal cortex decreases cue-induced nicotine craving and EEG delta power. *Brain Stimul.* 7, 226–233. doi: 10.1016/j.brs.2013.11.003

Shen, X., Finn, E. S., Scheinost, D., Rosenberg, M. D., Chun, M. M., Papademetris, X., et al. (2017). Using connectome-based predictive modeling to predict individual behavior from brain connectivity. *Nat. Protoc.* 12, 506–518. doi: 10.1038/nprot.2016.178

Szucs, D., and Ioannidis, J. P. (2020). Sample size evolution in neuroimaging research: an evaluation of highly-cited studies (1990-2012) and of latest practices (2017-2018) in high-impact journals. *Neuroimage* 221:117164. doi: 10.1016/j.neuroimage.2020.117164

Terraneo, A., Leggio, L., Saladini, M., Ermani, M., Bonci, A., and Gallimberti, L. (2016). Transcranial magnetic stimulation of dorsolateral prefrontal cortex reduces cocaine use: a pilot study. *Eur. Neuropsychopharmacol.* 26, 37–44. doi: 10.1016/j.euroneuro.2015.11.011

Tonigan, J. S., and Miller, W. R. (2002). The inventory of drug use consequences (InDUC): test-retest stability and sensitivity to detect change. *Psychol. Addict. Behav.* 16, 165–168.

Turner, B. O., Paul, E. J., Miller, M. B., and Barbey, A. K. (2018). Small sample sizes reduce the replicability of task-based fMRI studies. *Commun. Biol.* 1, 1–10. doi: 10.1038/s42003-018-0073-z

Vabalas, A., Gowen, E., Poliakoff, E., and Casson, A. J. (2019). Machine learning algorithm validation with a limited sample size. *PLoS One* 14:e0224365. doi: 10.1371/journal.pone.0224365

Varma, S., and Simon, R. (2006). Bias in error estimation when using cross-validation for model selection. *BMC Bioinformatics* 7:91. doi: 10.1186/1471-2105-7-91

Volkow, N. D., Koob, G. F., and McLellan, A. T. (2016). Neurobiologic advances from the brain disease model of addiction. *N. Engl. J. Med.* 374, 363–371. doi: 10.1056/NEJMra1511480

Whelan, R., and Garavan, H. (2014). When optimism hurts: inflated predictions in psychiatric neuroimaging. *Biol. Psychiatry* 75, 746–748. doi: 10.1016/j.biopsych.2013.05.014

Zhai, T., Salmeron, B. J., Gu, H., Adinoff, B., Stein, E. A., and Yang, Y. (2021). Functional connectivity of dorsolateral prefrontal cortex predicts cocaine relapse: implications for neuromodulation treatment. *Brain Commun.* 3:fcab120. doi: 10.1093/braincomms/fcab120

Conflict of Interest: The authors declare that the research was conducted in the absence of any commercial or financial relationships that could be construed as a potential conflict of interest.

frontiers in Neuroscience

ORIGINAL RESEARCH
published: 13 December 2021
doi: 10.3389/fnins.2021.763966

Dynamic Functional Connectivity Better Predicts Disability Than Structural and Static Functional Connectivity in People With Multiple Sclerosis

Ceren Tozlu[1], *Keith Jamison*[1], *Susan A. Gauthier*[1,2,3] *and Amy Kuceyeski*[1,4]*

[1] Department of Radiology, Weill Cornell Medicine, New York, NY, United States, [2] Judith Jaffe Multiple Sclerosis Center, Weill Cornell Medicine, New York, NY, United States, [3] Department of Neurology, Weill Cornell Medical College, New York, NY, United States, [4] Brain and Mind Research Institute, Weill Cornell Medicine, New York, NY, United States

OPEN ACCESS

Edited by:
Zachory Wei,
Emory University, United States

Reviewed by:
Yanbo Zhang,
University of Alberta, Canada
Shuanglin Wang,
Tianjin Medical University General Hospital, China
Stephanie Fountain-Zaragoza,
Medical University of South Carolina, United States

***Correspondence:**
Amy Kuceyeski
amk2012@med.cornell.edu

Specialty section:
This article was submitted to Brain Imaging Methods, a section of the journal Frontiers in Neuroscience

Received: 24 August 2021
Accepted: 17 November 2021
Published: 13 December 2021

Citation:
Tozlu C, Jamison K, Gauthier SA and Kuceyeski A (2021) Dynamic Functional Connectivity Better Predicts Disability Than Structural and Static Functional Connectivity in People With Multiple Sclerosis. Front. Neurosci. 15:763966. doi: 10.3389/fnins.2021.763966

Background: Advanced imaging techniques such as diffusion and functional MRI can be used to identify pathology-related changes to the brain's structural and functional connectivity (SC and FC) networks and mapping of these changes to disability and compensatory mechanisms in people with multiple sclerosis (pwMS). No study to date performed a comparison study to investigate which connectivity type (SC, static or dynamic FC) better distinguishes healthy controls (HC) from pwMS and/or classifies pwMS by disability status.

Aims: We aim to compare the performance of SC, static FC, and dynamic FC (dFC) in classifying (a) HC vs. pwMS and (b) pwMS who have no disability vs. with disability. The secondary objective of the study is to identify which brain regions' connectome measures contribute most to the classification tasks.

Materials and Methods: One hundred pwMS and 19 HC were included. Expanded Disability Status Scale (EDSS) was used to assess disability, where 67 pwMS who had EDSS<2 were considered as not having disability. Diffusion and resting-state functional MRI were used to compute the SC and FC matrices, respectively. Logistic regression with ridge regularization was performed, where the models included demographics/clinical information and either pairwise entries or regional summaries from one of the following matrices: SC, FC, and dFC. The performance of the models was assessed using the area under the receiver operating curve (AUC).

Results: In classifying HC vs. pwMS, the regional SC model significantly outperformed others with a median AUC of 0.89 (p <0.05). In classifying pwMS by disability status, the regional dFC and dFC metrics models significantly outperformed others with a median AUC of 0.65 and 0.61 (p < 0.05). Regional SC in the dorsal attention, subcortical and cerebellar networks were the most important variables in the HC vs. pwMS classification task. Increased regional dFC in dorsal attention and visual networks and decreased regional dFC in frontoparietal and cerebellar networks in certain dFC states was associated with being in the group of pwMS with evidence of disability.

Discussion: Damage to SCs is a hallmark of MS and, unsurprisingly, the most accurate connectomic measure in classifying patients and controls. On the other hand, dynamic FC metrics were most important for determining disability level in pwMS, and could represent functional compensation in response to white matter pathology in pwMS.

Keywords: multiple sclerosis, structural connectivity, functional connectivity, machine learning, predictive modeling

1. INTRODUCTION

Multiple Sclerosis (MS) is a chronic disease characterized by inflammatory and demyelinating lesions within the central nervous system (Weinshenker et al., 1991). One key observation is that the disease burden in the brain, as measured with conventional imaging, is not always proportional to an individual's disability. Individuals can have identical lesion volume and very different levels of disability (Barkhof, 2002), making prognostication in this disease challenging. Advanced neuroimaging techniques may enable us to better understand the neuropathological mechanisms of MS, how they cause disability in MS and how the brain may compensate for this pathology. Brain connectivity network analysis, or connectomics, provides a promising tool with which to map the effect of MS-related pathology and to potentially capture reorganization mechanisms in response to pathology. Inflammation, demyelination, and axonal loss in people with MS (pwMS) disrupts the brain's structural connectome (SC), which may contribute to some of the changes observed in the brain's regional activation patterns, or functional connectome (FC) (Rocca et al., 2010, 2012, 2018; Roosendaal et al., 2010; Tona et al., 2014; Schoonheim et al., 2015).

Previous studies have used SC and FC separately or together to identify differences between pwMS and healthy controls (HC), to compare different clinical categories of MS, and to classify pwMS by disability or cognitive impairment level (Richiardi et al., 2012; Kocevar et al., 2016; Zhong et al., 2017; Saccà et al., 2018; Zurita et al., 2018; Has Silemek et al., 2020). It has been shown that alterations in the SC and/or FC in particular networks are associated with motor and cognitive impairment in pwMS (Faivre et al., 2012; Rocca et al., 2012; Basile et al., 2014; Filippi et al., 2015; Kuceyeski et al., 2015, 2018). SC damage may cause an upregulation of FC in specific networks as a compensatory mechanism in the early stages of MS, which then wanes in the later stages of the disease. In particular, the Expanded Disability Status Scale (EDSS) threshold of 3 was previously identified as the cut-off for functional reorganization and adaptation in MS (Hawellek et al., 2011; Faivre et al., 2012; Tommasin et al., 2018). Two individuals with the same pattern of SC damage may have different disability levels depending on where they are in the trajectory of compensatory FC, thus, FC may be more informative of disability than SC in this case.

An individual's FC is usually obtained by correlating regional Blood Oxygenation Level Dependent (BOLD) signals acquired over the entire functional MRI (fMRI) scan; however, this "static" FC derivation does not consider the fluctuations in the brain network topology that can occur over time (Biswal et al., 1995; Damaraju et al., 2014). Dynamic FC (dFC) approaches allow assessment of the varying topology of FC over time by using sliding windows to assess dynamic FCs (Allen et al., 2014). There is increased interest in using dFC to investigate pathological mechanisms in psychiatric disorders, and stroke (Damaraju et al., 2014; Rashid et al., 2016; Sambataro et al., 2017; Mennigen et al., 2018; Bonkhoff et al., 2020, 2021). In MS, recent studies have used dFC to (1) compare clinically isolated syndrome (CIS) patients to HC (Rocca et al., 2019), (2) analyze relationships with information processing speed in relapsing-remitting (RR) pwMS (van Geest et al., 2018), and (3) classify cognitively impaired vs. preserved pwMS (d'Ambrosio et al., 2019; Eijlers et al., 2019). However, no study to date has performed a rigorous analysis of the relative contributions of multi-modal imaging data including SC, static FC, and dynamic FC in classifying HC vs. pwMS and/or pwMS by disability status. Understanding the relative contributions of the various modalities may provide insight into disability-relevant disease or compensatory mechanisms.

Therefore, the principal aim of the present study was to compare the performance of either pairwise or regional SC, FC, and dFC metrics in classifying (1) HC vs. pwMS and (2) pwMS who had no disability vs. those who had evidence of disability. The secondary aim was to identify the most important pairwise and regional connections as well as dFC metrics for the classification tasks. Diffusion and resting-state functional MRI were used to compute the SC and FC matrices, respectively. We hypothesized that models including SC could best distinguish HC from pwMS, as white matter lesions impacting SC networks are a hallmark of the disease. Furthermore, we hypothesized that models containing FC and/or dFC would best distinguish disability levels in pwMS as this modality likely is sensitive to functional compensation mechanisms that may underlie disability in MS. Overall, our goal is to better understand mechanisms of pathology and resilience in MS, knowledge which could be used to improve the accuracy of prognoses and even develop novel therapies to reduce disability.

2. MATERIALS AND METHODS

2.1. Subjects

One hundred pwMS (median age: 45.5 [36.7, 56.0], 66% females) with a diagnosis of Clinically Isolated Syndrome (CIS)/MS based on the 2010 McDonald criteria (Polman et al., 2011) [CIS = 7, relapsing-remitting MS (RRMS) = 88, primary progressive MS (PPMS) and secondary progressive MS (SPMS) = 5] and 19 HC (median age: 45 [35, 49], 55% females) were included in our

study. Seven people with CIS were included in the group of pwMS as they are likely an early form of MS, they were all in the no disability group (EDSS < 2). MRIs and demographic data were collected (age, sex, and race for both HC and pwMS, clinical phenotype, and disease duration for pwMS). All subjects with SC and FC networks available were included in our study and a power analysis was not performed prior to the statistical analysis. Participants were excluded if they had contraindications to MRI or had ever been diagnosed or were currently on medication for a neurological or psychological disorder (other than a diagnosis of or medication for treatment of MS for the pwMS group, of course). The spinal cord lesion category was estimated from the patient's clinical radiology report, with 0 indicating those with no spinal lesions, 1 indicating those with one spinal lesion or 2 indicating those with more than one spinal lesion. The EDSS is the most frequently used disability scale in MS and captures mostly the motor functioning. EDSS ranges from 0 to 10 with 0.5-unit increments, where 0 indicates no disability and the increase in EDSS indicates higher level of disability. EDSS was used to quantify disability in our study, where an EDSS of 2 was used as a threshold to categorize disablity status: no disability (EDSS < 2) vs. evidence of disability (EDSS ≥ 2). This group division was based on EDSS values of 0–1.5 representing some abnormal signs in neurological examination but no functional impairment is appreciated. This was a cross-sectional study, and the MRIs and demographics/clinical data were collected the same year. All studies were approved by an ethical standards committee on human experimentation and written informed consent was obtained from all patients.

2.2. Image Acquisition, Processing, and Connectome Extraction

MRI data were acquired on a 3T Siemens Skyra scanner (Siemens, Erlangen, Germany) with a 20-channel head-neck coil and a 32-channel spine-array coil. Anatomical MRI (T1/T2/T2-FLAIR, 1 mm3 iso-voxel), resting-state fMRI (6 min, TR = 2.3 s, 3.75 $\times$ 3.75 $\times$ 4 mm voxels) and diffusion MRI (55 directions HARDI, b = 800, 1.8 $\times$ 1.8 $\times$ 2.5 mm voxels) acquisitions were performed. Sagittal STIR images were acquired for identification of spinal lesions (TR = 3.5 s, TI = 220 ms, TE = 45 ms, in-plane resolution 0.43 mm, FOV = 22 mm, slice thickness 3 mm). Multi-echo 2D GRE fieldmaps were collected for use with both fMRI and diffusion MRI (0.75 $\times$ 0.75 $\times$ 2 mm voxels, TE1 = 6.69 ms, $\triangle$TE = 4.06 ms, number of TEs = 6). The white and gray matter surfaces were checked for each subject on Freesurfer and hand-edited with control points and reconstruction editing if necessary.

White matter (WM) and gray matter (GM) were segmented and GM further parcellated into 86 regions of interest (68 cortical and 18 subcortex/cerebellum) using FreeSurfer (Fischl and Dale, 2000). As described elsewhere (Kuceyeski et al., 2016), fMRI preprocessing included simultaneous nuisance regression and removal of WM and cerebrospinal fluid (CSF) effects (Hallquist et al., 2013), followed by band-pass filtering (0.008–0.09 Hz) using the CONN v18b toolbox (Whitfield-Gabrieli and Nieto-Castanon, 2012) and SPM12 in Matlab. Nuisance regressors included 24 motion parameters (6 rotation and translation, temporal derivatives, and squared version of each) and the top 5 eigenvectors from eroded masks of both WM and CSF. The mean fMRI signal over all voxels in a region was calculated and the mean regional time series correlated (Pearson's correlation) between every pair of regions to obtain pairwise FC matrices. Regional FC node strengths were calculated by taking the sum of the columns in the FC matrix after removing the negative entries.

Diffusion MRI was interpolated to isotropic 1.8 mm voxels, and then corrected for eddy current, motion, and EPI-distortion with the eddy command from FSL 5.0.11 (Andersson and Sotiropoulos, 2016) using the outlier detection and replacement option (Andersson et al., 2016). MRtrix3Tissue (https://3Tissue.github.io), a fork of MRtrix3 (Tournier et al., 2019) was used to estimate a voxel-wise single-shell, 3-tissue constrained spherical deconvolution model (SS3T-CSD) and then compute whole-brain tractography for each subject. The SC matrix was constructed by taking the sum of the SIFT2 weights of streamlines connecting pairs of regions and then dividing by the sum of the two regions' volumes. In addition to the pairwise SC measures, regional SC node strength was quantified by taking the sum of each of the columns in the SC matrix.

2.3. Dynamic FC Analysis

Dynamic FC matrices were calculated using a tapered, sliding window approach in the GIFT toolbox (http://mialab.mrn.org/software/gift) (Allen et al., 2014; Damaraju et al., 2014). The BOLD time series that were extracted from 86 regions of FreeSurfer atlas (same atlas used for static FC and SC analysis) were used as an input to the GIFT toolbox. As suggested by Allen et al. (2014) and previous studies (Bonkhoff et al., 2020, 2021), dFC between two regional time courses was computed using a sliding window approach with a window size of 22 TR (50.6 s) in steps of 1 TR (2.3 s). A rectangular window of 22 time points convolved with a Gaussian of 3 TR (6.9 s) was used for tapering along the edges, resulting in 153 tapered time windows per subject. Once the dFC matrices were calculated, k-means clustering was applied to all dFC matrices to identify clusters of reoccurring dFC states. The elbow criterion, i.e. the ratio of within-cluster to between-cluster Manhattan (L1) distances, was used to identify the optimal number of clusters. The following metrics were extracted from the dFC analysis: (1) mean dwell time in each state (= how long the individual remains in a state once they transition to it), (2) transition probability from one dFC state to another between two consecutive time points, and (3) the number of overall state transitions in the scan. We extracted individuals' cluster centroids for each of the dFC states as the mean dFC of each dFC assigned to a particular cluster. Further, we took the node strength of the individuals' cluster centroids as a "regional dFC" measure (after removing negative entries in the dFC). Network-level interpretations were enabled by assigning each of the 86 gray matter regions to one of the 7 Yeo functional networks, plus a subcortical and a cerebellum network (Yeo et al., 2011).

2.4. Mass Univariate Analysis

First, demographics and clinical variables were tested for differences between the groups [(1) HC vs. pwMS and (2) pwMS

who had no disability (EDSS < 2) vs. evidence of disability (EDSS ≥ 2)] using Chi-squared test for qualitative variables, Wilcoxon rank-sum test for quantitative variables. As a *post-hoc* analysis, ANOVA was applied to compare the age, EDSS, and phenotypes between two MS disability groups A *t*-test was used to compare pairwise entries in static FC and dFC summary metrics, while Wilcoxon rank-sum test was performed to compare SC values between groups. Only pairwise connections in the SC that were non-zero in more than half of the controls were tested for differences between groups to minimize the effect of false positives in the tractography results. Differences were considered significant when $p < 0.05$ after Benjamini-Hochberg (BH) correction for multiple comparisons (Benjamini and Hochberg, 1995). All statistical analyses and graphs were performed using R (www.r-project.org), version 3.4.4 and Matlab (https://www.mathworks.com/) version R2020a.

2.5. Classification Analysis

Logistic regression with ridge regularization was used to classify (1) HC vs. pwMS and (2) pwMS who had no disability (EDSS < 2) vs. evidence of disability (EDSS ≥ 2). The classification models used demographics/clinical information (sex, age, race, disease duration, clinical phenotype, and spinal lesion burden category) and one of the pairwise or regional imaging data: SC, FC, dFC. For the HC vs. pwMS classification, only sex, age, and race were used as demographics/clinical variables. **Figure 1** shows the overall workflow of the study including the input datasets (SC, FC, and dFC in addition to the demographics and clinical variables) that were used in the various models.

The models were trained with outer and inner loops of k-fold cross-validation ($k = 5$) to optimize the hyperparameters and test model performance. The folds for both inner and outer loops were stratified to ensure that each fold contained the same proportion of subjects in the two classes as the original dataset. The inner loop (repeated over 5 different partitions of the training dataset only) optimized the set of hyperparameters that maximized validation AUC. A model was then fitted using the entire training dataset and those optimal hyperparameters, which was then assessed on the hold-out test set from the outer loop. The outer loop was repeated for 100 different random partitions of the data (see **Supplementary Figure 5**). The median of AUC (over all 5-folds $\times$ 100 iterations = 500 test sets) were calculated to assess the performance of the models. In addition to the AUC results; sensitivity, specificity, balanced accuracy (average of sensitivity and specificity), and F1 scores ($\frac{\mathrm{TP}}{\mathrm{TP}+1/2\times(\mathrm{FP}+\mathrm{FN})}$) where TP is the number of true positives, FP is the number of false positives, and FN is the number of false negatives are also provided to compare the results of the current study with previous findings. The classification performance of different models were compared using a permutation test (David, 2008). Differences were considered significant when $p < 0.05$ after BH correction for multiple comparisons (Benjamini and Hochberg, 1995).

When the data contains class imbalance, models may tend to favor the majority class. Due to the class imbalance in our data (19 HC vs. 100 pwMS and 67 pwMS with no disability vs. 33 pwMS with evidence of disability), the over-sampling approach Synthetic Majority Over-sampling Technique (SMOTE) (Chawla et al., 2002) was used to obtain a balanced training dataset during the cross-validation. SMOTE compensates for imbalanced classes by creating synthetic examples using nearest neighbor information and has been shown to be among the most robust and accurate methods with which to control for imbalanced data (Santos et al., 2018).

We considered feature weights in the ridge classification method to be the average parameter coefficient over all 500 models (100 partitions of the data $\times$ 5-folds). Feature weights of the pairwise connections were represented using a circle plot and summarized at a network level, while feature weights of the regional connections were illustrated via glass brains and summarized at a network level via circle plots. Important connectomic features were identified as those that had both large group differences (via the mass univariate statistical tests) and large feature weights from the ridge classifier (Tian et al., 2021).

3. RESULTS

3.1. Patient Characteristics

Table 1 shows the subjects' demographic and clinical information including sex, age, disease duration, EDSS, and spinal cord lesion number. Age and sex were not significantly different between HC and pwMS (corrected $p > 0.05$ for both). Unsurprisingly, pwMS who had no disability were younger (corrected $p < 0.05$) and had a trend toward shorter disease duration (corrected $p = 0.06$) compared to pwMS who had evidence of disability. The phenotype and disability groups were not independent (corrected $p < 0.05$), where the pwMS who had CIS phenotype were included in the no disability group and those who had progressive disease were included in the evidence of disability group. The *F*-values obtained with the ANOVA for the age was 16.65 ($p <$ 9.17e-05), for the EDSS 143.3 ($p <$ 2e-16), and for the phenotypes 7.67 ($p < 0.0008$). However, the two disability groups did not have a significant difference in sex ratio, number of spinal cord lesions, and brain lesion volume (corrected $p > 0.05$ for all).

3.2. Dynamic FC Results

Four clusters in the dynamic FC analysis was identified as optimal (see **Supplementary Figure 1**). **Figure 2** illustrates the 4 cluster centroids, or dynamic brain states (top panel), which are also summarized in the bottom panel by averaging the pairwise dFC values over Yeo network assignments separately for both the positive and negative values. All states show strong positive connections between ventral attention and somatomotor and between dorsal attention and visual networks, while the negative values vary more widely across the states. State 1 has more negative connections from ventral attention to visual and limbic networks. State 2 shows overall smaller magnitude negative connections and larger magnitude positive connections compared to other states. State 3 has more negative connections from fronto-parietal to somatomotor networks. State 4 differs from other states with larger magnitude negative connections from dorsal attention to default mode and ventral attention networks. **Figure 2** also depicts the mean dwell time and total number of state transitions for HC, pwMS, pwMS who had no

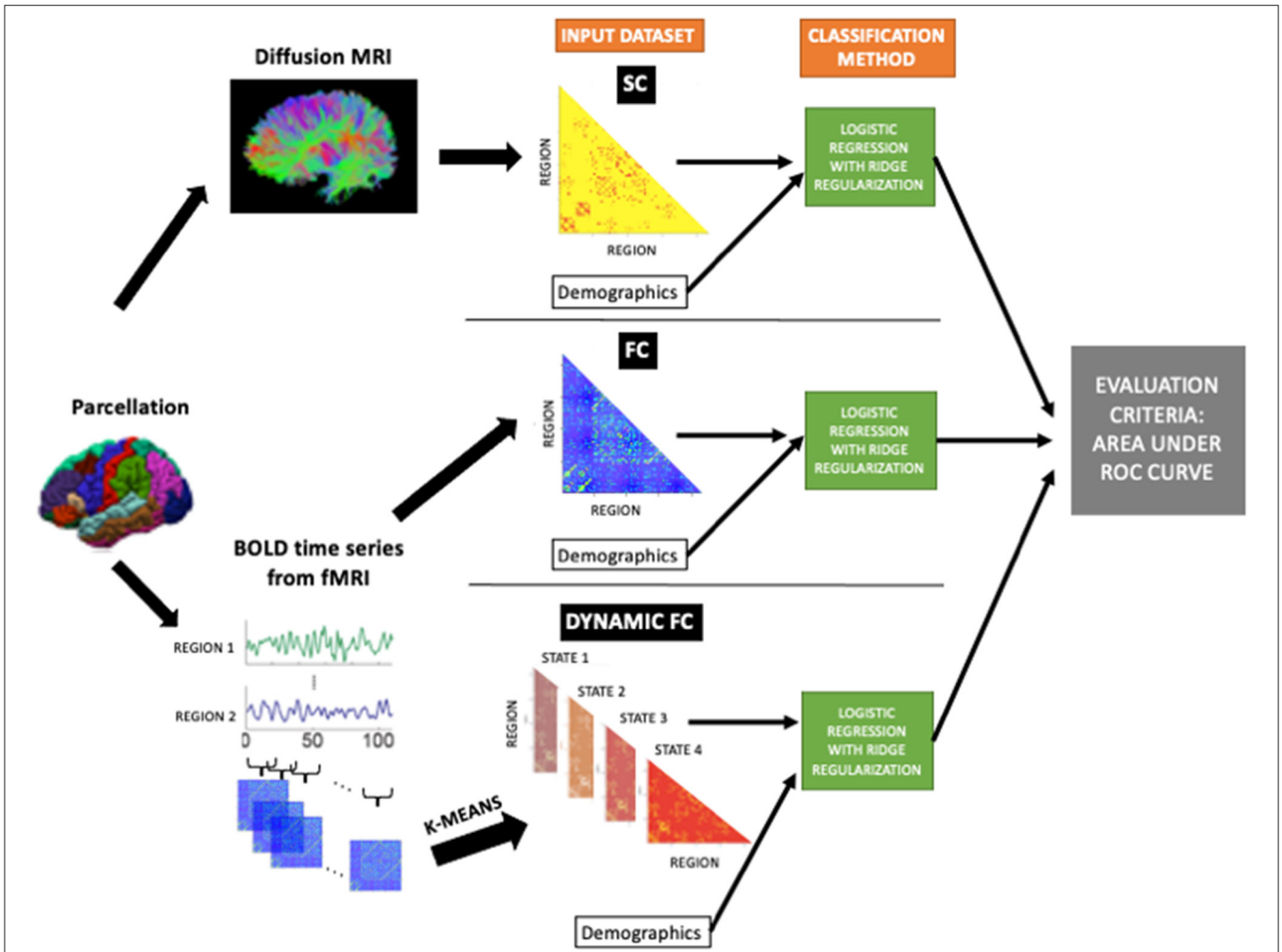

FIGURE 1 | The workflow of the study. Structural connectomes (SC), static functional connectomes (FC), and dynamic functional connectome (dFC) metrics were used as input, in addition to the demographics/clinical variables, to the classification model (logistic regression with ridge regularization technique). The classification performance of each model was assessed using the area under the ROC curve (AUC).

TABLE 1 | Subject demographics and clinical information.

Variable	HC (n = 19)	pwMS (n = 100)	p-value	pwMS: no disability (n = 67)	pwMS: evidence of disability (n = 33)	p-value
Age	45 [35.55, 49.50]	45.50 [36.75, 56]	0.84	40 [35, 50]	56 [46, 58]	0.0001
Female (%)	11 (55)	66 (66)	0.49	46 (69%)	20 (61%)	0.56
Disease duration	-	11 [7,16]	-	10 [7,15]	13 [9,17]	0.06
EDSS	-	1 [0, 2]	-	0 [0, 1]	2 [2, 3]	<2.2e-16
Number of spinal cord lesions	-	1 [0,3]	-	1 [0,3]	2 [0,3]	0.46
Phenotype	-	7 CIS, 88 RRMS, 5 Progressive MS	-	7 CIS, 60 RRMS	28 RRMS, 5 Progressive MS	< 2.2e-16
Lesion volume (mm^3)	-	2,065 [717, 4,779]	-	1,995 [734, 4,200]	2,482 [453, 7,788]	0.49

Values are presented as median [1st, 3rd quantile] for the continuous variables as the number/percent for sex and phenotype. The HC vs. pwMS as well as two disability groups of pwMS were tested for differences; p-*values shown are corrected for multiple comparisons.*

disability, and pwMS who had evidence of disability. A Student's t-test was used to compare the dFC metrics between groups. The pwMS who had disability had significantly higher dwell time compared to those without disability in State 1 ($p = 0.05$). While there was no significant difference in mean dwell time between groups in other states or in number of state transitions ($p > 0.05$ for both comparisons), the pwMS with disability tend to have greater number of state transitions compared to HC and pwMS

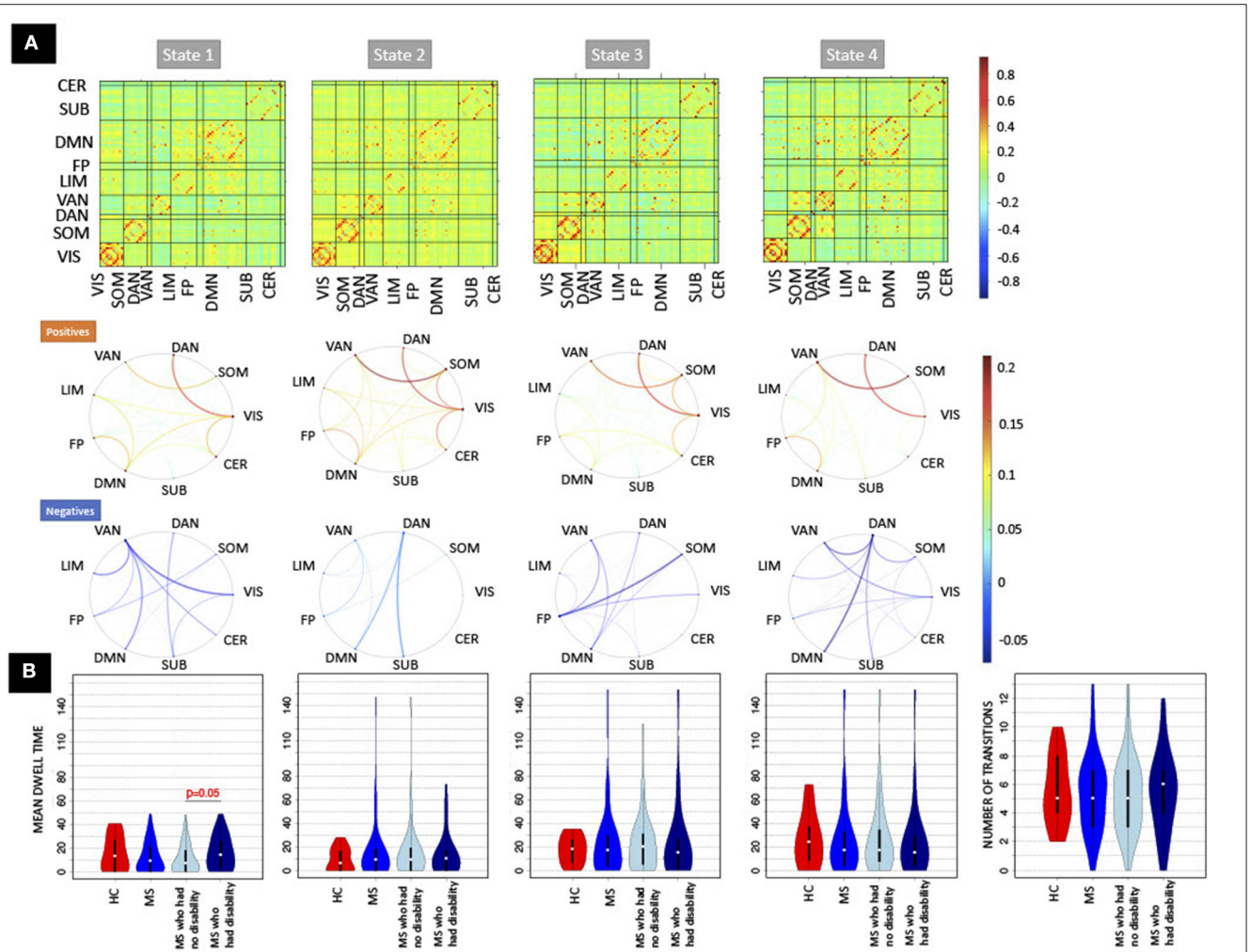

FIGURE 2 | The recurring dynamic FC brain states obtained with k-means clustering and the dFC metrics (dwell time and number of transitions). **(A)** (Top row) Heat maps show the dynamic functional connectivity centroids for the four states, while [bottom two rows of **(A)**] the circle plots summarize the dFC centroids at a network level with the positive and negative dFC entries averaged separately. The color bar of the circle plot is not symmetrical, as to better visualize the network-level values. **(B)** The dFC metrics (mean dwell time and number of transitions) obtained for HC, pwMS, pwMS who had no disability, and pwMS who had evidence of disability. DAN, Dorsal Attention; VAN, Ventral Attention; LIM, Limbic; FP, Fronto-Parietal; DMN, Default-Mode Network; SUB, Subcortex; CER, Cerebellum; VIS, Visual; SOM, Somatomotor.

who had no disability. The transition probability between states are presented in **Supplementary Figure 2**.

3.3. Mass Univariate Group Comparison of Connectivity Measures

There were no significant differences in pairwise or regional FC and dFC between HC vs. pwMS, however, 24 pairwise SCs and 2 regions' SC node strengths (left and right accumbens) were significantly different between HC vs. pwMS after multiple comparison correction, see **Supplementary Figure 3**. There were no significant differences in pairwise and regional SC or FC between pwMS who had no disability vs. had evidence of disability (corrected $p > 0.05$ for all comparisons). However, the regional dFC in the right superior parietal was greater in pwMS who had evidence of disability compared to those without disability (corrected $p = 0.02$; see **Supplementary Figure 4**). PwMS with evidence of disability spent significantly more time in dFC brain state 1 compared to those pwMS with no disability (corrected $p = 0.05$), transition probability from state 4 to 3 trended toward greater values in HC compared to pwMS (uncorrected $p = 0.03$), and transition probability from state 3 to 2 trended toward greater values in pwMS who had evidence of disability compared to those with no disability (uncorrected $p = 0.01$). There was no significant difference or trend in number of transitions between HC vs. MS as well as between subgroups of pwMS.

3.4. Classification Results

Figure 3 shows the distribution of AUC values (over the 500 hold-out test sets) for the models based on pairwise or regional SC, FC, and dFC separately as well as the model including dFC metrics for both classification tasks (HC vs. pwMS and

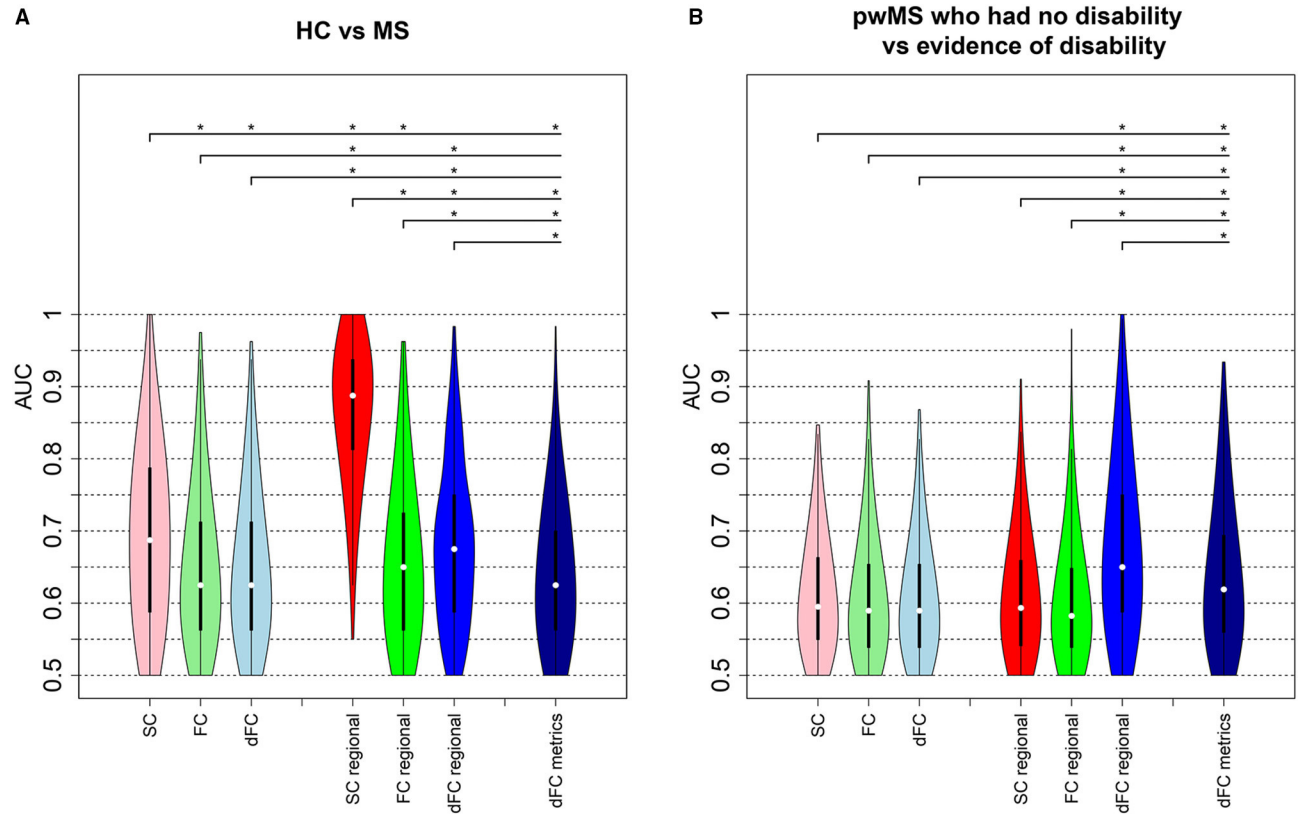

FIGURE 3 | Classification analysis results. AUC values obtained from the models classifying **(A)** HC vs. pwMS and **(B)** pwMS according to their disability level. The first three violin plots show the AUC results from the models including pairwise connectivity information. The number of the imaging variables was 3,655 for pairwise SC and FC, while 14,620 (= 3655 × 4 dFC states) variables included in the pairwise dFC model. The next set of three violin plots show the AUC values from the regional models where regional SC and FC models each included 86 imaging variables and the regional dFC model included 344 (= 86 × 4 dFC states) imaging variables. The last model that included dFC metrics contained 21 imaging variables. The plots show the median (white dot), 1st and 3rd quartiles (black bar) over the 500 hold-out test sets. Asterisks indicate significant differences (p <0.05, BH corrected) in the distribution of AUC values between different models.

pwMS disability subgroups). Unsurprisingly, the AUC results were generally higher for HC vs. pwMS classification than the AUCs obtained for the pwMS subgroup classification. For the HC vs. pwMS classification, the regional SC model performed significantly better than all other models, with a median AUC of 0.89. The regional models better classified HC and pwMS than pairwise models. The regional dFC model (node strength of the individual dFC cluster centroids) showed better classification accuracy than pairwise FC and pairwise dFC cluster centroids. For the classification of pwMS according to their disability level, the median AUC values ranged between 0.59 and 0.65, where the models that included regional dFC and dFC metrics performed significantly better than other models.

Supplementary Figure 6 shows other performance metrics (sensitivity, specificity, balanced accuracy, and F1) of all the models in classifying HC vs. pwMS and pwMS by disability level, respectively. Similar to AUC results, pairwise and regional SC models have better performance than other models in classifying HC vs. MS, while regional dFC and dFC metrics have better performance in distinguishing between pwMS having no disability vs. evidence of disability.

3.5. Feature Weights

Figure 4 depicts the scaled feature weights (relative to the maximum magnitude feature weight) for the pairwise and regional SC models that had the highest AUCs for the HC vs. pwMS classification task. Weaker SC between visual and dorsal attention/cerebellar networks and between somatomotor and dorsal attention networks, and stronger SC between the dorsal attention and subcortical networks were associated with being in the group of pwMS. This largely agreed with the regional SC feature weights showing weaker SC in regions of the dorsal attention, subcortical and cerebellar networks were associated with being in the group of pwMS.

The regional dFC (node strength) model that had the best performance in classifying the pwMS into subgroups showed that increased dFC in the dorsal attention and visual networks of state 2, increased dFC in the default mode network of state 3, decreased dFC in the frontoparietal of state 2 and decreased dFC in the cerebellum of state 3 were most strongly associated with evidence of disability (see **Figure 5**). The univariate results were in concordance with these results and increased dFC in dorsal attention and visual networks of state 2 was found in

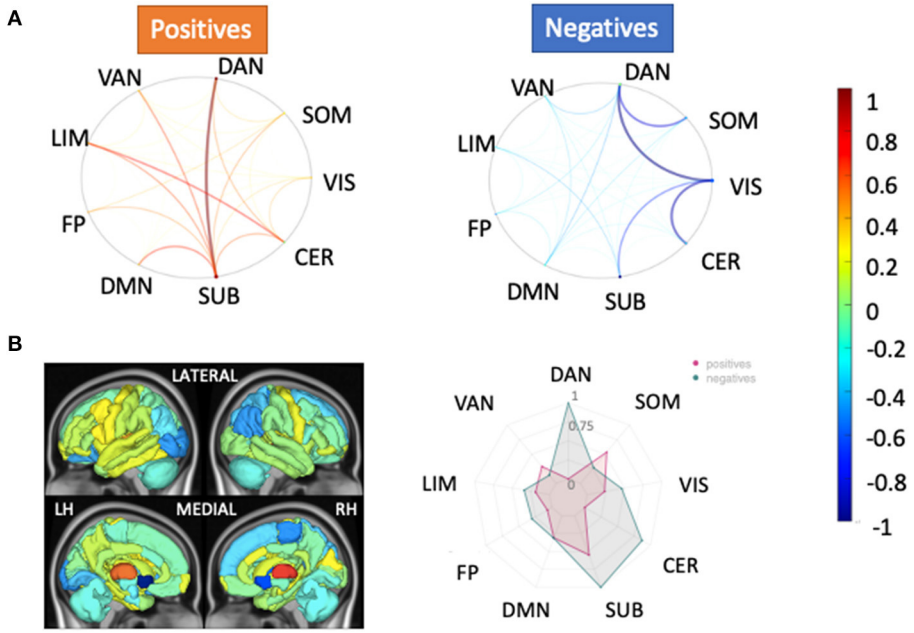

FIGURE 4 | Relative feature weights of the SC models for the HC vs. pwMS classification task. The relative feature weights (scaled by the maximum magnitude feature weight) for the variables used in the two models with the best classification performance in the HC vs. pwMS task: **(A)** pairwise SC and **(B)** regional SC (node strength). The circle plots in **(A)** illustrate the positive (hot colors) and negative (cool colors) model feature weights, respectively, for the pairwise SC model, averaged across the Yeo functional networks. The glass brain and radial plot figures in **(B)** show the relative feature weights from the regional SC (node strength) model, where the redial plot shows the positive and negative values averaged over the Yeo functional networks. Negative values (cooler colors) indicate those connections where larger values were associated with greater probability of being in the HC group while positive values (hotter colors) indicate those connections where larger values were associated with greater probability of being in the pwMS group. DAN, dorsal attention; VAN, ventral attention; LIM, limbic; FP, fronto-parietal; DMN, default-mode network; SUB, subcortex; CER, cerebellum; VIS, visual; SOM, somato-motor.

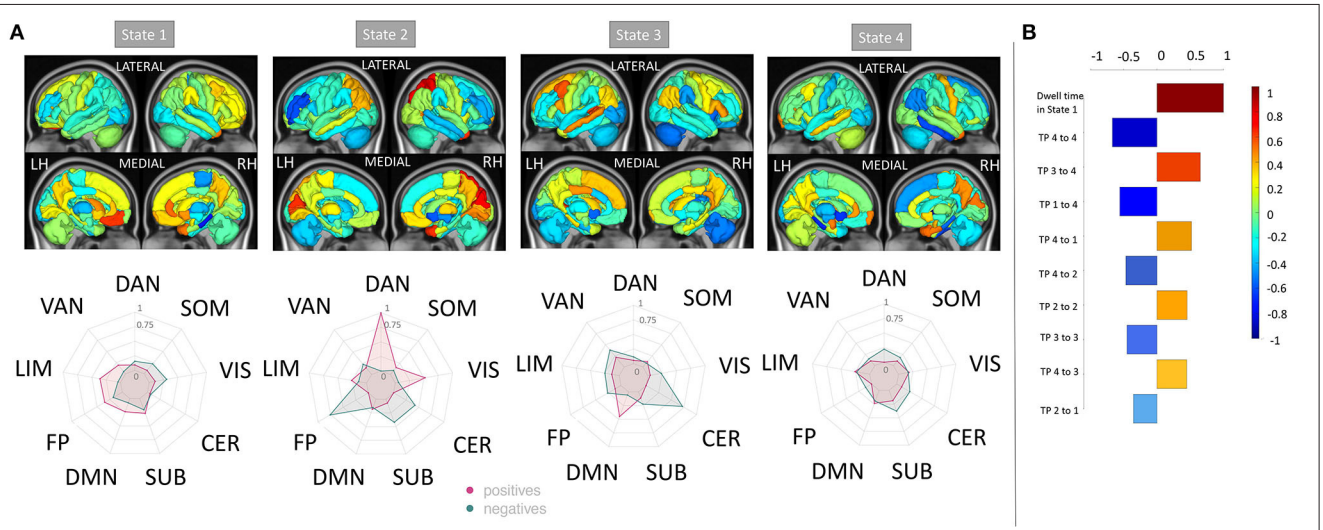

FIGURE 5 | Relative feature weights of the regional dFC model for the MS subgroup classification task. The relative feature weights (scaled by the feature weight with maximum magnitude) of the variables used in classifying pwMS by disability status using **(A)** regional dFC (node strength) and **(B)** dFC summary metrics (top 10 important features). The glass brain and radial plots in **(A)** show the relative feature weights from the regional dFC model and summarize the average of the regional dFC values over the Yeo functional networks (positive and negatives averaged separately). Negative values (cooler colors) indicate those connections where larger values were associated with greater probability of being in the HC group while positive values (hotter colors) indicate those connections where larger values were associated with greater probability of being in the pwMS group. DAN, dorsal attention; VAN, ventral attention; LIM, limbic; FP, fronto-parietal; DMN, default-mode network; SUB, subcortex; CER, cerebellum; VIS, visual; SOM, somato-motor.

pwMS who had evidence of disability compared to those without disability (see **Supplementary Figure 4**). In the dFC metrics model, dwell time in state 1, which was characterized by larger magnitude negative FC from the ventral attention network to several other networks, was the most important feature. This agreed with the univariate group comparisons indicating a significant increase in state 1 dwell time for pwMS with evidence of disability.

4. DISCUSSION

In this study, we investigated the prediction ability of pairwise or regional SC, FC and dFC as well as dFC metrics in classifying HC vs. pwMS and pwMS who had no disability vs. evidence of disability. Our main findings were that (1) the regional SC (node strength) model had the highest AUC when discriminating between HC and pwMS, but the regional dFC and dFC metrics better distinguished pwMS into groups defined by disability level, (2) the most important regional SCs in distinguishing HC from pwMS were found in the dorsal attention, subcortical, and cerebellar networks, while regional dFC in the dorsal attention and visual networks were the most important in classifying pwMS into disability groups, and (3) mean dwell time in a state characterized by more negative FC from ventral attention to several other networks was the most important dFC metric for the classification of pwMS into disability groups.

4.1. Comparison With Previous Studies Using SC, Static FC, and Dynamic FC in MS

Previous studies have used statistical methods to differentiate between pwMS and HC, and pwMS according to their disability severity or phenotype (Richiardi et al., 2012; Leonardi et al., 2013; Stamile et al., 2015; Kocevar et al., 2016; Muthuraman et al., 2016; Ion-Mărgineanu et al., 2017; Zhao et al., 2017; Zhong et al., 2017; Saccà et al., 2018; Zurita et al., 2018) showed 82% sensitivity, similar to our results (median sensitivity = 0.85), in distinguishing pwMS from HC using static FC and/or lesion load. In one of the most similar studies to date in sample size, availability of multi-modal data types and nature of classification tasks, Zurita et al. (2018), showed that using SC and static FC resulted in high accuracy of 87% in classifying HC and pwMS but the accuracy of classifying pwMS according to EDSS dropped to 63%. Here, we show 77% balanced accuracy (AUC of 0.89) in pwMS vs. HC and 60% balanced accuracy (AUC = 0.64) in classifying pwMS by disability status. In contrast to our results, they found that static FC was more important than SC in classifying HC and pwMS. However, they did not investigate dynamic FC and their dMRI acquisition only had 15 directions compared to our higher resolution 55 directions acquisition, which likely means our SC matrices had increased sensitivity to detecting MS-related damage.

Ours is the first study to use dynamic FC to classify HC vs. pwMS or pwMS by disability level using machine learning. However, previous studies have investigated dFC differences between HC vs. pwMS as well as associations with cognition. One study showed that 50 CIS patients (47 of which converted to MS) had similar dFC properties compared to controls at baseline but one of the dFC measurements, the distance traveled in dynamic state-space, increased in CIS/pwMS over 2 years to levels above and beyond HC (Rocca et al., 2019). In another recent study, dFC metrics were compared between (i) pwMS and HC and (ii) pwMS with cognitive disability vs. preservation (d'Ambrosio et al., 2019). There, they showed no differences between HC and pwMS but pwMS without cognitive disability showed increased dynamic fluidity compared to pwMS with cognitive disability by exhibiting longer distance traveled in dynamic state-space, more dynamic states visited, and more frequent changes between states. A few limitations of that study were that the data was collected across 7 sites; the authors discuss this as having a non-negligible effect on the results. Still, both of these studies indicate that, at least early on in the disease, pwMS may compensate for MS-related damage by increased dynamism of FC.

4.2. Structural Damage to the Dorsal Attention Network Is Central in Distinguishing HC vs. pwMS

It has been suggested (Tian et al., 2021) that the parameter coefficients of the prediction models can be unreliable to assess the feature importance. Therefore, similar to our recent work that compared the prediction ability of observed vs. estimated SC and FC networks in classifying pwMS by disability status (Tozlu et al., 2021), here we report the important features that had high feature weight from the classification models and that also showed a larger difference in the mass univariate group comparisons.

Our study showed that the most discriminative pairwise SCs in distinguishing HC from pwMS were found from dorsal attention to subcortical and visual networks. SC node strength in regions in the dorsal attention network were also found to be important features in the HC vs. pwMS classification, as this network had the highest feature weight in the HC vs. pwMS classification model and the univariate analysis showed a large difference in this network between HC vs. MS. Connections between dorsal attention and other networks (limbic and frontoparietal) also had greater feature weights compared to other connections in the pairwise FC model. The prominence of the dorsal attention network in both analyses (classification and univariate analyses) is in line with a previous study that compared dFC metrics between HC and pwMS and found decreased dFC within dorsal attention in pwMS compared to HCs (Huang et al., 2019).

4.3. Dynamic FC Metrics May Capture Compensatory Functional Upregulation in pwMS

In our study, the univariate analyses showed decreased pairwise structural connections between dorsal attention and visual networks in pwMS with evidence of disability. The univariate analysis as well as the feature weights from the

classification models showed that increased dFC in the dorsal attention network was associated with evidence of disability in MS. Moreover, the right superior parietal region of the dorsal attention network was the only region which was significantly higher in the pwMS who had evidence of disability compared to those without disability. We hypothesize the dorsal attention network's increased dFC in pwMS who had evidence of disability could be the result of either a pathological or compensatory upregulation of functional coordination, in response to disease-related damage to SC, i.e., the "less wiring more firing" phenomena (Daselaar et al., 2015). This provides further evidence that MS is characterized by damage to the SC but disability level within pwMS may be more related to functional compensation, specifically the level of dynamism of FC that is reflected in the dFC measures.

4.4. Decreased Connectivity in the Cerebellum Is Related to Disability

Our recent study that investigated the association between structural disconnectivity due to paramagnetic rim lesions and disability in MS showed that the cerebellum is one of the most important regions for the classification of pwMS by disability status and, further, that greater damage to the cerebellum is related to worse disability in MS (Tozlu et al., 2020). Previous studies have also shown the association between motor/cognitive disability and altered FC in the cerebellum (Dogonowski et al., 2014; Pasqua et al., 2020). Our results were in concordance with these previous findings in that decreased connectivity in the cerebellum was associated with evidence of disability in pwMS in all regional models (SC and dFC of states 2 and 3).

4.5. Limitations

The main limitations of our study were the cross-sectional nature and size of the sample. We were restricted to inferring cross-sectional relationships of brain networks properties and disability; a more clinically applicable model would be one capable of predicting with reasonable accuracy future disability for better patient management. There were only 33 pwMS who had evidence of disability and 19 controls which limited the ability to train robust models accurate in novel data. Future work including larger, longitudinal datasets from a similar cohort are required to validate the findings of the current study. EDSS primarily captures physical disability, so this is likely what is being mapped in this work. Future studies using more specific measures of different types of disability including cognition may allow further insights about brain-behavior relationships. In addition, the MRI acquisition parameters could be improved to obtain higher resolution information, including reducing the TR of the fMRI scan, increasing the duration of the entire fMRI scan, and increasing the number of *b*-values in the dMRI scan. Finally, in our dFC analysis, the BOLD time series was divided using a fixed window length; however, wavelet transforms may allow different lengths for different frequency bands and will also be explored in future studies.

5. CONCLUSION

In conclusion, regional SC proved to be the most discriminative modality in classifying HC vs. pwMS, and pwMS exhibited weaker SC within the dorsal attention network, cerebellum, and subcortex. Furthermore, models including dFC metrics outperformed others in classifying pwMS into disability status categories; there, the most important regional dFCs were in the dorsal attention and visual networks and the most important dFC metric was dwell time in a state characterized by more negative FC from ventral attention to other networks. These results suggest that damage to SC are hallmarks of MS, while dynamic FC may reveal functional connectivity differences that are associated with varying levels of disability in pwMS. Various brain connectivity network approaches may enable more accurate prognoses and, possibly, a better understanding of disease mechanisms, eventually leading to the development of novel therapeutics.

DATA AVAILABILITY STATEMENT

The raw data supporting the conclusions of this article will be made available by the authors, without undue reservation.

ETHICS STATEMENT

The studies involving human participants were reviewed and approved by Weill Cornell IRB. The patients/participants provided their written informed consent to participate in this study.

AUTHOR CONTRIBUTIONS

CT helped with image post-processing, carried out the statistical analyses, and wrote the article. KJ collected the data, performed pre- and post-processing of MRI data, and reviewed the article. SG collected the data, helped the interpret results, and reviewed the article. AK designed and supervised the study, collected the data, and edited the article. All authors contributed to the article and approved the submitted version.

FUNDING

This work was supported by the NIH R21 NS104634-01 (AK), NIH R01 NS102646-01A1 (AK), and grant UL1 TR000456-06 (SG) from the Weill Cornell Clinical and Translational Science Center (CTSC).

SUPPLEMENTARY MATERIAL

The Supplementary Material for this article can be found online at: https://www.frontiersin.org/articles/10.3389/fnins.2021.763966/full#supplementary-material

REFERENCES

Allen, E. A., Damaraju, E., Plis, S. M., Erhardt, E. B., Eichele, T., and Calhoun, V. D. (2014). Tracking whole-brain connectivity dynamics in the resting state. *Cereb. Cortex* 24, 663–676. doi: 10.1093/cercor/bhs352

Andersson, J. L., Graham, M. S., Zsoldos, E., and Sotiropoulos, S. N. (2016). Incorporating outlier detection and replacement into a non-parametric framework for movement and distortion correction of diffusion MR images. *Neuroimage* 141, 556–572. doi: 10.1016/j.neuroimage.2016.06.058

Andersson, J. L., and Sotiropoulos, S. N. (2016). An integrated approach to correction for off-resonance effects and subject movement in diffusion MR imaging. *Neuroimage* 125, 1063–1078. doi: 10.1016/j.neuroimage.2015.10.019

Barkhof, F. (2002). The clinico-radiological paradox in multiple sclerosis revisited. *Curr. Opin. Neurol.* 15, 239–245. doi: 10.1097/00019052-200206000-00003

Basile, B., Castelli, M., Monteleone, F., Nocentini, U., Caltagirone, C., Centonze, D., et al. (2014). Functional connectivity changes within specific networks parallel the clinical evolution of multiple sclerosis. *Mult. Scler. J.* 20, 1050–1057. doi: 10.1177/1352458513515082

Benjamini, Y., and Hochberg, Y. (1995). Controlling the false discovery rate: a practical and powerful approach to multiple testing. *J. R. Stat. Soc. Ser. B Methodol.* 57, 289–300. doi: 10.1111/j.2517-6161.1995.tb02031.x

Biswal, B., Zerrin Yetkin, F., Haughton, V. M., and Hyde, J. S. (1995). Functional connectivity in the motor cortex of resting human brain using echo-planar MRI. *Magnet. Reson. Med.* 34, 537–541. doi: 10.1002/mrm.1910340409

Bonkhoff, A. K., Espinoza, F. A., Gazula, H., Vergara, V. M., Hensel, L., Michely, J., et al. (2020). Acute ischaemic stroke alters the brain's preference for distinct dynamic connectivity states. *Brain* 143, 1525–1540. doi: 10.1093/brain/awaa101

Bonkhoff, A. K., Schirmer, M. D., Bretzner, M., Etherton, M., Donahue, K., Tuozzo, C., et al. (2021). Abnormal dynamic functional connectivity is linked to recovery after acute ischemic stroke. *Human Brain Mapp.* 42, 2278–2291. doi: 10.1002/hbm.25366

Chawla, N. V., Bowyer, K. W., Hall, L. O., and Kegelmeyer, W. P. (2002). SMOTE: synthetic minority over-sampling technique. *J. Artif. Intell. Res.* 16, 321–357. doi: 10.1613/jair.953

Damaraju, E., Allen, E. A., Belger, A., Ford, J. M., McEwen, S., Mathalon, D. H., et al. (2014). Dynamic functional connectivity analysis reveals transient states of dysconnectivity in schizophrenia. *Neuroimage Clin.* 5, 298–308. doi: 10.1016/j.nicl.2014.07.003

d'Ambrosio, A., Valsasina, P., Gallo, A., De Stefano, N., Pareto, D., Barkhof, F., et al. (2019). Reduced dynamics of functional connectivity and cognitive impairment in multiple sclerosis. *Mult. Scler. J.* 26, 476–488. doi: 10.1177/1352458519837707

Daselaar, S. M., Iyengar, V., Davis, S. W., Eklund, K., Hayes, S. M., and Cabeza, R. E. (2015). Less wiring, more firing: low-performing older adults compensate for impaired white matter with greater neural activity. *Cereb. Cortex* 25, 983–990. doi: 10.1093/cercor/bht289

David, H. A. (2008). The beginnings of randomization tests. *Am. Stat.* 62, 70–72. doi: 10.1198/000313008X269576

Dogonowski, A. M., Andersen, K. W., Madsen, K. H., Sørensen, P. S., Paulson, O. B., Blinkenberg, M., et al. (2014). Multiple sclerosis impairs regional functional connectivity in the cerebellum. *Neuroimage Clin.* 4, 130–138. doi: 10.1016/j.nicl.2013.11.005

Eijlers, A. J. C., Wink, A. M., Meijer, K. A., Douw, L., Geurts, J. J. G., and Schoonheim, M. M. (2019). Reduced network dynamics on functional MRI signals cognitive impairment in multiple sclerosis. *Radiology* 292, 449–457. doi: 10.1148/radiol.2019182623

Faivre, A., Rico, A., Zaaraoui, W., Crespy, L., Reuter, F., Wybrecht, D., et al. (2012). Assessing brain connectivity at rest is clinically relevant in early multiple sclerosis. *Mult. Scler. J.* 18, 1251–1258. doi: 10.1177/1352458511435930

Filippi, M., Valsasina, P., Vacchi, L., Leavitt, V., Comi, G., Falini, A., et al. (2015). Consistent decreased functional connectivity among the main cortical and subcortical functional networks in MS: relationship with disability and cognitive impairment. *Neurology* 84.

Fischl, B., and Dale, A. M. (2000). Measuring the thickness of the human cerebral cortex from magnetic resonance images. *Proc. Natl. Acad. Sci. U.S.A.* 97, 11050–11055. doi: 10.1073/pnas.200033797

Hallquist, M. N., Hwang, K., and Luna, B. (2013). The nuisance of nuisance regression: spectral misspecification in a common approach to resting-state fMRI preprocessing reintroduces noise and obscures functional connectivity. *Neuroimage* 82, 208–225. doi: 10.1016/j.neuroimage.2013.05.116

Has Silemek, A. C., Fischer, L., Pöttgen, J., Penner, I. K., Engel, A. K., Heesen, C., et al. (2020). Functional and structural connectivity substrates of cognitive performance in relapsing remitting multiple sclerosis with mild disability. *Neuroimage Clin.* 25:102177. doi: 10.1016/j.nicl.2020.102177

Hawellek, D. J., Hipp, J. F., Lewis, C. M., Corbetta, M., and Engel, A. K. (2011). Increased functional connectivity indicates the severity of cognitive impairment in multiple sclerosis. *Proc. Natl. Acad. Sci. U.S.A.* 108, 19066–19071. doi: 10.1073/pnas.1110024108

Huang, M., Zhou, F., Wu, L., Wang, B., Guo, L., Zhao, Y., et al. (2019). White matter lesion loads associated with dynamic functional connectivity within attention network in patients with relapsing-remitting multiple sclerosis. *J. Clin. Neurosci.* 65, 59–65. doi: 10.1016/j.jocn.2019.03.034

Ion-Mărgineanu, A., Kocevar, G., Stamile, C., Sima, D. M., Durand-Dubief, F., Van Huffel, S., et al. (2017). Machine learning approach for classifying multiple sclerosis courses by combining clinical data with lesion loads and magnetic resonance metabolic features. *Front. Neurosci.* 11:398. doi: 10.3389/fnins.2017.00398

Kocevar, G., Stamile, C., Hannoun, S., Cotton, F., Vukusic, S., Durand-Dubief, F., et al. (2016). Graph theory-based brain connectivity for automatic classification of multiple sclerosis clinical courses. *Front. Neurosci.* 10:478. doi: 10.3389/fnins.2016.00478

Kuceyeski, A., Monohan, E., Morris, E., Fujimoto, K., Vargas, W., and Gauthier, S. A. (2018). Baseline biomarkers of connectome disruption and atrophy predict future processing speed in early multiple sclerosis. *Neuroimage Clin.* 19, 417–424. doi: 10.1016/j.nicl.2018.05.003

Kuceyeski, A., Navi, B. B., Kamel, H., Relkin, N., Villanueva, M., Raj, A., et al. (2015). Exploring the brain's structural connectome: a quantitative stroke lesion-dysfunction mapping study. *Hum. Brain Mapp.* 36, 2147–2160. doi: 10.1002/hbm.22761

Kuceyeski, A., Shah, S., Dyke, J., Bickel, S., Abdelnour, F., Schiff, N., et al. (2016). The application of a mathematical model linking structural and functional connectomes in severe brain injury. *Neuroimage Clin.* 11, 635–647. doi: 10.1016/j.nicl.2016.04.006

Leonardi, N., Richiardi, J., Gschwind, M., Simioni, S., Annoni, J. M., Schluep, M., et al. (2013). Principal components of functional connectivity: a new approach to study dynamic brain connectivity during rest. *Neuroimage* 83, 937–950. doi: 10.1016/j.neuroimage.2013.07.019

Mennigen, E., Miller, R. L., Rashid, B., Fryer, S. L., Loewy, R. L., Stuart, B. K., et al. (2018). Reduced higher-dimensional resting state fMRI dynamism in clinical high-risk individuals for schizophrenia identified by meta-state analysis. *Schizophrenia Res.* 201, 217–223. doi: 10.1016/j.schres.2018.06.007

Muthuraman, M., Fleischer, V., Kolber, P., Luessi, F., Zipp, F., and Groppa, S. (2016). Structural brain network characteristics can differentiate CIS from early RRMS. *Front. Neurosci.* 10:14. doi: 10.3389/fnins.2016.00014

Pasqua, G., Tommasin, S., Bharti, K., Ruggieri, S., Petsas, N., Piervincenzi, C., et al. (2020). Resting-state functional connectivity of anterior and posterior cerebellar lobes is altered in multiple sclerosis. *Mult. Scler. J.* 27, 539–548. doi: 10.1177/1352458520922770

Polman, C., Reingold, S. C., Banwell, B., Clanet, C., Cohen, J. A., Filippi, M., et al. (2011). Diagnostic criteria for multiple sclerosis: 2010 revisions to the McDonald criteria. *Ann. Neurol.* 69, 292–302. doi: 10.1002/ANA.22366

Rashid, B., Arbabshirani, M. R., Damaraju, E., Cetin, M. S., Miller, R., Pearlson, G. D., et al. (2016). Classification of schizophrenia and bipolar patients using static and dynamic resting-state fMRI brain connectivity. *Neuroimage* 134, 645–657. doi: 10.1016/j.neuroimage.2016.04.051

Richiardi, J., Gschwind, M., Simioni, S., Annoni, J.-M., Greco, B., Hagmann, P., et al. (2012). Classifying minimally disabled multiple sclerosis patients from resting state functional connectivity. *Neuroimage* 62, 2021–2033. doi: 10.1016/j.neuroimage.2012.05.078

Rocca, M. A., Hidalgo de La Cruz, M., Valsasina, P., Mesaros, S., Martinovic, V., Ivanovic, J., et al. (2019). Two-year dynamic functional network connectivity in clinically isolated syndrome. *Mult. Scler. J.* 26, 645–658. doi: 10.1177/1352458519837704

Rocca, M. A., Valsasina, P., Absinta, M., Riccitelli, G., Rodegher, M. E., Misci, P., et al. (2010). Default-mode network dysfunction and

cognitive impairment in progressive MS. *Neurology* 74, 1252–1259. doi: 10.1212/WNL.0b013e3181d9ed91

Rocca, M. A., Valsasina, P., Leavitt, V. M., Rodegher, M., Radaelli, M., Riccitelli, G. C., et al. (2018). Functional network connectivity abnormalities in multiple sclerosis: Correlations with disability and cognitive impairment. *Mult. Scler. J.* 24, 459–471. doi: 10.1177/1352458517699875

Rocca, M. A., Valsasina, P., Martinelli, V., Misci, P., Falini, A., Comi, G., et al. (2012). Large-scale neuronal network dysfunction in relapsing-remitting multiple sclerosis. *Neurology* 79, 1449–1457. doi: 10.1212/WNL.0b013e31826d5f10

Roosendaal, S. D., Schoonheim, M. M., Hulst, H. E., Sanz-Arigita, E. J., Smith, S. M., Geurts, J. J. G., et al. (2010). Resting state networks change in clinically isolated syndrome. *Brain* 133, 1612–1621. doi: 10.1093/brain/awq058

Saccá, V., Sarica, A., Novellino, F., Barone, S., Tallarico, T., Filippelli, E., et al. (2018). Evaluation of machine learning algorithms performance for the prediction of early multiple sclerosis from resting-state FMRI connectivity data. *Brain Imaging Behav*. 13, 1103–1114. doi: 10.1007/s11682-018-9926-9

Sambataro, F., Visintin, E., Doerig, N., Brakowski, J., Holtforth, M. G., Seifritz, E., et al. (2017). Altered dynamics of brain connectivity in major depressive disorder at-rest and during task performance. *Psychiatry Res. Neuroimaging* 259, 1–9. doi: 10.1016/j.pscychresns.2016.11.001

Santos, M. S., Soares, J. P., Abreu, P. H., Araujo, H., and Santos, J. (2018). Cross-validation for imbalanced datasets: avoiding overoptimistic and overfitting approaches. *IEEE Comput. Intell. Mag.* 13, 59–76. doi: 10.1109/MCI.2018.2866730

Schoonheim, M. M., Meijer, K. A., and Geurts, J. J. (2015). Network collapse and cognitive impairment in multiple sclerosis. *Front. Neurol*. 6:82. doi: 10.3389/fneur.2015.00082

Stamile, C., Kocevar, G., Hannoun, S., Durand-Dubief, F., and Sappey-Marinier, D. (2015). "A graph based classification method for multiple sclerosis clinical forms using support vector machine," in *Lecture Notes in Computer Science* (Cham: Springer), 57–64. doi: 10.1007/978-3-319-27929-9_6

Tian, Y., Zalesky, A., Ye, D., Level, T., Building, A. G., Level, A. Z., et al. (2021). Machine learning prediction of cognition from functional connectivity: are feature weights reliable? *bioRxiv* 2021:446059. doi: 10.1101/2021.05.27.446059

Tommasin, S., De Giglio, L., Ruggieri, S., Petsas, N., Gianní, C., Pozzilli, C., et al. (2018). Relation between functional connectivity and disability in multiple sclerosis: a non-linear model. *J. Neurol.* 265, 2881–2892. doi: 10.1007/s00415-018-9075-5

Tona, F., Petsas, N., Sbardella, E., Prosperini, L., Carmellini, M., Pozzilli, C., et al. (2014). Multiple sclerosis: altered thalamic resting-state functional connectivity and its effect on cognitive function. *Radiology* 271, 814–821. doi: 10.1148/radiol.14131688

Tournier, J. D., Smith, R., Raffelt, D., Tabbara, R., Dhollander, T., Pietsch, M., et al. (2019). MRtrix3: a fast, flexible and open software framework for medical image processing and visualisation. *NeuroImage*. 202:116137. doi: 10.1101/551739

Tozlu, C., Jamison, K., Gu, Z., Gauthier, S. A., and Kuceyeski, A. (2021). Estimated connectivity networks outperform observed connectivity networks when classifying people with multiple sclerosis into disability groups. *bioRxiv* 2021:447376. doi: 10.1016/j.nicl.2021.102827

Tozlu, C., Jamison, K., Nguyen, T., Zinger, N., Kaunzner, U., Pandya, S., et al. (2020). Structural disconnectivity from quantitative susceptibility mapping rim+ lesions is related to disability in people with multiple sclerosis. *medRxiv* 1-13. doi: 10.1101/2020.12.10.20244939

van Geest, Q., Douw, L., van't Klooster, S., Leurs, C. E., Genova, H. M., Wylie, G. R., et al. (2018). Information processing speed in multiple sclerosis: relevance of default mode network dynamics. *Neuroimage Clin*. 19, 507–515. doi: 10.1016/j.nicl,.2018.05.015

Weinshenker, B. G., Rice, G. P. A., Noseworthy, J. H., Carriere, W., Baskerville, J., and Ebers, G. C. (1991). The natural history of multiple sclerosis: a geographically based study. *Brain* 114, 1045–1056. doi: 10.1093/brain/114.2.1045

Whitfield-Gabrieli, S., and Nieto-Castanon, A. (2012). Conn: a functional connectivity toolbox for correlated and anticorrelated brain networks. *Brain Connect*. 2, 125–141. doi: 10.1089/brain.2012.0073

Yeo, B. T. T., Krienen, F. M., Sepulcre, J., Sabuncu, M. R., Lashkari, D., Hollinshead, M., et al. (2011). The organization of the human cerebral cortex estimated by intrinsic functional connectivity. *J. Neurophysiol*. 106, 1125–1165. doi: 10.1152/jn.00338.2011

Zhao, Y., Healy, B. C., Rotstein, D., Guttmann, C. R. G., Bakshi, R., Weiner, H. L., et al. (2017). Exploration of machine learning techniques in predicting multiple sclerosis disease course. *PLoS ONE* 12:e0174866. doi: 10.1371/journal.pone.0174866

Zhong, J., Chen, D. Q., Nantes, J. C., Holmes, S. A., Hodaie, M., and Koski, L. (2017). Combined structural and functional patterns discriminating upper limb motor disability in multiple sclerosis using multivariate approaches. *Brain Imaging Behav*. 11, 754–768. doi: 10.1007/s11682-016-9551-4

Zurita, M., Montalba, C., Labbé, T., Cruz, J. P., Dalboni da Rocha, J., Tejos, C., et al. (2018). Characterization of relapsing-remitting multiple sclerosis patients using support vector machine classifications of functional and diffusion MRI data. *Neuroimage Clin*. 20, 724–730. doi: 10.1016/j.nicl.2018.09.002

Conflict of Interest: The authors declare that the research was conducted in the absence of any commercial or financial relationships that could be construed as a potential conflict of interest.

Publisher's Note: All claims expressed in this article are solely those of the authors and do not necessarily represent those of their affiliated organizations, or those of the publisher, the editors and the reviewers. Any product that may be evaluated in this article, or claim that may be made by its manufacturer, is not guaranteed or endorsed by the publisher.

frontiers in Neuroscience

ORIGINAL RESEARCH
published: 28 March 2022
doi: 10.3389/fnins.2022.833320

Alteration in the Functional Organization of the Default Mode Network Following Closed Non-severe Traumatic Brain Injury

Muhammad Riddha Abdul Rahman[1,2,3], Aini Ismafairus Abd Hamid[1,3,4], Nor Azila Noh[5], Hazim Omar[1,3,4], Wen Jia Chai[1,3], Zamzuri Idris[1,3,4], Asma Hayati Ahmad[6], Diana Noma Fitzrol[1,3,4], Ab. Rahman Izaini Ghani Ab. Ghani[1,3,4], Wan Nor Azlen Wan Mohamad[1,3,4], Mohamed Faiz Mohamed Mustafar[1,3,4], Muhammad Hafiz Hanafi[1,3,4], Mohamed Faruque Reza[1,3,4], Hafidah Umar[1,3,4], Mohd Faizal Mohd Zulkifly[1,3,4], Song Yee Ang[1,3,4], Zaitun Zakaria[1,3,4], Kamarul Imran Musa[7], Azizah Othman[8], Zunaina Embong[9], Nur Asma Sapiai[10], Regunath Kandasamy[11], Haidi Ibrahim[12], Mohd Zaid Abdullah[12], Kannapha Amaruchkul[13], Pedro Valdes-Sosa[14,15], Maria Luisa-Bringas[14,15], Bharat Biswal[16], Jitkomut Songsiri[17], Hamwira Sakti Yaacob[18], Putra Sumari[19], Paramjit Singh Jamir Singh[20], Azlinda Azman[20] and Jafri Malin Abdullah[1,3,4]**

[1] Department of Neurosciences, School of Medical Sciences, Universiti Sains Malaysia, Kota Bharu, Malaysia, [2] School of Medical Imaging, Faculty of Health Sciences, Universiti Sultan Zainal Abidin, Kuala Nerus, Malaysia, [3] Brain and Behavior Cluster, School of Medical Sciences, Universiti Sains Malaysia, Kota Bharu, Malaysia, [4] Hospital Universiti Sains Malaysia, Universiti Sains Malaysia, Kota Bharu, Malaysia, [5] Faculty of Medicine and Health Sciences, Universiti Sains Islam Malaysia, Nilai, Malaysia, [6] Department of Physiology, School of Medical Sciences, Universiti Sains Malaysia, Kota Bharu, Malaysia, [7] Department of Community Medicine, School of Medical Sciences, Universiti Sains Malaysia, Kota Bharu, Malaysia, [8] Department of Paediatrics, School of Medical Sciences, Universiti Sains Malaysia, Kota Bharu, Malaysia, [9] Department of Ophthalmology, School of Medical Sciences, Universiti Sains Malaysia, Kota Bharu, Malaysia, [10] Department of Radiology, School of Medical Sciences, Universiti Sains Malaysia, Kota Bharu, Malaysia, [11] Gleneagles Hospital Kuala Lumpur, Kuala Lumpur, Malaysia, [12] School of Electrical and Electronic Engineering, Universiti Sains Malaysia, Nibong Tebal, Malaysia, [13] Graduate School of Applied Statistics, National Institute of Development Administration (NIDA), Bangkok, Thailand, [14] The Clinical Hospital of Chengdu Brain Science Institute, MOE Key Lab for Neuroinformation, University of Electronic Science and Technology of China, Chengdu, China, [15] The Cuban Neurosciences Center, Havana, Cuba, [16] Department of Biomedical Engineering, New Jersey Institute of Technology, Newark, NJ, United States, [17] EE410 Control Systems Laboratory, Department of Electrical Engineering, Faculty of Engineering, Chulalongkorn University, Bangkok, Thailand, [18] Department of Computer Science, Kulliyah of Information and Communication Technology, International Islamic University Malaysia, Kuala Lumpur, Malaysia, [19] School of Computer Sciences, Universiti Sains Malaysia, Gelugor, Malaysia, [20] School of Social Sciences, Universiti Sains Malaysia, Gelugor, Malaysia

The debilitating effect of traumatic brain injury (TBI) extends years after the initial injury and hampers the recovery process and quality of life. In this study, we explore the functional reorganization of the default mode network (DMN) of those affected with non-severe TBI. Traumatic brain injury (TBI) is a wide-spectrum disease that has heterogeneous effects on its victims and impacts everyday functioning. The functional disruption of the default mode network (DMN) after TBI has been established, but its link to causal effective connectivity remains to be explored. This study investigated the differences in the DMN between healthy participants and mild and moderate TBI, in terms of functional and effective connectivity using resting-state functional magnetic resonance imaging (fMRI). Nineteen non-severe TBI (mean age 30.84 ± 14.56) and twenty-two healthy (HC; mean age 27.23 ± 6.32) participants were

OPEN ACCESS

Edited by:
Zachory Wei,
Emory University, United States

Reviewed by:
Anup Das,
Columbia University, United States
Xiaopeng Song,
Harvard Medical School, United States
Feiqiu Wen,
Shenzhen Children's Hospital, China

***Correspondence:**
Aini Ismafairus Abd Hamid
aini_ismafairus@usm.my
Jafri Malin Abdullah
brainsciences@gmail.com

Specialty section:
This article was submitted to Brain Imaging Methods, a section of the journal Frontiers in Neuroscience

Received: 11 December 2021
Accepted: 04 February 2022
Published: 28 March 2022

Citation:
Abdul Rahman MR, Abd Hamid AI, Noh NA, Omar H, Chai WJ, Idris Z, Ahmad AH, Fitzrol DN, Ab Ghani ARIG, Wan Mohamad WNA, Mohamed Mustafar MF, Hanafi MH, Reza MF, Umar H, Mohd Zulkifly MF, Ang SY, Zakaria Z, Musa KI, Othman A, Embong Z, Sapiai NA, Kandasamy R, Ibrahim H, Abdullah MZ, Amaruchkul K, Valdes-Sosa P, Luisa-Bringas M, Biswal B, Songsiri J, Yaacob HS, Sumari P, Jamir Singh PS, Azman A and Abdullah JM (2022) Alteration in the Functional Organization of the Default Mode Network Following Closed Non-severe Traumatic Brain Injury. Front. Neurosci. 16:833320. doi: 10.3389/fnins.2022.833320

recruited for this study. Resting-state fMRI data were obtained at the subacute phase (mean days 40.63 ± 10.14) and analyzed for functional activation and connectivity, independent component analysis, and effective connectivity within and between the DMN. Neuropsychological tests were also performed to assess the cognitive and memory domains. Compared to the HC, the TBI group exhibited lower activation in the thalamus, as well as significant functional hypoconnectivity between DMN and LN. Within the DMN nodes, decreased activations were detected in the left inferior parietal lobule, precuneus, and right superior frontal gyrus. Altered effective connectivities were also observed in the TBI group and were linked to the diminished activation in the left parietal region and precuneus. With regard to intra-DMN connectivity within the TBI group, positive correlations were found in verbal and visual memory with the language network, while a negative correlation was found in the cognitive domain with the visual network. Our results suggested that aberrant activities and functional connectivities within the DMN and with other RSNs were accompanied by the altered effective connectivities in the TBI group. These alterations were associated with impaired cognitive and memory domains in the TBI group, in particular within the language domain. These findings may provide insight for future TBI observational and interventional research.

Keywords: default mode network, traumatic brain injury, functional connectivity, effective connectivity, neuropsychology

INTRODUCTION

Traumatic brain injury (TBI) is one of the most common causes of debilitating neurodegenerative diseases that affect more than 10 million people each year globally (Humphreys et al., 2013; Moreno-López et al., 2016). TBI most commonly affects people who are in their productive years, therefore incurring significant economic losses. In addition, TBI also puts a burden on the public healthcare system, as TBI survivors often require assistance and hardly return to a quality life (Majdan et al., 2017). Therefore, research into how TBI affects the functions of the human brain is crucial to understanding the mechanism of injury and how they can be prevented to help manage the TBI survivors to return to the quality of life.

The debilitating effect of TBI can range from mild cognitive disruption to adverse reduction in brain function, depending on the severity of the injury. In severe TBI, the deleterious effects on the brain were more pronounced in more severe cases (Khanmohammadi et al., 2018). As for mild TBI, they are often misdiagnosed (Palacios et al., 2017; Vergara et al., 2018), thus risks being left untreated. This is concerning because the effect of mild TBI can be harmful to the integrity of the brain function and increase the risk of neurodegenerative diseases later in life, however, small the initial concussion might be (Vergara et al., 2018). Therefore, all trauma to the head must receive a proper diagnosis and the integrity of the brain function assessed properly to prevent premature neurodegenerative diseases in TBI survivors.

In achieving this, the resting-state fMRI (rsfMRI) is an indispensable tool to study the extent of functional alterations caused by TBI. Since its inception in 1995, rsfMRI studies have been conducted increasingly to study the brain networks that emerged from seemingly resting conditions; among them is the default mode network (DMN) (Nakamura et al., 2009). The resting-state paradigm is relatively easier to conduct, requiring no explicit tasks and able to accommodate a wide range of participants across all levels of consciousness and cognitive abilities.

The total force of trauma to the head often disrupted the structural integrity of the brain in the form of axonal injury, thus affecting functional connectivity (FC) and cognitive performance (Sours et al., 2017; Gordon et al., 2018; Wooten et al., 2019). However, damaged structural tracts may create juxtaposed effects toward FCs, in which it becomes increased especially involving network hubs (Hillary et al., 2014). Researchers attribute this paradox as the compensatory effect orchestrated by the brain, mainly to cope with inefficient information transfer due to the recruitment of longer tracts (Porter et al., 2017; Wooten et al., 2019). This functional hyperconnectivity is often resolved longitudinally, as the brain finds the balance between optimal performance and network costs (Hillary and Grafman, 2017). Nevertheless, cases of diminished FCs due to trauma were also reported, especially in the earlier stages of TBI (Manning et al., 2019).

The FCs can be illustrated as the statistical connections between cerebral signals across time, which may be used to draw inferences about functional interactions between two or more brain areas. On the other hand, there is another type of brain connectivity termed effective connectivity (EC) which seeks to describe causal links through

experimental paradigms or models rather than just looking at correlations between brain activity (Gaudet et al., 2020). This enables the direction of interactions between various brain areas to be deduced.

In this study, we examined the brain responses in healthy controls (HC) and TBI groups and compare them to find any significant difference in the functional organization of the resting-state network, specifically the DMN. Specifically, we investigated the group activations modeled after the low-frequency fluctuation of the brain and compare them to look for significant differences that may account for the TBI effects. In addition, we also analyzed the FCs of both groups to see any changes. Finally, we also correlated the FCs with their performance in psychological tests.

MATERIALS AND METHODS

Participants

Nineteen non-severe TBI participants (mean age 30.84 ± 14.56) were recruited from the emergency department, Hospital Universiti Sains Malaysia. Twenty-two matching controls (mean age 27.23 ± 6.32) were also recruited. All participants were right-handed Malay males aged between 18 and 65 years. All TBI participants sustained non-severe TBI, measured using the Glasgow Coma Scale of between 8 and 15, and scanned at the subacute phase (4-6 weeks) of the injury. The exclusion criteria include any previous TBI history, psychiatric illness, history of drug abuse, ocular injuries, and contraindications to MRI. Participants also gave written consent before being enrolled in the study. The study protocol and procedures were approved by the Institutional Ethics Committee (IEC) of Universiti Sains Malaysia (IEC Code: USM/JEPeM/15110485 and USM/JEPeM/20080406) and carried out under the latest version of the Declaration of Helsinki.

Neuropsychological Assessment

A subset of the HC and TBI participants was cognitively assessed using neuropsychological tests that comprised the Wechsler Abbreviated Scale of Intelligence 1st edition (WASI; block design and matrix reasoning) to estimate general cognitive ability (McCrimmon and Smith, 2013), Rey Auditory Verbal Learning Test (RAVLT; immediate and delayed recall) to assess the verbal memory function (Bean, 2011; Khosravi Fard et al., 2016), Rey Complex Figure Test and Recognition Trial (RCFT; immediate and delayed recall) to assess the visual memory and perception (Sargénius et al., 2017), Comprehensive Trail-Making Test (CTMT) to assess the psychomotor speed and cognitive flexibility (Gray, 2006; Beratis et al., 2018), and Wisconsin Card Sorting Test (WCST) to measure the executive functioning (Kolakowsky-Hayner, 2011). These tests were appropriate to assess the cognitive domains that are often impaired following TBI. The results are calculated based on the standard scores that are corrected for age and education level. In total, thirteen HC and sixteen TBI participants took part in the neuropsychological tests.

Magnetic Resonance Imaging Scanning Parameters

The structural and functional MRI data were obtained using a 3.0-T MRI machine (Philips Achieva, Best, The Netherlands) equipped with a 32-channel head coil. The structural images were acquired using T1-weighted imaging, with a Magnetisation Prepare Gradient Echo (MPRAGE) sequence, a 256 × 256 matrix, and 160 sagittal slices. The structural repetition time (TR) was set at 2,000 ms, echo time (TE) was set at 30 ms, flip angle (FA) was set at 8°, and the final resolution of structural images was 1 mm × 1 mm × 1 mm.

Functional images were obtained using the T2* echo planar imaging (EPI) sequence, with a 96 × 96 matrix size and 32 oblique slices, set parallel to the orbitofrontal cortex to reduce the sinus artifact. The TR was set at 1,700 ms, TE at 33 ms, and FA at 78°. The field of view of functional images was set at 192 mm^2 with slice thickness set at 3 mm with a 0-mm gap. The slice acquisition was interleaved, and a total of 250 scans were obtained in 7 min. During the scanning, participants were asked to close their eyes and remain still without any mental task engagement.

Data Preprocessing

The acquired fMRI data underwent anonymization and converted from DICOM to NIFTI format for subsequent data analysis. Before preprocessing, the first ten volumes of the data were removed to avoid the initial MRI signal instability and account for participants' adaptation to the

TABLE 1 | Functionally defined nodes of the default mode network as outlined in the CONN Toolbox.

Nodes	Central coordinate		
Medial prefrontal cortex	1	55	−3
Posterior cingulate cortex	1	−61	38
L lateral parietal	−39	−77	33
R lateral parietal	47	−67	29

R: right, L: left. Coordinates follow the standard Montreal Neurological Institute (MNI) template in millimeters (mm).

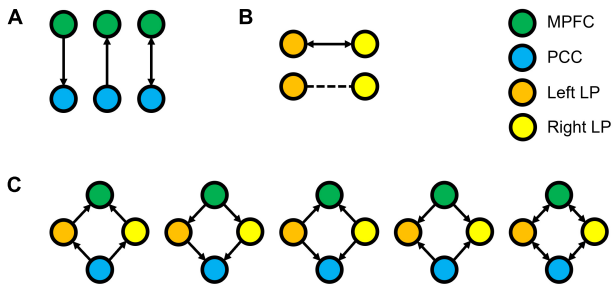

FIGURE 1 | Three families of the DCM models, where **(A)** denotes the possible connectivity directions between MPFC and PCC, **(B)** denotes the possible connectivity directions between the LLP and RLP, and **(C)** denotes the possible connectivity directions between MPFC, PCC, LLP, and RLP. The combination of these families yielded 30 possible DCM models that were compared to find the winning model.

TABLE 2 | Demographics and neuropsychological characteristics.

	Mean HC (SD)	Mean TBI (SD)	*t*	p[2]	Effect size[b]
Age	27.23 (6.32)	30.84 (14.56)	–-1.00	0.326	0.33
Education (HC: *n* = 13, TBI: *n* = 17)	15.54 (1.94)	12.59 (2.83)	3.22	0.003	1.19
Days since injury	–	40.63 (10.14)	–	–	–
GCS (median)	–	15	–	–	–
WASI (HC: *n* = 13, TBI: *n* = 16)					
Block design	51.69 (9.04)	49.69 (6.18)	0.708	0.485	0.26
Matrix reasoning	51.08 (10.61)	43.38 (12.48)	1.765	0.089	0.66
RAVLT (HC: *n* = 13, TBI: *n* = 16)					
Immediate recall	46.77 (9.05)	40.75 (10.88)	1.595	0.122	0.60
Delayed recall	10.08 (2.78)	8.31 (4.06)	1.331	0.194	0.50
RCFT (HC: *n* = 13, TBI: *n* = 16)					
Immediate recall	52.38 (11.01)	42 (19.03)	1.742	0.093	0.65
Delayed recall	47.08 (14.67)	40.63 (17.53)	1.059	0.299	0.40
CTMT (HC: *n* = 13, TBI: *n* = 16)	85.08 (21.64)	84.13 (17.32)	0.132	0.896	0.05
WCST (HC: *n* = 13, TBI: *n* = 16)	37.15 (10.39)	32.69 (15.41)	0.892	0.38	0.33

WASI, Wechsler Abbreviated Scale of Intelligence; RAVLT, Rey Auditory Verbal Learning Test; RCFT, Rey Complex Figure Test and Recognition Trial; CTMT, Comprehensive Trail-Making Test; WCST, Wisconsin Card Sorting Test; HC, Healthy control; TBI, traumatic brain injury; SD, standard deviation.
[a]Two-tailed independent sample t-test at $p < 0.05$.
[b]Cohen's corrected d (Hedge's g).

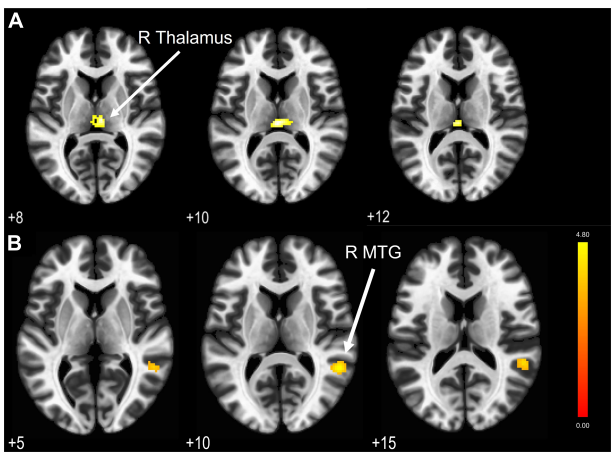

FIGURE 2 | (A) LFF BOLD activation comparison revealed a significant hypoactivation area in the TBI group compared to HC with cluster extent threshold $k = 79$. **(B)** Significantly activated areas in the TBI group (correspond to the middle temporal gyrus) due to hypoconnectivity from PCC as the seed region. Results are thresholded at voxel-level $p_{unc} < 0.001$ and cluster extent thresholded at $p_{FDR} < 0.05$. The color bar represents the T-score.

scanner (Li et al., 2019). Data were preprocessed using Statistical Parametric Mapping 12 (SPM12)[1] software package implemented in MATLAB (v. R2021a)[2] using a standard preprocessing pipeline. First, functional data underwent slice timing correction and realignment to correct the motion artifact and then co-registered to individual T1 anatomical images. The anatomical images were then fitted into standard space according to Montreal Neurological Institute (MNI), and the normalized parameters were applied to the functional data. Lastly, a Gaussian blur set at 8 mm full width half maximum (FWHM) was applied to the functional data to obtain better inference of the neighboring voxels. Artifact Detection Toolbox (ART)[3] implemented in MATLAB was used to detect any outlier scans. The global mean threshold was set at a 3 standard deviation (SD) limit with a movement threshold of 0.5 mm (Dailey et al., 2018), corresponding to a conservative 95% confidence interval.

Statistical Analysis

Demography, neuropsychological scores, and correlational analysis were carried out using Statistical Product and Service Solutions (SPSS 26). The results of demography and neuropsychological data were compared between groups using an independent-sample t-test with a p-value set at 0.05, and Levene's test for assumption of equal variance was conducted simultaneously.

In addition to statistical analysis, effect size calculations were also performed to compare the effect of the sample size of each group. Due to the difference in group size, corrected Cohen's d (Hedge's g) was used to estimate the effect size and aid in result interpretation (Gerchen et al., 2021; Pernet et al., 2021). Following the rule of thumb set by Cohen, an effect size of 0.2 is considered as a small effect, 0.5 as a medium effect, and 0.8 as a large effect (Lakens, 2013).

Low-Frequency Fluctuations Modeling

The general linear model (GLM) was designed according to the steps outlined in the technical paper by Di and Biswal (2014). The low-frequency fluctuations (LFF) were modeled into eight-block functions that represented the following frequencies: 0.01, 0.02, 0.04, and 0.08 Hz, with a 90° offset for each frequency

[1]www.fil.ion.ucl.ac.uk/spm/software/spm12
[2]https://www.mathworks.com/products/matlab.html
[3]https://www.nitrc.org/projects/artifact_detect

TABLE 3 | LFF statistical analysis with significantly hypoactivated areas in the TBI group compared to the HC.

Area	Coordinate (*x y z*)			Cluster size[a]	*T*
R thalamus	0	−24	10	79	4.54

R, right. Coordinates follow the standard Montreal Neurological Institute (MNI) template in millimeters (mm).
[a]$p_{FDR} < 0.05$.

(Di and Biswal, 2014). Preprocessed data of each participant were entered into the GLM and subjected to one-sample t-tests to obtain the activation of the brain areas. The peak voxel activations were thresholded at $p < 0.001$ (uncorrected, p_{unc}), while cluster size activation was adjusted to correct for false discovery rate (FDR) at p-value < 0.05 (p_{FDR}) (Sours et al., 2017). Afterward, the GLMs from each group were entered into 2nd-level analysis to find any significant differences in the activation patterns. For this purpose, a two-sample t-test was used with similar peak voxel and cluster size activation threshold ($p_{unc} < 0.001$ and $p_{FDR} < 0.05$, respectively).

Functional Connectivity Analysis

The FC analysis was conducted using CONN Toolbox (v.20b; RRID: SCR_009550)[4], open-source software based on MATLAB/SPM12 for FC analysis of fMRI data (Whitfield-Gabrieli and Nieto-Castanon, 2012). Preprocessed images underwent denoising step, which removes signals from the white matter and cerebrospinal fluids and discards outlier scans caused by motion artifacts. In addition, a temporal bandpass filtering was applied to account for the LFF, set between 0.009 and 0.08 Hz.

Following that, seed-based and region of interest (ROI)-based FC analyses were performed. The DMN consists of four nodes indicated *a priori* by the CONN Toolbox. The nodes included the medial prefrontal cortex (MPFC), posterior cingulate cortex (PCC), and left and right lateral parietal (LP), outlined in **Table 1**. For the ROI-to-ROI analysis, 32 nodes from 8 resting-state networks were set based on the CONN network *a priori* groups implemented in CONN Toolbox as follows: DMN (4 nodes), sensorimotor network (SN; 3 nodes), visual network (VN; 4 nodes), salience network (SN; 7 nodes), dorsal attention network (DAN; 4 nodes), frontoparietal network (FPN; 4 nodes), language network (LN; 4 nodes), and cerebellar network (CN; 2 nodes). Similar to LFF modeling, multiple comparisons in the cluster level were corrected using $p_{FDR} < 0.05$ and voxel-level threshold set at $p_{unc} < 0.001$ (Sours et al., 2017).

Dynamic Causal Modeling

We analyzed the ECs of the DMN using Dynamic Causal Modeling embedded within the SPM12 (DCM10.5). The LFF signal from four nodes of the DMN, precuneus, MPFC, and bilateral angular gyrus was extracted from the *a priori* DMN nodes specified in the CONN Toolbox previously. For this purpose, we set a sphere of 8-mm radius as the volume of interest centered on the peak coordinates of each node. In the analysis, the LFF signals of these DMN nodes were regressed against the LFF signals from white matter and cerebrospinal fluids to remove any effects that may be contributed by these components.

The endogenous connectivities between these nodes were modeled following the methods outlined by Di and Biswal (2014), in which the connectivity was varied between three possible combination families: PCC–MPFC, LLP–RLP, and PCC/MPFC–LLP/RLP, as outlined in **Figure 1** (Di and Biswal, 2014). The resulting number of models was subsequently analyzed using cross-spectral density, as resting-state data are appropriately analyzed using the frequency domain. All models were compared using Bayesian model selection (BMS) using random-effect inference to determine the best model. Random-effect BMS is favorable as it is impervious to outliers, thus ensuring group heterogeneity (Sadeghi et al., 2020). The probability graph of each model was plotted, and the winning model was selected according to the maximum probability among all the models. The winning model from each group was then averaged using Bayesian Parameter Averaging, a method of integrating the individual posterior densities and utilizing the posterior from one subject as the prior for the successive subject (Stephan et al., 2010).

RESULTS

Demographics and Neuropsychological Results

The demographic and neuropsychological information and results are detailed in **Table 2**. Our cohort of participants consisted of a homogenous sample in terms of race and gender (Malay males). Sixteen TBI and thirteen HCs from the sample size were administered the neuropsychological tests. The independent t-test revealed no significant difference between TBI and HC in the WASI, RAVLT, RCFT, CTMT, and WCST domains. However, medium effect sizes were observed on the matrix reasoning domain in WASI ($t[27] = 1.77$, $p = 0.089$, Hedge's $g = 0.66$), both domains of the RAVLT (immediate verbal recall, $t[27] = 1.60$, $p = 0.122$, Hedge's $g = 0.60$; delayed verbal recall, $t[27] = 1.33$, $p = 0.194$, Hedge's $g = 0.50$), and the immediate recall domain in RCFT ($t[27] = 1.74$, $p = 0.093$, Hedge's $g = 0.65$), which indicated medium practical differences. These results suggest that the TBI group performed moderately worse than HC in general cognitive ability, verbal memory, and visual memory. Other domains and tests recorded either small or trivial effect sizes.

Brain Structural Evaluations

The T1-weighted structural images were evaluated independently by three senior neurosurgeons with more than 15 years of experience from the Department of Neurosciences, Hospital Universiti Sains Malaysia. No significant structural alterations were identified in the brain morphometry.

Low-Frequency Fluctuations Activations Comparison

We compared the BOLD activations to find any difference in the LFF between HC and TBI groups. The independent sample t-test showed no significant activations when we applied the

[4]www.nitrc.org/projects/conn

TABLE 4 | The regions that displayed significant activation in the HC > TBI, based on seed regions of individual DMN nodes.

Seed	Activated regions	Coordinate *(x y z)*			Cluster size	p[a]	Effect size[b]
PCC	Middle temporal gyrus	54	−46	10	183	0.013	0.79

PCC, posterior cingulate cortex. Coordinates follow the standard Montreal Neurological Institute (MNI) template in millimeters (mm).
[a] $p_{FDR} < 0.05$.
[b] *Cohen' s corrected d (Hedge's g).*

cluster-level threshold at $p_{FDR} < 0.05$. Nevertheless, by using the lower cluster threshold ($p_{unc} < 0.05$), we found a significant hypoactivation (see **Figure 2A**) in the TBI group at the right thalamus (peak MNI coordinate 0 -24 10, t[39] = 4.54, $p < 0.05$). Results are outlined in **Table 3**.

Functional Connectivity in Healthy Controls and Traumatic Brain Injury Groups

We computed seed-based and ROI-based analyses to measure the FC in both HC and TBI. In essence, the seed-based connectivity measures the connectivity of a seed region to other areas of the brain, while ROI-based connectivity compares the parameter of connectivity between different regions of interest associated with a particular network. The parameters of each participants' FC were then compared between HC and TBI.

Seed-Based Analysis

The four DMN nodes that were set as seeds are outlined in **Table 1**. **Figure 2B** shows the result of seed-based analysis of the DMN nodes, which reveals a significantly reduced FC in the TBI group between the PCC and middle temporal gyrus (MTG; peak MNI coordinate 54 -46 10, cluster-level p_{FDR} = 0.013, Hedge's g = 0.79). The result is outlined in **Table 4**.

Region of Interest -Based Analysis

Network-based F-statistics analysis in eight *a priori* RSNs revealed no significant difference in FC between groups at network level $p_{FDR} < 0.05$. The FC matrices are presented in **Figures 3A,B**. However, the independent t-test for individual nodes FC reveals significant hypoconnectivity in ROI pairs between DMN and LN in the TBI group, in PCC and right posterior superior temporal gyrus (pSTG) (t[39] = 2.93, p = 0.006, Hedge's g = 0.92), and right LP and right pSTG (t[39] = 2.26, p = 0.029, Hegde's g = 0.71). Additionally, the effect size estimates for two ROI pairs between DMN and FPN indicated to have potential medium practical differences, thus suggesting that the TBI group was hypoconnected between left LP and right lateral prefrontal cortex (LPFC) (t[39] = 1.63, p = 0.112, Hedge's g = 0.51) and between right LP and right posterior parietal cortex (PPC) (t[39] = 1.56, p = 0.126, Hedge's g = 0.29). The results are outlined in **Table 5**, and the FC matrices are presented in **Figure 3C**. In addition, based on our findings in LFF activation, we analyzed the FC between DMN nodes and thalamus. We did not find any significant difference in terms of FC between the HC and TBI. Moreover, the effect size is negligible.

Correlation Between Neuropsychological Performance and Default Mode Network Connectivity

We performed correlation analysis between the neuropsychological performance and the FC in the TBI group. Our results suggested that the alterations in the FC within and between the DMN and other RSNs formed significant associations with the scores of the neuropsychology assessment. We found that higher scores in the following tests are significantly correlated with higher FC: (1) T-block with PCC–left pSTG (R = 0.63, p = 0.008) and left LP–right LP (R = 0.63, p = 0.009); (2) verbal memory with PCC–left pSTG (immediate recall R = 0.57, p = 0.022; delayed recall R = 0.53, p = 0.034), left LP–right LP (immediate recall R = 0.054, p = 0.031; delayed recall R = 0.511, p = 0.043), and left LP–left IFG (delayed recall R = 0.52, p = 0.041); and 3) CTMT with PCC–right pSTG (R = 0.50, p = 0.048), PCC–right PPC (R = 0.58, p = 0.019), PCC–right LPFC (R = 0.54, p = 0.032), and right LP–right IFG (R = 0.61, p = 0.012). We also found that higher scores in the following tests are significantly correlated with lower FC: (1) matrix reasoning with PCC–VN (R = −0.51, p = 0.042); (2) visual memory with PCC–VN (immediate recall R = −0.56, p = 0.026; delayed recall R = −0.58, p = 0.020); and 3) CTMT with MPFC–PCC (R = −0.51, p = 0.045). The results are outlined in **Table 6** (correlation graphs are available in **Supplementary Material**).

Effective Connectivity Following Traumatic Brain Injury

The resulting ECs are presented as either excitatory or inhibitory, characterized by positive and negative values, respectively. Two types of ECs are reported: the self-connection or intrinsic EC, and outgoing connections or extrinsic ECs. The detailed statistical results are presented in **Table 7**, while **Figure 4** visualizes the endogenous ECs in both HC and TBI. After comparing all possible models using random-effect BMS, we found that the full connectivity model is the most optimal model for both HC and TBI groups, in which all regions mutually influence each other (see **Figures 5**, **6**). While the full connectivity model was favorable in the HC group, the connectivity between the left LP and the PCC did not achieve statistical significance. This left the HC group with eleven extrinsic ECs versus twelve in the TBI group. Out of the twelve extrinsic connections, seven ECs in the TBI group are inhibitory (PCC → MPFC, PCC → LLP, MPFC → PCC, MPFC → LLP, MPFC → RLP, LLP → PCC, and LLP → RLP), compared to five in HC (PCC

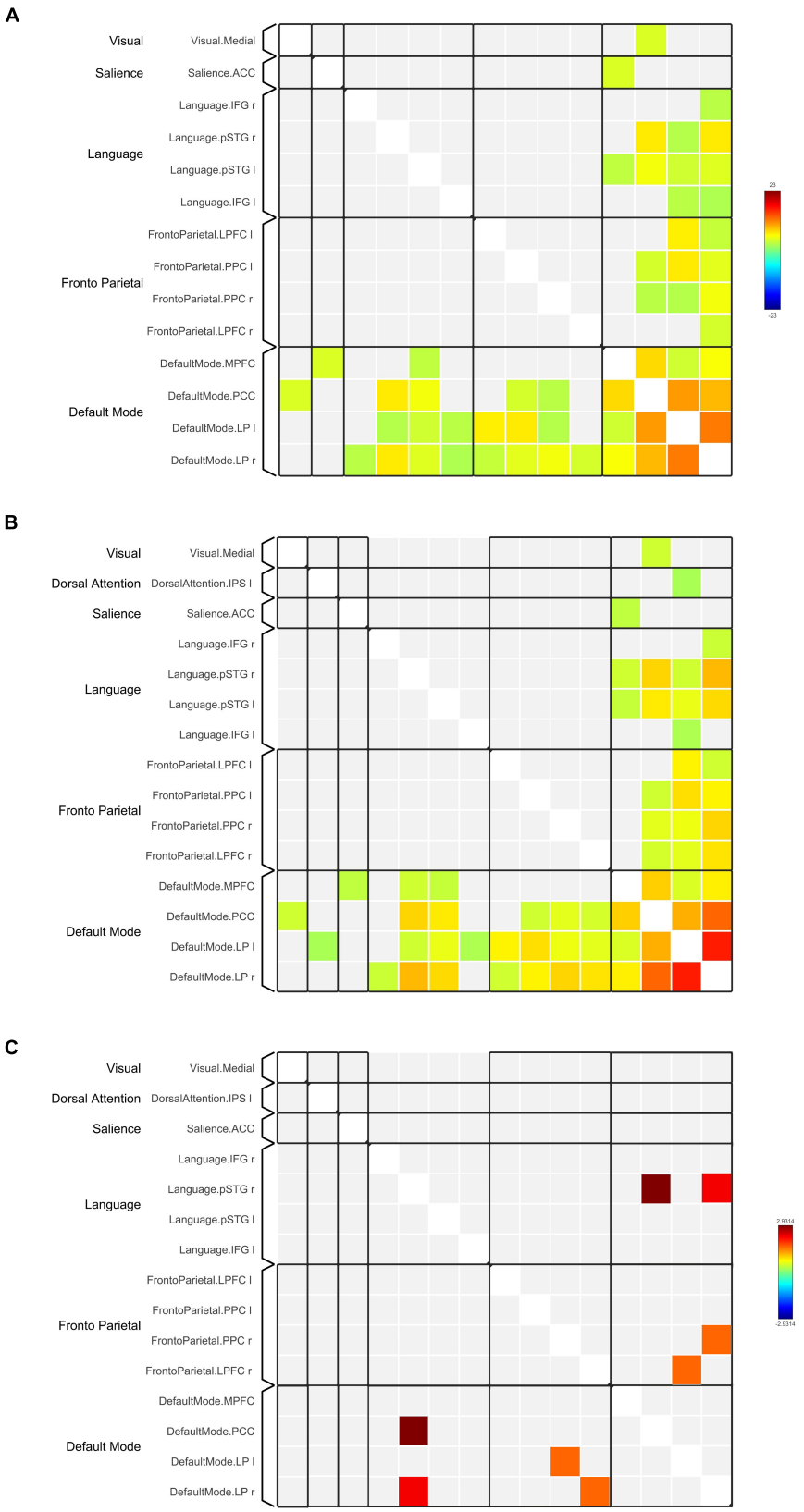

FIGURE 3 | Functional connectivity matrices within the DMN and between the DMN and other RSNs in **(A)** HC and **(B)** TBI groups. Results in **(A,B)** are thresholded at voxel-level $p_{unc} < 0.001$ and cluster extent thresholded at $p_{FDR} < 0.05$, corrected for multiple comparisons. **(C)** The 2-sample *t*-test between HC and TBI groups show functional connectivity matrices that achieve moderate to high effect size. The color bars represent the T-score.

TABLE 5 | The effect size of the ROI pairs between HC and TBI groups that achieve moderate to high effect as per Cohen's recommendations.

Inter-DMN connectivity	ROI pair	Mean HC (SD)	Mean TBI (SD)	*t*	p^2	Effect size[b]
DMN–LN	PCC-R pSTG	0.42 (0.22)	0.24 (0.16)	2.93	0.006*	0.92
DMN–LN	R LP-R pSTG	0.49 (0.27)	0.32 (0.21)	2.26	0.029*	0.71
DMN–FPN	L LP-R LPFC	0.20 (0.23)	0.08 (0.23)	1.63	0.112	0.51
DMN–FPN	R LP-R PPC	0.46 (0.29)	0.33 (0.28)	1.56	0.126	0.49

R, right; L, left; pSTG, posterior superior temporal gyrus; LP, lateral parietal; LPFC, lateral prefrontal cortex; PPC, posterior parietal cortex; DMN, default mode network; LN, language network; FPN, fronto-parietal network.
[a] *Two-tailed independent-sample t-test.*
[b] *Cohen's corrected d (Hedge's g).*
*$p < 0.05$.

TABLE 6 | The correlation between the ROI connectivity values and neuropsychological scores in the TBI group.

Domain	Inter-DMN FC	ROI pair	R	p^2
WASI				
Block design	DMN–DMN	L LP–R LP	0.63	0.009
	DMN–LN	PCC–L pSTG	0.63	0.008
Matrix reasoning	DMN-VN	PCC–Visual medial	−0.51	0.042
RAVLT				
Immediate	DMN–DMN	L LP–R LP	0.54	0.031
	DMN–LN	PCC–L pSTG	0.57	0.022
Delayed	DMN–DMN	L LP–R LP	0.51	0.043
	DMN–LN	L LP–L IFG	0.52	0.041
	DMN–LN	PCC–L pSTG	0.53	0.034
RCFT				
Immediate	DMN–VN	PCC–visual medial	−0.56	0.026
Delayed	DMN–VN	PCC–visual medial	−0.58	0.020
CTMT	DMN – DMN	MPFC-PCC	−0.51	0.045
	DMN-LN	PCC–R pSTG	0.50	0.048
	LN	R LP–R IFG	0.61	0.012
	FPN	PCC–R PPC	0.58	0.019
	FPN	PCC–R LPFC	0.54	0.032

R, right; L, left; LP, lateral parietal; PCC, posterior cingulate cortex; pSTG, posterior superior temporal gyrus; IFG, inferior frontal gyrus; MPFC, medial prefrontal cortex; PPC, posterior parietal cortex; LPFC, lateral prefrontal cortex; WASI, Wechsler Abbreviated Scale of Intelligence; RAVLT, Rey Auditory Verbal Learning Test; RCFT, Rey Complex Figure Test and Recognition Trial; CTMT, Comprehensive Trail-Making Test; WCST, Wisconsin Card Sorting Test; DMN, default mode network; LN, language network; VN, visual network; FPN, fronto-parietal network.
[a] *$p < 0.05$.*

TABLE 7 | Statistics of the endogenous connectivity parameter of the winning model.

Connection	BPA ECP		p^2	Effect size[b]
	HC	TBI		
PCC	−0.8	−1.28	-	-
MPFC	−1.28	−0.71	-	-
LLP	−0.40	0.41	-	-
RLP	−0.40	−0.70	-	-
PCC→ MPFC	−0.15	−0.06	0.585	0.17
PCC → LLP	–	−0.01	0.160	0.45
PCC→ RLP	−0.09	0.02	0.439	0.24
MPFC → PCC	0.32	−0.26	0.185	0.42
MPFC → LLP	−1.28	−0.71	0.805	0.08
MPFC→ RLP	−0.19	−0.04	0.257	0.36
LLP→ PCC	0.01	−0.12	0.213	0.40
LLP→ MPFC	0.10	0.11	0.875	0.05
LLP→ RLP	−0.40	−0.41	0.687	0.13
RLP→ PCC	0.05	0.30	0.354	0.29
RLP→ MPFC	0.06	0.26	0.554	0.19
RLP→ LLP	0.40	0.16	0.136	0.48

PCC: posterior cingulate cortex, MPFC: medial prefrontal cortex, LLP: left lateral parietal, RLP: right lateral parietal, BPA: Bayesian parameter averaging, ECP: endogenous connectivity parameter, TBI: traumatic brain injury.
[a] *Independent sample t-test of the individual endogenous parameters from each group, thresholded at $p < 0.05$.*
[b] *Cohen's corrected d (Hedge's g).*

→ MPFC, PC → RLP, MPFC → LLP, MPFC → RLP, and LLP → RLP). Two mutual inhibitory ECs were observed in the TBI group, between the PCC and MPFC, and between LLP and PCC, while one mutual excitatory EC was observed in the HC, between MPFC and RLP. Both groups displayed right hemispheric lateralization, particularly characterized by ECs involving the RLP and MPFC. The intrinsic connectivity of all DMN nodes in both groups displayed self-inhibition, with the strongest inhibitory value observed in the PCC for TBI, and in MPFC for the HC group. The RLP displayed the strongest outgoing ECs in both groups. Also, a statistical comparison of connectivity from the RLP → LLP reaches a near-moderate effect size, suggesting moderately stronger extrinsic excitatory EC in HC compared to the TBI group originating from RLP to LLP ($p = 0.136$, Hedge's $g = 0.48$).

DISCUSSION

We analyzed the DMN *via* rsfMRI data in HC and TBI groups using LFF activations, ICA extraction, FC analysis, and ECs *via* cross-spectral density analysis. Our results demonstrated that compared to HC, TBI participants experienced alterations in the functional organization of the DMN. In particular, lower neuropsychological performance, decreased regional activations, lower FC values, and altered ECs were observed within the TBI group compared to HC. The neuropsychological test results have shown that the TBI group performed moderately worse than HC in the domains of general cognitive ability, verbal memory,

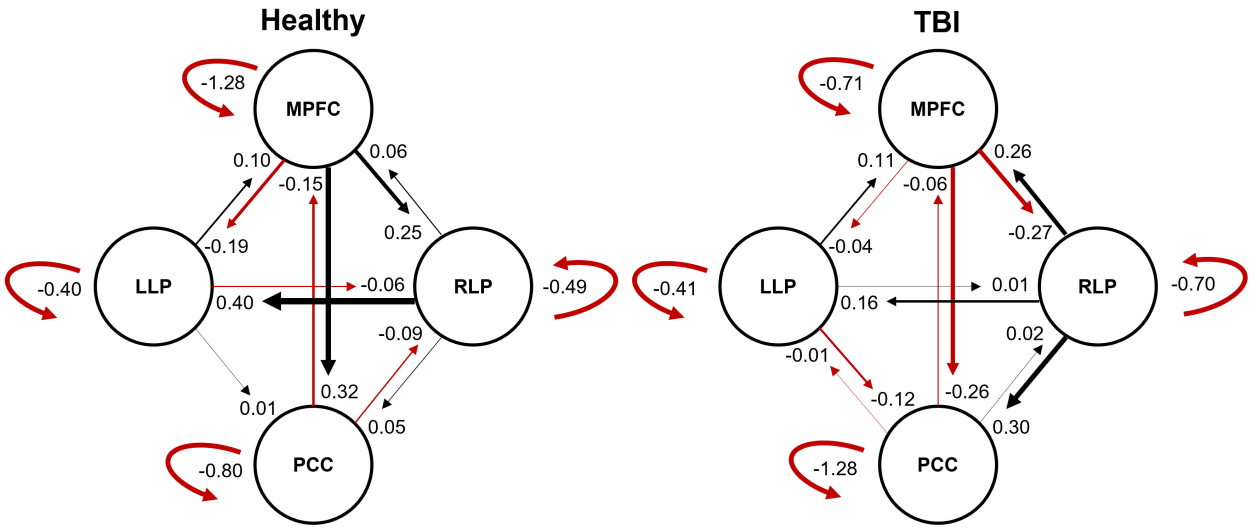

FIGURE 4 | The endogenous connectivity parameters for HC and TBI groups. The effective connectivity between PCC and LLP did not survive statistical significance for the HC group. The thickness of the arrow represents the strength (Hz) of the connection. The black arrow denotes positive connectivity value, which suggests excitation, and the red arrow denotes negative connectivity value, which suggests inhibition.

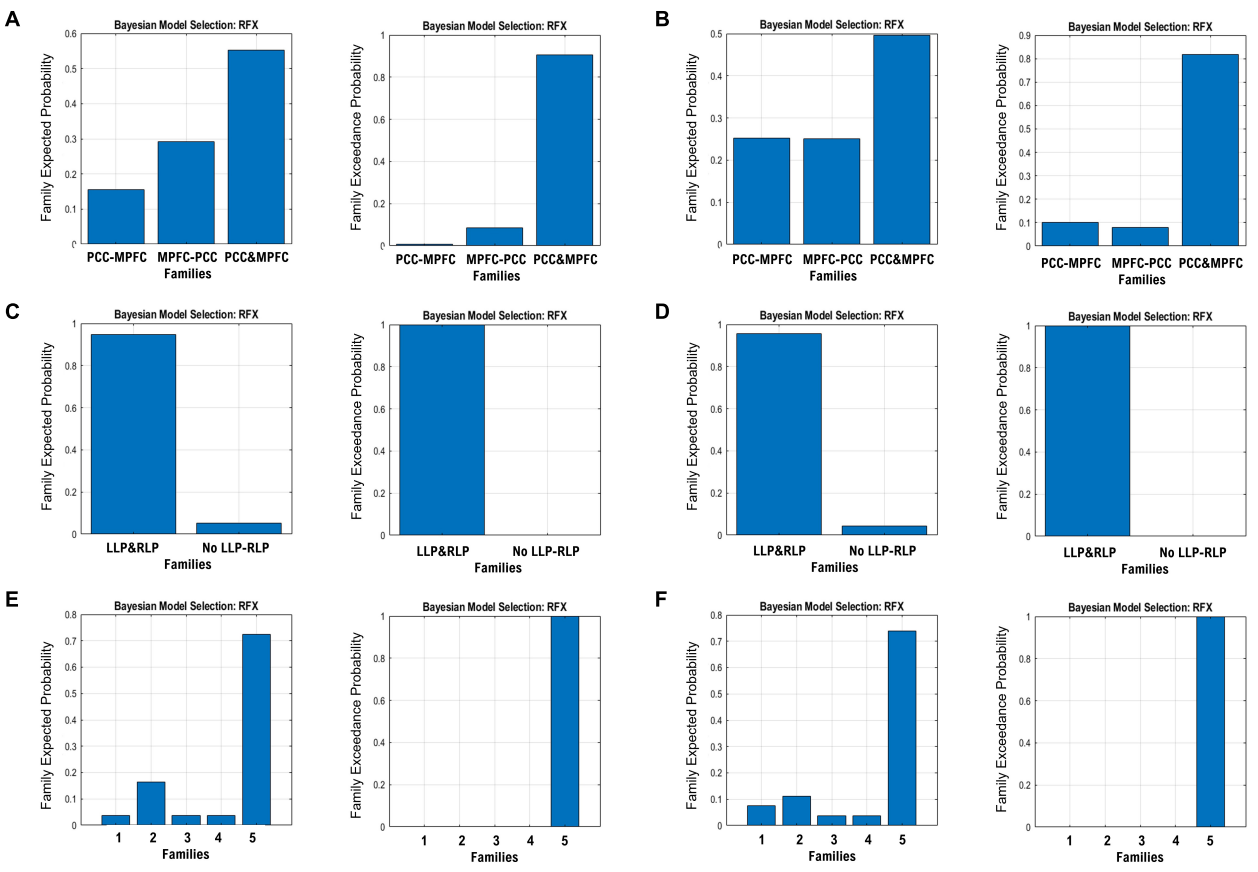

FIGURE 5 | The expected probability (left) and exceedance probability (right) for the three DCM families specified in **Figure 1**. The BMS results are shown for the MPFC-PCC family in the **(A)** HC group and **(B)** TBI group, LLP-RLP families in the **(C)** HC group and **(D)** TBI group, and bilateral LP and PCC/MPFC families in the **(E)** HC group and **(F)** TBI group.

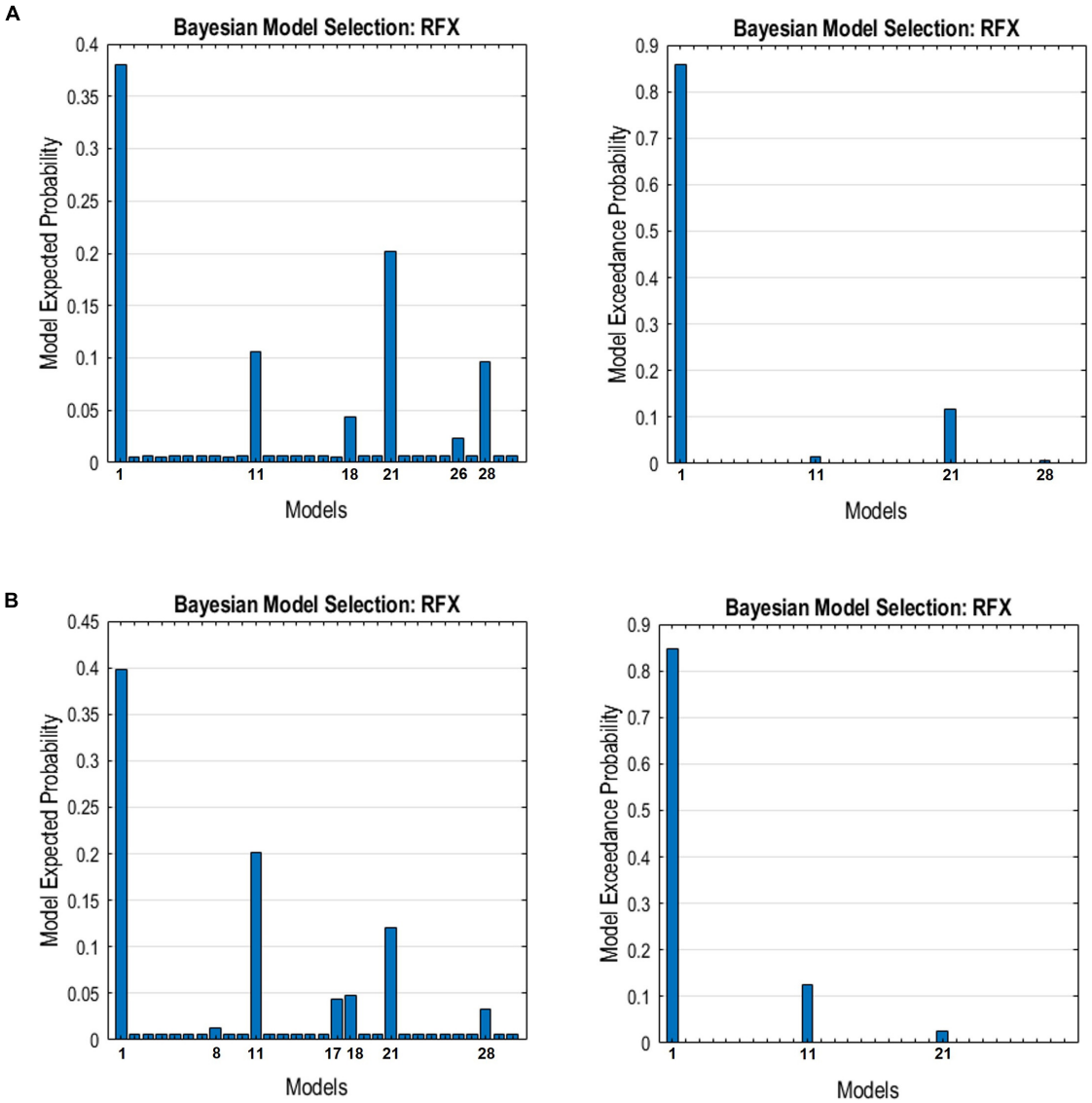

FIGURE 6 | The expected probability (left) and exceedance probability (right) for the individual models compared using Bayesian model selection for the DMN connectivity models in the **(A)** HC group and **(B)** TBI group.

and visual memory. Cognitive and memory deficits following TBI have been well-documented, where studies have shown impairments in verbal memory, visual memory, and cognitive domain among the TBI survivors (Caeyenberghs et al., 2014; Robb Swan et al., 2015; Huang et al., 2017; Lutkenhoff et al., 2020; Li et al., 2021). However, we did not find any significant difference between groups on other neuropsychological domains, which established the asynchrony between impaired connectivity and cognitive deficits commonly reported in the literature (van der Horn et al., 2016; Rajesh et al., 2017).

The result of LFF activations showed that the thalamus was hypoactivated in TBI compared to HC, in line with previous literature (Leung et al., 2016), particularly in patients with complaints (Grossman and Inglese, 2016). The thalamus is implicated in the regulation of awareness and consciousness and filters information between the brain and the body, essentially functioning as a relay station (Wang et al., 2014), and damage to the thalamus has been shown to affect the attention, executive function, and memory (Lutkenhoff et al., 2020). Previous studies have demonstrated the structural and FC of the thalamus with the DMN (Fransson, 2005; Cunningham et al., 2017), therefore indicating that the thalamus has a key role in DMN functions (Alves et al., 2019), especially during mindfulness and consciousness (Wang et al., 2014; He et al., 2015). Studies have also shown that the FC between the DMN nodes and thalamus was increased in TBI compared to HC in acute (Sours et al., 2015), subacute (Tang et al., 2011; Banks et al., 2016), and chronic stages (Nordin et al., 2016) that may be accompanied by increased

structural connectivity (Munivenkatappa et al., 2016). Other studies found diminished FC in the thalamus in the chronic stage of TBI (Moreno-López et al., 2016; Xiong et al., 2016). However, despite the thalamic hypoactivation, we found no significant difference in FC between the nodes of the DMN and thalamus in our HC and TBI cohorts, and the effect size comparison revealed a negligible effect.

In terms of the FCs between other brain regions, the TBI group displayed significantly lower FCs between the DMN and other RSNs compared to the HC group. This finding is in contrast with previous research that indicated hyperconnectivity as a common response to TBI, especially involving network hubs in the chronic stage (Hillary et al., 2014, 2015; Hillary and Grafman, 2017; Roy et al., 2017). On that note, decreased FC in the acute and subacute stages has been established in the literature (Manning et al., 2019), while diminished FC in PCC and precuneus regions was found in the subacute mild TBI cohort (Iraji et al., 2015), corroborating our findings. In the acute stage, reduced FCs within the nodes of the DMN were also found (Dall'Acqua et al., 2017), which gradually increased and served as a compensatory mechanism. The additional connectivity recruitments culminated in the functional hyperconnectivity within the first year of recovery after the initial injury (Hillary et al., 2014), with peak hyperconnectivity at 6 months post-injury (Roy et al., 2017) before being reduced as the brain is found to be the most optimal route to balance between performance and metabolic cost (Hillary and Grafman, 2017; Roy et al., 2017). Using seed-level analysis, we found that the FC from the PCC to the MTG is significantly reduced in the HC group. The MTG corresponds to Brodmann's area 22 and is involved in language processing. In addition, ROI-to-ROI analysis also indicated decreased FC between the DMN and LN, as well as between the DMN and FPN. Several studies have shown that TBI may impair the language domain, notably language comprehension, production, and coherence (Marini et al., 2014; Shumskaya et al., 2017; Huang et al., 2020). Hence, the impaired FC between the DMN and LN is corroborated.

Building on our findings in neuropsychology scores and the FCs, we performed correlation analysis between these two results and found significant correlations between inter-network FC and several neuropsychological domains. Our results showed that lower FCs between DMN and LN nodes significantly correlate with lower test scores in general cognitive ability and verbal memory domain in the TBI group. The verbal memory domain also subserves language components (Acheson and MacDonald, 2009; Schwering and MacDonald, 2020); thus, this correlation indicates a possible association between diminished FC involving the LN and lower test scores in the verbal memory tests. On the other hand, scores in matrix reasoning and visual memory were negatively correlated with the FC strength between PCC and visual medial node. This finding suggests that an increase in FC between the DMN and VN may affect the performance in visual memory and matrix reasoning. Additionally, correlation analysis revealed that the PCC was implicated in all significant correlation results, implying an important role played by the PCC as the network hub between the DMN and other RSNs (Hillary and Grafman, 2017).

Finally, the EC of the TBI group also showed alterations compared to HC. Hemispheric asymmetry was observed in both groups, with the ECs lateralized to the right hemisphere. The DMN is established to be asymmetrically organized, determined by the influence of the parietal regions (Almgren et al., 2018). For extrinsic ECs, our results showed that the TBI group exhibited a near moderate decrease in EC particularly from RLP to LLP, characterized by a lower excitatory EC parameter compared to the HC. In this case, the lower excitatory influence exerted by the RLP to the LLP was translated into hypoactivated left parietal areas. Moreover, the TBI group displayed more inhibitory connectivity compared to HC. This finding is in line with our previous study, which found more negative ECs in the TBI group with higher strength (Abdul Rahman et al., 2020). The extrinsic inhibitory connections are the negative influence exerted by one region to another, also known as the baseline inhibition (Stephan and Friston, 2010), due to the population of inhibitory neurons. The excess of negative ECs in TBI may signal the higher number of inhibitory neurons in brain connectivity that play a role in exerting baseline inhibitions between different regions.

Within the intrinsic ECs, all four nodes displayed self-inhibition in both groups. Greater inhibitory strengths were observed in the nodes that exert greater influence, especially in the MPFC and RLP. This observation is expected, as the dominant nodes of the network typically exhibit prolonged and uninhibited activity (Almgren et al., 2018). However, the greatest self-inhibition parameter in the TBI group was observed in PCC even though it did not have any dominant ECs originating from it. This finding may explain the lower precuneus activation that we found in the TBI group. The self-inhibition connections represent the decay rate of neural activity in each area and characterize the region's susceptibility to the outside influence, with lesser self-inhibition indicating a region's increased sensitivity to the inputs from other regions (Esménio et al., 2020). Therefore, lower sensitivity toward the outside influence resulted in lower activity observed in the precuneus region.

LIMITATION AND CONCLUSION

There are a few limitations to this study that should be considered when interpreting the findings. First, we rely on admission to the emergency department for recruitment of our samples, and the recent outbreak of the coronavirus pandemic has hindered us to recruit more participants; thus, our sample size remains small. Consequently, our small sample size may have precluded statistical significance on multiple comparison corrections at the cluster level. Nevertheless, while our findings are valid for the sample that we have recruited, extrapolation to the general population must be done cautiously and with the support of future studies with a bigger sample size. Based on our observation, the effect size analysis of our results suggested that a bigger sample size can lead to significant results after the correction for multiple comparisons. Second, at best, these findings are initial steps in understanding the heterogeneous nature of non-severe TBI across multiple factors, and we have

explored these effects against a sample of homogeneous race and gender among the Malaysian population. Notwithstanding that, our study is reproducible to analyze other contributing factors that may change the findings observed in this study, such as the inclusion of different races and gender, or from the perspective of education and socioeconomic factors.

In conclusion, TBI resulted in the functional reorganization of the brain, from the aspect of activity and connectivity. These aberrations subsequently altered the EC of the DMN, changing the intrinsic and extrinsic influence patterns exerted by the nodes. Furthermore, lower performance within verbal memory, visual memory, and cognitive flexibility was widespread among the TBI group. Therefore, our observations suggest that these changes in brain organization and functions were linked to the debilitating effects of TBI, and this knowledge can be applied in interventional plans and recovery of TBI survivors.

DATA AVAILABILITY STATEMENT

The raw data supporting the conclusions of this article will be made available by the authors, without undue reservation.

ETHICS STATEMENT

The studies involving human participants were reviewed and approved by Institutional Ethics Committee (IEC) of Universiti Sains Malaysia. The patients/participants provided their written informed consent to participate in this study.

AUTHOR CONTRIBUTIONS

AIAH, NN, HO, ZI, AHA, ARA, MR, KM, AO, ZE, NS, RK, HI, MA, KA, PV-S, ML-B, BB, JS, HY, PS, PSJ, AA, and JMA: conceptualization. AIAH, NN, and JMA: project administration. MRAR: investigation (literature reviews) and writing—original draft. MRAR, AIAH, HO, and WJC: methodology. MRAR, HO, WJC, AHA, DF, WW, MM, HU, MFMZ, SA, and ZZ: data collection. MRAR, HO, and WJC: data curation. MRAR, HO, WJC, and WW: data analysis. MRAR, AIAH, HI, AO, PV-S, ML-B, and JMA: writing — review and editing. MRAR: visualization. All authors contributed to the article and approved the submitted version.

FUNDING

Translational Research Grant Scheme, Ministry of Higher Education Malaysia (TRGS/1/2015/USM/01/6/3). Funding for the data collections and project administrations. Research University Grant (RUI), Universiti Sains Malaysia (1001/PPSP/8012307). Funding for the data collections and project administrations.

ACKNOWLEDGMENTS

We acknowledge the funding from the Translational Research Grant Scheme, Ministry of Higher Education (TRGS/1/2015/USM/01/6/3) and the Research University Grant (RUI), Universiti Sains Malaysia (1001/PPSP/8012307). We would also like to thank the MRI technologists Wan Nazyrah Abdul Halim, Che Munirah Che Abdullah, and Siti Afidah Mamat and science officer Alwani Liyana Ahmad.

SUPPLEMENTARY MATERIAL

The Supplementary Material for this article can be found online at: https://www.frontiersin.org/articles/10.3389/fnins.2022.833320/full#supplementary-material

REFERENCES

Abdul Rahman, M. R., Abd Hamid, A. I., Noh, N. A., Idris, Z., and Abdullah, J. M. (2020). The effective connectivity of the default mode network following moderate traumatic brain injury. *J. Phys. Conf. Ser.* 1497:012008. doi: 10.1088/1742-6596/1497/1/012008

Acheson, D. J., and MacDonald, M. C. (2009). Verbal Working Memory and Language Production: common Approaches to the Serial Ordering of Verbal Information. *Psychol. Bull.* 135, 50–68. doi: 10.1037/a0014411

Almgren, H., Van de Steen, F., Kühn, S., Razi, A., Friston, K., and Marinazzo, D. (2018). Variability and reliability of effective connectivity within the core default mode network: a multi-site longitudinal spectral DCM study. *Neuroimage* 183, 757–768. doi: 10.1016/j.neuroimage.2018.08.053

Alves, P. N., Foulon, C., Karolis, V., Bzdok, D., Margulies, D. S., Volle, E., et al. (2019). An improved neuroanatomical model of the default-mode network reconciles previous neuroimaging and neuropathological findings. *Commun. Biol.* 21, 1–14. doi: 10.1038/s42003-019-0611-3

Banks, S. D., Coronado, R. A., Clemons, L. R., Abraham, C. M., Pruthi, S., Conrad, B. N., et al. (2016). Thalamic Functional Connectivity in Mild Traumatic Brain Injury: longitudinal Associations With Patient-Reported Outcomes and Neuropsychological Tests. *Arch. Phys. Med. Rehabil.* 97, 1254–1261. doi: 10.1016/j.apmr.2016.03.013

Bean, J. (2011). "Rey Auditory Verbal Learning Test, Rey AVLT," in *Encyclopedia of Clinical Neuropsychology*, eds J. S. Kreutzer, J. DeLuca, and B. Caplan (New York, NY: Springer New York), 2174–2175. doi: 10.1007/978-0-387-79948-3_1153

Beratis, I. N., Andronas, N., Fragkiadaki, S., Kontaxopoulou, D., Pavlou, D., Papantoniou, P., et al. (2018). Exploring the association of the Comprehensive Trail Making Test with driving indexes in patients with Parkinson's disease. *Transp. Res. Part F Traffic Psychol. Behav.* 59, 535–544. doi: 10.1016/j.trf.2017.10.007

Caeyenberghs, K., Leemans, A., Leunissen, I., Gooijers, J., Michiels, K., Sunaert, S., et al. (2014). Altered structural networks and executive deficits in traumatic brain injury patients. *Brain Struct. Funct.* 219, 193–209. doi: 10.1007/s00429-012-0494-2

Cunningham, S. I., Tomasi, D., and Volkow, N. D. (2017). Structural and functional connectivity of the precuneus and thalamus to the default mode network. *Hum. Brain Mapp.* 38, 938–956. doi: 10.1002/hbm.23429

Dailey, N. S., Smith, R., Vanuk, J. R., Raikes, A. C., and Killgore, W. D. S. (2018). Resting-state functional connectivity as a biomarker of aggression in mild traumatic brain injury. *Neuroreport* 29, 1413–1417. doi: 10.1097/WNR.0000000000001127

Dall'Acqua, P., Johannes, S., Mica, L., Simmen, H.-P., Glaab, R., Fandino, J., et al. (2017). Functional and Structural Network Recovery after Mild Traumatic

Brain Injury: a 1-Year Longitudinal Study. *Front. Hum. Neurosci.* 11:280. doi: 10.3389/fnhum.2017.00280

Di, X., and Biswal, B. B. (2014). Identifying the default mode network structure using dynamic causal modeling on resting-state functional magnetic resonance imaging. *Neuroimage* 86, 53–59. doi: 10.1016/j.neuroimage.2013.07.071

Esménio, S., Soares, J. M., Oliveira-Silva, P., Gonçalves, ÓF., Friston, K., and Fernandes Coutinho, J. (2020). Changes in the Effective Connectivity of the Social Brain When Making Inferences About Close Others vs. the Self. *Front. Hum. Neurosci.* 14:151. doi: 10.3389/fnhum.2020.00151

Fransson, P. (2005). Spontaneous low-frequency BOLD signal fluctuations: an fMRI investigation of the resting-state default mode of brain function hypothesis. *Hum. Brain Mapp.* 26, 15–29. doi: 10.1002/hbm.20113

Gaudet, I., Hüsser, A., Vannasing, P., and Gallagher, A. (2020). Functional Brain Connectivity of Language Functions in Children Revealed by EEG and MEG: a Systematic Review. *Front. Hum. Neurosci.* 14:62. doi: 10.3389/fnhum.2020.00062

Gerchen, M. F., Kirsch, P., and Feld, G. B. (2021). Brain-wide inferiority and equivalence tests in fMRI group analyses: selected applications. *Hum. Brain Mapp.* 42, 5803–5813. doi: 10.1002/hbm.25664

Gordon, E. M., Scheibel, R. S., Zambrano-Vazquez, L., Jia-Richards, M., May, G. J., Meyer, E. C., et al. (2018). High-Fidelity Measures of Whole-Brain Functional Connectivity and White Matter Integrity Mediate Relationships between Traumatic Brain Injury and Post-Traumatic Stress Disorder Symptoms. *J. Neurotrauma* 35, 767–779. doi: 10.1089/neu.2017.5428

Gray, R. (2006). Comprehensive Trail Making Test. *J. Psychoeduc. Assess.* 24, 88–91. doi: 10.1177/0734282905282415

Grossman, E. J., and Inglese, M. (2016). The role of thalamic damage in mild traumatic brain injury. *J. Neurotrauma* 33, 163–167. doi: 10.1089/neu.2015.3965

He, J. H., Cui, Y., Song, M., Yang, Y., Dang, Y. Y., Jiang, T. Z., et al. (2015). Decreased functional connectivity between the mediodorsal thalamus and default mode network in patients with disorders of consciousness. *Acta Neurol. Scand.* 131, 145–151. doi: 10.1111/ane.12299

Hillary, F. G., and Grafman, J. H. (2017). Injured Brains and Adaptive Networks: the Benefits and Costs of Hyperconnectivity. *Trends Cogn. Sci.* 21, 385–401. doi: 10.1016/j.tics.2017.03.003

Hillary, F. G., Rajtmajer, S. M., Roman, C. A., Medaglia, J. D., Slocomb-Dluzen, J. E., Calhoun, V. D., et al. (2014). The rich get richer: brain injury elicits hyperconnectivity in core subnetworks. *PLoS One* 9:e104021. doi: 10.1371/journal.pone.0104021

Hillary, F. G., Roman, C. A., Venkatesan, U., Rajtmajer, S. M., Bajo, R., and Castellanos, N. D. (2015). Hyperconnectivity is a fundamental response to neurological disruption. *Neuropsychology* 29, 59–75. doi: 10.1037/neu0000110

Huang, M. X., Harrington, D. L., Robb Swan, A., Angeles Quinto, A., Nichols, S., Drake, A., et al. (2017). Resting-State Magnetoencephalography Reveals Different Patterns of Aberrant Functional Connectivity in Combat-Related Mild Traumatic Brain Injury. *J. Neurotrauma* 34, 1412–1426. doi: 10.1089/neu.2016.4581

Huang, M. X., Huang, C. W., Harrington, D. L., Nichols, S., Robb-Swan, A., Angeles-Quinto, A., et al. (2020). Marked Increases in Resting-State MEG Gamma-Band Activity in Combat-Related Mild Traumatic Brain Injury. *Cereb. Cortex* 30, 283–295. doi: 10.1093/cercor/bhz087

Humphreys, I., Wood, R. L., Phillips, C. J., and Macey, S. (2013). The costs of traumatic brain injury: a literature review. *Clinicoecon. Outcomes Res.* 5, 281–287. doi: 10.2147/CEOR.S44625

Iraji, A., Benson, R. R., Welch, R. D., O'Neil, B. J., Woodard, J. L., Ayaz, S. I., et al. (2015). Resting State Functional Connectivity in Mild Traumatic Brain Injury at the Acute Stage: independent Component and Seed-Based Analyses. *J. Neurotrauma* 32, 1031–1045. doi: 10.1089/neu.2014.3610

Khanmohammadi, S., Laurido-Soto, O., Eisenman, L. N., Kummer, T. T., and Ching, S. N. (2018). Intrinsic network reactivity differentiates levels of consciousness in comatose patients. *Clin. Neurophysiol.* 129, 2296–2305. doi: 10.1016/j.clinph.2018.08.004

Khosravi Fard, E., L Keelor, J., Akbarzadeh Bagheban, A., and W Keith, R. (2016). Comparison of the Rey Auditory Verbal Learning Test (RAVLT) and Digit Test among Typically Achieving and Gifted Students. *Iran. J. Child Neurol.* 10, 26–37.

Kolakowsky-Hayner, S. A. (2011). "Wisconsin Card Sorting Test," in *Encyclopedia of Clinical Neuropsychology*, eds J. S. Kreutzer, J. DeLuca, and B. Caplan (New York, NY: Springer New York), 2719–2720. doi: 10.1007/978-0-387-79948-3_1913

Lakens, D. (2013). Calculating and reporting effect sizes to facilitate cumulative science: a practical primer for t-tests and ANOVAs. *Front. Psychol.* 4:863. doi: 10.3389/FPSYG.2013.00863

Leung, A., Shukla, S., Yang, E., Canlas, B., Kadokana, M., Heald, J., et al. (2016). Diminished supraspinal pain modulation in patients with mild traumatic brain injury. *Mol. Pain* 12, 1–13. doi: 10.1177/1744806916662661

Li, F., Lu, L., Chen, H., Wang, P., Chen, Y. C., Zhang, H., et al. (2019). Disrupted brain functional hub and causal connectivity in acute mild traumatic brain injury. *Aging* 11, 10684–10696. doi: 10.18632/aging.102484

Li, G., Han, X., Gao, L., Tong, W., Xue, Q., Gong, S., et al. (2021). Association of Anxiety and Depressive Symptoms with Memory Function following Traumatic Brain Injury. *Eur. Neurol.* 84, 340–347. doi: 10.1159/000513195

Lutkenhoff, E. S., Wright, M. J., Shrestha, V., Real, C., McArthur, D. L., Buitrago-Blanco, M., et al. (2020). The subcortical basis of outcome and cognitive impairment in TBI: a longitudinal cohort study. *Neurology* 95, e2398–e2408. doi: 10.1212/WNL.0000000000010825

Majdan, M., Plancikova, D., Maas, A., Polinder, S., Feigin, V., Theadom, A., et al. (2017). Years of life lost due to traumatic brain injury in Europe: a cross-sectional analysis of 16 countries. *PLoS Med.* 14:e1002331. doi: 10.1371/journal.pmed.1002331

Manning, K. Y., Llera, A., Dekaban, G. A., Bartha, R., Barreira, C., Brown, A., et al. (2019). Linked MRI signatures of the brain's acute and persistent response to concussion in female varsity rugby players. *NeuroImage Clin.* 21:101627. doi: 10.1016/j.nicl.2018.101627

Marini, A., Zettin, M., and Galetto, V. (2014). Cognitive correlates of narrative impairment in moderate traumatic brain injury. *Neuropsychologia* 64, 282–288. doi: 10.1016/j.neuropsychologia.2014.09.042

McCrimmon, A. W., and Smith, A. D. (2013). Review of the Wechsler Abbreviated Scale of Intelligence, Second Edition (WASI-II). *J. Psychoeduc. Assess.* 31, 337–341. doi: 10.1177/0734282912467756

Moreno-López, L., Sahakian, B. J., Manktelow, A., Menon, D. K., and Stamatakis, E. A. (2016). Depression following traumatic brain injury: a functional connectivity perspective. *Brain Inj.* 30, 1319–1328. doi: 10.1080/02699052.2016.1186839

Munivenkatappa, A., Devi, B. I., Shukla, D. P., and Rajeswaran, J. (2016). Role of the thalamus in natural recovery of cognitive impairment in patients with mild traumatic brain injury. *Brain Inj.* 30, 388–392. doi: 10.3109/02699052.2015.1089599

Nakamura, T., Hillary, F. G., and Biswal, B. B. (2009). Resting Network Plasticity Following Brain Injury. *PLoS One* 4:e8220. doi: 10.1371/journal.pone.0008220

Nordin, L. E., Möller, M. C., Julin, P., Bartfai, A., Hashim, F., and Li, T. Q. (2016). Post mTBI fatigue is associated with abnormal brain functional connectivity. *Sci. Rep.* 6, 1–12. doi: 10.1038/srep21183

Palacios, E. M., Yuh, E. L., Chang, Y.-S., Yue, J. K., Schnyer, D. M., Okonkwo, D. O., et al. (2017). Resting-State Functional Connectivity Alterations Associated with Six-Month Outcomes in Mild Traumatic Brain Injury. *J. Neurotrauma* 34, 1546–1557. doi: 10.1089/neu.2016.4752

Pernet, C. R., Belov, N., Delorme, A., and Zammit, A. (2021). Mindfulness related changes in grey matter: a systematic review and meta-analysis. *Brain Imaging Behav.* 15, 2720–2730. doi: 10.1007/s11682-021-00453-4

Porter, S., Rajwani, Z., Torres, I. J. J., Hyder, A., Panenka, W., Fawcett, D., et al. (2017). Changes in brain-behavior relationships following a 3-month pilot cognitive intervention program for adults with traumatic brain injury. *Heliyon* 3:e00373. doi: 10.1016/j.heliyon.2017.e00373

Rajesh, A., Cooke, G. E., Monti, J. M., Jahn, A., Daugherty, A. M., Cohen, N. J., et al. (2017). Differences in Brain Architecture in Remote Mild Traumatic Brain Injury. *J. Neurotrauma* 34, 3280–3287. doi: 10.1089/neu.2017.5047

Robb Swan, A., Nichols, S., Drake, A., Angeles, A., Diwakar, M., Song, T., et al. (2015). Magnetoencephalography Slow-Wave Detection in Patients with Mild Traumatic Brain Injury and Ongoing Symptoms Correlated with Long-Term Neuropsychological Outcome. *J. Neurotrauma* 32, 1510–1521. doi: 10.1089/neu.2014.3654

Roy, A., Bernier, R. A., Wang, J., Benson, M., French, J. J., Good, D. C., et al. (2017). The evolution of cost-efficiency in neural networks during recovery

from traumatic brain injury. *PLoS One* 12:e0170541. doi: 10.1371/journal.pone.0170541

Sadeghi, S., Mier, D., Gerchen, M. F., Schmidt, S. N. L., and Hass, J. (2020). Dynamic Causal Modeling for fMRI With Wilson-Cowan-Based Neuronal Equations. *Front. Neurosci.* 14:593867. doi: 10.3389/fnins.2020.593867

Sargénius, H. L., Bylsma, F. W., Lydersen, S., and Hestad, K. (2017). Visual-Constructional Ability in Individuals with Severe Obesity: rey Complex Figure Test Accuracy and the Q-Score. *Front. Psychol.* 8:1629. doi: 10.3389/fpsyg.2017.01629

Schwering, S. C., and MacDonald, M. C. (2020). Verbal Working Memory as Emergent from Language Comprehension and Production. *Front. Hum. Neurosci.* 14:68. doi: 10.3389/fnhum.2020.00068

Shumskaya, E., van Gerven, M. A. J., Norris, D. G., Vos, P. E., and Kessels, R. P. C. (2017). Abnormal connectivity in the sensorimotor network predicts attention deficits in traumatic brain injury. *Exp. Brain Res.* 235, 799–807. doi: 10.1007/s00221-016-4841-z

Sours, C., George, E. O., Zhuo, J., Roys, S., and Gullapalli, R. P. (2015). Hyper-connectivity of the thalamus during early stages following mild traumatic brain injury. *Brain Imaging Behav.* 9, 550–563. doi: 10.1007/s11682-015-9424-2

Sours, C., Raghavan, P., Medina, A. E., Roys, S., Jiang, L., Zhuo, J., et al. (2017). Structural and Functional Integrity of the Intraparietal Sulcus in Moderate and Severe Traumatic Brain Injury. *J. Neurotrauma* 34, 1473–1481. doi: 10.1089/neu.2016.4570

Stephan, K. E., and Friston, K. J. (2010). Analyzing effective connectivity with fMRI. *Wiley Interdiscip. Rev. Cogn. Sci.* 1, 446–459. doi: 10.1002/wcs.58.Analyzing

Stephan, K. E., Penny, W. D., Moran, R. J., den Ouden, H. E. M., Daunizeau, J., and Friston, K. J. (2010). Ten simple rules for dynamic causal modeling. *Neuroimage* 49, 3099–3109. doi: 10.1016/j.neuroimage.2009.11.015

Tang, L., Ge, Y., Sodickson, D. K., Miles, L., Zhou, Y., Reaume, J., et al. (2011). Thalamic resting-state functional networks: disruption in patients with mild traumatic brain injury. *Radiology* 260, 831–840. doi: 10.1148/radiol.11110014

van der Horn, H. J., Liemburg, E. J., Scheenen, M. E., de Koning, M. E., Spikman, J. M., and van der Naalt, J. (2016). Post-concussive complaints after mild traumatic brain injury associated with altered brain networks during working memory performance. *Brain Imaging Behav.* 10, 1243–1253. doi: 10.1007/s11682-015-9489-y

Vergara, V. M., Mayer, A. R., Kiehl, K. A., and Calhoun, V. D. (2018). Dynamic functional network connectivity discriminates mild traumatic brain injury through machine learning. *NeuroImage Clin.* 19, 30–37. doi: 10.1016/j.nicl.2018.03.017

Wang, X., Xu, M., Song, Y., Li, X., Zhen, Z., Yanga, Z., et al. (2014). The network property of the thalamus in the default mode network is correlated with trait mindfulness. *Neuroscience* 278, 291–301. doi: 10.1016/j.neuroscience.2014.08.006

Whitfield-Gabrieli, S., and Nieto-Castanon, A. (2012). Conn: a Functional Connectivity Toolbox for Correlated and Anticorrelated Brain Networks. *Brain Connect.* 2, 125–141. doi: 10.1089/brain.2012.0073

Wooten, D. W., Ortiz-Terán, L., Zubcevik, N., Zhang, X., Huang, C., Sepulcre, J., et al. (2019). Multi-Modal Signatures of Tau Pathology, Neuronal Fiber Integrity, and Functional Connectivity in Traumatic Brain Injury. *J. Neurotrauma* 36, 3233–3243. doi: 10.1089/neu.2018.6178

Xiong, K. L., Zhang, J. N., Zhang, Y. L., Zhang, Y. L., Chen, H., and Qiu, M. G. (2016). Brain functional connectivity and cognition in mild traumatic brain injury. *Neuroradiology* 58, 733–739. doi: 10.1007/s00234-016-1675-0

Conflict of Interest: The authors declare that the research was conducted in the absence of any commercial or financial relationships that could be construed as a potential conflict of interest.

Publisher's Note: All claims expressed in this article are solely those of the authors and do not necessarily represent those of their affiliated organizations, or those of the publisher, the editors and the reviewers. Any product that may be evaluated in this article, or claim that may be made by its manufacturer, is not guaranteed or endorsed by the publisher.

frontiers | Frontiers in Neuroscience

ORIGINAL RESEARCH
published: 25 April 2022
doi: 10.3389/fnins.2022.861402

Tracing Evolving Networks Using Tensor Factorizations vs. ICA-Based Approaches

Evrim Acar[1]*, *Marie Roald*[1,2], *Khondoker M. Hossain*[3], *Vince D. Calhoun*[4] and *Tülay Adali*[3]

[1] Simula Metropolitan Center for Digital Engineering, Oslo, Norway, [2] Oslo Metropolitan University, Oslo, Norway, [3] Department of Computer Science and Electrical Engineering, University of Maryland Baltimore County, Baltimore, MD, United States, [4] Department of Psychology, Georgia State University, Atlanta, GA, United States

Analysis of time-evolving data is crucial to understand the functioning of dynamic systems such as the brain. For instance, analysis of functional magnetic resonance imaging (fMRI) data collected during a task may reveal spatial regions of interest, and how they evolve during the task. However, capturing underlying spatial patterns as well as their change in time is challenging. The traditional approach in fMRI data analysis is to assume that underlying spatial regions of interest are static. In this article, using fractional amplitude of low-frequency fluctuations (fALFF) as an effective way to summarize the variability in fMRI data collected during a task, we arrange time-evolving fMRI data as a *subjects* by *voxels* by *time windows* tensor, and analyze the tensor using a tensor factorization-based approach called a PARAFAC2 model to reveal spatial dynamics. The PARAFAC2 model jointly analyzes data from multiple time windows revealing subject-mode patterns, evolving spatial regions (also referred to as networks) and temporal patterns. We compare the PARAFAC2 model with matrix factorization-based approaches relying on independent components, namely, joint independent component analysis (ICA) and independent vector analysis (IVA), commonly used in neuroimaging data analysis. We assess the performance of the methods in terms of capturing evolving networks through extensive numerical experiments demonstrating their modeling assumptions. In particular, we show that (i) PARAFAC2 provides a compact representation in all modes, i.e., *subjects*, *time*, and *voxels*, revealing temporal patterns as well as evolving spatial networks, (ii) joint ICA is as effective as PARAFAC2 in terms of revealing evolving networks but does not reveal temporal patterns, (iii) IVA's performance depends on sample size, data distribution and covariance structure of underlying networks. When these assumptions are satisfied, IVA is as accurate as the other methods, (iv) when subject-mode patterns differ from one time window to another, IVA is the most accurate. Furthermore, we analyze real fMRI data collected during a sensory motor task, and demonstrate that a component indicating statistically significant group difference between patients with schizophrenia and healthy controls is captured, which includes primary and secondary motor regions, cerebellum, and temporal lobe, revealing a meaningful spatial map and its temporal change.

Keywords: PARAFAC2, independent vector analysis (IVA), independent component analysis (ICA), tensor factorizations, spatial dynamics, evolving networks, time-evolving data

OPEN ACCESS

Edited by:
Xiaopeng Song,
Harvard Medical School,
United States

Reviewed by:
Guoqiang Hu,
Dalian University of Technology, China
Nizhuan Wang,
ShanghaiTech University, China
Yongjie Zhu,
University of Helsinki, Finland

***Correspondence:**
Evrim Acar
evrim@simula.no

Specialty section:
This article was submitted to Brain Imaging Methods, a section of the journal Frontiers in Neuroscience

Received: *24 January 2022*
Accepted: *07 March 2022*
Published: *25 April 2022*

Citation:
Acar E, Roald M, Hossain KM, Calhoun VD and Adali T (2022) Tracing Evolving Networks Using Tensor Factorizations vs. ICA-Based Approaches. Front. Neurosci. 16:861402. doi: 10.3389/fnins.2022.861402

1. INTRODUCTION

Time-evolving data analysis is crucial in terms of understanding complex dynamic systems such as the brain. Various neuroimaging techniques such as functional magnetic resonance imaging (fMRI) and electroencephalography (EEG) are used to collect temporal data in order to understand how the brain functions. The analysis of such temporal data may capture the underlying patterns as well as their temporal evolution revealing the underlying mechanisms, and how those differ across different groups of people, e.g., healthy controls vs. patients. For instance, the relation between dynamic functional connectivity and various disorders such as schizophrenia, autism, and Alzheimer's disease has been studied with the goal of finding biomarkers (Preti et al., 2017).

Dynamic functional connectivity (also referred to as time-varying functional connectivity) has been an important topic of research to study brain function (Chang and Glover, 2010; Hutchison et al., 2013a; Calhoun et al., 2014; Preti et al., 2017; Lurie et al., 2020). The most commonly used approach for dynamic functional connectivity analysis is the sliding window-based method (Sakoglu et al., 2010), where correlations between time courses corresponding to different spatial regions of interest are used to construct a connectivity matrix for each time window. Functional connectivity patterns from each window are then analyzed using various methods such as graph mining to understand the change in time. Often there is the simplifying assumption that spatial regions of interest are static, and it is only the connectivity between those static spatial regions that changes in time. On the other hand, it has been previously shown that there are changes in spatial regions as well even in the resting state (during awake as well as anesthetized states; Kiviniemi et al., 2011; Hutchison et al., 2013b; Ma et al., 2014).

Our focus here is on the analysis of fMRI signals collected during a task with the goal of revealing spatial regions of interest as well as the temporal evolution of those regions (i.e., spatial dynamics; Iraji et al., 2020). Low-rank data approximations [matrix factorizations as well as tensor factorizations (Acar and Yener, 2009; Kolda and Bader, 2009; Comon, 2014), i.e., extensions of matrix factorizations to higher-order data] have proved useful in terms of revealing the underlying patterns in complex data in many fields including neuroscience, e.g., revealing spatial regions of interest/networks (McKeown et al., 1998; Bai et al., 2017). Recently, various matrix factorization-based approaches including independent component analysis (ICA) and principal component analysis (PCA) have been studied in terms of tracking functional connectivity by arranging magnetoencephalography (MEG) signals as a *connectivity* by *time* matrix and factorizing the matrix into temporal patterns and connectivity patterns revealing brain networks (Tabbal et al., 2021) with the assumption that networks relying on predefined regions of interests stay the same in time. However, capturing patterns evolving in time from dynamic data such as evolving networks, evolving spatial regions or evolving communities remains a challenging data mining problem (Rossetti and Cazabet, 2018). Previously, ICA (Comon, 1994) was used together with a sliding time window-based approach to study the changes in spatial maps, focusing on the changes within default mode networks (DMN) in time in the resting state (Kiviniemi et al., 2011). Similarly, Ma et al. (2014) used independent vector analysis (IVA) (Kim et al., 2006; Anderson et al., 2012), i.e., an extension of ICA to multiple datasets, to find time-varying brain networks during the resting state. These studies focus on resting-state dynamics, and also are limited due to either the focus on a single network (Kiviniemi et al., 2011), or not revealing compact patterns in the *time* mode explicitly (Kiviniemi et al., 2011; Ma et al., 2014).

As higher-order tensors are natural data representations for temporal data, with one of the modes representing time, in this article, through the use of fractional amplitude of low-frequency fluctuations (fALFF), we arrange fMRI data collected during a task as a third-order tensor with modes: *subjects*, *voxels*, and *time windows*, and use a tensor factorization method called the PARAFAC2 model (Harshman, 1972; Kiers et al., 1999), which compactly summarizes the dynamic data by revealing the underlying networks (spatial regions of interest), their change in time as well as temporal patterns (see **Figure 1**). More specifically, we use the PARAFAC2 model to jointly factorize multiple matrices in the form of *subjects* by *voxels* matrices, $\mathbf{X}_k$ for $k = 1, ..., K$, corresponding to different time windows, coupled in the *subjects* mode, where K denotes the number of time windows. The PARAFAC2 model summarizes the data using low-rank patterns in the *subjects*, *voxels*, and *time windows* modes, and the patterns in the *voxels* mode change from one window to another revealing the evolving patterns. Patterns in the *time windows* mode correspond to temporal patterns, and patterns in the *subjects* mode can be used to explore differences between healthy controls and patients, or for patient stratification.

While the use of tensor factorizations in neuroimaging signal analysis has been widespread (Cong et al., 2015; Hunyadi et al., 2017), to the best of our knowledge, their potential for revealing spatial dynamics has not been explored. Neuroimaging data, e.g., EEG (Miwakeichi et al., 2004), fMRI (Andersen and Rayens, 2004), MEG (Becker et al., 2012), local field potential (LFP) (Geddes et al., 2020) signals, can be represented as higher-order tensors. Tensor methods can reveal interpretable patterns from such complex data disentangling different sources as a result of their uniqueness properties (Kolda and Bader, 2009), avoiding additional constraints on the underlying patterns such as orthogonality or statistical independence. For instance, multi-channel EEG signals have been arranged as a *time* by *frequency* by *channels* tensor, and analyzed using the CANDECOMP/PARAFAC (CP) (Hitchcock, 1927; Carroll and Chang, 1970; Harshman, 1970) tensor model revealing spatial, spectral and temporal signatures of brain activities (Miwakeichi et al., 2004; Acar et al., 2007; De Vos et al., 2007). In the case of multiple subjects/conditions, the CP model has similarly shown promising performance in terms of revealing the underlying patterns (Möcks, 1988; Mørup et al., 2006). The higher-order structure of fMRI signals has also been studied using tensor methods, e.g., by arranging fMRI signals as a *trials* by *voxels* by *time* tensor, and analyzing the tensor using the CP model (Andersen and Rayens, 2004), or analyzing multi-subject fMRI data in the form of a *subjects*

by *voxels* by *time* tensor using tensor probabilistic independent component analysis (PICA) (Beckmann and Smith, 2005). Such CP-based models, for instance when analyzing multi-subject fMRI data, extract subject-mode patterns, spatial patterns as well as temporal patterns with the modeling assumption that subject-mode patterns and spatial patterns are the same in all time slices (up to a scaling) (Beckmann and Smith, 2005); therefore, not accounting for spatial dynamics. While brain images are unfolded and treated as vectors of voxels resulting in third-order tensors in these studies, higher-order fMRI data as fourth and fifth-order tensors have also been studied by preserving the spatial structure (Chatzichristos et al., 2019). Recently, the PARAFAC2 model, which is more flexible than the CP model, has been used to study functional connectivity using multi-subject fMRI signals by letting the temporal patterns change across subjects (Madsen et al., 2017; Helwig and Snodgress, 2019) assuming common (and static) spatial patterns for all subjects. In the context of dynamic functional connectivity, Zhu et al. (2019, 2020) have arranged MEG signals as a *time* by *frequency* by *connectivity* tensor, where connectivities rely on predefined anatomical regions, and analyzed the tensor using a CP model to reveal connectivity factors showing functional networks. However, none of these studies accounts for evolving spatial patterns or evolving networks but rather all rely on static spatial patterns/networks.

This article is an extended version of our preliminary study (Roald et al., 2020), where we demonstrated the promise of the PARAFAC2 model in terms of revealing evolving networks using simulations and real task fMRI data analysis. In this work, we provide an extensive study comparing the performance of the PARAFAC2 model with ICA-based approaches, in particular, joint ICA (Calhoun et al., 2006) and IVA, in terms of capturing evolving networks using different simulation set-ups demonstrating the effect of sample size, similar or overlapping networks, and differences in subject-mode patterns across time windows. Both joint ICA and IVA are extensions of ICA to multiple datasets but rely on different modeling assumptions. Their use in the comparison is attractive as IVA is less constrained than PARAFAC2 by letting subject-mode patterns change from one time window to another and has been previously used for capturing spatial dynamics (Ma et al., 2014) while joint ICA is similar to PARAFAC2 in the way it models the subject-mode patterns but differs in terms of constraints imposed on the evolving networks. We also use our observations from simulations to guide our analysis of multi-site multi-subject fMRI data (Gollub et al., 2013) collected during a sensory motor task. While our preliminary results (Roald et al., 2020) focused on the analysis of a subset of the data from several sites using a PARAFAC2 model, in this article, we use the data from all sites, and study the application of all three methods to this task-related fMRI data, and compare their performances. Our experiments demonstrate that (i) PARAFAC2 provides a compact representation revealing temporal patterns and evolving spatial networks accurately, (ii) joint ICA is as effective as PARAFAC2 in terms of revealing evolving networks but does not reveal temporal patterns explicitly, (iii) IVA's performance depends on sample size. We also show its assumptions on data distribution and covariance structure of underlying networks in the **Supplementary Material**. When these assumptions are fulfilled, IVA is as accurate as the other methods in terms of capturing underlying networks, and in addition, (iv) IVA can reveal evolving networks accurately when subject-mode patterns differ across time windows, (v) in real fMRI data analysis, a meaningful component indicating statistically significant group difference between patients with schizophrenia and healthy controls is captured by all methods revealing a spatial network of potential interest as well as its change in time. Guided by the simulations, we discuss the accuracy of estimated components and their significance in terms of group difference.

2. MATERIALS AND METHODS

2.1. Background

We first briefly discuss modeling assumptions of the three methods we focus on, namely, PARAFAC2, IVA, and joint ICA.

2.1.1. PARAFAC2

Given a third order tensor, $\mathcal{X} \in \mathbb{R}^{I \times J \times K}$, the PARAFAC2 model represents each slice, $\mathrm{X}_k \in \mathbb{R}^{I \times J}$, as follows:

$$\mathrm{X}_k \approx \mathrm{A}\mathrm{diag}(\mathrm{c}(k,:))\mathrm{B}_k^{\mathsf{T}}, \tag{1}$$

where $\mathrm{A} \in \mathbb{R}^{I \times R}$, $\mathrm{B}_k \in \mathbb{R}^{J \times R}$, R is the number of components, and $\mathrm{diag}(\mathrm{c}(k,:))$ is a diagonal matrix with entries of the kth row of $\mathrm{C} \in \mathbb{R}^{K \times R}$ on the diagonal. Additionally, B_k-matrices satisfy the constant cross product constraint, $\mathrm{B}_{k_1}^{\mathsf{T}}\mathrm{B}_{k_1} = \mathrm{B}_{k_2}^{\mathsf{T}}\mathrm{B}_{k_2}$ for all $1 \leq k_1, k_2 \leq K$. The PARAFAC2 model reveals unique factors (up to scaling and permutation ambiguities) as long as there are enough slices (K) (see Kiers et al., 1999 for a detailed discussion on uniqueness conditions of PARAFAC2). The traditional algorithmic approach to fit the model is by solving the following optimization problem using an alternating least squares (ALS)—based algorithm (Kiers et al., 1999):

$$\min_{\mathrm{A},\{\mathrm{B}_k\}_{k\leq K},\mathrm{C}} \sum_{k=1}^{K} \left\| \mathrm{X}_k - \mathrm{A}\mathrm{diag}(\mathrm{c}(k,:))\mathrm{B}_k^{\mathsf{T}} \right\|_F^2, \tag{2}$$

where $\mathrm{B}_k = \mathrm{P}_k\mathrm{B}$, and $\mathrm{P}_k^{\mathsf{T}}\mathrm{P}_k = \mathrm{I}$ so that the constant cross product constraint is implicitly satisfied; $\mathrm{I} \in \mathbb{R}^{R \times R}$ denotes the identity matrix, $\mathrm{B} \in \mathbb{R}^{R \times R}$ is common for all B_k, $k = 1, ..., K$, and $\| \cdot \|_F$ denotes the Frobenius norm. Note that there may be an additional sign ambiguity in PARAFAC2, where each entry in $\mathrm{diag}(\mathrm{c}(k,:))$ may flip sign arbitrarily (Harshman, 1972), and one possible solution to fix that ambiguity is to impose non-negativity constraints on matrix C (Harshman, 1972; Kiers et al., 1999).

If X_ks correspond to *subjects* by *voxels* matrices at different time windows, PARAFAC2 reveals subject-mode patterns (A) that are constant in time, and time-mode patterns (C) shared between subjects. The number of components R corresponds to the number of patterns. The PARAFAC2 model also reveals spatial networks (B_k) that are shared between subjects but may evolve with time (as shown in **Figure 1**). This is a more flexible modeling approach than the most commonly used CP tensor

model, which represents each slice $\mathbf{X}_k \in \mathbb{R}^{I\times J}$ of a third-order tensor, $\mathcal{X} \in \mathbb{R}^{I\times J\times K}$, as follows:

$$\mathbf{X}_k \approx \mathbf{A}\text{diag}(\mathbf{c}(k,:))\mathbf{B}^{\mathsf{T}}, \tag{3}$$

where $\mathbf{B} \in \mathbb{R}^{J\times R}$ representing spatial networks are assumed to be the same (more precisely, they can only change up to a scalar) across different time windows. We have previously demonstrated that the CP model fails to reveal underlying networks accurately when analyzing data generated using evolving network patterns while PARAFAC2 achieves to reveal the underlying networks as well as their change in time (Roald et al., 2020). Similar to CP, tensor PICA (Beckmann and Smith, 2005) also relies on (3), with the additional constraint that columns of B, e.g., spatial networks, are statistically independent. Therefore, both CP and PICA assume that spatial networks are the same across time slices, i.e., they do not account for evolving spatial networks as the PARAFAC2 model does by introducing $\mathbf{B}_k$s that allow for spatial networks to change more than a scalar factor.

Determining the number of components in tensor factorizations is a challenging task. There are various diagnostic approaches that can potentially be used to determine the number of components for PARAFAC2 such as the core consistency diagnostic (Kamstrup-Nielsen et al., 2012), and split-half analysis (Harshman and De Sarbo, 1984); both of which are also used to determine the number of components when fitting a CP model. However, a good practice is to use such diagnostic methods while taking into account also the factors and residuals (Bro and Kiers, 2003; Kamstrup-Nielsen et al., 2012). Note that uniqueness conditions of the PARAFAC2 model may also limit the number of components. For instance, one of the uniqueness conditions indicates that $K \geq \frac{R(R+1)(R+2)(R+3)}{24}$, where K and R denote the number of slices and components, respectively. This is a sufficient (not necessary) condition for the uniqueness of the model, and other studies have reported uniqueness using much fewer slices in practice (Kiers et al., 1999).

While the use of PARAFAC2 is not as widespread as the CP model, it has shown promising performance in applications from different disciplines, e.g., chemometrics (Bro et al., 1999), text mining (Chew et al., 2007), electronic health record analysis (Afshar et al., 2018; Yin et al., 2020), and neuroimaging data analysis (Madsen et al., 2017; Helwig and Snodgress, 2019). The use of PARAFAC2 in time-evolving data analysis, on the other hand, has been limited, where the model is used to analyze temporal data by letting the patterns change across subjects (Timmerman and Kiers, 2003; Madsen et al., 2017), or across channels (Weis et al., 2010) but not revealing dynamic networks.

2.1.2. Independent Vector Analysis (IVA)

Similar to PARAFAC2, IVA also jointly analyzes multiple matrices. However, unlike PARAFAC2, IVA (Kim et al., 2006; Anderson et al., 2012; Adali et al., 2014) extracts statistically independent components (sources) from each matrix while taking into account the dependence across the datasets. In many applications using ICA and IVA, reducing the dimensionality of the observed dataset prior to analysis, i.e., identifying a signal subspace where to perform the decomposition enables better generalization performance decreasing the effect of noise and artifacts, also improving stability of the decompositions (see, e.g., Li et al., 2007). This is typically achieved using a PCA step, where the dimensionality of the observation matrix $\mathbf{X} \in \mathbb{R}^{I\times J}$ is reduced from $\mathbf{X} \in \mathbb{R}^{I\times J}$ to $\bar{\mathbf{X}} \in \mathbb{R}^{R\times J}$ where $R \leq I$.

Given K dimension-reduced observation matrices $\bar{\mathbf{X}}_k \in \mathbb{R}^{R\times J}$, for $k = 1, ..., K$, IVA models each dataset as a linear mixture of R independent sources:

$$\bar{\mathbf{X}}_k = \bar{\mathbf{A}}_k \mathbf{S}_k, \tag{4}$$

where $\bar{\mathbf{A}}_k \in \mathbb{R}^{R\times R}$ corresponds to the nonsingular mixing matrix, and $\mathbf{S}_k \in \mathbb{R}^{R\times J}$ denotes the samples of independent sources for the kth matrix[1]. Corresponding components in $\mathbf{S}_k$ matrices form, the source component vectors (SCV), which are shown as matrices assuming a given set of observations, in **Figure 1**. IVA estimates the demixing matrices $\mathbf{W}_k$ to recover source estimates through $\mathbf{Y}_k = \mathbf{W}_k\bar{\mathbf{X}}_k$ by maximizing independence across the SCVs through mutual information minimization (Adali et al., 2014), which can be shown to be equivalent to maximum likelihood (ML) estimation. The estimated mixing matrices are then back reconstructed in the original dimensionality as explained in Jia et al. (2021), which implies that we effectively have the generative model shown in **Figure 1**. Thus, here, we show the IVA and joint ICA models in the original dimensionality to allow easier comparison with the PARAFAC2 model, which does not involve such a dimension reduction stage.

By modeling the multivariate probability density function (pdf) of an SCV, IVA takes the statistical dependence across the datasets into account, and depending on the chosen pdf, either, only second-order statistics (SOS), or all-order statistical information can be taken into account. In this work, we use IVA-L-SOS where a full multivariate Laplacian pdf model, also computing the scatter matrices is used (Bhinge et al., 2019b), hence taking all-order statistics into account. As fMRI sources tend to be super-Gaussian in nature (Correa et al., 2007; Calhoun et al., 2013), IVA-L-SOS provides a good match to their properties.

It can be shown that IVA has very general conditions for the identifiability of the model. For the case we consider where sample dependence is not taken into account and all-order statistics are used, the model is uniquely identifiable as long as the covariance matrices $\mathbf{R}_l$ and $\mathbf{R}_m$ of any two SCVs, l and m, are multivariate Gaussian and do not satisfy $\mathbf{R}_l = \mathbf{D}\mathbf{R}_m\mathbf{D}$ where D is any full rank diagonal matrix (Anderson et al., 2012; Adali et al., 2014). When only a subset of Gaussian components satisfy the equality, a subspace of their mixtures is identified and not the specific Gaussian components.

When $\mathbf{X}_k$ matrices represent *subjects* by *voxels* matrices at different time windows, IVA captures subject-mode patterns ($\mathbf{A}_k$) for each time window, and spatial components/networks, $\mathbf{S}_k$, changing from one window to another. Rows of $\mathbf{S}_k$s are related across the time windows through SCVs in such a way that mutual information within each SCV, i.e., statistical

[1]Both ICA and IVA are traditionally introduced using random variable/vector models. Here to keep the discussion simple across the three models, we use observations for all three models.

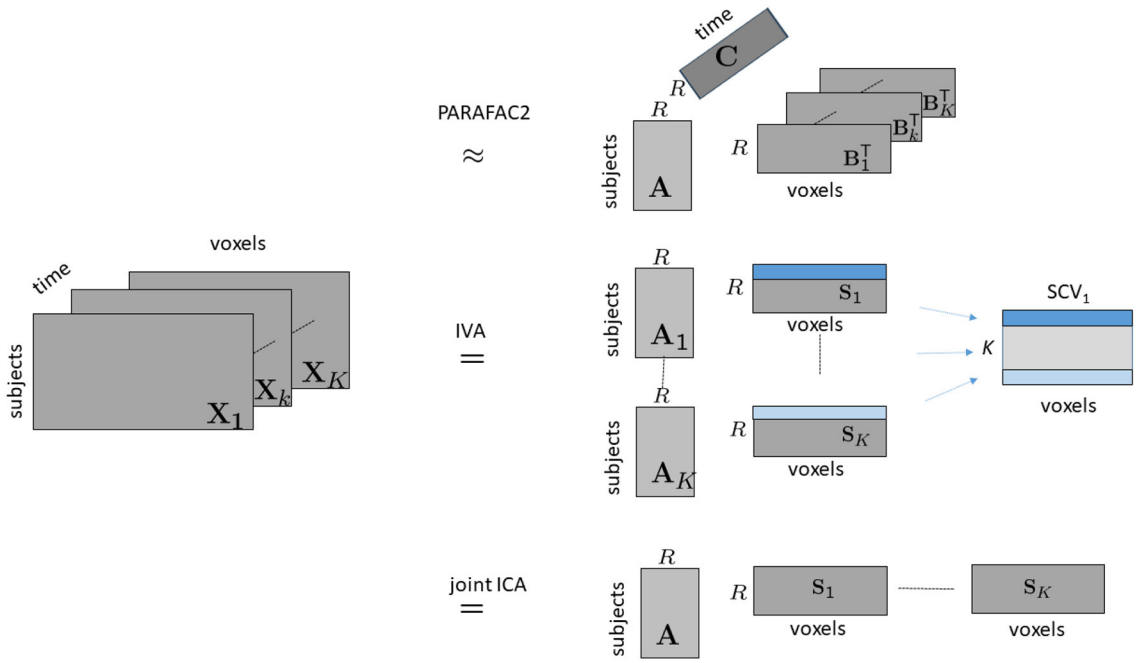

FIGURE 1 | Illustration of modeling time-evolving data in the form of a *subjects* by *voxels* by *time* tensor using PARAFAC2, IVA and joint ICA. Following the notation in the literature on ICA/IVA, we use S_k, for $k = 1, ..., K$, to denote the factor matrix in the *voxels* mode for joint ICA and IVA, where $S_k = B_k^T$.

dependence, is maximized. Hence, the desire to capture the relationship among components in different S_ks makes IVA another candidate approach for capturing evolving networks. IVA has been previously used to study dynamics in multi-subject resting-state fMRI data (Ma et al., 2014; Bhinge et al., 2019a,b; Long et al., 2021). For instance, Ma et al. (2014) arranges the data in a specific time window from a subject as a matrix in the form of *time samples* by *voxels*. Subject-specific temporal and spatial patterns are identified on a per window basis. This allows study of both temporal and spatial patterns of dynamics, however, the complexity of the model grows with the number of time windows, which negatively affects the performance of IVA (Long et al., 2020). Our approach in this article makes use of the synchrony across subjects in the task, and decreases the dimensionality of the problem by collapsing the time dimension through the use of fALFF as features for each time window (see section 2.2.4 for more details). As such, this provides an attractive formulation for dynamic analysis using IVA (Hossain et al., 2022).

2.1.3. Joint Independent Component Analysis

Another approach to jointly analyze multiple matrices, $X_k \in \mathbb{R}^{I \times J}$, for $k = 1, ..., K$, is to concatenate different time windows, and then analyze the constructed matrix using an ICA model, which is called the joint ICA (Calhoun et al., 2006) method. We again write the model using dimension-reduced observations matrices $\bar{X}_k \in \mathbb{R}^{R \times J}$, such that we have

$$[\bar{X}_1 \quad \bar{X}_2 \ldots \bar{X}_K] = \bar{A}S, \tag{5}$$

where $\bar{A} \in \mathbb{R}^{R \times R}$ corresponds to the non-singular mixing matrix that is common for all time windows, and $S \in \mathbb{R}^{R \times JK}$ represents the source signals corresponding to the spatial networks concatenated in time. Source signals, i.e., rows of S, are assumed to be statistically independent. ICA reveals unique components and mixing matrices, up to scaling and permutation ambiguities (Comon, 1994). When only non-Gaussianity is used as signal diversity ignoring sample dependence, any signal except multiple Gaussians can be identified with the model (Cardoso, 2001; Adali et al., 2014). Among various algorithmic approaches, in our experiments, we use an ICA algorithm based on entropy bound minimization (ICA-EBM), which uses a flexible pdf model, and hence can effectively model sources from a rich class of distributions (Li and Adali, 2010).

Again in **Figure 1**, we show the model for joint ICA following back-reconstruction where X_k and A are brought to their original dimensionality following ICA. Then, with X_k matrices corresponding to *subjects* by *voxels* matrices at different time windows, joint ICA reveals subject-mode patterns, A, shared by all time windows, and different spatial components/networks for each time window, i.e., $S = [S_1 \; S_2 \ldots S_K]$.

For ICA and IVA, a common approach for determining the number of components is the use of information theoretic criteria (ITC) such as minimum description length based on a PCA formulation (Wax and Kailath, 1985). ITC are based on a likelihood formulation based on the multivariate Gaussian assumption for the mixtures (a good match to the ICA/IVA mixing model). Since fMRI data exhibits sample correlation,

usually a corrected version of the criteria are commonly employed as in Fu et al. (2014).

2.1.4. PARAFAC2 vs. IVA vs. Joint ICA

Here we recap the modeling assumptions of different methods, specifically focusing on our application of interest, where X_k matrices correspond to *subjects* by *voxels* matrices at different time windows k.

- *Subject-mode patterns* (i.e., A_k): Joint ICA extracts patterns that are the same in each time window, i.e., $\mathrm{A}_k = \mathrm{A}$, for $k = 1, ..., K$; PARAFAC2 reveals patterns that are the same up to a scaling in each time window, i.e., $\mathrm{A}_k = \mathrm{A}\mathrm{diag}(\mathrm{c}(k, :))$ while IVA is the most flexible one with no constraints on A_ks.
- *Spatial components* (i.e., $\mathrm{B}_k^{\mathsf{T}}$ or S_k): In IVA, S_ks are more constrained than PARAFAC2 and joint ICA. In the IVA model, in each S_k, the components are statistically independent, and across different S_ks, the components are related through the SCVs; in PARAFAC2, there is the constant cross product constraint, $\mathrm{B}_{k_1}^{\mathsf{T}}\mathrm{B}_{k_1} = \mathrm{B}_{k_2}^{\mathsf{T}}\mathrm{B}_{k_2}$ for all $1 \leq k_1, k_2 \leq K$, while in joint ICA, there is the assumption of statistically independent components, and no relation between different S_ks except that the sources in corresponding rows are all assumed to come from the same distribution.
- *Temporal components* (i.e., C): Among the three methods, the PARAFAC2 model is the most compact and reveals *temporal patterns* in addition to subject-mode and voxel-mode patterns while joint ICA and IVA only reveal patterns in *subjects* and *voxels* modes. In joint ICA and IVA, further postprocessing, possibly with additional assumptions, is needed to reveal temporal patterns.

2.2. Experiments

By using both real and simulated time-evolving data, we demonstrate the performance of PARAFAC2, IVA, and joint ICA in terms of capturing evolving networks. In simulations, we assess the performance of the methods in terms of how well they reveal the underlying ground truth. In the analysis of multi-subject fMRI data collected during a sensory motor task from patients with schizophrenia and healthy controls, the performance of the methods is assessed in terms of revealing meaningful components indicating statistically significant group differences.

2.2.1. Implementation Details

All experiments were performed using MATLAB. Both simulated and real data are in the form of third-order tensors consisting of K frontal slices. The PARAFAC2 model is fit using the implementation in the PLS_Toolbox 8.6.2 (by Eigenvector Research Inc., WA, USA). In order to handle the sign ambiguity in PARAFAC2, non-negativity constraint is imposed in the *time windows* mode. For IVA, we first performed rank reduction on each frontal slice using the true (or given) number of components, and then used IVA-L-SOS (Bhinge et al., 2019b) to find the demixing matrices. For joint ICA, the third-order tensor is unfolded in the first mode. Following rank reduction of the unfolded data using the given number of components, an ICA algorithm based on entropy bound minimization (ICA-EBM)[2] (Li and Adali, 2010) is used. We fit every method using multiple random initializations, and use the solution corresponding to the minimum cost value.

2.2.2. Performance Evaluation

We assess the performance of the methods using the following approaches:

- *Factor similarity score*: In order to quantify how well the spatial components extracted by the methods match with ground truth components, we use a similarity score defined as:

$$\mathrm{Sim}_{\mathrm{B}} = \frac{1}{K}\sum_{k=1}^{K}\frac{1}{R}\sum_{r=1}^{R}\mathrm{B}_k(:, r)^{\mathsf{T}}\hat{\mathrm{B}}_k(:, r), \tag{6}$$

  where $\mathrm{B}_k(:, r)$ and $\hat{\mathrm{B}}_k(:, r)$ denote the true and estimated rth column of the factor matrix in the *voxels* mode corresponding to the kth time window, respectively (after fixing the permutation and scaling ambiguity in the methods). Similarly, similarity scores for the first and third mode are computed as follows:

$$\mathrm{Sim}_{\mathrm{A}} = \frac{1}{R}\sum_{r=1}^{R}\mathrm{A}(:, r)^{\mathsf{T}}\hat{\mathrm{A}}(:, r), \quad \mathrm{Sim}_{\mathrm{C}} = \frac{1}{R}\sum_{r=1}^{R}\mathrm{C}(:, r)^{\mathsf{T}}\hat{\mathrm{C}}(:, r) \tag{7}$$

  Due to different modeling assumptions of each method, all methods can only be compared in terms of $\mathrm{Sim}_{\mathrm{B}}$. In addition, we report $\mathrm{Sim}_{\mathrm{A}}$ and $\mathrm{Sim}_{\mathrm{C}}$ for PARAFAC2, and $\mathrm{Sim}_{\mathrm{A}}$ for joint ICA.
- *Two-sample t-test*: Using two-sample t-test on each column of the factor matrix corresponding to the *subjects* mode, i.e., A in PARAFAC2 and joint ICA, and A_k, for $k = 1, ..., K$ in IVA, we identify the statistically significant subject-mode factor vectors in terms of revealing group differences, allowing for unequal variances for healthy and patient groups.

2.2.3. Simulated Data and Experimental Set-Up

We simulate time-evolving data arranged as a third-order tensor $\mathcal{X} \in \mathbb{R}^{I \times J \times K}$, with K time slices, with the following underlying structure (using $R = 3$ components):

- *Subject-mode patterns*, i.e., $\mathrm{A} \in \mathbb{R}^{I \times R}$, are generated such that one column of A discriminates between two subject groups each containing $\frac{I}{2}$ subjects. Entries corresponding to subjects from different groups are sampled randomly from uniform distributions with different means. Other columns have entries randomly sampled from the standard normal distribution. All columns are normalized to unit norm. The same A with $I = 250$ is used in the experiments (**Figure 2A**), where the two-sample t-test gives the following p-values: 0, 0.88, and 0.35.
- *Evolving networks/components* are generated as the columns of $\mathrm{B}_k \in \mathbb{R}^{J \times R}$ (or rows of $\mathrm{S}_k \in \mathbb{R}^{R \times J}$). We generate

[2]The implementation of `IVA_L_SOS` and `ICA_EBM` in MATLAB are available at: http://mlsp.umbc.edu/

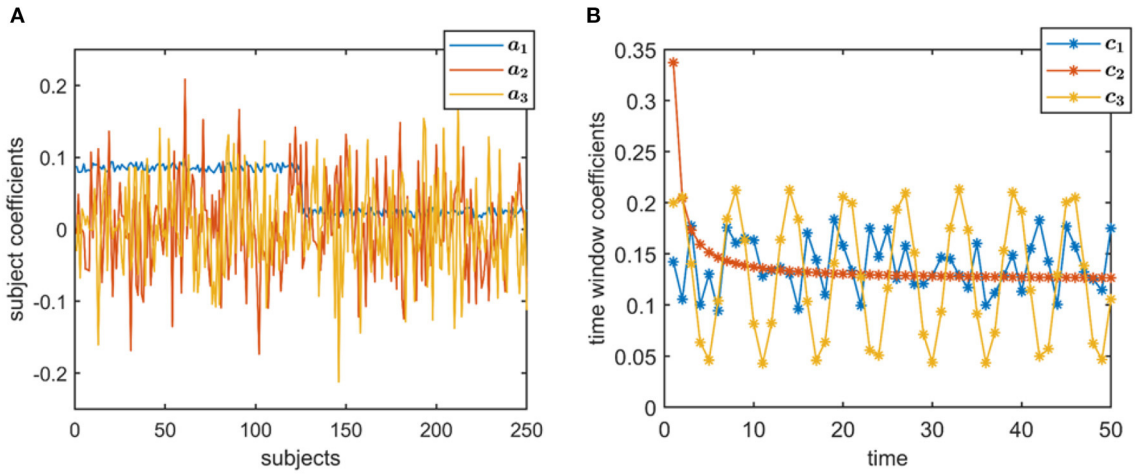

FIGURE 2 | True factors used to generate simulated data. **(A)** Subject-mode factors, where a_r indicates the columns of A, for $r = 1, 2, 3$, and **(B)** Temporal patterns, where c_r indicates the columns of C, for $r = 1, 2, 3$. Time, here, is in the resolution of time windows, but may also correspond to time samples depending on the application.

$R = 3$ evolving networks: The first one is a network that is shifting and increasing in density, the second is increasing in density, and the third one is a random network as shown in **Figure 3A**. All columns are normalized to unit norm. See the **Supplementary Material** for more details on the generation of evolving components.

- *Temporal patterns*, i.e., $\mathrm{C} \in \mathbb{R}^{K \times R}$, are generated as (i) a random pattern with uniformly distributed entries, (ii) an exponential decay pattern, and (iii) a pattern following a sinusodial function (see **Figure 2B**). All columns are normalized to unit norm.

Once factor matrices are generated, the tensor $\mathcal{X} \in \mathbb{R}^{I \times J \times K}$ is constructed based on (1), and a noisy tensor $\mathcal{X}_{\text{noisy}}$ is generated as follows:

$$\mathcal{X}_{\text{noisy}} = \mathcal{X} + \eta \mathcal{N} \frac{\| \mathcal{X} \|_F}{\| \mathcal{N} \|_F}, \tag{8}$$

where $\mathcal{N} \in \mathbb{R}^{I \times J \times K}$ has entries randomly drawn from the standard normal distribution, and η indicates the noise level. In the experiments, we use $\eta = 0.5$. We use PARAFAC2, IVA, and joint ICA to analyze $\mathcal{X}_{\text{noisy}}$ using the correct number of components, i.e., $R = 3$, assuming that it is known, and assess their performance in terms of revealing the evolving networks as well as capturing the group difference in the *subjects* mode. We modify the underlying factor matrices for different experimental set-ups of interest and study the relative performance of the methods in the following cases (see the **Supplementary Material** for additional experiments not specifically focusing on evolving networks):

- *Case 1 (Different sample sizes, different network types):* Here, we study the effect of sample size as well as overlapping and similar networks. In Case 1a, we analyze $\mathcal{X}_{\text{noisy}}$ generated using different number of dimensions in the *voxels* mode, i.e., J, demonstrating the effect of sample size on the performance of the methods. We use $J = 10,000$ and downsampled versions with a downsampling factor of 20 (i.e., $J = 500$) and 60 (i.e., $J = 167$). Using the same set-up, we also study the effect of the number of time slices, i.e., $K = 20$ and $K = 50$. In Case 1b, with $J = 10,000, K = 50$, we assess the performance of the methods when evolving networks are overlapping as in **Figure 3B**. Finally, in Case 1c, we consider evolving networks with similar structures, i.e., two of the components are shifting and increasing in density as in **Figure 3C**. Matrix A and C are as in **Figure 2**.
- *Case 2 (Different subject-mode matrices):* In this scenario, we study the effect of different subject-mode patterns in different time slices. Each X_k matrix is constructed using a different $\mathrm{A}_k \in \mathbb{R}^{I \times R}$ matrix in (1). More precisely, $\mathrm{A}_k = \mathrm{A} + \gamma \mathrm{N}_k \frac{\| \mathrm{A}_k \|_F}{\| \mathrm{N}_k \|_F}$ for odd values of $k \leq K$, where γ denotes the noise level and is set to $\gamma = 0.3$, and $\mathrm{N}_k \in \mathbb{R}^{I \times R}$ is the noise matrix with entries randomly drawn from the standard normal distribution. For even values of $k \leq K$, A_k are random matrices with entries drawn from the standard normal distribution. This set-up violates assumptions of joint ICA and PARAFAC2 in the subject-mode, and is of interest especially when different subject-mode patterns are possibly expected in different slices, e.g., task vs. rest windows or different tasks. Matrices $\mathrm{B}_k \in \mathbb{R}^{J \times R}$ are as in **Figure 3A**, downsampled by a factor of 10, i.e., $J = 1,000$, and matrix $\mathrm{C} \in \mathbb{R}^{K \times R}$ with $K = 50$ is generated in a similar way as in **Figure 2B**.
- *Case 3 (Strong discriminating component):* Compared with other cases, in this set-up, the main difference is omitting the normalization of the columns of factor matrices A and C resulting in higher 2-norm, i.e., a factor of 4, for the component revealing the group difference. As the evolving components, we use the B_k matrices in **Figure 3A** but only the

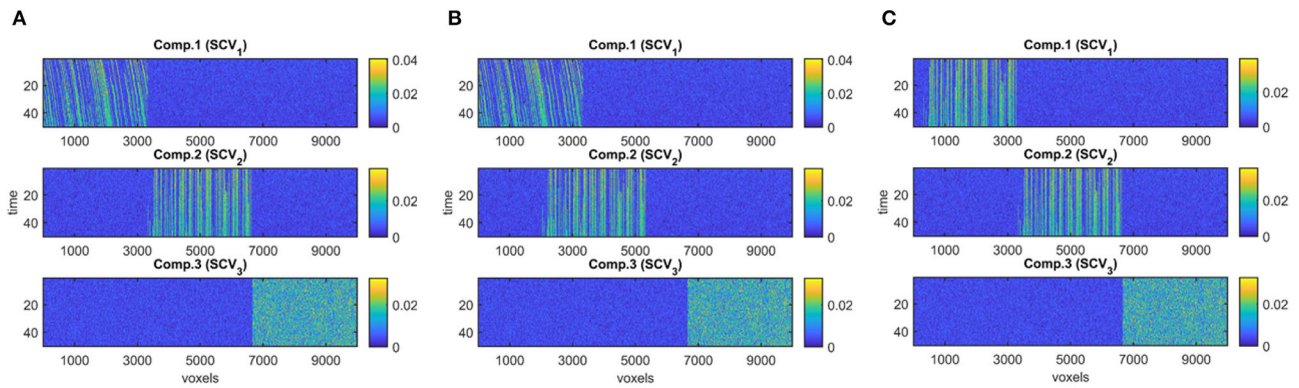

FIGURE 3 | True evolving components ($R = 3$), where each component corresponds to a column of B_k, for $k = 1, ..., 50$, used to generate simulated data with **(A)** evolving networks, **(B)** overlapping networks, **(C)** similar networks.

first 15 time slices to match with the number of time slices in real data.

2.2.4. Real fMRI Data

As a real dataset, we analyze images from the MCIC collection (Gollub et al., 2013), a multi-site multi-subject collection of fMRI images from healthy controls and patients with schizophrenia, collected during various tasks. In particular, we use data from the sensory motor (SM) task collected at four research sites: the University of New Mexico, the University of Minnesota, Massachusetts General Hospital, and the University of Iowa. During the SM task, the study participants were equipped with headphones and instructed to listen for sounds of increasing pitch, with a fixation period between each sound. The participants were instructed to press a button whenever they heard a tone. To ensure that conditions were consistent across scan sessions and sites, the MCIC consortium performed meticulous cross-site calibration. For example, the sites had matching button press devices, the intensity of the auditory stimuli were calibrated and the quality assurance procedures recommended by the Biomedical Informatics Research Network for multi-center fMRI studies (Friedman et al., 2006, 2008) were followed.

Based on the blood-oxygenation-level-dependent signal from the SM task, we extracted fALFF (Zou et al., 2008) in sliding time windows, which yields a time-evolving measure of brain activity within each voxel. Note that this approach—using the synchrony across subjects during the task—collapses the time dimension into time windows using fALLF as a feature representing the activity in each time window for each voxel for each subject allowing us to align signals from multiple subjects. The fALFF is calculated by first discarding the high- and low-frequency components to remove noise and signal from the vasculature system. Then, the amplitudes of the frequency components are computed to get the low-frequency fluctuation which is divided by the total amplitude of all frequencies in the time window to obtain the fALFF. To compute the fALFF, we used the REST software v1.8_130615 (Song et al., 2011). We set the window size and stride length to 16 seconds, corresponding to precisely one rest- or task-block in each time window, with no overlap. The low- and high-frequency cutoff for fALFF were set to 0.01 and 0.15, respectively. To construct the data tensor, we used the fALFF values for voxels that correspond to gray matter as feature vectors for each time window and each subject. Each such feature vector has 67,747 elements, leading to a data tensor of size 253 *subjects* by 67,747 *voxels* by 14 *time windows*. No additional preprocessing is carried out to account for site effects (see section 3.2 for more information). Out of 253 subjects, 147 are healthy controls and 106 are patients with schizophrenia.

3. RESULTS

Through numerical experiments, we demonstrate that PARAFAC2 and joint ICA capture the underlying networks, their evolution, and reveal the discriminating component accurately irrespective of the sample size as long as the factor matrix in the *subjects* mode stays the same (or differ up to a scaling) across time windows (Case 1 and 3). For these cases, while IVA performs well for large sample size, we often observe that IVA reveals additional components that are statistically significant in terms of group difference in some time windows even though that does not match the ground truth—showing that IVA is more prone to false-positives [i.e., identifying patterns as potentially important (or markers) for group difference] compared to PARAFAC2 and joint ICA. On the other hand, if different time windows have different factor matrices in the *subjects* mode as in Case 2, IVA performs better in terms of revealing the underlying networks. Among the three methods, PARAFAC2 is the only one that reveals compact temporal patterns explicitly.

Our analysis of real task fMRI data demonstrates that all methods (PARAFAC2, IVA, and joint ICA) capture a component including both primary motor, supplementary motor, cerebellum, and temporal regions engaged by the task. This component is also identified as statistically significant

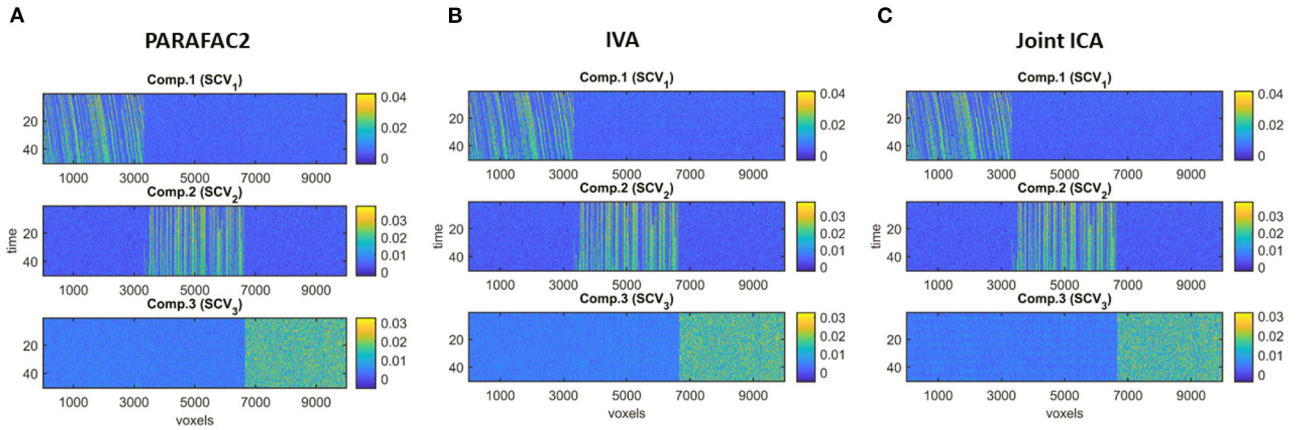

FIGURE 4 | Case 1a. Evolving components (B_k or S_k, for $k = 1, ..., K$) captured by each method after fixing the scaling and permutation ambiguity: **(A)** PARAFAC2, **(B)** IVA, **(C)** joint ICA. All methods recover the underlying evolving components accurately.

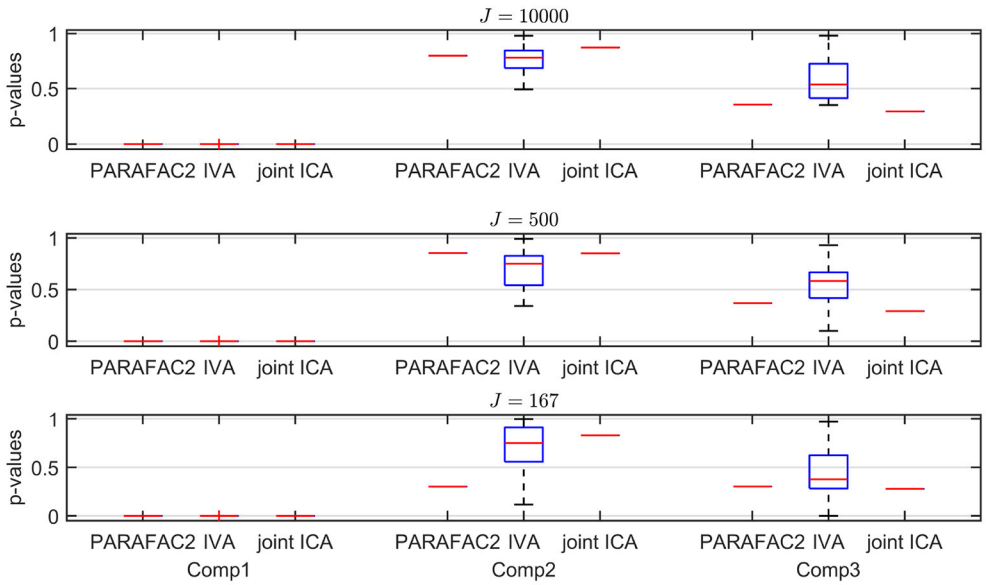

FIGURE 5 | Case 1a ($K = 20$). p-values obtained using the two-sample t-test on the subject-mode patterns (A or A_k) using different methods as the number of voxels (i.e., J) changes, where the number of time slices (i.e., K) is set to 20. Based on the true subject-mode patterns, true p-values are 0, 0.88, and 0.35 for component 1, 2, and 3, respectively. For large sample size, i.e., $J = 10,000$, all methods can identify that the first component is the statistically significant one in terms of group difference. As J decreases, in addition to the first component, IVA returns small p-values for other components in some windows corresponding to false-positive cases while PARAFAC2 and joint ICA work well regardless of the sample size.

in terms of differentiating between healthy controls and patients with schizophrenia. Additional components show up as statistically significant in terms of group difference in IVA in some time windows. However, given the results of our simulations, where we observe small p-values for non-discriminating components at some time windows, we discard those components as potential false-positive markers.

3.1. Simulations

Figure 4 demonstrates the evolving components captured by the three methods in Case 1a with $J = 10,000$ voxels showing that all methods can recover the true underlying evolving networks accurately. **Table 1** shows the similarity scores [defined in (6) and (7)] also demonstrating that underlying networks are accurately captured with a similarity score of 1.00 using all methods. Furthermore, all methods perform well in terms of capturing the component discriminating between the subject groups as shown in the top plot in **Figure 5**. The first component is the one that can separate the two subject groups, with all methods revealing p-values around 0, and p-values for non-discriminating components are large enough to discard them. Note that since IVA extracts different A_k matrices, for $k =$

TABLE 1 | For each case, dataset sizes (I, J, K), similarity scores (Sim_A, Sim_B, Sim_C) showing the accuracy of the methods in terms of capturing the underlying patterns in the first (subject), second (network/voxel), and third (time) modes, respectively, and whether methods give false positive (FP) markers, i.e., identifying components that are not indicating group difference as potential markers with statistically significant group difference.

				PARAFAC2				IVA		Joint ICA		
	I	J	K	Sim_A	Sim_B	Sim_C	FP	Sim_B	FP	Sim_A	Sim_B	FP
Case 1a	250	10,000	50	1.00	1.00	1.00	No	1.00	No	1.00	1.00	No
Case 1a	250	10,000	20	1.00	1.00	1.00	No	1.00	No	1.00	1.00	No
Case 1a	250	500	50	1.00	1.00	1.00	No	1.00	No	1.00	1.00	No
Case 1a	250	500	20	1.00	1.00	1.00	No	1.00	No	1.00	1.00	No
Case 1a	250	167	50	1.00	1.00	1.00	No	1.00	No* (**Supplementary Figure 1**)	1.00	1.00	No
Case 1a	250	167	20	1.00	0.99	1.00	No	0.99	Yes (**Figure 5**)	1.00	1.00	No
Case 1b	250	10,000	50	1.00	1.00	1.00	No	1.00	No	1.00	1.00	No
Case 1c	250	10,000	50	1.00	1.00	1.00	No	1.00	No	1.00	1.00	No
Case 2	250	1,000	50	0.99	0.68	0.85	No	0.98	Yes (**Figure 8**)	0.96	0.74	Yes
Case 3 ($R = 3$)	250	10,000	15	1.00	0.99	1.00	No	0.99	Yes (**Figure 9**)	1.00	0.99	No
Case 3 ($R = 4$)	250	10,000	15	1.00	0.98	1.00	Yes	0.99	Yes (**Supplementary Figure 2**)	1.00	0.99	No

**Indicates that even though there are no false positives, p-values get quite small.*

$1, \ldots, K$, different p-values are obtained from each matrix and shown as box-plots.

Sample Size. As we decrease the number of samples/voxels (i.e., J), we observe differences in the performances of the methods. While all methods can still capture the evolving networks accurately (see **Table 1**), IVA gets smaller p-values even for non-discriminating components in some slices while PARAFAC2 and joint ICA can still clearly identify non-discriminating vs. discriminating components (**Figure 5**). We observe that the third component also shows up as a statistically significant component in terms of group difference for some time windows using IVA as a false-positive marker. See **Supplementary Material** also for $K = 50$ (**Supplementary Figure 1**), where IVA performs better but still returns smaller p-values for some components in some windows.

Different Network Types. In the case of different network types, i.e., when we have overlapping evolving components as in **Figure 3B**, or components evolving in the same way as in **Figure 3C** resulting in the same covariance structure as in **Figure 6C**, all methods perform equally well in terms of capturing the underlying components (see the similarity scores in **Table 1**). The motivation for having overlapping networks is to demonstrate the performance of the methods when networks overlap in space, i.e., *voxels* mode, which may be expected in real applications. Even though the networks overlap, the average correlation of networks, i.e., correlation between columns of B_k averaged over K slices, is small, e.g., $\leq$ 0.1 in **Figure 3B**; therefore, not affecting the performance of IVA and joint ICA. Even when there is a larger overlap in space, the correlation is still not high when network structures are different, e.g., shifting vs. non-shifting.

Different Subject-Mode Patterns. When the assumption of the same subject-mode patterns in different time windows is violated, both PARAFAC2 and joint ICA do not capture the underlying evolving components as shown in **Figures 7A,C**, and with low similarity scores given in **Table 1** for Case 2. On the other hand, **Figure 7B** shows that IVA recovers the evolving components almost accurately with a similarity score of 0.98. Furthermore, IVA also captures that there is a component discriminating between the subject groups in every other window. **Figure 8** shows the p-values obtained using the A_k matrices corresponding to each one of the $K = 50$ time slices indicating the statistical significance of the first component in terms of group difference in every other window. For the other components, there are again some small p-values as we have also previously observed as a drawback of IVA in Case 1a. Nevertheless, compared to PARAFAC2 and joint ICA, which cannot reveal subject-mode patterns changing from one time slice to another, IVA performs well and can capture such information in one component.

Strong Discriminating Component. In the presence of a strong component, which is also responsible for the group separation, all methods successfully reveal the underlying evolving components shown by the high similarity scores in **Table 1**. In the *subjects* mode, **Figure 9A** demonstrates that PARAFAC2 and joint ICA identify the first component as the discriminating component successfully while IVA has one component that is statistically significant in terms of group difference in all windows and the two other components in some time windows. This set-up is motivated by the real data, where we observe a consistent spatial/voxel-mode pattern using all methods; however, methods differ in terms of subject-mode patterns as a result of their modeling assumptions. PARAFAC2 and joint ICA can reveal the same subject-mode patterns (up to a scaling) in all time windows while IVA may reveal different subject-mode patterns in every time window. In our experiments, we observe that the flexibility of IVA hurts its performance resulting in potentially false-positive markers. Finally, **Figure 9B** demonstrates the temporal patterns captured by PARAFAC2, revealing the underlying true patterns accurately. Neither joint ICA nor IVA can extract temporal patterns in a compact way.

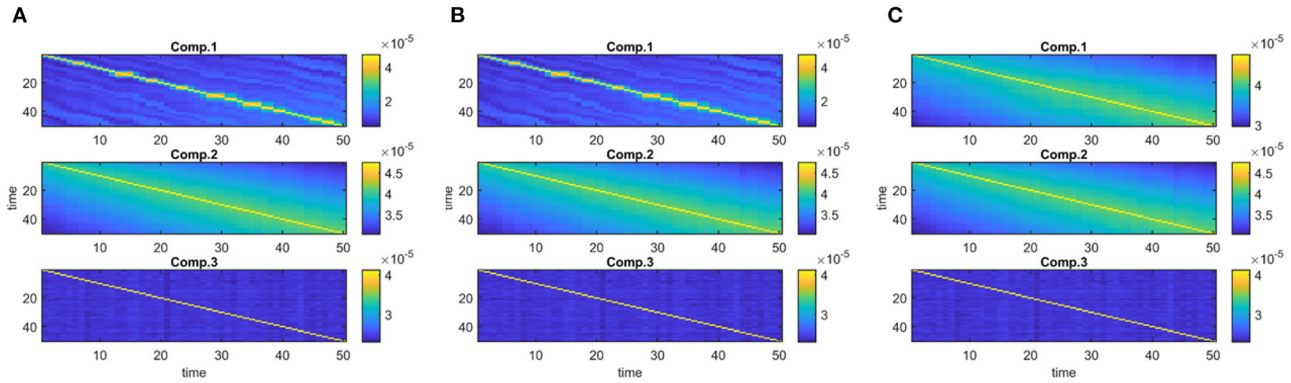

FIGURE 6 | Covariance matrices of size K by K showing the covariance structure of true components across $K = 50$ time slices for **(A)** evolving networks, **(B)** overlapping networks, **(C)** similar networks.

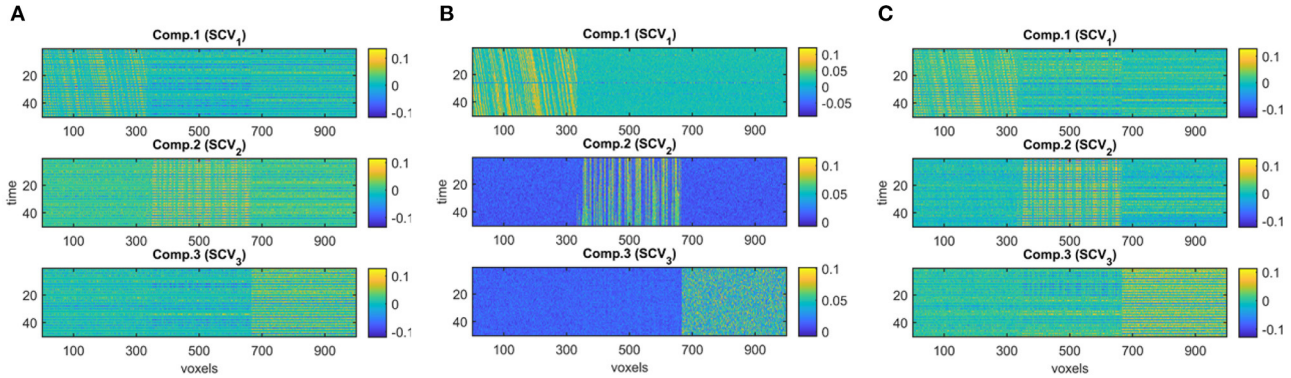

FIGURE 7 | Case 2. Evolving components (B_k or S_k, for $k = 1, ..., K$) captured by each method: **(A)** PARAFAC2, **(B)** IVA, **(C)** joint ICA. PARAFAC2 and joint ICA fail to capture the underlying networks while IVA can reveal the evolving components accurately.

When using IVA, one can focus on how the average subject-mode patterns change from one time window to another (Hossain et al., 2022); however, that relies on the assumption that the average would be representative.

3.2. Task fMRI Data Analysis

The fMRI data tensor (constructed as described in section 2.2.4) is in the form of 253 *subjects* by 67,747 *voxels* by 14 *time windows*. Before the analysis, the tensor is preprocessed by subtracting the mean fALFF signal across the *voxels* mode, and dividing each *voxels* mode fiber, i.e., the vector containing the tensor entries for a fixed subject and a time window index, by its standard deviation. The preprocessed tensor is then analyzed using PARAFAC2, IVA and joint ICA in order to capture patterns/networks in the *voxels* mode (as well as their change in time) that can reveal group differences between healthy and patient groups.

Figure 10A shows the spatial maps captured by a 2-component PARAFAC2 model. These maps correspond to columns of B_k for the first time window, i.e, $k = 1$. In this article, for all methods, we only show the spatial maps for the first time window. In order to see evolving spatial maps, we refer the reader to the videos in the GitHub repository[3]. The p-values are 7.8×10^{-6} and 7.7×10^{-1} for the first and second component, respectively. The first component is of particular interest since it is statistically significant in terms of group difference. Furthermore, this is a strong discriminating component with a norm that is almost twice the norm of the second component. Importantly, this component includes regions expected to be engaged by the task, e.g., primary and secondary motor and cerebellum, as well as auditory cortex. These regions have also been implicated in schizophrenia (Friston and Frith, 1995; Pearlson and Calhoun, 2007). In **Figure 10B**, we observe that the first component has a temporal pattern that follows the task-rest pattern. This component is consistently observed when we change the number of components or used data from a subset of the sites. As previously noted, it is challenging to determine the right number of components. We fitted the PARAFAC2 model using $R = 2, 3, 4$ components. While all models had a high core consistency value, i.e., $\geq$ 81%, highly correlated factor vectors

[3]https://github.com/eacarat/TracingEvolvingNetworks

in the subject-mode were observed using 3-component and 4-component models with the spatial maps in **Figure 10A** being split into more than one component. Therefore, we focus on the 2-component model, and the fact that the component of interest was also captured as a statistically significant component using a 3-component model gives more confidence in the results we interpret. While we analyze in this article the fMRI data from the four sites available in the MCIC collection (Gollub et al., 2013), in our previous study we only focused on the analysis of two of the sites (Roald et al., 2020) to avoid potential scanner differences and site effects. We observe that despite site effects in the case of four sites, the individual sites show group effects in the same direction relying on the same patterns; therefore we get the same consistent patterns (i.e., spatial maps and the temporal pattern) in both studies confirming that site effects do not have a substantial effect on the patterns of interest.

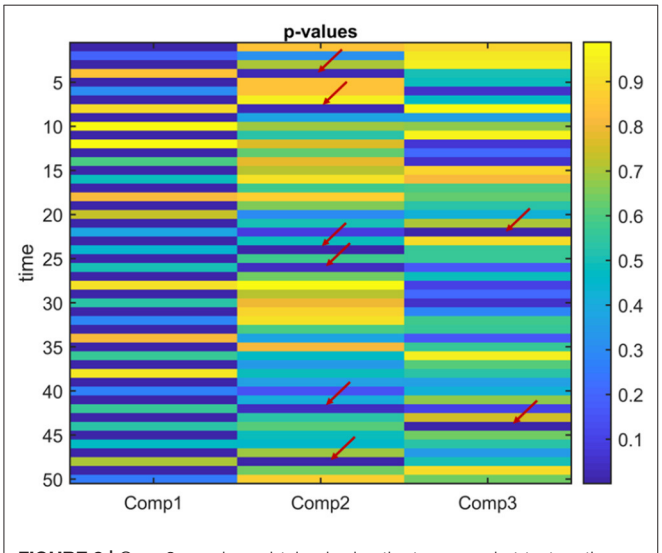

FIGURE 8 | Case 2. *p*-values obtained using the two-sample *t*-test on the subject-mode patterns (A_k) using IVA. IVA successfully captures that the first component is statistically significant in terms of group difference in every other window. In the other components, in some time windows, there are false positives marked with a red arrow.

When we analyze the data tensor, i.e., multiple matrices in the form of *subjects* by *voxels* matrices corresponding to different time windows, using IVA, we also capture a similar statistically significant sensorimotor component as shown in **Figure 11A**, i.e., component 5 with activations in the same areas as in component 1 in the PARAFAC2 model (**Figure 10A**). Since methods have different modeling assumptions, they are not necessarily comparable using the same number of components. We explore a wide range of component numbers to see the performance of the methods using different number of components and compare their best performances. Regardless of the number of components, i.e., $R = 2, 10$, and $R = 40$, IVA reveals this component as a statistically significant component in all but one or two time windows. Here, we report the results using $R = 40$ (see the **Supplementary Material** for the spatial maps extracted using $R = 2$, which are also very similar to $R = 40$ in terms of the component of interest). Only one out of 40 components is statistically significant in most of the time windows, and that is component 5 in **Figure 11A** (as also shown in Hossain et al., 2022 on the same dataset). **Figure 11B** shows that except for one time window, component 5 has a *p*-value $\leq$ 0.05. **Figure 11A** shows component 12, which seems to match with the second component in PARAFAC2 (see **Figure 10A**—Component 2). However, this component is not

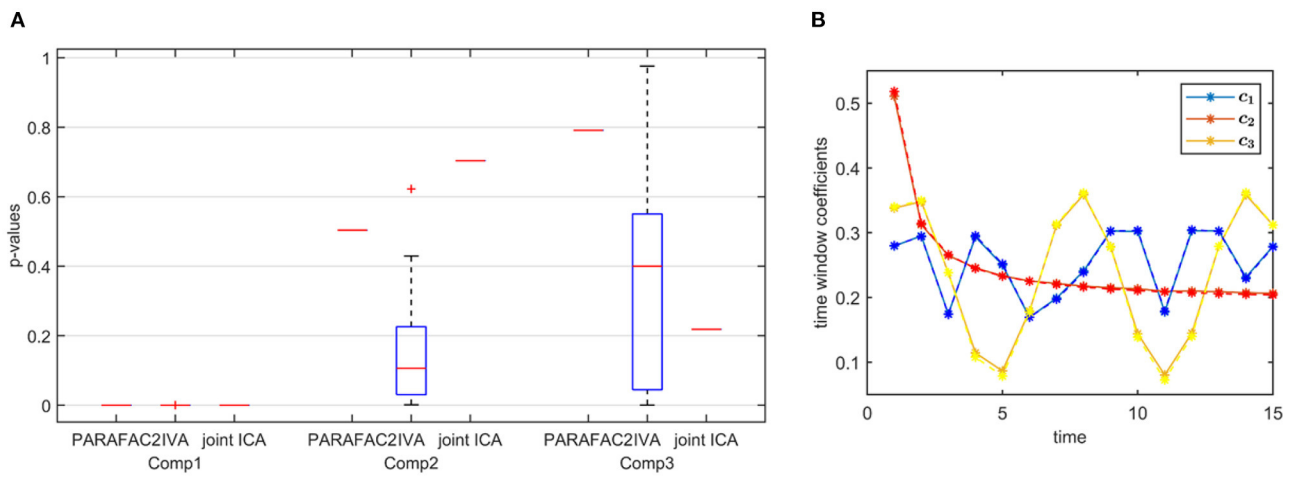

FIGURE 9 | Case 3. **(A)** *p*-values obtained using the two-sample *t*-test on the subject-mode patterns (A or A_k) using different methods. Based on the true subject-mode patterns, true *p*-values are 0, 0.88, and 0.35 for component 1, 2 and 3, respectively. All methods identify the first component as the component differentiating between the subject groups. While PARAFAC2 and joint ICA identify the second and third components as not statistically significant in terms of group difference, IVA wrongly identifies them as statistically significant in some windows. **(B)** Temporal patterns, i.e., columns of factor matrix C, extracted from the *time* mode using PARAFAC2. True patterns are shown using dashed lines. PARAFAC2 correctly captures the true temporal patterns.

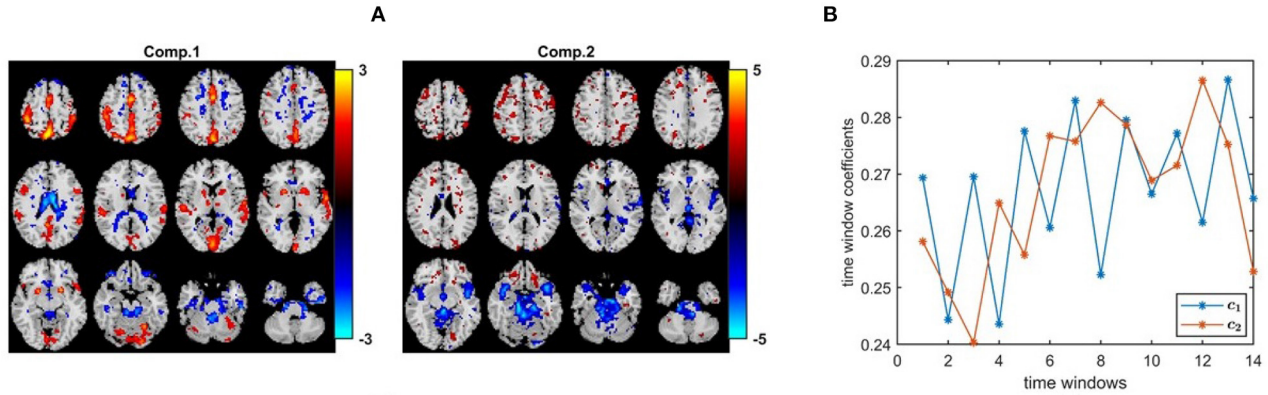

FIGURE 10 | PARAFAC2 analysis of task fMRI data. **(A)** Spatial components, i.e., columns of B_k. Here, we plot columns of only B_1 corresponding to the first time window. The corresponding p-values are 7.8×10^{-6} for component 1, and 7.7×10^{-1} for component 2. The first component includes primary and secondary motor and cerebellum, as well as auditory cortex expected to be engaged by the task. Spatial maps are plotted using the patterns from the *voxels* mode as z-maps and thresholding at $|z| \geq 1.5$ such that red voxels indicate an increase in controls over patients, and blue voxels indicate an increase in patients over controls. **(B)** Temporal patterns, i.e., columns of matrix C.

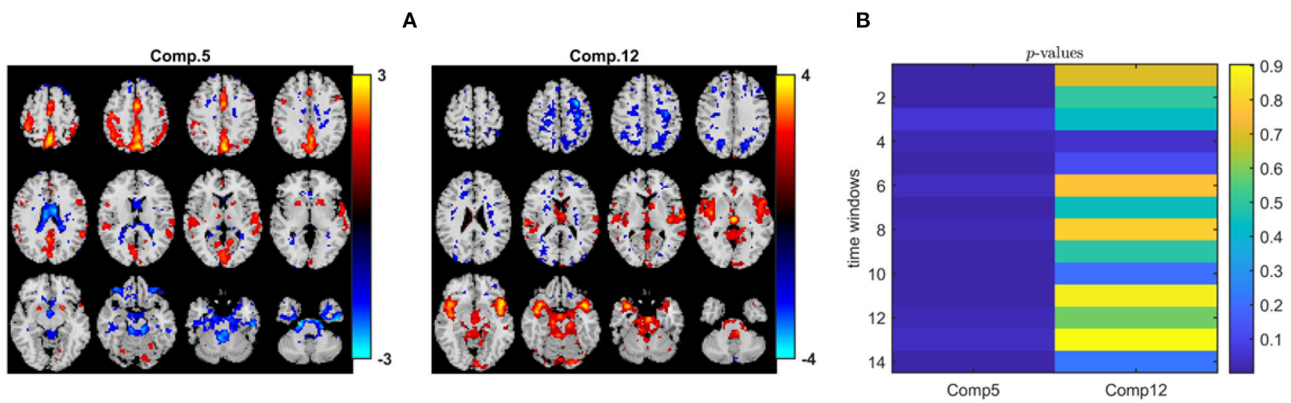

FIGURE 11 | IVA analysis of task fMRI data. **(A)** Spatial components, i.e., rows of S_k. Here, we only plot two of the rows of S_1 corresponding to the first time window. Spatial maps are plotted using the patterns from the *voxels* mode as z-maps and thresholding at $|z| \geq 1.5$ such that red voxels indicate an increase in controls over patients, and blue voxels indicate an increase in patients over controls. **(B)** p-values for the two components in each time window. While component 5 is statistically significant in all but one time window (i.e., time window 3), component 12 is not in any of the time windows.

statistically significant in terms of group difference in PARAFAC2 or IVA[4].

When joint ICA is used to analyze the fMRI tensor, as **Figure 12** shows, the sensorimotor component is again captured. Here, we include the joint ICA results using $R = 2$ components. The p-value for the first component is 1.1×10^{-4} while the p-value for the second one is $\geq$ 0.05. As we increase the number of components (e.g., $R = 5, 10$), joint ICA still reveals the sensorimotor component as the statistically significant one in terms of group difference and no other important component shows up while p-values get higher (results not shown). Using higher number of components, e.g., $R = 40$, we observe that the component of interest splits into several components.

Note that while we report p-values for comparing how the methods perform in terms of identifying potential components of interest, we do not claim that one is better than the other based on how low the p-values are.

Based on the results of our experiments on simulated data, we know that (i) all methods capture the discriminating component when subject-mode patterns do not change from one time window to another, (ii) IVA often reveals some components that are statistically significant in terms of group difference in few windows—which correspond to false-positive markers. We make the same observations in our real fMRI data analysis. In order to see if the same or similar subject-mode patterns are available in task and rest windows, we analyze only the task windows (i.e., a

[4]The sign of the test statistic is used to fix the sign ambiguity in the models. Both component 2 in PARAFAC2 and component 12 in IVA have a small test statistic; therefore, the uncertainty in the signs and mismatching colors in the maps.

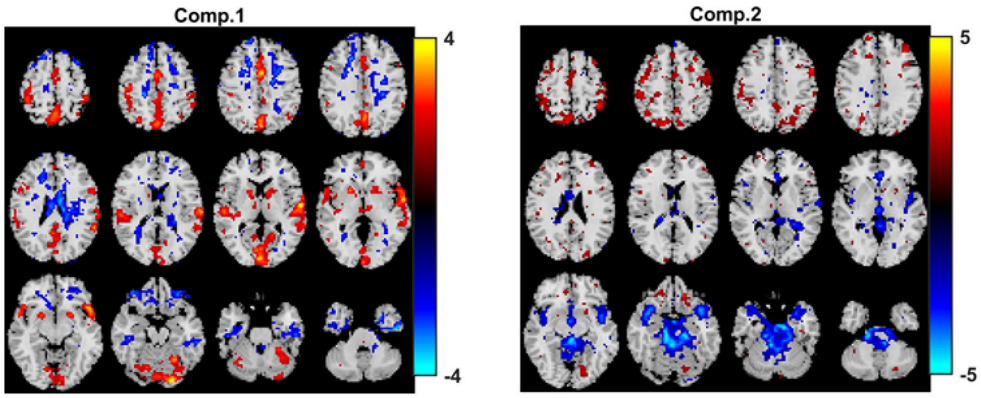

FIGURE 12 | Joint ICA analysis of task fMRI data. Spatial components, i.e., rows of S_k. Here, we only plot rows of S_1 corresponding to the first time window. Spatial maps are plotted using the patterns from the *voxels* mode as z-maps and thresholding at $|z| \geq 1.5$ such that red voxels indicate an increase in controls over patients, and blue voxels indicate an increase in patients over controls. The *p*-values are 1.1×10^{-4} for component 1, and 1.4×10^{-1} for component 2.

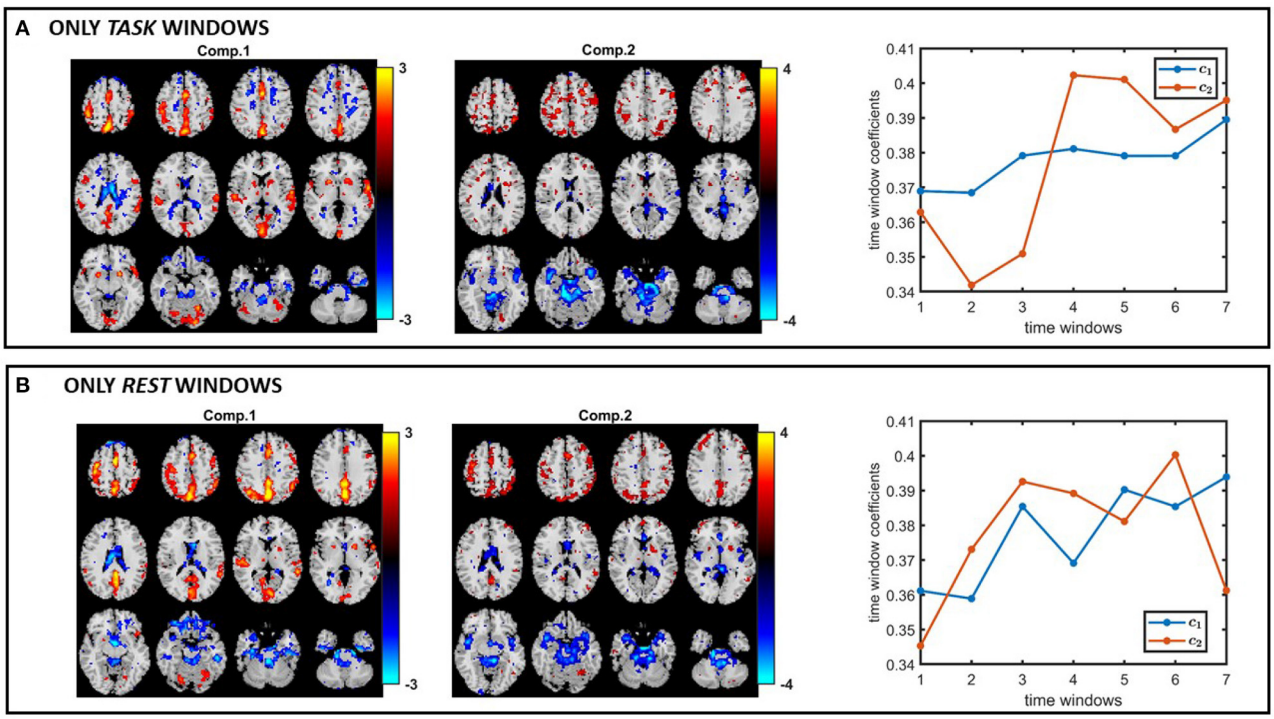

FIGURE 13 | PARAFAC2 analysis of **(A)** only task windows: Spatial components, i.e., columns of B_k, for $k = 1$, as well as the temporal patterns, i.e., columns of C. The *p*-values are 2.1×10^{-4} for component 1, and 2.7×10^{-1} for component 2. **(B)** Only rest windows: Spatial components, i.e., columns of B_k, for $k = 1$, as well as the temporal patterns, i.e., columns of C. The *p*-values are 6.6×10^{-3} for component 1, and 8.5×10^{-1} for component 2. The first component shows statistical significance in terms of group difference in both task and rest windows; therefore, supporting the modeling assumptions of PARAFAC2 and joint ICA. Spatial maps are plotted using the patterns from the *voxels* mode as z-maps and thresholding at $|z| \geq 1.5$ such that red voxels indicate an increase in controls over patients, and blue voxels indicate an increase in patients over controls.

tensor of size 253 *subjects* by 67,747 *voxels* by 7 *time windows*, for $K = 1, 3, 5, ..13$) as well as only the rest windows (i.e., a tensor of size 253 *subjects* by 67,747 *voxels* by 7 *time windows*, for $K = 2, 4, ..14$). **Figures 13A,B** show the spatial maps captured using a 2-component PARAFAC2 model from the task tensor and the rest tensor. We observe that the sensorimotor component is statistically significant in terms of group difference in both tensors; therefore, supporting the argument for similar or same

subject-mode patterns in different time windows, and making PARAFAC2 and joint ICA suitable approaches for analyzing such time-evolving data.

4. DISCUSSION

Overall, all three methods show promising performance in temporal data mining as long as their modeling assumptions are satisfied. Our focus here on addressing the problem of capturing spatial dynamics through the analysis of task fMRI data falls under a temporal data mining problem, where we expect similar group differences (in other words, similar subject-mode patterns) in different time windows. Therefore, PARAFAC2 presents itself as a suitable model providing a compact summary revealing underlying networks, their change in time as well as the temporal patterns in the data. In other scenarios, for instance, when the goal is to analyze multi-task fMRI data, where different slices correspond to fMRI signals collected during different tasks (rather than different time windows), if each task cannot reveal the same group differences, such data may rather follow the modeling assumptions of IVA (Lehmann et al., 2022).

One remaining challenge as a future study is the sensitivity of the methods to the selection of number of components. In simulations, we have assumed that the true number of components is known. While there are various approaches for determining the number of components, often in real applications, the number of components is overestimated. In our real data analysis, we have therefore focused on a component that is consistently observed regardless of the number of components avoiding the sensitivity problem. In order to see the effect of overfactoring, for Case 3, we have fitted PARAFAC2, IVA, and joint ICA using $R = 4$ components, where the true number of components is 3. As shown in **Table 1**, all methods reveal the evolving networks accurately. However, their performance differs in terms of how well they identify the discriminating component. As we have previously observed in Case 3 when using the true number of components, IVA still identifies additional components as statistically significant in terms of group difference in some slices resulting in many false-positives. In the case of overfactoring, PARAFAC2 also wrongly identifies the additional component as statistically significant in terms of group difference. Joint ICA performs well without any false-positive components. These experiments demonstrate the sensitivity of the methods to the number of components. Note that when the number of component is misspecified, how we select the best run (e.g., the one giving the minimum function value out of multiple initializations) also needs to be studied further, and with the current best run selection approach, the PARAFAC2 model might benefit from regularization in order to prevent overfitting.

There are several other computational aspects that need more research. First, the scalability of the algorithms for fitting the PARAFAC2 model to large-scale data needs to be studied further for dense datasets. The scalability of PARAFAC2 has previously been studied for large-scale sparse data (Perros et al., 2017; Afshar et al., 2018). Another key issue in terms of using PARAFAC2 for time-evolving data analysis is the PARAFAC2 constraint, i.e., constant cross-product constraint. In many applications, that constraint does not have an application-specific justification. We intend to relax the PARAFAC2 constraint, and incorporate additional constraints that will make the analysis time-aware in future studies. While PARAFAC2 ALS algorithm is not flexible enough to incorporate constraints on the evolving patterns, recent work introduces an alternating direction method of multipliers (ADMM)-based algorithm for fitting the PARAFAC2 model enabling imposing constraints in all modes (Roald et al., 2021). It is also worth mentioning that regardless of these advances in computational and modeling aspects of the PARAFAC2 model, the model—as it is—has the potential to reveal time-evolving connectivity patterns if it were to be used in previous connectivity studies assuming static networks (Zhu et al., 2019, 2020).

In this article, we have used different modeling approaches to reveal evolving maps in time and provided them as videos. While such videos show the spatial dynamics to some extent, further work is still needed to quantify and/or better characterize the temporal change from one time window to another—which may be achieved using a postprocessing step or by incorporating relevant constraints into the model.

5. CONCLUSIONS

Analysis of time-evolving data is challenging especially when the goal is to extract the underlying patterns as well as their evolution. Such analysis is crucial to improve our understanding of complex systems such as the brain. In this article, we study a tensor factorization-based approach called the PARAFAC2 model in comparison with joint ICA and IVA in terms of analyzing time-evolving data and capturing the underlying evolving patterns. Through simulations, we study the performance of these three methods showing that when subject-mode patterns across different time slices are the same, PARAFAC2 and joint ICA perform better in terms of capturing the underlying patterns and are less prone to false-positive markers. On the other hand, if subject-mode patterns differ (more than a scaling factor) from one time window to another, IVA performs the best. In our analysis of real task fMRI data, we observe that all methods capture one consistent component, that is also statistically significant in terms of differentiating between healthy controls and patients with schizophrenia. IVA identifies additional components as statistically significant in terms of group difference; however, those are discarded as potential false positives. Compared to other methods, PARAFAC2 reveals a compact temporal pattern showing the task-rest pattern clearly.

Methods studied in this article are of interest in not only neuroscience but also other fields such as metabolomics to understand the temporal change in human metabolome (i.e., the complete set of small biochemical compounds in the body).

For instance, through the analysis of longitudinal metabolomics data as well as data from other sources, it may be possible to capture early signs of diseases (Price et al., 2017). Recently, tensor factorizations have been used to analyze dynamic metabolomics data (Li et al., 2022) but how to capture evolving patterns from such data is yet to be studied.

DATA AVAILABILITY STATEMENT

The data analyzed in this study is subject to the following licenses/restrictions: While some of the data are available through the COINS (COllaborative Informatics Neuroimaging Suite) database, some of the data are not publicly available (not sharable per the IRB). Requests to access these datasets should be directed to https://coins.trendscenter.org/.

ETHICS STATEMENT

Ethical review and approval was not required for this study as it was deemed 'not human subjects' *via* the institutional review board. The patients/participants provided their written informed consent to participate in this study.

AUTHOR CONTRIBUTIONS

EA and TA conceived the project and designed the experiments. EA conducted the experiments, with MR being involved in simulated data generation and real data analysis, and KH being involved in real data analysis. EA, MR, TA, and VC were involved in the writing of the manuscript. All authors have given approval to the final version of the manuscript. All authors contributed to the article and approved the submitted version.

FUNDING

This work was supported in part by the Research Council of Norway through project 300489 (IKTPLUSS) and by the grants NSF-NCS1631838, NSF-HRD2112455, NIH R01MH118695, and NIH R01MH123610.

SUPPLEMENTARY MATERIAL

The Supplementary Material for this article can be found online at: https://www.frontiersin.org/articles/10.3389/fnins.2022.861402/full#supplementary-material

REFERENCES

Acar, E., Bingol, C. A., Bingol, H., Bro, R., and Yener, B. (2007). Multiway analysis of epilepsy tensors. *Bioinformatics* 23, i10–i18. doi: 10.1093/bioinformatics/btm210

Acar, E., and Yener, B. (2009). Unsupervised multiway data analysis: a literature survey. *IEEE Trans. Knowl. Data Eng.* 21, 6–20. doi: 10.1109/TKDE.2008.112

Adali, T., Anderson, M., and Fu, G.-S. (2014). Diversity in independent component and vector analyses: Identifiability, algorithms, and applications in medical imaging. *IEEE Signal Proc. Mag.* 31, 18–33. doi: 10.1109/MSP.2014.2300511

Afshar, A., Perros, I., Papalexakis, E. E., Searles, E., Ho, J., and Sun, J. (2018). "COPA: constrained PARAFAC2 for sparse & large datasets," in *CIKM'18: Proceedings of the 27th ACM International Conference on Information and Knowledge Management* (Torino), 793–802. doi: 10.1145/3269206.3271775

Andersen, A. H., and Rayens, W. S. (2004). Structure-seeking multilinear methods for the analysis of fMRI data. *NeuroImage* 22, 728–739. doi: 10.1016/j.neuroimage.2004.02.026

Anderson, M., Adali, T., and Li, X.-L. (2012). Joint blind source separation with multivariate Gaussian model: algorithms and performance analysis. *IEEE Trans. Signal Process.* 60, 1672–1683. doi: 10.1109/TSP.2011.2181836

Bai, Z., Walker, P., Tschiffely, A., Wang, F., and Davidson, I. (2017). "Unsupervised network discovery for brain imaging data," in *KDD'17: Proceedings of the 23rd ACM SIGKDD International Conference on Knowledge Discovery and Data Mining* (Halifax, NS), 55–64. doi: 10.1145/3097983.3098023

Becker, H., Comon, P., Albera, L. (2012). "Tensor-based preprocessing of combined EEG/MEG data," in *2012 Proceedings of the 20th European Signal Processing Conference (EUSIPCO)*, p. 275–279.

Beckmann, C. F., and Smith, S. M. (2005). Tensorial extensions of independent component analysis for multisubject fMRI analysis. *NeuroImage* 25, 294–311. doi: 10.1016/j.neuroimage.2004.10.043

Bhinge, S., Long, Q., Calhoun, V. D., and Adali, T. (2019a). Spatial dynamic functional connectivity analysis identifies distinctive biomarkers in schizophrenia. *Front. Neurosci.* 13, 6. doi: 10.3389/fnins.2019.01006

Bhinge, S., Mowakeaa, R., Calhoun, V. D., and Adali, T. (2019b). Extraction of time-varying spatio-temporal networks using parameter-tuned constrained IVA. *IEEE Trans. Med. Imaging* 38, 1715–1725. doi: 10.1109/TMI.2019.2893651

Bro, R., Andersson, C. A., and Kiers, H. A. L. (1999). PARAFAC2-Part II. Modeling chromatographic data with retention time shifts. *J. Chemometr.* 13, 295–309. doi: 10.1002/(SICI)1099-128X(199905/08)13:3/4<295::AID-CEM547>3.0.CO;2-Y

Bro, R., and Kiers, H. A. L. (2003). A new efficient method for determining the number of components in PARAFAC models. *J. Chemometr.* 17, 274–286. doi: 10.1002/cem.801

Calhoun, V. D., Adali, T., Pearlson, G., and Kiehl, K. (2006). Neuronal chronometry of target detection: fusion of hemodynamic and event-related potential data. *NeuroImage* 30, 544–553. doi: 10.1016/j.neuroimage.2005.08.060

Calhoun, V. D., Miller, R., Pearlson, G., and Adali, T. (2014). The chronnectome: time-varying connectivity networks as the next frontier in fMRI data discovery. *Neuron* 84, 262–274. doi: 10.1016/j.neuron.2014.10.015

Calhoun, V. D., Potluru, V. K., Phlypo, R., Silva, R. F., Pearlmutter, B. A., Caprihan, A., et al. (2013). Independent component analysis for brain fMRI does indeed select for maximal independence. *PLoS ONE* 8, e73309 doi: 10.1371/annotation/52c7b854-2d52-4b49-9f9f-6560830f9428

Cardoso, J.-F. (2001). "The three easy routes to independent component analysis, contrasts and geometry," in *Proc. ICA 2001* (San Diego, CA), 1–6.

Carroll, J. D., and Chang, J. J. (1970). Analysis of individual differences in multidimensional scaling *via* an N-way generalization of "Eckart-Young" decomposition. *Psychometrika* 35, 283–319. doi: 10.1007/BF02310791

Chang, C., and Glover, G. H. (2010). Time-frequency dynamics of resting-state brain connectivity measured with fMRI. *NeuroImage* 50, 81–98. doi: 10.1016/j.neuroimage.2009.12.011

Chatzichristos, C., Kofidis, E., Morante, M., and Theodoridis, S. (2019). Blind fMRI source unmixing *via* higher-order tensor decompositions. *J. Neurosci. Methods* 315, 17–47. doi: 10.1016/j.jneumeth.2018.12.007

Chew, P. A., Bader, B. W., Kolda, T. G., and Abdelali, A. (2007). "Cross-language information retrieval using PARAFAC2," in *KDD'07: Proceedings of the 13th ACM SIGKDD International Conference on Knowledge Discovery and Data Mining* (San Jose, CA), 143–152. doi: 10.1145/1281192.1281211

Comon, P. (1994). Independent component analysis, a new concept? *Signal Process.* 36, 287–314. doi: 10.1016/0165-1684(94)90029-9

Comon, P. (2014). Tensors: a brief introduction. *Signal Process. Mag.* 31, 44–53. doi: 10.1109/MSP.2014.2298533

Cong, F., Lin, Q.-H., Kuang, L.-D., Gong, X.-F., Astikainen, P., and Ristaniemi, T. (2015). Tensor decomposition of EEG signals: a brief review. *J. Neurosci. Methods* 248, 59–69. doi: 10.1016/j.jneumeth.2015.03.018

Correa, N., Adalı, T., and Calhoun, V. D. (2007). Performance of blind source separation algorithms for fMRI analysis using a group ICA method. *Magn. Reson. Imaging* 25, 684–694. doi: 10.1016/j.mri.2006.10.017

De Vos, M., Vergult, A., De Lathauwer, L., De Clercq, W., Van Huffel, S., Dupont, P., et al. (2007). Canonical decomposition of ictal scalp EEG reliably detects the seizure onset zone. *NeuroImage* 37, 844–854. doi: 10.1016/j.neuroimage.2007.04.041

Friedman, L., Glover, G. H., and Consortium, F. (2006). Reducing interscanner variability of activation in a multicenter fMRI study: controlling for signal-to-fluctuation-noise-ratio (SFNR) differences. *Neuroimage* 33, 471–481. doi: 10.1016/j.neuroimage.2006.07.012

Friedman, L., Stern, H., Brown, G. G., Mathalon, D. H., Turner, J., Glover, G. H., et al. (2008). Test-retest and between-site reliability in a multicenter fMRI study. *Human Brain Mapp*. 29, 958–972. doi: 10.1002/hbm.20440

Friston, K. J., and Frith, C. D. (1995). Schizophrenia: a disconnection syndrome? *Clin. Neurosci*. 3, 89–97.

Fu, G.-S., Anderson, M., and Adali, T. (2014). Likelihood estimators for dependent samples and their application to order detection. *IEEE Trans. Signal Process*. 62, 4237–4244. doi: 10.1109/TSP.2014.2333551

Geddes, J., Einevoll, G., Acar, E., and Stasik, A. (2020). Multi-linear population analysis (MLPA) of LFP data using tensor decompositions. *Front. Appl. Math. Stat*. 6, 41 doi: 10.3389/fams.2020.00041

Gollub, R. L., Shoemaker, J. M., King, M. D., White, T., Ehrlich, S., Sponheim, S. R., et al. (2013). The MCIC collection: a shared repository of multi-modal, multisite brain image data from a clinical investigation of schizophrenia. *Neuroinformatics* 11, 367–388. doi: 10.1007/s12021-013-9184-3

Harshman, R. A. (1970). Foundations of the PARAFAC procedure: Models and conditions for an "explanatory" multi-modal factor analysis. *UCLA Work. Pap. Phonet*. 16, 1–84.

Harshman, R. A. (1972). PARAFAC2: Mathematical and technical notes. *UCLA Work. Pap. Phonet*. 22, 30–47.

Harshman, R. A., and De Sarbo, W. S. (1984). "An application of PARAFAC to a small sample problem, demonstrating preprocessing, orthogonality constraints, and split-half diagnostic techniques," in *Research Methods for Multimode Data Analysis* (New York, NY: Praeger), 602–642.

Helwig, N. E., and Snodgress, M. A. (2019). Exploring individual and group differences in latent brain networks using cross-validated simultaneous component analysis. *NeuroImage* 201, 116019. doi: 10.1016/j.neuroimage.2019.116019

Hitchcock, F. L. (1927). The expression of a tensor or a polyadic as a sum of products. *J. Math. Phys*. 201, 116019 doi: 10.1002/sapm192761164

Hossain, K., Bhinge, S., Long, Q., Calhoun, V. D., and Adali., T. (2022). "Data-driven spatio-temporal dynamic brain connectivity analysis using fALFF: application to sensorimotor task data," in *CISS 2022: 56th Annual Conference on Information Sciences and Systems* (Princeton, NJ).

Hunyadi, B., Dupont, P., Van Paesschen, W., and Van Huffel, S. (2017). Tensor decompositions and data fusion in epileptic electroencephalography and functional magnetic resonance imaging data. *WIREs Data Mining Knowl. Discov*. 7, e1197. doi: 10.1002/widm.1197

Hutchison, R. M., Womelsdorf, T., Allen, E. A., Bandettini, P. A., Calhoun, V. D., Corbetta, M., et al. (2013a). Dynamic functional connectivity: promise, issues, and interpretations. *NeuroImage* 80, 360–378. doi: 10.1016/j.neuroimage.2013.05.079

Hutchison, R. M., Womelsdorf, T., Gati, J. S., Everling, S., and Menon, R. S. (2013b). Resting-state networks show dynamic functional connectivity in awake humans and anesthetized macaques. *Hum. Brain Mapp*. 34, 2154–2177. doi: 10.1002/hbm.22058

Iraji, A., Miller, R., Adali, T., and Calhoun, V. D. (2020). Space: a missing piece of the dynamic puzzle. *Trends Cogn. Sci*. 24, 135–149. doi: 10.1016/j.tics.2019.12.004

Jia, C., Akhonda, M. A. B. S., Levin-Schwartz, Y., Long, Q., Calhoun, V. D., and Adali, T. (2021). Consecutive independence and correlation transform for multimodal data fusion: discovery of one-to-many associations in structural and functional imaging data. *Appl. Sci*. 11, 8382 doi: 10.3390/app11188382

Kamstrup-Nielsen, M. H., Johnsen, L. G., and Bro, R. (2012). Core consistency diagnostic in PARAFAC2. *J. Chemometr*. 27, 99–105. doi: 10.1002/cem.2497

Kiers, H. A., Ten Berge, J. M., and Bro, R. (1999). PARAFAC2 - part i. a direct fitting algorithm for the PARAFAC2 model. *J. Chemometr*. 13, 275–294. doi: 10.1002/(SICI)1099-128X(199905/08)13:3/4<275::AID-CEM543>3.0.CO;2-B

Kim, T., Eltoft, T., and Lee, T.-W. (2006). "Independent vector analysis: an extension of ICA to multivariate components," in *Independent Component Analysis and Blind Signal Separation*, eds J. Rosca, D. Erdogmus, J. C. Príncipe, and S. Haykin (Berlin; Heidelberg: Springer Berlin Heidelberg), 165–172. doi: 10.1007/11679363_21

Kiviniemi, V., Vire, T., Remes, J., Elseoud, A. A., Starck, T., Tervonen, O., et al. (2011). A sliding time-window ICA reveals spatial variability of the default mode network in time. *Brain Connect*. 1, 339–347. doi: 10.1089/brain.2011.0036

Kolda, T. G., and Bader, B. W. (2009). Tensor decompositions and applications. *SIAM Rev*. 51, 455–500. doi: 10.1137/07070111X

Lehmann, I., Acar, E., Hasija, T., Akhonda, M. A., Calhoun, V. D., Schreier, P. J., et al. (2022). "Multi-task fMRI data fusion using IVA and PARAFAC2," in *ICASSP'22: Proceedings of the IEEE International Conference on Acoustics, Speech and Signal Processing* (Singapore).

Li, L., Hoefsloot, H., de Graaf, A. A., Acar, E., and Smilde, A. K. (2022). Exploring dynamic metabolomics data with multiway data analysis: a simulation study. *BMC Bioinformatics* 23, 31. doi: 10.1186/s12859-021-04550-5

Li, X.-L., and Adali, T. (2010). Independent component analysis by entropy bound minimization. *IEEE Trans. Signal Process*. 58, 5151–5164. doi: 10.1109/TSP.2010.2055859

Li, Y.-O., Adalı, T., and Calhoun, V. D. (2007). Estimating the number of independent components for fMRI data. *Hum. Brain Mapp*. 28, 1251–1266. doi: 10.1002/hbm.20359

Long, Q., Bhinge, S., Calhoun, V. D., and Adali, T. (2020). Independent vector analysis for common subspace analysis: application to multi-subject fMRI data yields meaningful subgroups of schizophrenia. *NeuroImage* 216, 116872. doi: 10.1016/j.neuroimage.2020.116872

Long, Q., Bhinge, S., Calhoun, V. D., and Adali, T. (2021). Graph-theoretical analysis identifies transient spatial states of resting-state dynamic functional network connectivity and reveals dysconnectivity in schizophrenia. *J. Neurosci. Methods* 350:109039. doi: 10.1016/j.jneumeth.2020.109039

Lurie, D. J., Kessler, D., Bassett, D. S., Betzel, R. F., Breakspear, M., Kheilholz, S., et al. (2020). Questions and controversies in the study of time-varying functional connectivity in resting fMRI. *Netw. Neurosci*. 4, 30–69. doi: 10.1162/netn_a_00116

Ma, S., Calhoun, V. D., Phlypo, R., and Adali, T. (2014). Dynamic changes of spatial functional network connectivity in healthy individuals and schizophrenia patients using independent vector analysis. *NeuroImage* 90, 196–206. doi: 10.1016/j.neuroimage.2013.12.063

Madsen, K., Churchill, N., and Mørup, M. (2017). Quantifying functional connectivity in multi-subject fMRI data using component models. *Hum. Brain Mapp*. 38, 882–899. doi: 10.1002/hbm.23425

McKeown, M. J., Makeig, S., Brown, G. G., Jung, T. P., Kindermann, S. S., Bell, A. J., et al. (1998). Analysis of fMRI data by blind separation into independent spatial components. *Hum. Brain Mapp*. 6, 160–188. doi: 10.1002/(SICI)1097-0193(1998)6:3<160::AID-HBM5>3.0.CO;2-1

Miwakeichi, F., Martínez-Montes, E., Valdés-Sosa, P. A., Nishiyama, N., Mizuhara, H., and Yamaguchi, Y. (2004). Decomposing EEG data into space-time-frequency components using parallel factor analysis. *NeuroImage* 22, 1035–1045. doi: 10.1016/j.neuroimage.2004.03.039

Möcks, J. (1988). Topographic components model for event-related potentials and some biophysical considerations. *IEEE Trans. Biomed. Eng*. 35, 482–484. doi: 10.1109/10.2119

Mørup, M., Hansen, L. K., Herrmann, C. S., Parnas, J., and Arnfred, S. M. (2006). Parallel factor analysis as an exploratory tool for wavelet transformed event-related EEG. *NeuroImage* 29, 938–947. doi: 10.1016/j.neuroimage.2005.08.005

Pearlson, G. D., and Calhoun, V. (2007). Structural and functional magnetic resonance imaging in psychiatric disorders. *Can. J. Psychiatry* 52, 158–166. doi: 10.1177/070674370705200304

Perros, I., Papalexakis, E. E., Wang, F., Vuduc, R., Searles, E., Thompson, M., et al. (2017). "SPARTan: scalable PARAFAC2 for large & sparse data," in *KDD'2017: Proceedings of the 23rd ACM SIGKDD International Conference on Knowledge Discovery and Data Mining* (Halifax, NS), 375–384.

Preti, M. G., Bolton, T. A. W., and Van De Ville, D. (2017). The dynamic functional connectome: state-of-the-art and perspectives. *NeuroImage* 160, 41–54. doi: 10.1016/j.neuroimage.2016.12.061

Price, N. D., Magis, A. T., Earls, J. C., Glusman, G., Levy, R., Lausted, C., et al. (2017). A wellness study of 108 individuals using personal, dense, dynamic data clouds. *Nat. Biotechnol*. 35, 747–756. doi: 10.1038/nbt.3870

Roald, M., Bhinge, S., Jia, C., Calhoun, V. D., Adali, T., and Acar, E. (2020). "Tracing network evolution using the PARAFAC2 model," in *ICASSP 2020: Proceedings of the IEEE International Conference on Acoustics, Speech and Signal Processing* (Barcelona: IEEE), 1100–1104. doi: 10.1109/ICASSP40776.2020.9053902

Roald, M., Schenker, C., Cohen, J. E., and Acar, E. (2021). "PARAFAC2 AO-ADMM: constraints in all modes," in *EUSIPCO'21: Proceedings of the 29th European Signal Processing Conference* (Dublin). doi: 10.23919/EUSIPCO54536.2021.9615927

Rossetti, G., and Cazabet, R. (2018). Community discovery in dynamic networks: a survey. *ACM Comput. Surveys* 51, 35 doi: 10.1145/3172867

Sakoglu, U., Pearlson, G. D., Kiehl, K. A., Wang, Y. M., Michael, A. M., and Calhoun, V. D. (2010). A method for evaluating dynamic functional network connectivity and task-modulation: application to schizophrenia. *Magn. Reson. Mater. Phys. Biol. Med.* 23, 351–366. doi: 10.1007/s10334-010-0197-8

Song, X.-W., Dong, Z.-Y., Long, X.-Y., Li, S.-F., Zuo, X.-N., Zhu, C.-Z., et al. (2011). REST: a toolkit for resting-state functional magnetic resonance imaging data processing. *PLoS ONE* 6, e25031. doi: 10.1371/journal.pone.0025031

Tabbal, J., Kabbara, A., Khalil, M., Benquet, P., and Hassan, M. (2021). Dynamics of task-related electrophysiological networks: a benchmarking study. *NeuroImage* 231, 117829. doi: 10.1016/j.neuroimage.2021.117829

Timmerman, M. E., and Kiers, H. A. L. (2003). Four simultaneous component models for the analysis of multivariate time series from more than one subject to model intraindividual and interindividual differences. *Psychometrika* 68, 105–121. doi: 10.1007/BF02296656

Wax, M., and Kailath, T. (1985). Detection of signals by information theoretic criteria. *IEEE Trans. Acoust. Speech Signal Process.* 33, 387–392. doi: 10.1109/TASSP.1985.1164557

Weis, M., Jannek, D., Roemer, F., Guenther, T., Haardt, M., and Husar, P. (2010). "Multi-dimensional PARAFAC2 component analysis of multi-channel EEG data including temporal tracking," in *Proceedings of 32nd Annual International Conference of the IEEE EMBS* (Buenos Aires: IEEE), 5375–5378. doi: 10.1109/IEMBS.2010.5626484

Yin, K., Afshar, A., Ho, J. C., Cheung, W. K., Zhang, C., and Sun, J. (2020). "LogPar: logistic PARAFAC2 factorization for temporal binary data with missing values," in *KDD'20: Proceedings of the 26th ACM SIGKDD International Conference on Knowledge Discovery and Data Mining*, 1625–1635. doi: 10.1145/3394486.3403213

Zhu, Y., Liu, J., Mathiak, K., , Ristaniemi, T., and Cong, F. (2019). Deriving electrophysiological brain network connectivity *via* tensor component analysis during freely listening to music. *IEEE Trans. Neural Syst. Rehabil. Eng.* 28, 409–418. doi: 10.1109/TNSRE.2019.2953971

Zhu, Y., Liu, J., Ye, C., Mathiak, K., Astikainen, P., Ristaniemi, T., and Cong, F. (2020). Discovering dynamic task-modulated functional networks with specific spectral modes using MEG. *NeuroImage* 218, 116924 doi: 10.1016/j.neuroimage.2020.116924

Zou, Q.-H., Zhu, C.-Z., Yang, Y., Zuo, X.-N., Long, X.-Y., Cao, Q.-J., et al. (2008). An improved approach to detection of amplitude of low-frequency fluctuation (ALFF) for resting-state fMRI: fractional ALFF. *J. Neurosci. Methods* 172, 137–141. doi: 10.1016/j.jneumeth.2008.04.012

Conflict of Interest: The authors declare that the research was conducted in the absence of any commercial or financial relationships that could be construed as a potential conflict of interest.

Publisher's Note: All claims expressed in this article are solely those of the authors and do not necessarily represent those of their affiliated organizations, or those of the publisher, the editors and the reviewers. Any product that may be evaluated in this article, or claim that may be made by its manufacturer, is not guaranteed or endorsed by the publisher.

Advantages of publishing in Frontiers

OPEN ACCESS
Articles are free to read for greatest visibility and readership

FAST PUBLICATION
Around 90 days from submission to decision

HIGH QUALITY PEER-REVIEW
Rigorous, collaborative, and constructive peer-review

TRANSPARENT PEER-REVIEW
Editors and reviewers acknowledged by name on published articles

Frontiers
Avenue du Tribunal-Fédéral 34
1005 Lausanne | Switzerland

Visit us: www.frontiersin.org
Contact us: frontiersin.org/about/contact

REPRODUCIBILITY OF RESEARCH
Support open data and methods to enhance research reproducibility

DIGITAL PUBLISHING
Articles designed for optimal readership across devices

FOLLOW US
@frontiersin

IMPACT METRICS
Advanced article metrics track visibility across digital media

EXTENSIVE PROMOTION
Marketing and promotion of impactful research

LOOP RESEARCH NETWORK
Our network increases your article's readership